Chapters 2 & 3 are substantially based upon:

Andersen, J. A. and Z. Kuang, 2008: A Toy Model of the Instability in the Equatorially Trapped Convectively Coupled Waves on the Equatorial Beta Plane, *J. Atmos. Sci.*, **65**, 3736-3757, and

Andersen, J. A. and Z. Kuang, 2012: Moist Static Energy Budget of MJO-like disturbances in the atmosphere of a zonally symmetric aquaplanet, *J. Climate*, **25**, 2782–2804, doi: 10.1175/JCLI-D-11-00168.1 respectively.

Professor Zhiming Kuang Joseph Andersen

Investigations of the Convectively Coupled Equatorial Waves and the Madden-Julian Oscillation

Abstract

The Madden-Julian Oscillation (MJO) and the Convectively Coupled Equatorial Waves (CCEW) are coherent structures of convection and various large-scale fields. These phenomena are not well understood, despite their importance to the tropical climate.

A toy model of the CCEW consisting of a pair of shallow water wave modes coupled by a simple convective parameterization is considered. The linear behavior of the system is analyzed, showing a growth spectrum that is similar to the spectrum that is observed.

To explore the processes involved in propagation and maintenance of the MJO disturbance, we analyze the MSE budget of the disturbance within a numerical model. In an idealized experiment, the column-integrated long-wave heating is the only significant source of column-integrated MSE acting to maintain the MJO-like anomaly balanced against the combination of column-integrated horizontal and vertical advection of MSE and Latent Heat Flux. Eastward propagation of the MJO-like disturbance is associated with MSE generated by both column-integrated horizontal and vertical advection of MSE, with the column long-wave heating generating MSE that retards the propagation.

The contribution to the eastward propagation by the column-integrated horizontal advection term is dominated by meridional advection of MSE by anomalous synoptic eddies caused by the suppression of eddy activity ahead of the MJO convection. This suppression is linked to the barotropic conversion mechanism; with the gradients of the low frequency wind experienced by the synoptic eddies within the MJO envelope acting to modulate the Eddy Kinetic Energy. The meridional eddy advection's contribution to poleward propagation is dominated by the mean state's (meridionally varying) eddy activity acting on the anomalous MSE gradients associated with the MJO.

In a follow-up experiment, the variations in the propagation speed of MJO with variations in the imposed SST distribution are seen to be driven by the variations in meridional advection of the mean MSE profile by the MJO-related winds, which are in turn dominated by the variations in the mean MSE profile due to the variations of the SST.

A brief investigation of the MSE budget for a more realistic case shows an increase in the MSE sink due to meridional advection as the MJO progresses from genesis over the Indian Ocean to decay in the central Pacific. The increase in this sink appears to be the cause of MJO's demise.

Acknowledgements

General

I want to thank my family: Allan, Cheryl, Peta, Mir, Robert, and Thomas for their constant support throughout my time working on this project.

I thank all members of the Kuang group – past and present – for their assistance and feedback throughout the time I have worked here. I also want to thank the administrations of the Physics and Earth and Planetary Sciences departments for their continued assistance and support throughout my time at Harvard. Specific thanks go to Sheila Ferguson for her encouragement and generally making sure that my progress here continued.

Chapter 2

This work was partly supported by the Modeling, Analysis, and Prediction (MAP) Program in the NASA Earth Science Division and by NSF Grant ATM-0754332. The author thanks William Boos, David Romps, and Christopher Walker for helpful comments and suggestions during the drafting of this paper. Comments by Matthew Wheeler, David Raymond, and an anonymous third reviewer also improved the paper. The discussions of the moist static energy budget and wave-CISK were prompted by conversations with Adam Sobel, Chris Bretherton, and David Raymond. Comments by Chris Bretherton considerably sharpened our view on wave-CISK.

Chapter 3

The author thanks Marat Khairoutdinov and the CMMAP team for making the SPCAM model available; George Kiladis and an anonymous reviewer for their useful comments during the review process; and Mary Moore and Ji Nie for providing valuable feedback on drafts of this paper. This research was supported by NSF grant ATM-0754332. The Harvard Odyssey cluster provided the computing resources for this study.

Chapter 4

The author thanks Marat Khairoutdinov and the CMMAP team for making the SPCAM model available. This research was supported by NSF grant ATM-0754332. The Harvard Odyssey cluster provided the computing resources for this study.

Chapter 5

The author thanks Marat Khairoutdinov and the CMMAP team for making the SPCAM model available. This research was supported by NSF grant ATM-0754332. The Harvard Odyssey cluster provided the computing resources for this study.

Chapter 6

The author thanks Eric Maloney for his input into the discussion of future projects extending the MJO MSE budget analysis

Table of Contents

List of Figures

List of Tables

List of Acronyms

While care has been taken to define acronyms in the text where they first appear, we have collected them here also, to assist the reader.

ARM:	Atmospheric Radiation Measurment (Climate Research Facility)
CAM:	Community Atmospheric Model
CAPE:	Convective Available Potential Energy
CISK:	Conditional Instability of the Second Kind (e.g. Lindzen 1974)
CCEW:	Convectively Coupled Equatorial Waves
CSRM:	Cloud System Resolving Model
ECHAM/OPYC:	*EC*MWF-*HAM*burg (GCM)/*O*cean model in iso*PCY*nal coordinates
ECMWF:	European Centre for Medium-range Weather Forecasting
EIG:	Eastward Inertio-Gravity (wave)
EKE:	Eddy Kinetic Energy
ER:	Equatorial Rossby (wave)
GCM:	General Circulation Model (or Global Climate Model)
GMS:	Gross Moist Stability
IG:	Inertia-Gravity (wave)
ITCZ:	Inter-Tropical Convergence Zone
KW:	Kelvin Wave
LHF:	Latent Heat Flux
LW:	Long Wave (as in radiation)
MCD:	Moist Convective Damping
MJO:	Madden-Julian Oscillation
MRG:	Mixed Rossby-Gravity (wave)
MSE:	Moist Static Energy
NCAR:	National Center for Atmospheric Research
NGMS:	Normalized Gross Moist Stability
NOAA:	National Oceanic and Atmospheric Administration
OLR:	Outgoing Longwave Radiation
SHF:	Sensible Heat Flux – flux of thermal energy
SP-CAM:	(Super Parameterized) Community Atmospheric Model
SST:	Sea Surface Temperature
SW:	Short Wave (as in Radiation)
TOGA-COARE:	Tropical Ocean Global Atmosphere-Coupled Ocean Atmosphere Response Experiment
WIG:	Westward Inertia-Gravity (wave)
WISHE:	Wind Induced Surface Heat Exchange (e.g. Emanuel *et al.* 1994)
U850:	zonal wind (U) at 850 hPa.

To paraphrase Kerry Emanuel:

There's a reason it's sometimes referred to as the Maddening-Julian Oscillation…

and:

If you ask 10 theorists about the MJO, you'll get at least 11 different explanations.

Chapter 1 - Introduction

This work describes an extended exploration of the fundamental mechanisms related to the existence of Convectively-Coupled Equatorial Waves (CCEW) and the Madden-Julian Oscillation (MJO) in the tropical atmosphere. In particular, the interactions between cumulus convection and the larger-scale atmospheric flows in the tropics are investigated in both a simplified wave model and numerical simulations of the atmosphere. These phenomena are important to many aspects of the tropical and sub-tropical climate, but many aspects of these systems are poorly understood.

In this chapter, I provide some motivation for this project and introduce a number of important concepts.

1.1 Observations of the Convectively Coupled Equatorial Waves

In the satellite record of outgoing longwave radiation (OLR; Liebmann and Smith 1996)—a good proxy for deep tropical convection (see, e.g., Arkin and Andanuy 1989)—there are patterns of enhanced convection and precipitation organized on planetary scales. The waves are easily visualized in Hovmöller diagrams of the equatorial OLR (figure 1-1). This figure shows the OLR signal averaged between 7.5^{o}S and 7.5^{o}N for approximately a year of the OLR record (early October 1990 to early November 1991). Along with this is shown the OLR filtered to the Kelvin Wave (KW) and MJO spectral regions (discussed below), showing more clearly the presence of coherent waves of convection traversing the tropics.

The strongest and largest of these convective structures propagate eastwards at about 5 m/s with periods in the range of 30 to 90 days from the Indian Ocean to the central Pacific, coupled to planetary scale wind, temperature, and moisture anomalies. This disturbance is the MJO, which plays an important role in the global weather and climate (see below), so correctly simulating its behavior is an important goal for climate models. However, the MJO seen in most models is too weak and propagates too fast (e.g. Hayashi and Sumi 1986, Lau and Lau. 1986, Slingo *et al.* 1996, Maloney and Hartman 2001, Waliser *et al.* 2003, Zhang *et al.* 2006, Lin *et al.* 2006). The quality of the simulated MJO seems to be very sensitive to the details of the representation of convection (e.g. Wang and Schlesinger 1999, Maloney and Hartmann 2001, Zhu *et al.* 2009), indicating that the deficiencies in the modeling of the MJO may stem from a lack of understanding how convection interacts with the larger scale flows in reality.

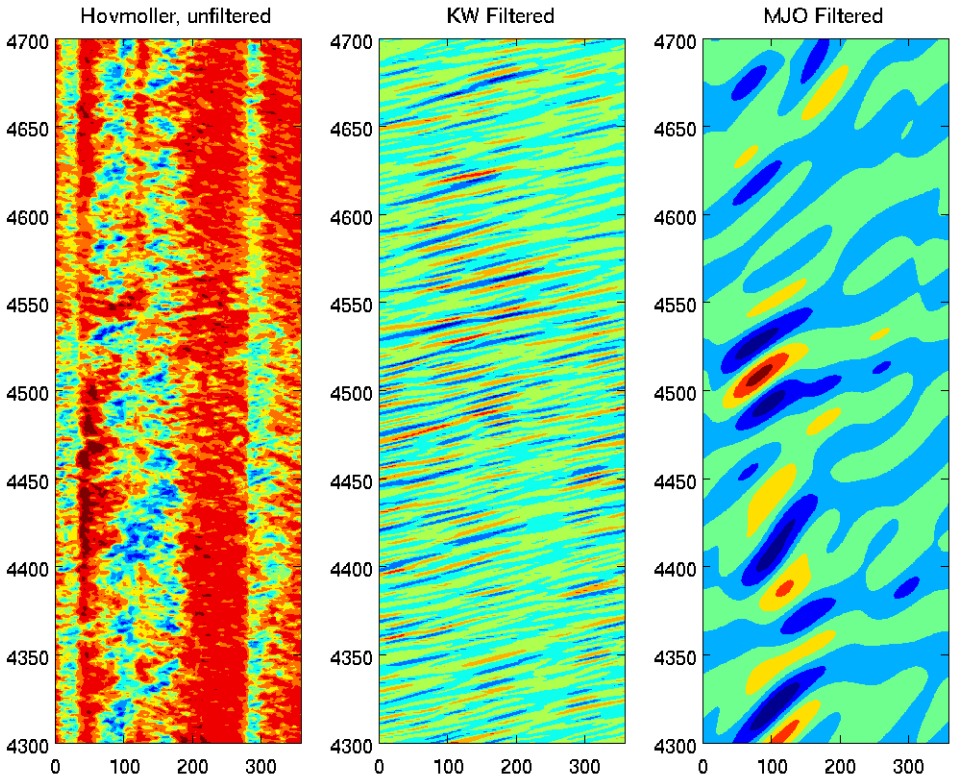

Figure 1-1. Hovmöller diagrams. a) Unfiltered OLR, b) Kelvin Wave-filtered OLR, and c) MJO-filtered OLR.

1.2 The equatorial wave spectrum

Less easily seen in the raw data are a variety of other waves, collectively referred to as the Convectively Coupled Equatorial Waves (CCEW), which propagate in both easterly and westerly directions with a variety of wavelengths, frequencies, and meridional structures. A variety of methods for observing/measuring these waves have been developed.

If the satellite OLR data within 15° of the equator is analyzed in zonal wavenumber–frequency space (Wheeler and Kiladis 1999, hereafter WK99; details in Appendix A) it shows a number of statistically significant peaks (figure 1-2). These propagating disturbances form a large part of the tropical synoptic-scale variation, organizing individual convective elements (typically 100 km across, persisting for a few hours) on large spatial (thousands of kilometers) and temporal (days) scales (e.g., Chang 1970; Nakazawa 1988). The wave activity peaks have been identified with the equatorially trapped waves of shallow water theory (see, e.g., WK99; Yang et al. 2007). Many of the properties of these waves are well described by rotating shallow water wave theories (Matsuno 1966 – details in Appendix B).

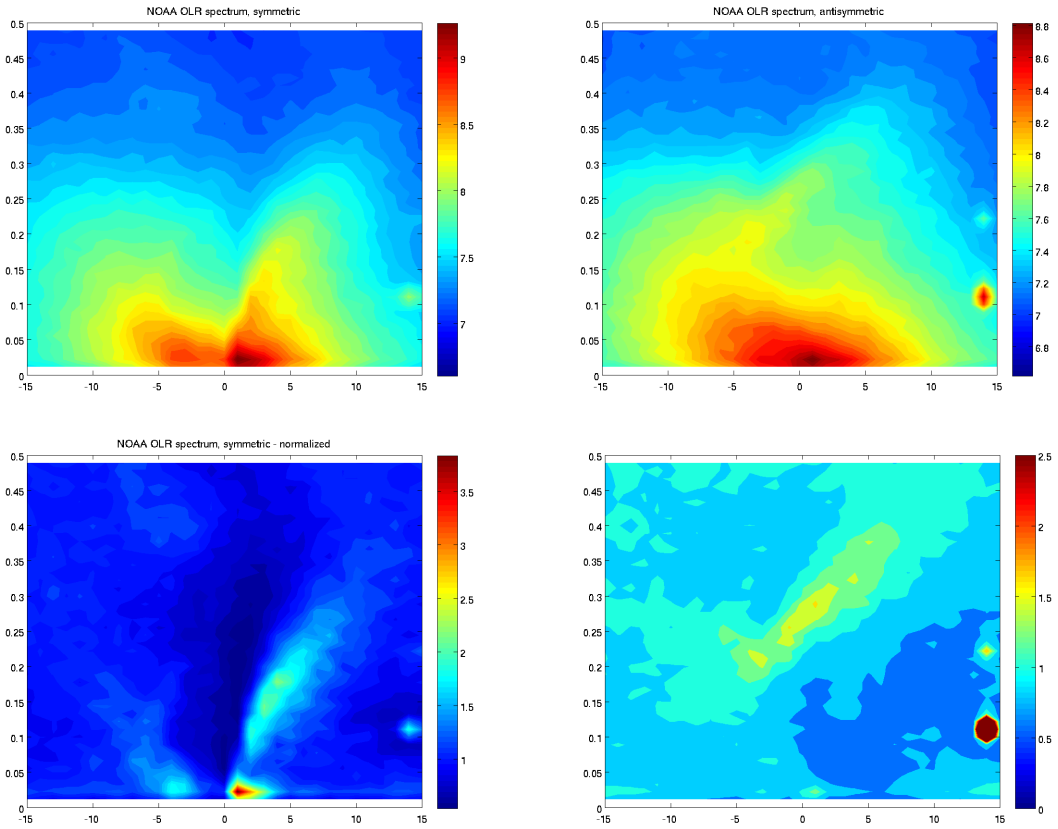

Figure 1-2.The time-space spectra of the satellite observed Outgoing Longwave Radiation (OLR), after WK99. The logarithm (base 10) of the spectral power for anomalies in OLR a) symmetric and b) anti-symmetric about the equator, averaged over the region from **15^o** S to **15^o** N; and the spectra divided by the assumed red background noise. The signals at wavenumber 14 are due to aliasing from the satellites' orbital motion.

The equatorially trapped shallow water waves arise from an analysis of the anomalies in temperature and wind of a zonally symmetric atmosphere linearized about a stationary mean state. Under the assumptions of constant stratification and a rigid upper boundary on the troposphere, the vertical structure equations can be separated from the horizontal dynamics, which are identical to the equations for shallow water modes, with the separation constant identified as the equivalent depth. Due to the rotation of the earth, the shallow water system has a number of specific modes propagating along the equator, as determined by Matsuno (1966). The convectively coupled shallow water waves tend to exist and propagate because of the interactions between convective heating and the temperature anomalies of the waves. The shallow water wave models are discussed in more detail in Chapter 2.

The strongest peak observed in the spectrum lies at small positive wavenumbers with in the 20-100 day region. This signal does not correspond to a Matsuno mode – instead it is identified with the Madden-Julian Oscillation (MJO).

1.3 The Madden-Julian Oscillation

1.3.A History

The disturbance known as the MJO was originally identified in rawinsonde data from Kanton Island ($3^oS, 172^oW$), as a coherent, significant, negative (out of phase) signal in the cospectrum of the lower and upper tropospheric winds at a frequency of about 50 days (Madden and Julian 1971, 1972, 2005). Evidence of the eastward

propagating cloudiness was found by Gruber (1974) and Zangvil (1975), both showing long wavelength (wavenumbers 1 and 2) intraseasonal signals.

1.3.B Importance

The MJO dynamics involve planetary scale circulations interacting with mesoscale convective systems and potentially the ocean, making it a challenging phenomenon to understand (e.g. Zhang 2005). However, understanding the MJO phenomena is important to our grasp of the tropical atmosphere and climate for many reasons. MJO related variations are among the dominant intraseasonal variabilities of the tropical ocean-atmosphere system, spanning the timescales between climate and weather (e.g. Lau and Wu 2010). For example, the MJO is seen to influence the rainfall over virtually all regions of the tropics, the subtropics and into the mid-latitudes: the Asian Monsoon (e.g. Lau and Chan 1986, Sui and Lau 1992, Lawrence and Webster 2002); the Australian Monsoon (e.g. Hendon and Liebmann 1990); over the Indonesian archipelagos (Hidayat and Kizu 2010); along the west coast of North America (Mo and Higgins 1998, Jones 2000, Bond and Vecchi 2003); in South America (Paegle et al. 2000, Liebmann et al 2004); and in Africa (Matthews 2004). The MJO has also been associated with El Nino-La Nina transitions (e.g. Kessler *et al.* 1995, Hendon *et al.* 2007, McPhaden 2008).

The MJO has also been observed to modulate the genesis of tropical cyclones in the Pacific, Atlantic, and Gulf of Mexico (e.g. Liebmann et al. 1994, Nieto Ferrira et al. 1996, Maloney and Hartmann 2000, Hall et al, 2001, Higgins and Shi 2001, Frank and Roundy 2006). It has been observed that improved forecasts of MJO dynamics

may help improve short term tropical cyclone forecasting (e.g. Leroy and Wheeler 2008). The MJO affects the global medium and long range weather forecasts (e.g. Ferranti et al. 1990, Hendon et al. 2000, Jones and Schemm 2000); modulates the global angular momentum and the length of the day (e.g. Langley et al. 1981, Gutzler and Ponte 1990, Weickmann et al. 1997); and modulates the Earth's electric and magnetic fields, with influence upon lightning activity (e.g. Anyamba et al. 2000).

The fact that the models cannot, in general, produce realistic MJO events limits their effectiveness for medium range prediction of the extreme events that can accompany the passage of an MJO event. It is apparent that improvements in the MJO simulated by the models will extend the range of useful predictions of events like tropical cyclones (e.g. Vitart *et al.* 2009).

1.3.C Character

MJO events are usually observed in the Indian and Western Pacific Oceans as large-scale, eastward propagating regions of strong, deep convection and precipitation separating regions of weak convection. The structure usually has a zonal wavenumber of 1 or 2, with a single active region existing at a time. An overturning zonal circulation that extends vertically through the entire troposphere connects the active and inactive phases. The circulation creates zonally converging winds in the boundary layer and lower troposphere (up to about 850 hPa) and zonally diverging winds at about 200 hPa (e.g. Madden and Julian 1972 and Zhang 2005). The coupled wind-convection system propagates at around 5 m/s. The MJO events can be clearly seen in Hovmöller plots of many observed quantities, such as equatorial zonal wind

(e.g., Xie and Arkin 1997), or as a very strong peak in wavenumber-frequency spectra of tropical variables such as OLR (e.g. WK99).

The description of the MJO as a purely eastward moving monolith of convection is not the whole picture. For example, the MJO convective region is a multiscale structure, consisting of an ensemble of convective systems moving at many different speeds in all directions (e.g. Nakazawa 1988). The convection in these mesoscale and smaller systems is enhanced by the large-scale conditions in the MJO active region and the motion of the active region is reflected in a general eastward trend in the locations these systems develop and then decay. Another important fact to consider is that MJO propagation is not always strictly eastwards - meridional motion, generally into the summer hemisphere, is observed over the east Pacific and over southern Asia in some seasons (typically boreal summer; Wang and Rui 1990a).

1.3.D Existing Theories

The MJO is one of the dominant structures in the tropical atmosphere and has been observed for almost four decades, so its structure has been quite well determined (e.g. Hendon and Salby 1994, Lau and Sui 1997, Yanai et al. 2000, Kikuchi and Takayuba 2004, Kiladis et al. 2005, Haertel et al. 2008), although a sufficiently accurate energy budget remains elusive. At the same time, the theoretical understanding of the mechanisms responsible for its growth and propagation has not kept pace (e.g., Zhang 2005, Waliser et al. 2006). As the MJO plays an important role in the global weather and climate, correctly simulating its behavior is an

important goal for climate models. In most models, however, the MJO – if present at all – is too weak and propagates too fast (e.g. Hayashi and Sumi 1986, Lau and Lau 1986, Slingo *et al.* 1996, Maloney and Hartman 2001, Waliser *et al.* 2003, Zhang *et al.* 2006, Lin *et al.* 2006).

Because the convectively coupled KW have many basic features in common with the MJO (propagation direction, scale, wind field structure), and because theories of the equatorial waves have shown some successes (e.g. Matsuno 1966, Wang 1988, Majda and Shefter 2001, Andersen and Kuang 2008, Kiladis et al. 2009; Also see Chapter 2), the KW and other equatorially trapped shallow water waves are commonly used as a fundamental part of MJO theories. However, the KW propagates much faster than the MJO and is quite distinct from the MJO in spectral space. Also, an analysis of the potential vorticity budget of the MJO (Zhang and Ling 2012) has shown that the dynamics of the MJO are distinct from those of the shallow water waves. This leads to the question - how does the convectively coupled KW differ from the MJO? For either of these wave types to exist in observations, some process or processes must supply energy (or an analogous quantity) to overcome dissipation selectively at the timescales, wavelengths and velocities of the disturbances. Most theories of the KW assume that the source of the energy for the wave comes from an interaction between convective heating and the large-scale temperature structure of the wave, with scale selection due to the varying sign of the heating/warm anomaly overlap. Such theories have had success replicating the nature of the KW (and other "rotating shallow water" modes) in simple models (e.g. Mapes 2000, Khouider and Majda 2006b, Kuang 2008b, Andersen and Kuang 2008).

Any theory of the MJO requires column Moist Static Energy (MSE) variance to be generated at intraseasonal and planetary scales, with slow eastward propagation. There are a number of potential sources of column MSE variability that are often considered:

1. An independently existing forcing such as a standing oscillation in the convection over the warm pool, with MJO propagation as a passive atmospheric response (e.g. Zhang and Hendon 1997);
2. The column MSE variability is generated by the coupling of convection and circulation. An example of this sort of mechanism is Wave-CISK (e.g. Lau and Peng 1987), where convection releases latent heat that drives further convection by creating more low-level convergence;
3. Wind Induced Surface Heat Exchange (WISHE; Emanuel 1987, Neelin et al. 1987), where surface wind anomalies lead to surface flux anomalies that may provide an energy source to the convection;
4. Instability arising from frictional moisture convergence feedback (e.g. Wang 1988);
5. Thermodynamic feedbacks - such as water vapor accumulation (Blade and Hartmann 1993) and convection-radiation feedback (Hu and Randall 1994, 1995, Raymond 2001).

1.3.E Poleward Propagation

While the eastward propagating MJO dominates the tropical intraseasonal variability, it is not the only significant source of variability on these timescales. For

example, there are prominent northward propagating oscillations during the Asian monsoon (Yasunari 1979, Lau and Chan 1986, Wang and Rui 1990a). It has been observed that the MJO eastward propagation weakens during boreal summer (Madden 1986, Wang and Rui 1990a) and a northward propagating feature in the intraseasonal frequencies becomes prominent over the Indian summer monsoon region (e.g. Yasanuri 1979, Sikka and Gadgil 1980, Krishnamurti and Subrahmanyam 1982, Goswami 2005). Several theories have been suggested to explain this observation:

Northward propagation as a result of feedback between the hydrological cycle and the dynamics over India (Webster 1983). Sensible heat flux in the boundary layer over land can destabilize the atmosphere ahead of the ascending zone, causing northward shifts in the convective region;

The interaction between equatorial moist KW and the monsoon flow can generate (in numerical experiments) unstable quasi-geostrophic baroclinic waves in the monsoon region, weakening the equatorial disturbance (Lau and Peng 1990);

In a model, continuous North West propagating Rossby waves are seen to emanate from an equatorial KW as it crosses the maritime continent, creating the northward moving rain-bands (Wang and Xie 1997);

Examination of the poleward propagating rain-bands in a high resolution cloud-system resolving model indicates that poleward propagation may be due to convectively coupled beta drift of low-level vorticity anomalies (Boos and Kuang 2010).

It seems likely that the poleward propagating modes originate from the same disturbance as the eastward propagating MJO (e.g. Lawrence and Webster 2002, Jiang et al. 2004). However, it is often observed that the poleward and eastward disturbances separate over the Indian Ocean and may propagate independently.

1.4 Wave-type Filtering

In order to see how the spectral signals translate into the space-time domain, we can filter the wavenumber-frequency data (after WK99). Typical filter regions are shown in figure 1-3, based upon the dispersion relationships for the Matsuno modes. The dispersion relationships used are for equivalent depths 8-90m. This wide range is chosen so as to encompass all of the observed wave activity. The symmetry (or anti-symmetry) about the equator of the various modes is enforced by separating the initial space-time records into symmetric and anti-symmetric parts. This separation is important, due to the small spectral separation between the modes in frequency space. For example, the Kelvin waves and the Eastward Mixed-Rossby Gravity waves would overlap, were it not for their different symmetry. Figure 1-4a shows the time variance of the Kelvin wave-filtered OLR for the observational record. Kelvin wave activity is strongest over the Indian Ocean and the West Pacific, with local maxima over the Amazon and Africa. Convectively coupled Kelvin Waves are less active over the East Pacific, where the equatorial cold tongue suppresses equatorial convection.

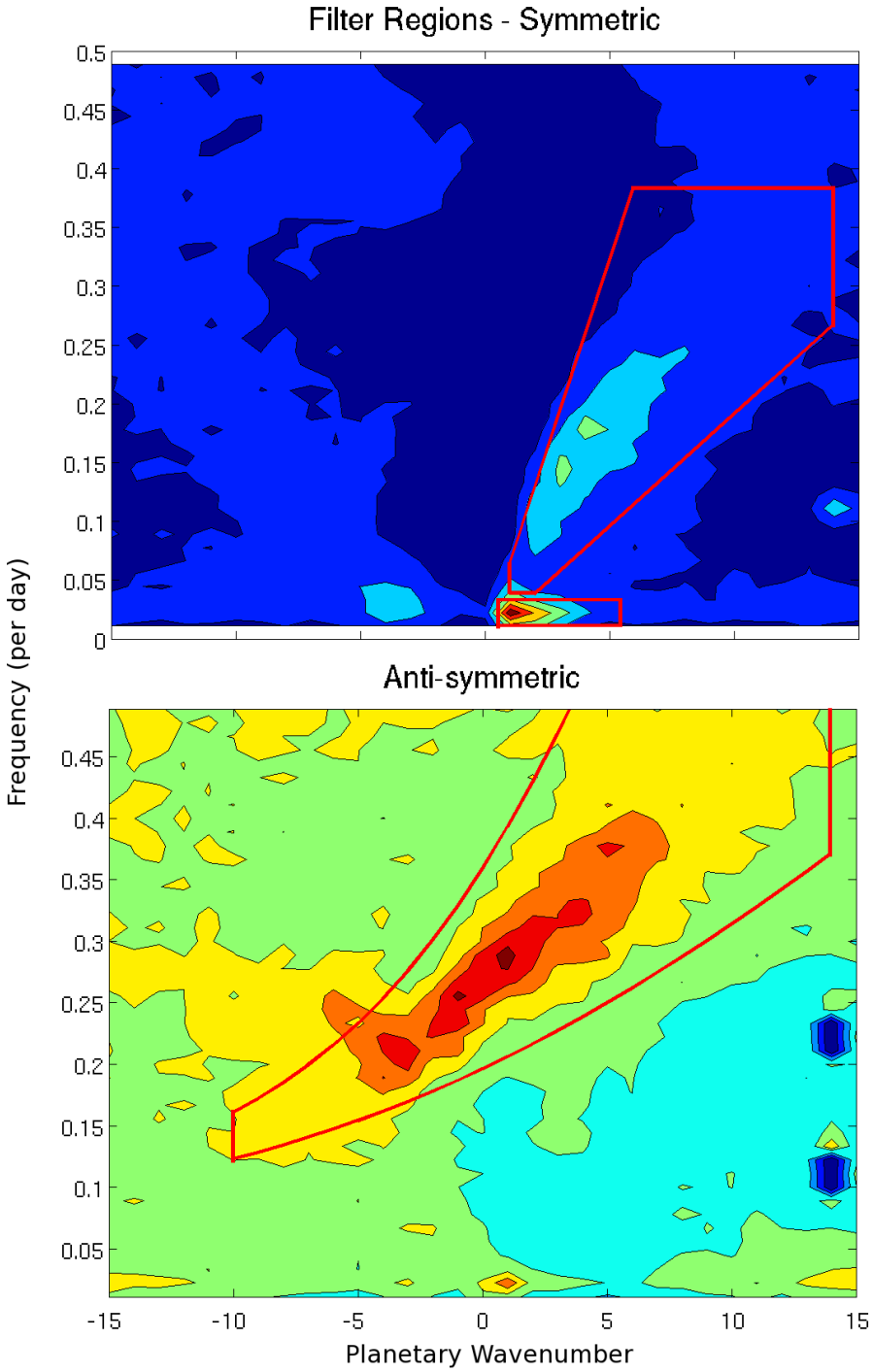

Figure 1-3. Symmetric and Antisymmetric parts of the OLR spectrum. Boxes indicate the filtering regions for Kelvin waves and the Madden-Julian Oscillation in the symmetric part and the Mixed-Rossby Gravity waves in the antisymmetric part.

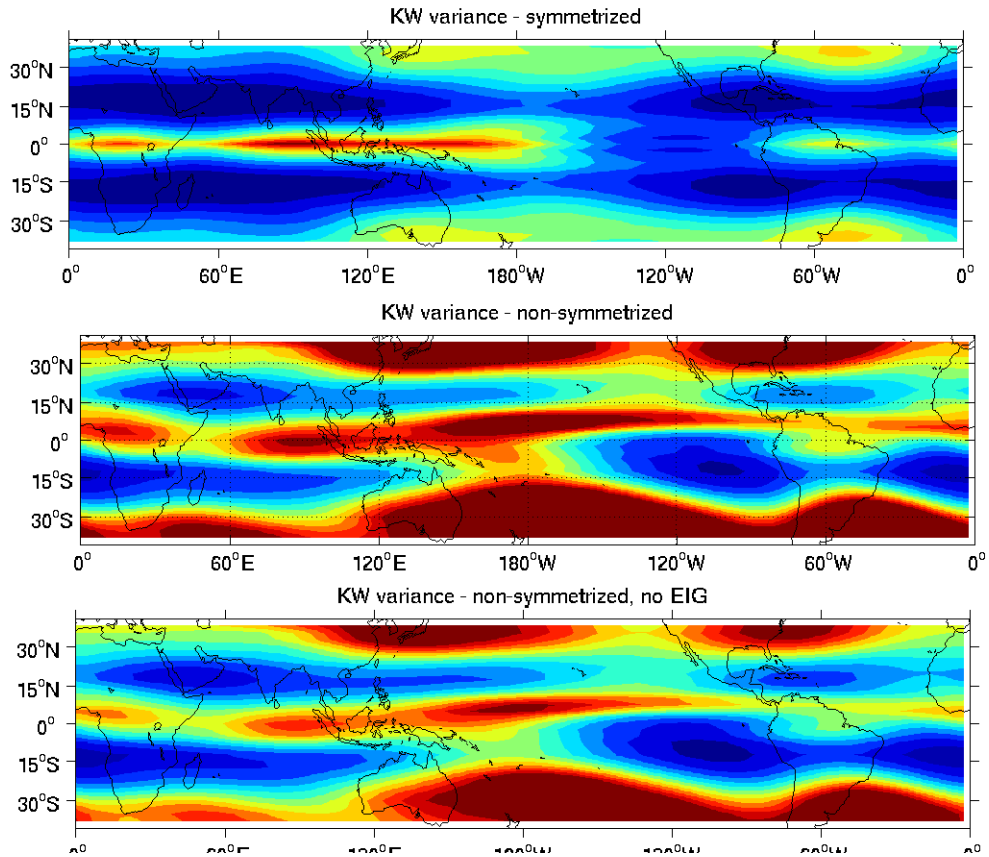

Figure 1-4. Time variance of the Kelvin wave filtered OLR. a) Filter applied to symmetric part only; b) Filter applied to both symmetric and anti-symmetric parts; c) Modified filter (skirting the MRG region) applied to both symmetric and anti-symmetric parts. Color scale goes from $\mathbf{20}\boldsymbol{Wm^{-2}}$ to $\mathbf{140}\boldsymbol{Wm^{-2}}$, saturating for the unsymmetrized variance.

In the non-symmetrized "Kelvin" filtered variance (figure 1-4b), the tropical region is dominated by a large variance signal located in the Northern Hemisphere, spanning the Pacific. This signal is also visible in the Atlantic and the western side of Africa. While it might be expected that this off equatorial signal is caused by contamination of the Kelvin signal by MRG wave variance, when the filter is modified to exclude the region of spectral space associated with MRG, the pattern of variance is almost unchanged. One explanation for this observation is that this activity lies largely atop the ITCZ region, which is predominantly in the northern hemisphere. The convectively coupled Kelvin waves, need not be symmetric about the equator, as they are coupled mixtures of the "dry" Kelvin waves with other wave types. In this case, there are some anti-symmetric waves coupled into the disturbance by the anti-symmetric nature of the convection modulated by the KW, leading to anti-symmetric heating. This is discussed further in Section 2.3.C.

The observed MJO resides largely within the region enclosed by wavenumbers 1-5 and frequencies 1/30 – 1/90 cycles per day. With no theoretical basis for expecting a particular symmetry, and observation of activity in the same spectral region of both the symmetric and anti-symmetric spectra, we want to allow the MJO to have both symmetric and anti-symmetric parts. Thus the same filter is applied to both parts of the spectrum (or, in practice, the unsymmetrized OLR data is used).

Figure 1-5 shows the variance of MJO filtered OLR, for the symmetrical part of the OLR (figure 1-5a) and for the non-symmetrized OLR (figure 1-5b). In either case, the MJO activity can be observed to increase in the Indian Ocean (moving west to east),

peaking over the Indonesian peninsula, and decaying over the western pacific towards the date line.

1.5 Moist Static Energy

MSE (denoted by h) in our analysis will be defined as:

$$h = c_p T + gZ + L_v q - L_f q_i, \tag{1.1}$$

where T is temperature, c_p is the specific heat at constant pressure, Z is the height, g is the gravitational acceleration, L_v and L_f are the latent heats of vaporization and sublimation (at 0°C), and q and q_i are the specific quantities of water vapor and ice respectively (this quantity is sometimes referred to as Frozen MSE). As constructed, the MSE is conserved under phase changes between the solid, liquid, and vapor phases of water and removal or addition of liquid water, all under hydrostatic motion. As a consequence, the column integral of h, $\langle h \rangle$, is approximately conserved in reality and in our model under convective adjustments. $\langle x \rangle$ represents the mass-weighted vertical integral of quantity x:

$$\langle x \rangle = \frac{1}{g} \int_{p_{top}}^{P_{surface}} x dp, \tag{1.2}$$

where the integral runs from some defined top of the atmosphere (for sufficiently high tops, the results do not depend upon the precise value chosen) to the surface and g is the gravitational acceleration. The residual terms arising from non-MSE-conserving effects are generally small compared to other energy budget terms and can usually be neglected (e.g. Neelin and Held 1987, Peters et al. 2008).

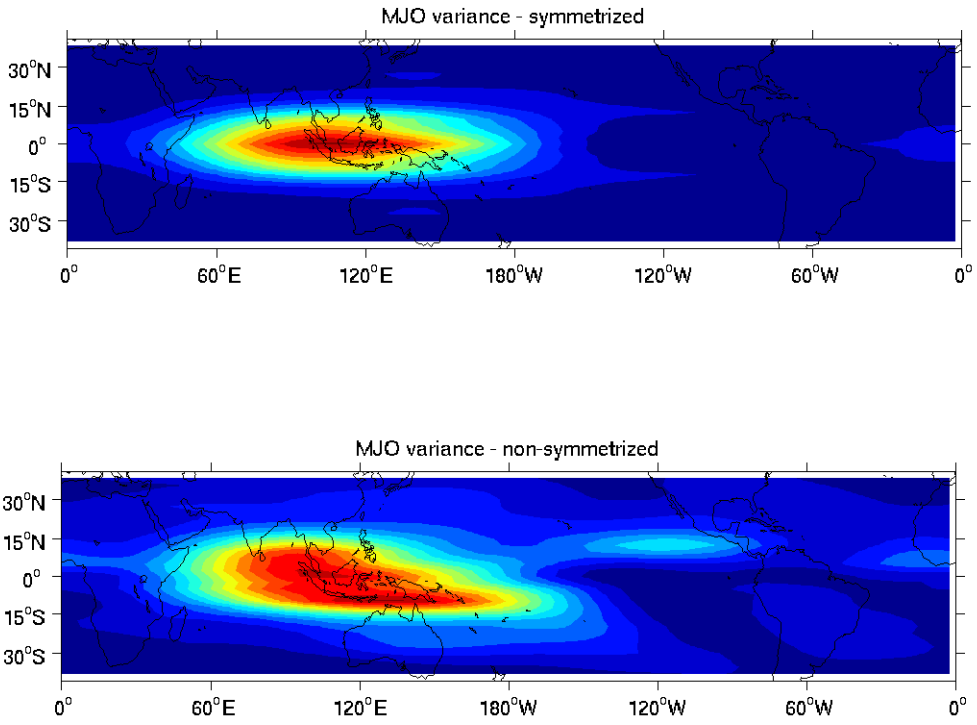

Figure 1-5. As figure 1-4 (a and b only), except for MJO filtered OLR.

1.6 Outline of document

Chapter 2 describes the development of a simple model of the Convectively Coupled Equatorial Waves based upon rotating shallow water waves and a simple convective parameterization, which combines the principle of convective quasi-equilibrium with a representation of the effects of lateral entrainment of environmental air by the rising convective parcel. This work was originally published as Andersen and Kuang (2008 and associated Corrigendum 2010).

Chapter 3 describes the investigation of the Moist Static Energy budget of the MJO observed in SP-CAM with a zonally symmetric SST, in order to determine the mechanisms that contribute to the maintenance and propagation of the MSE anomaly. This work has been published as Andersen and Kuang (2012)

Chapter 4 extends this analysis to further experiments, with variations in the SST profile used, in order to investigate further the mechanisms that contribute to the maintenance and propagation of the MJO anomaly.

Chapter 5 describes the analysis of the MJO in a realistic case. These two chapters will be described in publications currently in preparation.

Chapter 6 summarizes the work completed and discusses the potential future directions in which it can be taken.

Finally, there are a number of appendices that demonstrate detailed sections that would otherwise interrupt the flow of discussion in the main text.

Chapter 2 - Shallow Water Convectively Coupled Wave Model – Linear Analysis of a toy model

This chapter addresses the observation that the various wave types (e.g., Kelvin, Rossby, etc.) and wavenumbers show differing signal strength relative to a red background. It is hypothesized that this may be due to variations in the linear stability of the atmosphere in response to the various wave types depending on both the specific wave type and the wavenumber. A simple model of the convectively coupled waves on the equatorial beta plane is constructed to identify processes that contribute to this dependence. The linear instability spectrum of the resulting coupled system is evaluated by eigenvalue analysis. This analysis shows unstable waves with phase speeds, growth rates, and structures (vertical and horizontal) that are broadly consistent with the results from observations. The linear system, with an idealized single intertropical convergence zone (ITCZ) as a mean state, shows peak unstable Kelvin waves around zonal wavenumber 7 with peak growth rates of $\sim 0.08\ day^{-1}$ (e-folding time of ~13 days). The system also shows unstable Mixed Rossby–Gravity (MRG) and inertio-gravity waves with significant growth in the zonal wavenumber range from -15 (negative indicates westward phase speed) to $+10$ (positive indicates eastward phase speed). The peak MRG ($n = 0$) eastward inertio-gravity wave (EIG) growth rate is around one-third that of the Kelvin wave and occurs at zonal wavenumber 3. The Rossby waves in this system are almost stable, with very small growth-rates, and the Madden–Julian oscillation is not observed. Within this model, it is shown that in addition to the effect of the ITCZ configuration, the differing instabilities of the different wave modes are also related

to their different efficiency in converting input energy into divergent flow and also the efficiency with which the resulting convection couples to the temperature anomalies, generating more energy for the wave. This energy conversion efficiency difference is suggested as an additional factor that helps to shape the observed wave spectrum.

This work was originally published as Andersen and Kuang (2008; and associated Corrigendum 2010).

2.1 Introduction

As discussed in Section 1.1.2 and in Appendix A, if the satellite record of outgoing longwave radiation (OLR; Liebmann and Smith 1996)—a good proxy for deep tropical convection (see, e.g., Arkin and Andanuy 1989)—within 15° of the equator is analyzed in zonal wavenumber–frequency space (WK99) it shows a number of statistically significant peaks (figure 2-1). These propagating disturbances form a large part of the tropical synoptic-scale variation, organizing individual convective elements (typically 100 km across, persisting for a few hours) on large spatial (thousands of kilometers) and temporal (days) scales (e.g., Chang 1970; Nakazawa 1988). The wave activity peaks have been identified with the equatorially trapped waves of shallow water theory (see, e.g., WK99; Yang et al. 2007). Many of the properties of these waves are well described by rotating shallow water wave theories (Matsuno 1966). Here we attempt to address the observation that the various wave types (e.g., Kelvin, Rossby, etc.) and wavenumbers show differing amplitudes. It is hypothesized that this is due in part to the (linear) stability of the atmosphere to perturbations of the various wave types depending on the specific wave type and the wavenumber in question.

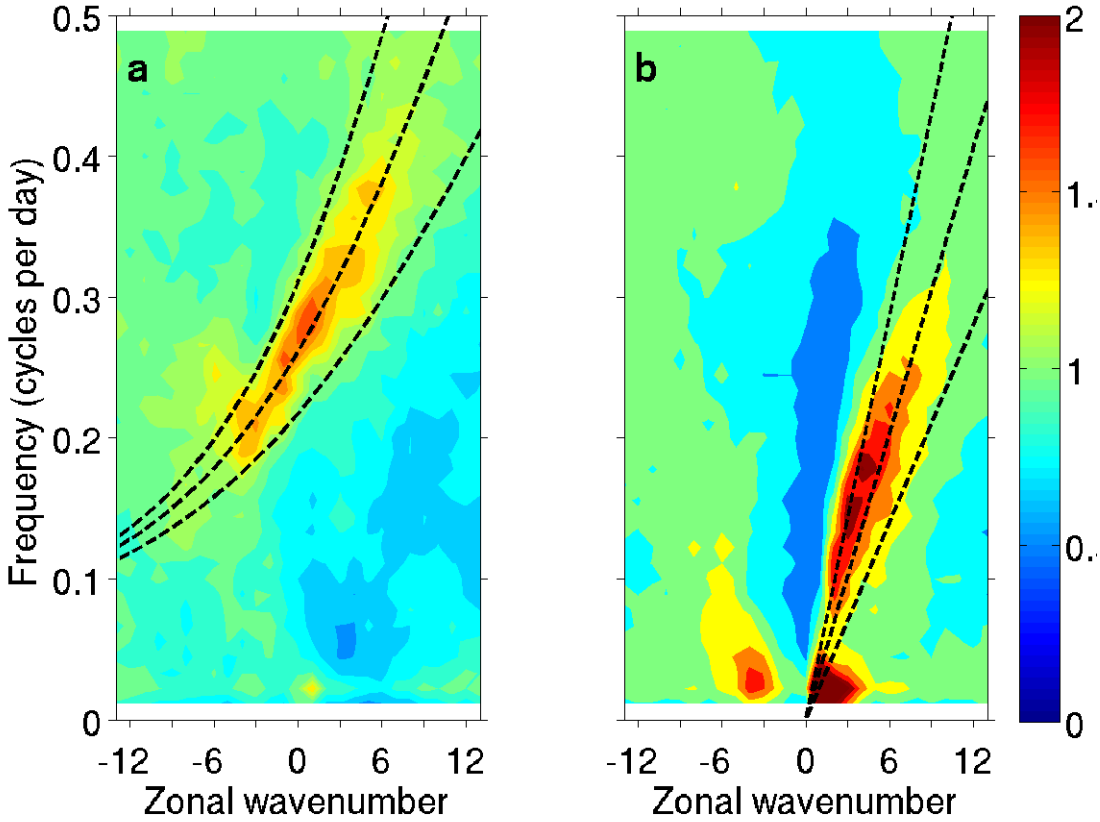

Figure 2-1. OLR power divided by background spectrum for signals that are (a) anti-symmetric and (b) symmetric about the equator. The power spectrum is averaged over the region 15°S to 15°N and is constructed from National Oceanic and Atmospheric Administration (NOAA) daily OLR data running from June 1974 to September 2011. Shallow water dispersion curves drawn are for equivalent depths of 12, 25, and 50m, in order of increasing frequency (After WK99).

We explore this using the simple model of the convectively coupled waves using the first two baroclinic vertical modes, mid-tropospheric moisture, and the sub-cloud layer developed in Kuang (2008b, hereafter K08b) extended to the equatorial beta plane. This model is part of a continuing effort in this field to construct models of minimal complexity to identify the basic instability mechanisms of these waves. There is a long history of such simple models, going back at least as far as 1969 (e.g., Yamasaki 1969; Hayashi 1970; Lindzen 1974; Neelin et al. 1987, Wang 1988; Mapes 2000; Majda and Shefter 2001; Khouider and Majda 2006a; Raymond and Fuchs 2007). The early models emphasized a first baroclinic structure that is of one sign over the full depth of the troposphere (e.g., Wang 1988; Neelin et al. 1987; Emanuel 1987). The importance of the second baroclinic component was recognized and included in the model of Mapes (2000), and an instability mechanism involving the second baroclinic temperature anomaly and deep convective and stratiform heating was identified (Mapes 2000). More recently, Khouider and Majda (2006a) included the interaction between free tropospheric moisture and deep convective and congestus heating in their model and found that moisture plays a major role in destabilizing the system. This is an important finding. However, the actual instability mechanism was not clearly identified. Khouider and Majda (2006a) described the process of a dry episode causing more congestus heating, which moistens and preconditions the free troposphere, leading to deep convection, which then returns the free troposphere to a dry condition. This description, while correct, does not reveal how the initial perturbation gets amplified and thus falls short of an

instability mechanism. This motivated the study of K08b, which continued the effort by Khouider and Majda (2006a) but sought to develop conceptually simple treatments of convection and to identify the basic instability mechanisms.

In K08b, the convective parameterization is based on the quasi-equilibrium (QE) concept—namely, that convection responds quickly to the changes in the large-scale flow and so can be considered to be in statistical equilibrium with the flow (Arakawa and Schubert 1974; Emanuel et al. 1994) by keeping the convective available potential energy (CAPE) constant for parcels rising from the boundary layer to the midtroposphere. The tropospheric moisture is included as an input to the convection calculation to represent the effect of entrainment of the drier tropospheric air into a rising convective cloud. This acts as a control on the depth of convection because with a moister mid-troposphere, updrafts lose less buoyancy from the entrainment of environmental air and can reach higher to form deep convection and subsequent stratiform rain; thus, for a given amount of lower-tropospheric convective heating, the upper-tropospheric heating will be greater.

Analysis in K08b identified a moisture–stratiform instability, in addition to the stratiform instability of Mapes (2000). To see it in its most basic form (as illustrated in figure 2-2) consider the horizontal propagation of a sinusoidal wave with a second-mode temperature structure in the vertical (figure 2-2a). The propagation of the wave modulates deep (first baroclinic) convective heating by perturbing the statistical equilibrium between the lower troposphere and the sub-cloud layer. More specifically, deep convection is enhanced behind a warm lower-tropospheric temperature anomaly (as large-scale ascent cools the lower troposphere) and is

reduced behind a cold lower-tropospheric temperature anomaly (figure 2-2b). The modulation on deep convection peaks a quarter-cycle behind temperature anomaly peaks. The combined effect of an enhanced deep convective heating and its induced vertical advection of moisture is to moisten the midtroposphere (figure 2-2c), leading to deeper (i.e. more stratiform) convection in a region where the initial temperature anomalies are positive in the upper troposphere and negative in the lower troposphere, amplifying the initial perturbation (figure 2-2d). It was also found that in addition to the Moist Convective Damping effect (MCD; e.g., Emanuel 1993; Neelin and Yu 1994) whereby the finite response time of convection damps high-frequency waves, the tendency of the second baroclinic mode convective heating to reduce existing midtropospheric moisture perturbations tends to reduce the instability at low wavenumbers. These two effects were suggested as contributors to the wavenumber selection in convectively coupled waves.

Extension of the model of K08b to the equatorial beta plane allows investigation of the equatorial Rossby (ER), mixed Rossby–gravity (MRG) and inertio-gravity (IG) wave types. These waves have significantly different convection/temperature/wind structures and observed amplitudes from the Kelvin-like waves studied in most previous work that are confined to a line along the equator. Our emphasis will be on identifying the basic factors that contribute to the differing instability of the different wave types and wavenumbers.

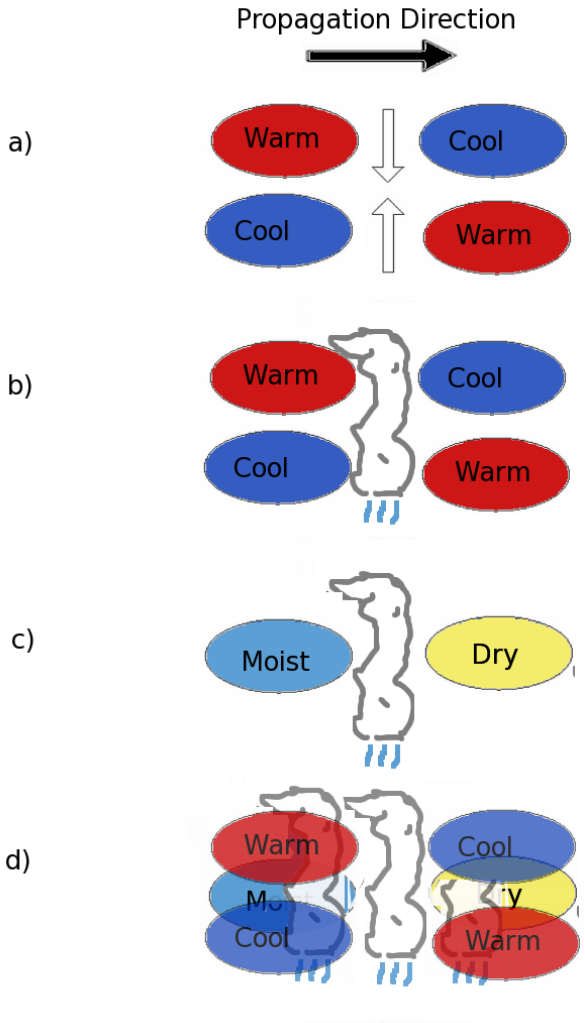

Figure 2-2. Schematic discussion of the moisture-stratiform instability. Considering a eastward propagating wave (in the reference frame of the wave) with a second baroclinic structure, we can see the temperature anomalies will lead to uplift in the lower troposphere and subsidence in the upper troposphere indicated by the arrows in (a). The uplift will destabilize the lower troposphere, leading to enhanced deep convection (b), which acts to maintain quasi-equilibrium between the boundary layer and the now cooler lower troposphere. In the frame moving with the wave, the moisture deposited by the deep convection acts to moisten the mid-troposphere behind the convection. The suppressed convection of the other phase of the wave will similarly create an anomalously dry midtroposphere ahead of the convection (c). The moist anomaly enhances stratiform heating of the upper troposphere and evaporative cooling of the lower troposphere. The dry anomaly enhances lower troposphere heating and upper troposphere cooling by acting as a barrier to deep convection (d). These heating anomalies reinforce the existing temperature anomalies, amplifying the wave. Based upon Figure 11 of Kuang (2008b).

The linear instability spectrum of the resulting coupled system is found by eigenvalue analysis. We use realistic model parameters estimated from Cloud System Resolving Model (CSRM) studies of the convectively coupled waves. The instability analysis produces unstable waves with phase speeds, growth rates, and structures (vertical and horizontal) that compare reasonably well with observations.

We will show that the instability's dependence upon wave type is related to the projection of mean-state Inter-Tropical Convergence Zone (ITCZ) heating onto the mode (as has been suggested in the past; e.g., Takayabu 1994; WK99) and to an energy feedback efficiency effect. This latter effect stems from the differing roles of divergent and rotational flows in the convective parameterization and the differing efficiencies with which the waves convert wave energy input from convective heating into divergent wind. We investigate this by analytical investigation of a simplified case to explore the details of the mechanisms responsible for wavenumber and wave type selection in the instability spectrum. The simplified case is chosen to remove the already understood mechanisms that exist within the model. Considering the instability in terms of the energy flow between the geopotential and wind fields shows that the instability strength is strongly influenced by the differing efficiencies of conversion from the energy input due to convective heating to divergent winds.

This chapter is organized as follows: Section 2 provides a brief description of the model used in this paper. Section 3 describes the results of an eigenvalue analysis conducted to determine the spectrum of unstable waves present in our model, as

well as tests of the sensitivity of the system to ITCZ configuration and to the parameters used. Section 4 describes a simplified limiting case of our model and an energy flow–based feedback mechanism that explains the differing instabilities of the different wave modes. Section 5 follows with a summary and discussion.

2.2 Model Description

2.2.A Model Equations

Our basic equations are a simple extension of the model of K08b to the equatorial beta plane. The relation to previous models was discussed in K08b and in the introduction. The model equations can be derived from the anelastic primitive equations for an atmosphere linearized about a resting mean state:

$$\partial_t u' - \beta y v' = -\frac{1}{\bar{\rho}}\partial_x p', \tag{2.1}$$

$$\partial_t v' + \beta y u' = -\frac{1}{\bar{\rho}}\partial_y p', \tag{2.2}$$

$$\partial_x(\bar{\rho}u') + \partial_y(\bar{\rho}v') + \partial_z(\bar{\rho}w') = 0, \tag{2.3}$$

$$\partial_t T' + w'\left(\partial_z \overline{T} + \frac{g}{c_p}\right) = J' - \epsilon T', \tag{2.4}$$

and,

$$\partial_z p' = \frac{g\bar{\rho}}{\bar{T}} T', \tag{2.5}$$

where ρ and T represent the density and temperature; u, v, and w represent the velocities in the zonal, meridional and vertical directions, respectively; and J represents the convective heating. Overbars represent mean quantities and primes denote deviation from this mean state (assumed to be small). A linear damping on

temperature, denoted by ϵ, represents radiative cooling/heating toward the mean temperature profile. The buoyancy frequency N is given by

$$N^2 = \frac{g}{\bar{T}}\left(\partial_z \bar{T} + \frac{g}{c_p}\right), \tag{2.6}$$

and βy is the linear expansion of the Coriolis parameter, f, for small displacements away from the equator.

Then, with the additional assumptions of a rigid lid and constant buoyancy frequency, we can expand equations (2.1)–(2.5) in terms of the baroclinic modes, numbered j, thus:

$$\frac{g\bar{\rho}}{\bar{T}}\left[T', J, w'\left(\partial_z \bar{T} + \frac{g}{c_p}\right)\right] = \sum_j [T, J, w]\,(x, y, t)\,\frac{\pi}{2} sin\left(\frac{j\pi z}{H_T}\right), \tag{2.7}$$

and

$$[\bar{\rho}u', \bar{\rho}v', p'] = \sum_j [u, v, p]\,(x, y, t)\,\frac{H_T}{2j} cos\left(\frac{j\pi z}{H_T}\right) \tag{2.8}$$

where H_T is the height of the lid at the top of the troposphere. We note that despite the above derivation, the use of these modes is based on empirical evidence rather than on their being normal modes of the dry atmosphere because the atmosphere does not possess a rigid lid at the tropopause—a fact emphasized in the context of convectively coupled waves by, for example, Lindzen (1974, 2003) and Raymond and Fuchs (2007).

Substituting the expansion forms [equations (2.7) and (2.8)] into our perturbation velocity equations [equations (2.1)–(2.3)] yields:

$$\partial_t \boldsymbol{u}_j = -\beta y\, \hat{k} \times \boldsymbol{u}_j + \nabla_H T_j, \tag{2.9}$$

and,

$$w_j = -c_j^2 \nabla_H \cdot \boldsymbol{u}_j, \tag{2.10}$$

where T is the temperature perturbation scaled to act similarly to a geopotential perturbation and ∇_H denotes the horizontal gradient vector operator $\nabla_H = (\partial_x, \partial_y)$ (See Appendix B for greater detail on this derivation).

The wave speeds c_j are given by:

$$c_j = \frac{NH_T}{j\pi}. \tag{2.11}$$

We can also make a modal expansion of the thermo- dynamic Eq. (2.4) by combining it with Eq. (2.10), generating

$$\partial_t T_j - c_{2j} \nabla_H \cdot \boldsymbol{u_j} = J_j - \epsilon T_j. \tag{2.12}$$

For the rest of this paper, we restrict ourselves to $j = 1, 2$—the first two baroclinic modes, which are sufficient to explain most of the convective activity (e.g. Mapes and Houze 1995). The heating anomalies associated with these two modes, J_1 and J_2, represent the convective heating broken into deep convective and congestus/stratiform components, respectively. The modal decomposition of convection heating is based on the cloud physics of convection. We note that the work by Raymond and Fuchs (2007) showed that one can produce a boomerang temperature structure with a first baroclinic - only convective heating profile and a radiating upper boundary condition, so the question of whether the two-mode structure observed in convectively coupled waves arises from cloud physics of convection or large- scale dynamics remains a matter of debate.

For the purposes of the convective parameterization, the heating is rewritten in terms of lower- (L) and upper- (U) tropospheric heating anomalies:

$$L = \frac{1}{2}(J_1 + J_2) \tag{2.13}$$

and

$$U = \frac{1}{2}(J_1 - J_2)\,. \tag{2.14}$$

The total upper-tropospheric heating is considered to be a fraction of the lower-tropospheric heating:

$$\frac{U_0+U}{L_0+L} = r_0 + r_q q, \tag{2.15}$$

where U_0 and L_0 are the mean-state heating and r_0 is the mean-state ratio between L_0 and U_0; q is the mid-tropospheric moisture anomaly and is evolved according to

$$\partial_t q = -a_1 c_1^2 \nabla_H \cdot \boldsymbol{u}_1 - a_2 c_2^2 \nabla_H \cdot \boldsymbol{u}_2 - d_1 J_1 - d_2 J_2 \tag{2.16}$$

where a_j and d_j give the mid-tropospheric moisture tendencies due to vertical advection and convection, respectively. We have neglected the effect of the horizontal advection of moisture in our formulation for simplicity and recognize that its effect should be evaluated in the future.

In a region of the mid-troposphere that is anomalously moist with positive q, the entrained air is moister than average and the associated evaporative cooling is smaller, leading to relatively increased buoyancy of parcels in this region. This in turn leads to parcels rising to greater altitude and heating the upper troposphere more. As parcels rise to form deep convection, the subsequent stratiform heating further enhances heating in the upper troposphere relative to the lower troposphere. The opposite holds for a region with an anomalously dry mid-troposphere.

The lower-tropospheric heating is considered to be relaxing quickly (over a time scale τ_L, typically a few hours) toward the quasi-equilibrium situation given by the constancy of lower-troposphere non-entraining CAPE. In our context, quasi-equilibrium will be enforced by keeping the difference between the boundary layer moist static energy (MSE), h_b, and the vertically averaged lower-tropospheric saturation moist static energy, $\langle h^* \rangle$, approximately constant. Note that h_b and $\langle h^* \rangle$ both vary under the action of convection—a positive convection anomaly dries and cools the boundary layer through the action of downdrafts and turbulent transport and modifies the lower-tropospheric saturation MSE primarily (in our model) by heating the atmosphere—to reach a consistent equilibrium state. Thus, for equilibrium to be reached instantaneously,

$$\partial_t h_b = \langle \partial_t h^* \rangle_{LT} \tag{2.17}$$

where LT is the region of the lower troposphere in which this QE formulation is assumed to hold, extending vertically up to the level where the effect of entrainment begins to become important. We shall neglect the surface flux anomalies in this chapter and write

$$\partial_t h_b = -b_1 J_1 - b_2 J_2 \tag{2.18}$$

The term b_j describes the reduction of boundary layer moist static energy by the convection J_j.

Meanwhile, we also assume that the average saturation moist static energy in the lower troposphere can be well approximated by a linear combination of the two baroclinic mode temperature anomalies:

$$\langle \partial_t h^* \rangle_{LT} = F \partial_t [\gamma T_1 + (1-\gamma) T_2]. \quad (2.19)$$

Here, F is a proportionality constant relating the change in lower-troposphere temperature to the change in moist static energy in the same region, and γ describes the relative influence of the two modes on the temperature of the lower troposphere. It is, loosely speaking, equivalent to the fractional depth of the troposphere through which this QE formulation can be assumed to hold before entrainment becomes an important effect.

Substituting these two relations [(2.18) and (2.19)] into Eq. (2.17) allows us to quantify the quasi-equilibrium in terms of our model, and by expanding the result using equations (2.12)–(2.15), we can find a lower-tropospheric heating L_{eq} that satisfies the quasi-equilibrium assumption for the large-scale variables (q, u, and T; see Appendix C for details):

$$L_{eq} = \frac{AL_0 r_q}{B} q - \frac{F\gamma c_1^2}{B}\left(\nabla_H \cdot \boldsymbol{u}_1 - \frac{\epsilon}{c_1^2} T_1\right) - \frac{F(1-\gamma)c_2^2}{B}\left(\nabla_H \cdot \boldsymbol{u}_2 - \frac{\epsilon}{c_2^2} T_2\right), \quad (2.20)$$

where:

$$B = F + (b_1 + b_2) - A\left(r_q q + r_0\right), \quad (2.21)$$

and

$$A = (b_2 - b_1) + F(1 - 2\gamma). \quad (2.22)$$

We can improve the realism of the model by assuming that the convection does not respond to changes in the large-scale environment instantly. Rather, we allow L to relax toward L_{eq} over a short time scale τ_L:

$$\partial_L = \frac{1}{\tau_L}\left(L_{eq} - L\right). \quad (2.23)$$

By introducing the meridional velocity fields u_j and the Coriolis force terms $\beta y\hat{k}\times\boldsymbol{u}_j$, this extension prevents the simple reduction of the dry part of the prognostic equations to temperature fields that occurs in K08b, leading to the presence of velocity fields in the equations for L_{eq} (2.20) and q (2.16) [c.f. his equations (23) and (11)].

2.2.B Parameter Choices

As described in K08b, our parameter values, such as $a_j, b_j, d_j, F, \gamma, r_0, r_q, \epsilon$, and τ_l, are estimated from the CSRM simulations of Kuang (2008a). This simulation showed spontaneously developing convectively coupled waves. The estimation is conducted by projecting the CSRM results onto the vertical structure of our modes and interpreting regression results in the framework of our convective parameterization. We consider this approach to be somewhat more rigorous than tuning our model to match observations, as well as more efficient given the pre-existence of the CSRM results.

Parameter values are given in Table 2.1 and are essentially identical to those used by K08b. The units of the parameters are based on measuring energies in the equivalent temperature change (in K) for 1 kg of dry air gaining that amount of energy. Moisture content is likewise measured by the temperature change that would result if all the stored latent heat in a volume of air were converted to thermal energy in an identical, but dry, air mass.

TABLE 2.1. Parameter Values used in the linear simple model of the Convectively Coupled Equatorial Waves

Symbol	*Value*	Description
b_1, b_2	1.0, 2.0	Tendency for reduction in boundary layer moist static energy per unit heating J_1 and J_2
a_1, a_2	1.4 K, 0.0K	Increase in q tendency per unit vertical velocity $(\partial_x u + \partial_y v)$ by advection
d_1, d_2	1.1, -1.0	Decrease in q tendency per unit heating J_1 and J_2
r_0	1.0	Background mean U/L ratio
r_q	1.0 K^{-1}	Linear dependence of U/L ratio on moisture deficit
F	4	Ratio between moist static energy and temperature in the lower-tropospheric "non-entraining" convection region
γ	0.5	Relative contribution of the first mode temperatures to the lower-tropospheric temperature anomaly
τ_L	2.0 hr	Adjustment time to approach QE over the lower troposphere
c_1, c_2	50m/s, 25m/s	Dry gravity wave speeds for the first and second modes
ϵ	0.15 day^{-1}	Temperature anomaly damping coefficient
σ_L	5.0^o	Meridional width of L_0 profile, representing the ITCZ structure

2.3 Beta-plane Linear Instability Analysis

In WK99, the observations are of waves of finite amplitude. If the waves are indeed unstable, in the observations the linear growth of the unstable waves is balanced by nonlinear terms and an equilibrium is reached. In this case, the equilibrium is of a statistical nature, with waves growing and dying as they move around and enter regions of differing forcing (due to the changing background state and wave–wave interactions), and is also time varying on various scales. In this chapter we investigate the linear regime of infinitesimal waves with a zonally and temporally fixed background state.

2.3.A Linearization

Calculation of the instability spectrum assumes that our system is growing from infinitesimal anomalies, so we can remove any nonlinear terms from the equation set. In our case, linearization is simply achieved by ignoring the first term in the second parentheses from the definition of B [equation (2.21)],

$$B = F + (b_1 + b_2) - Ar_0, \tag{2.24}$$

and linearizing Eq. (2.15) into:

$$U = L_0 r_q q + r_0 L. \tag{2.25}$$

Our linearized model consists of equations (2.9), (2.12), (2.13), (2.14), (2.16), (2.20), (2.22), (2.23), (2.24), and (2.25).

Our basic state, represented by the parameter $L_0(y)$, is an idealization of the zonal mean state. As shown in figure 2-3, the control profile consists of a Gaussian peak (of amplitude 0.7 $K\ day^{-1}$) in mean-state convection centered on the equator, with

a width of 5°, above a small, non-zero uniform offset that extends to the edges of the domain.

The linear system is then Fourier transformed to zonal wavenumber–frequency space and the resulting eigenvalue problem is solved on a meridionally discrete domain extending approximately 6000 km to the north and south, with 181 regularly spaced points. This large domain is utilized to reduce the influence of any edge-related errors and can be implemented without significant computational cost. The resulting complex frequency eigenvalues can be separated into the real part ω, which gives the modal frequency, and the imaginary part Γ, which gives the modal growth rate. The corresponding eigenvectors give the modal structure in the prognostic fields (u_1, v_1, etc).

2.3.B Results

The results from the linear analysis are shown in figure 2-4 and figure 2-5. Unstable waves are indicated in the frequency–wavenumber diagram, with the marker radius proportional to the growth rate. Unstable modes are assigned to an equivalent dry class (dispersion curve ranges shown dashed) based on their position in figure 2-4, relative to the dry dispersion curves indicated. Investigation of the modal structure (discussed below) shows that these identifications are warranted. The system contains unstable modes corresponding to Kelvin waves, $n = 1$ and $n = 2$ inertio-gravity waves, and Mixed Rossby–Gravity waves.

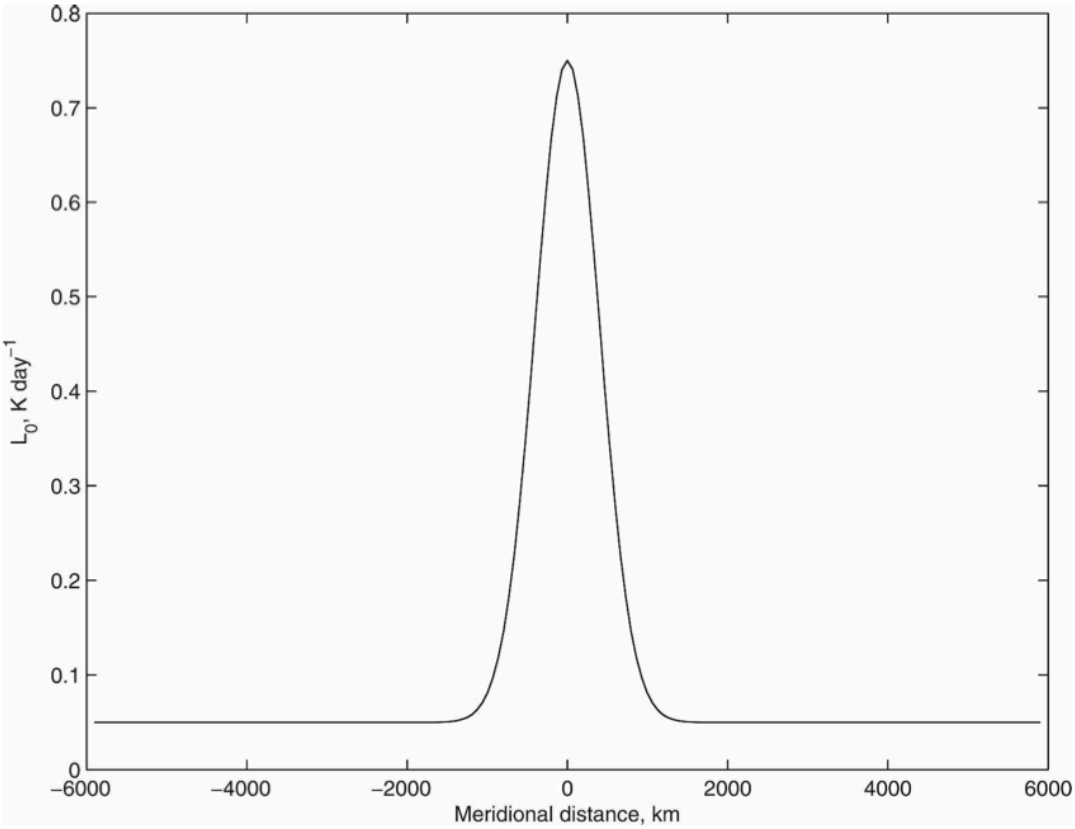

Figure 2-3. Background state lower-tropospheric convective heating used in the control instability experiment. The background state is an idealization of the zonal mean state, with an ITCZ-like Gaussian peak over the equator and a small mean convection over the rest of the domain.

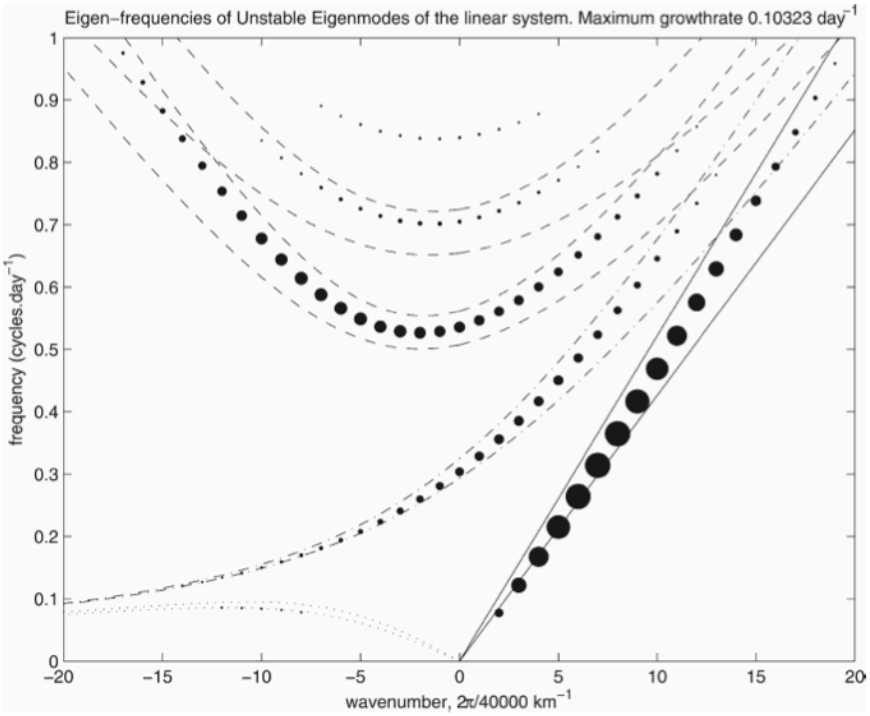

Figure 2-4. Eigenfrequencies for the linear system with an idealized zonal mean state. Data point diameter corresponds linearly to growth rate. Stable modes are omitted. Lines show theoretical dispersion curves for dry waves with equivalent depths of 40 and 60 m (in order of increasing frequency).

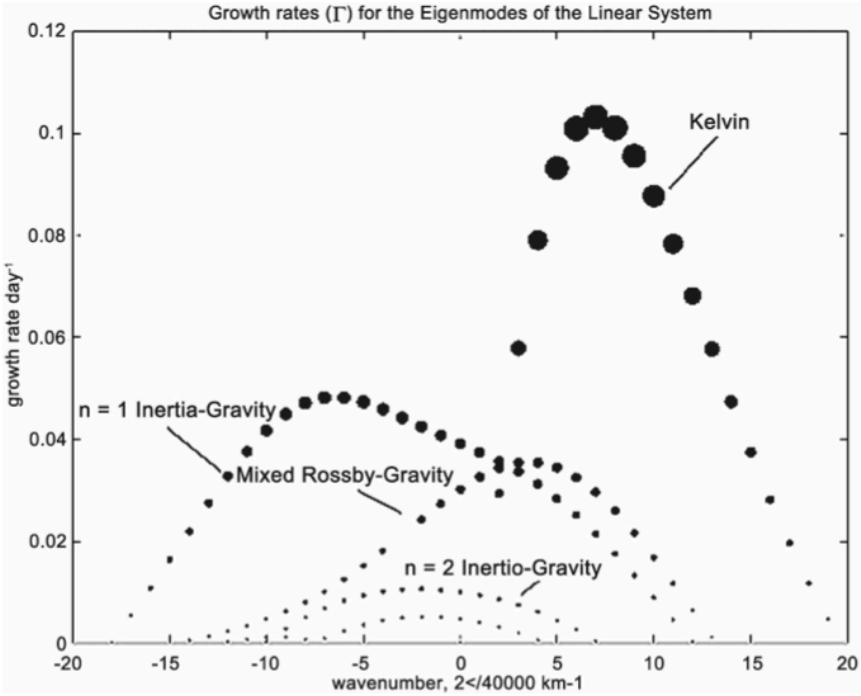

Figure 2-5. Growth rates for the linear systems with an idealized zonal mean state. Data point size encoding is included for ease of cross-referencing with Figure 2-4. The smooth curves visible to the eye correspond to the unstable wave types found in the system—Kelvin, n = 1 IG, MRG, and n = 2 IG.

Kelvin waves are the most unstable wave type. Wavelengths between about 13 000 and 2000 km (planetary wavenumbers 3 and 20) are unstable, with a maximum growth rate of ~0.10 day^{-1} occurring at wavelengths of around 5700 km (wavenumber 7). These waves have phase speeds between 20 and 25 $m\ s^{-1}$, slightly slower than the second baroclinic wave, with the speed deficit becoming stronger as the wavenumber decreases. The growth rate curve rises sharply between wavenumbers 3 and 7 and then decays more slowly as the wavenumber is further increased to 17.

Figure 2-6 shows the structure of this mode, along with vertical structure of temperature. The first baroclinic mode is approximately in quadrature with the second, leading to a tilted vertical temperature structure, similar to observations. Zonal winds blow in the standard dry wave directions. The meridional wind has a small nonzero component. This is not unexpected because the moist physics that couples our system mixes the modes together so that the convectively coupled "Kelvin" wave observed, although dominated by a Kelvin wave profile, will still contain a small amount of other waves in superposition with it. The wind fields are plotted for the lower troposphere at $z = 0$.

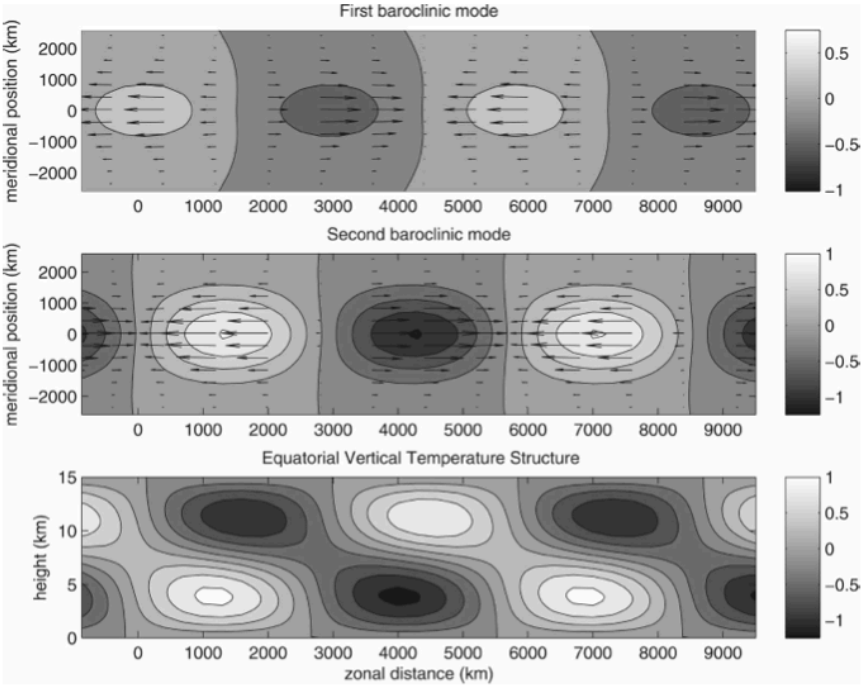

Figure 2-6. Structure of the coupled Kelvin wave at planetary wavenumber 7. (top), (middle) Temperature (contours) and wind anomalies (vectors) for the (top) first and (middle) second baroclinic modes; (bottom) reconstructed vertical temperature anomaly above the equator.

Figure 2-4 shows unstable MRG waves, approximately between wavenumbers -15 and 10, with a peak growth rate of $\sim 0.03\ day^{-1}$ occurring at wavenumber 3 ($\sim$13000 km wavelength). The phase speed of the MRG waves also appears to drop below the dry speed as the wavenumber decreases, although this become less visible at large negative wavenumbers as the dispersion curves converge. The modal structure of the (eastward) planetary wavenumber 7 Mixed Rossby-Gravity wave is shown in figure 2-7.

The system also shows instability in the $n = 1$ (eastward and westward) IG waves, with a bias toward westward IG (WIG) waves.

The $n = 2$ and IG modes are only marginally unstable in this model. We consider growth rates below a few percent of the peak values to be only marginally unstable and far too dependent on assumptions about parameters for us to draw solid conclusions about them. The sensitivity of our model to parameter variation is explored in section 2.3.D, below.

The reconstruction of the planetary wavenumber 7 Eastward IG (EIG) wave is shown in figure 2-8. In figure 2-9, the k = +7 WIG wave structure is also shown for comparison. These modes also show horizontal and vertical structures that compare well with observations.

All the reconstructed modes show first- and second-mode winds with similar amplitudes, broadly consistent with observations (see, e.g., Haertel and Kiladis 2004), as well as a vertically tilted structure, again generally consistent with observations (see, e.g., Straub and Kiladis 2002).

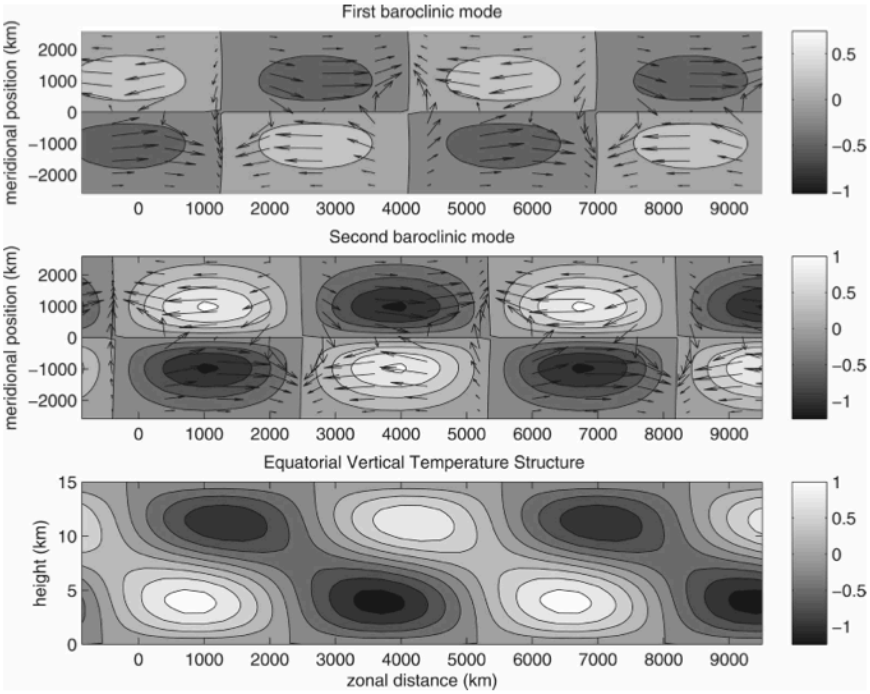

Figure 2-7. Structure of the coupled MRG n = 0 EIG wave at planetary wavenumber 7. (top), (middle) Temperature (contours) and wind anomalies (vectors) for the (top) first and (middle) second baroclinic modes; (bottom) reconstructed vertical structure at y = 1000 km (north of the equator), approximately the peak of the MRG profile.

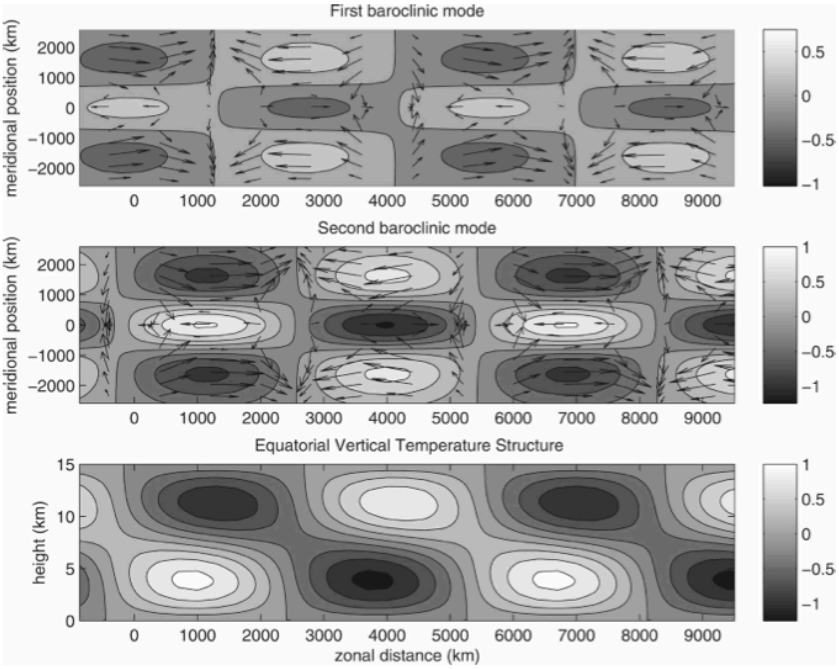

Figure 2-8. As in Figure 2-6, but for the coupled n = 1 EIG wave at planetary wavenumber 7.

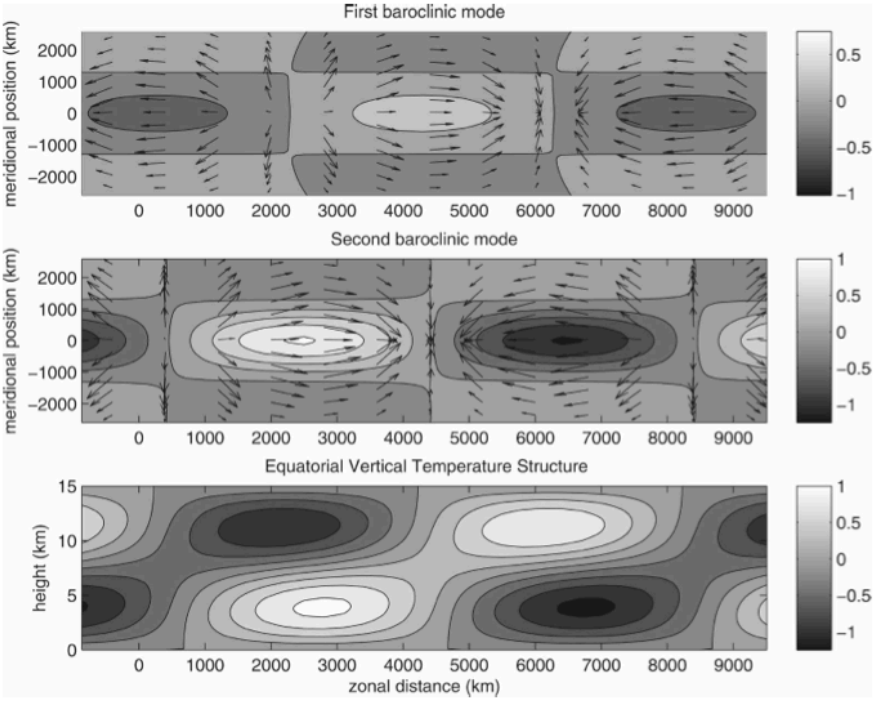

Figure 2-9. As in Figure 2-6, but for the coupled WIG wave at planetary wavenumber 7 ($\boldsymbol{k = -7}$).

Most noticeably absent from the instability spectrum are significant equatorial Rossby waves and the Madden–Julian Oscillation (MJO). The complete absence of the MJO signal indicates, not unexpectedly, that the current simple model is missing the physics responsible for the MJO. The Rossby waves exist in our system but are barely unstable within a range of parameter choices around our nominal values (discussed below in section 2.3.D). Because both these missing wave types are at similar, low frequencies, the model may have either a too strong damping at low frequencies or may be missing some other physics that destabilizes waves at these frequencies.

Comparison of figure 2-4 and figure 2-5 with figure 2-1 shows that:

(i) Peak Kelvin wave growth occurs at a wavelength comparable to the most active waves in the observations;

(ii) The ranges of wavenumber and wave type showing instability in our model match the ranges of waves that are observed in the OLR signals;

(iii) The Kelvin wave dispersion curves shift to higher equivalent depth at higher wavenumbers, opposite to the observed trend (the reason for this discrepancy is unclear);

(iv) The model possesses a preference for unstable westward n = 1, 2 IG modes (as opposed to eastward n = 1, 2 IG), similar to observations; and

(v) The waves possess a tilted vertical structure that is generally consistent with the observations, with low-level temperature anomalies preceding a brief period of deep anomaly followed by a period of “stratiform” temperature anomaly.

2.3.C Varying ITCZ configurations

Double ITCZ

To address the question of whether the dominance of Kelvin waves is due to the amount of overlap between the mean-state heating and the Kelvin wave profile being greater than that for other waves, we have conducted several additional experiments with different ITCZ configurations in our mean state.

Figure 2-10 shows a double-ITCZ mean state, with the two peaks approximately a second baroclinic deformation radius north and south of the equator, collocated approximately with the MRG temperature anomaly peaks determined from figure 2-7. Unstable modes for this case are shown in figure 2-11. Although moving the peak heating away from the equator does reduce the overall growth rate of the unstable Kelvin waves and increases that of the unstable MRG waves, the growth rates of the Kelvin waves are still strongest. The MRG growth rates surpass the $n = 1$ IG wave in the small wavenumber region of the spectrum. The ER waves are slightly more unstable, but still not significant. The reconstructed mode structures (not shown) are not significantly different from the single ITCZ case.

Two further experiments (not shown) placed (i) a double ITCZ at the off-equatorial peaks of the $n = 1$ IG temperature anomaly field and (ii) a single ITCZ at the northern MRG peak temperature anomaly position. Although the wave that had the greatest overlap with the convective envelope showed some enhancement of growth rate, neither of these experiments altered the general dominance of the Kelvin waves.

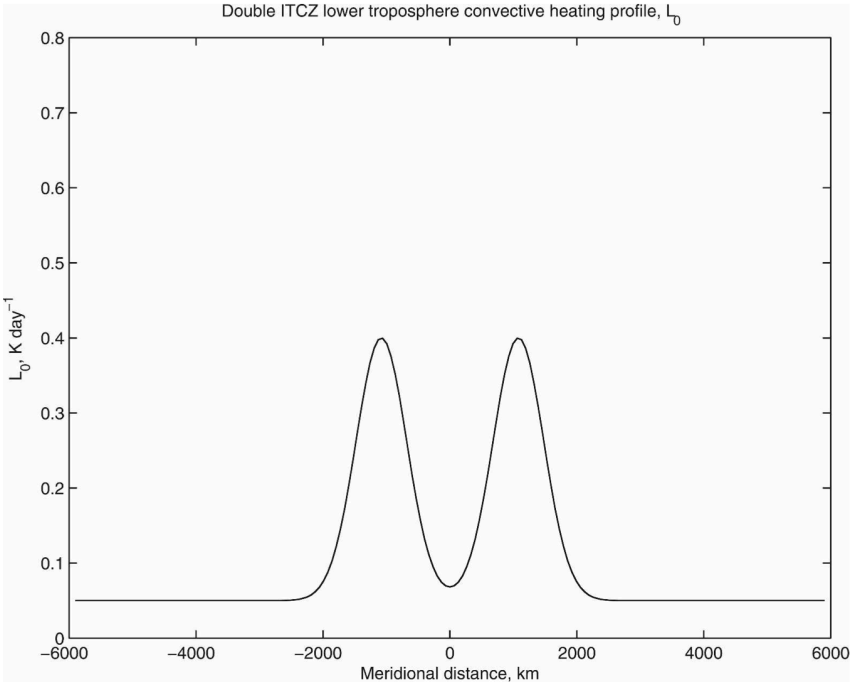

Figure 2-10. Background state lower-tropospheric convection used in double ITCZ experiment. The background state is an idealization with a pair of ITCZ-like Gaussian peaks centered 1000 km north and south of the equator and a small mean convection over the rest of the domain.

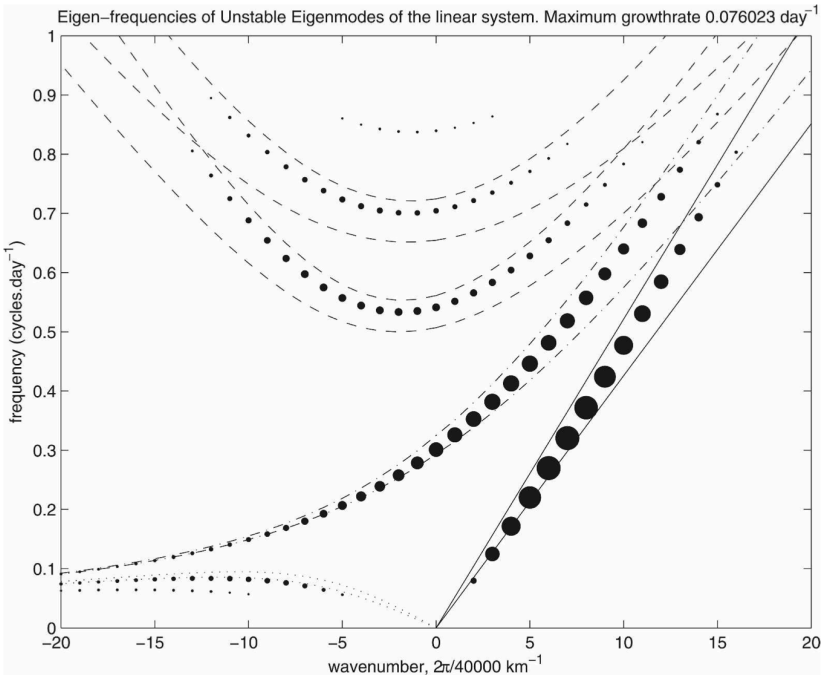

Figure 2-11. As in figure 2-4, but for a background state with a double ITCZ (Figure 2-10), located near the MRG meridional structure peaks (see Figure 2-7).

Infinitely Wide ITCZ

Another aspect of the observed activity profile that stands out as possibly being related to ITCZ configuration is the asymmetry between eastward and westward inertia-gravity waves—the observed activity of WIG waves is much stronger than that of EIG waves. It has been suggested that this is primarily because the latitudinal structure of the EIG waves is significantly more complex and a greater proportion of the EIG temperature anomaly is located away from the equator and the ITCZ (see, e.g., Takayabu 1994; WK99, Lui *et al.* 2011). To explore this possibility, a further experiment is shown in which the ITCZ is replaced with a meridionally constant mean-state heating of 0.75 K day^{-1}.

The results from the linear analysis are shown in figure 2-12. Kelvin waves are still the most unstable wave type. Wavelengths between about 13000 and 2300 km (planetary wavenumbers 3 and 17) are unstable, with a maximum growth rate of $\sim$0.11 day^{-1} occurring at wavelength of around 5000 km (wavenumber 8).

Unstable MRG waves (also referred to as $n = 0$ EIG waves for the $k > 0$ part of the spectrum) appear in the region approximately between wavenumbers -5 and 15, with a peak growth rate of $\sim$0.05 day^{-1} occurring at wavenumber 7 ($\sim$5700 km wavelength). The system also shows instability in the (eastward and westward) IG waves, with a significant instability bias toward WIG waves. Because of the extreme poleward extent of the mean-state convection in this case, there is significant instability in high meridional wavenumber (IG) modes.

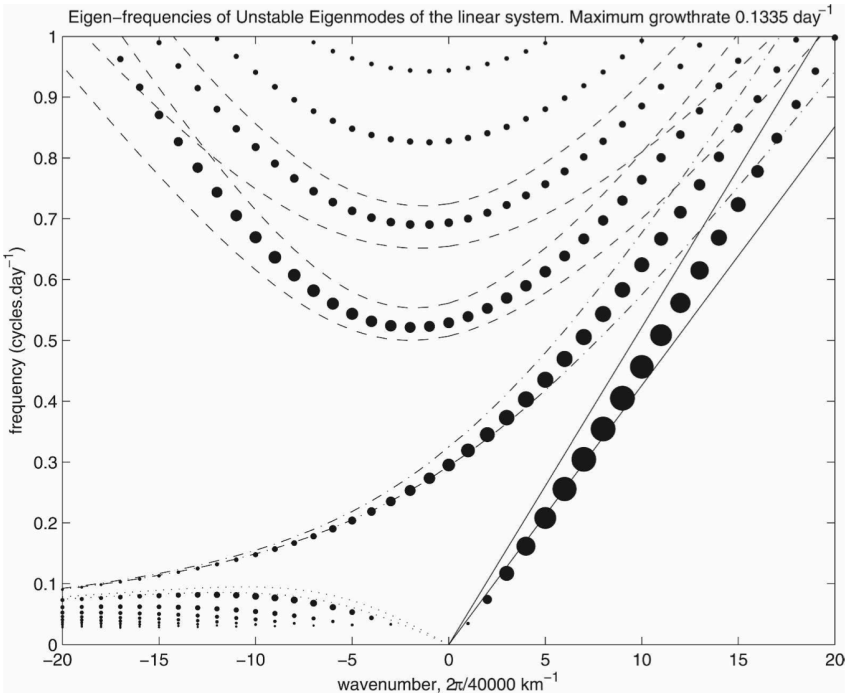

Figure 2-12. As in Figure 2-4, but for a background state with a meridionally constant lower-tropospheric heating.

In this situation, the projection of the ITCZ heating profile onto the EIG and WIG structures should be essentially the same. As can be seen, some but not the entire east–west asymmetry has been removed. It will be demonstrated below that some of this asymmetry is due to the differing efficiencies with which the eastward and westward IG waves convert convective heating into more convective heating.

Kelvin Wave Asymmetry

In Chapter 1, we discussed the method of wave filtering and the Kelvin filtered variance of the observed OLR spectrum was shown. It was noted that, while the Kelvin wave is typically considered to be a symmetric wave, even with the nearby (in spectral space) anti-symmetric MRG waves excluded from the filter region, the resulting variance still showed a significant anti-symmetry. It was suggested that this was the result of coupling the symmetrical dry KW with other anti-symmetric waves, due to the off-equatorial convection of the ITCZ in the east Pacific.

As a simple test of this hypothesis, we have repeated the calculations of the simple model with the ITCZ shifted a short distance from the equator. The ITCZ center is placed 0.1 Length units north of the equator (432 km, approximately 4^oN). The ITCZ profile is shown in figure 2-13b (with the control case of an on-equator ITCZ shown in figure 2-13a for ease of comparison). This small displacement has only a small effect on growth rates of the waves (compare figure 2-13c and d). The thermodynamic fields of the off-equatorial case are also barely changed–only a slight asymmetry is observed. However, the upper level heating (U) variance, which

is at least a qualitative proxy for OLR variance of the Kelvin waves, is quite asymmetrical, peaking over the center of the ITCZ.

This is consistent with observations of Kelvin waves in the east Pacific (e.g. Straub and Kiladis 2002), where KW are typically observed to be nearly symmetrical in their dynamical structure while the convective signal is typically located above the warmest SST.

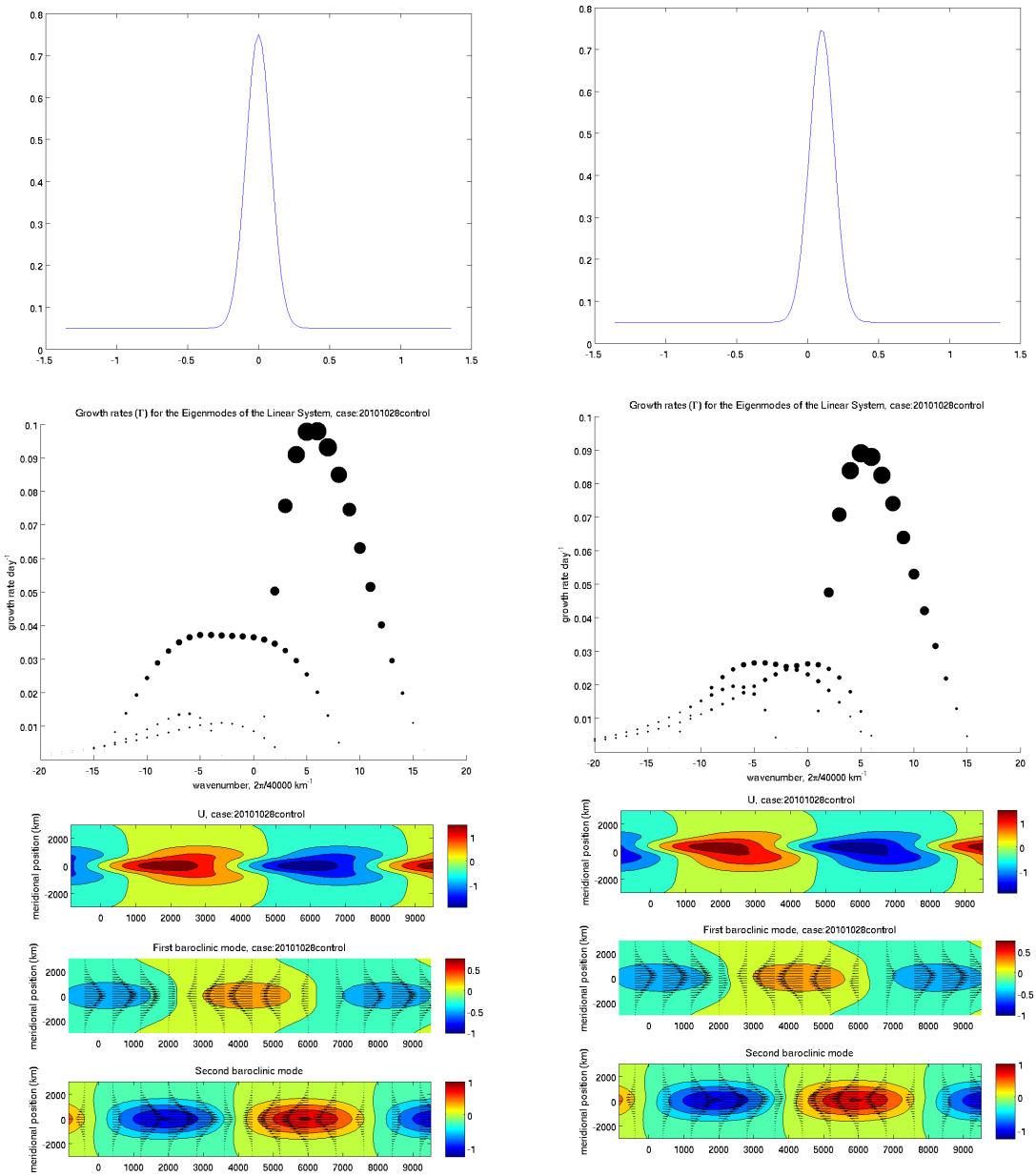

Figure 2-13. Simple model results, showing the shifting of the Kelvin wave by an off equatorial ITCZ. The left hand column shows the control results, where the ITCZ profile is centered on the Equator, while the right hand column shows the results when the ITCZ center is shifted 432km to the north – the ITCZ profiles are shown in the first row. The second row shows the growth rates as functions of wavenumber. The third row shows the upper level heating and the temperature and wind fields for the first and second baroclinic modes.

2.3.D Parameter Sensitivity

As mentioned above, the model does display some sensitivity to parameter variations. Figure 2-14 shows the growth rate curves for sensitivity experiments conducted with the damping ϵ and the convective equilibrium relaxation time τ_L increased and decreased by 10%. The instability for the Kelvin, equatorial Rossby, mixed Rossby–gravity and n=1 inertio-gravity waves are seen to be generally robust, with the location of the peak instabilities in these cases remaining approximately the same. The peak growth rates do change slightly, as expected, when the damping is varied. However, the $n = 2$ and higher IG modes can be observed to vary greatly in their instability character in this range of parameters. As would be expected from the moist convective damping theory, decreasing the convective relaxation time decreases the moist convective damping effect, which then decreases the damping applied to high-wavenumber instabilities, leading to an increase in instability for the $n = 2$ and $n = 3$ IG modes. For the same reason, the Kelvin wave peak instability can be seen to shift very slightly to higher frequencies when τ_L is decreased.

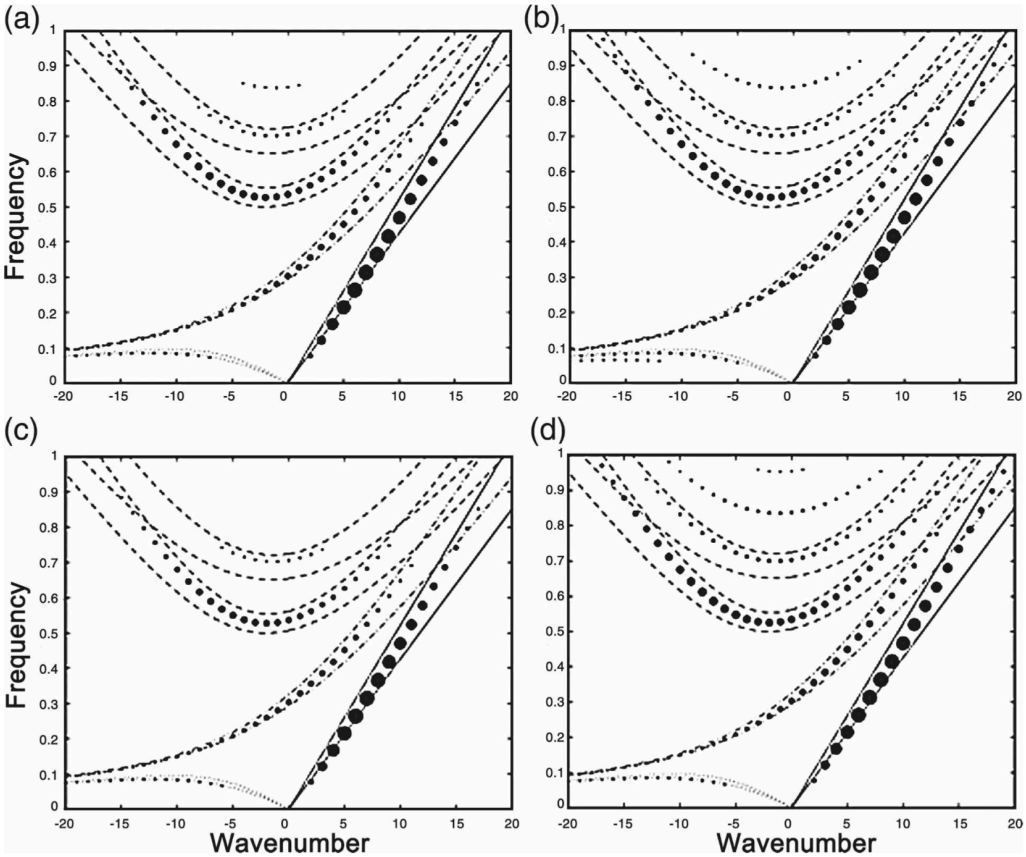

Figure 2-14. Damping sensitivity studies. As in Figure 2-4, but for modification of the damping parameters as follows: (a) $\boldsymbol{\epsilon}\rightarrow 1.1\times\boldsymbol{\epsilon}$,(b) $\boldsymbol{\epsilon}\rightarrow 0.9\times\boldsymbol{\epsilon}$,(c) $\boldsymbol{\tau_L}\rightarrow 1.1\times\boldsymbol{\tau_L}$, and(d) $\boldsymbol{\tau_L}\rightarrow 0.9\times\boldsymbol{\tau_L}$. Peak growth rates for each case are (a) $\mathbf{10\times10^{-2}}\boldsymbol{day^{-1}}$, (b) $\mathbf{11\times10^{-2}}\boldsymbol{day^{-1}}$, (c) $\mathbf{9\times10^{-2}}\boldsymbol{day^{-1}}$, and (d) $\mathbf{11\times10^{-2}}\boldsymbol{day^{-1}}$.

A similar sensitivity test was applied to all of the semi-empirical parameters contained within our model. Generally, for a 10% change in parameter value, variations in the spectrum were similar in character and amount to those discussed for damping above (not shown). The parameters r_0 and c_2 showed interesting sensitivity:

(i) When r_0 is varied, the position of the peak instability shifts to higher wavenumber for higher r_0. The reverse holds for reduced r_0.

(ii) A variation in the c_2 parameter leads to a similar variation in the speed of the unstable "Kelvin" modes. Any unstable mode speed variation caused by modification of c_1 is negligible. This indicates that the speed of the unstable modes is largely determined by the second mode.

The MJO is still not observed under any of these parameter variations.

These results are similar to the more detailed sensitivity study conducted for the 1D version of this model included in K08b.

2.4 Mid-Tropospheric Moisture versus Free-Tropospheric Moisture

As in K08b, we have used mid-tropospheric moisture instead of the vertically averaged free tropospheric moisture $\langle q \rangle$ in equation (2.16). This choice was based on the notion that $\langle q \rangle$ is not necessarily the most relevant quantity as a control on convection, which may be tied more strongly to certain weighted averages of free tropospheric moisture. We have used mid-tropospheric moisture although other and potentially better choices are certainly possible. The use of the column moist

static energy conservation constraint was not necessary in our case because the effects of convection on the mid-tropospheric moisture and on the boundary layer moist static energy were estimated separately from the CSRM simulations. It is also not an essential element for identifying the basic instability mechanisms.

However, for other issues such as understanding the column MSE budget of the system, it is desirable to use $\langle q \rangle$ so that the column MSE conservation constraint is automatically satisfied, as done in Khouider and Majda (2006b). Let us (in this subsection only) replace q_{mid} with $\langle q \rangle$ in Eq. (2.15), so that the column MSE budget equation can be written as:

$$\partial_t[(\langle q \rangle + T_1)M_T + h_b M_b] = M_T\left[(1 - \langle a_1 \rangle)c_1^2 \boldsymbol{\nabla_H} \cdot \boldsymbol{u_1} - \langle a_2 \rangle c_2^2 \boldsymbol{\nabla_H} \cdot \boldsymbol{u_2}\right] + [(1 - \langle d_1 \rangle)M_T - b_1 M_b]J_1 + [-\langle d_2 \rangle M_T - b_2 M_b]J_2, \quad (2.26)$$

where M_T and M_b are the mass in the troposphere and the boundary layer, respectively, and the other parameters retain their meanings defined above, except with a $\langle\ \rangle$ to denote that they are associated with $\langle q \rangle$. Column MSE conservation requires that

$$(1 - \langle d_1 \rangle)M_T = b_1 M_b, \text{ and} \quad (2.27)$$

$$-\langle d_2 \rangle M_T = b_2 M_b \quad (2.28)$$

so that we can therefore infer values of $\langle d_1 \rangle$ and $\langle d_2 \rangle$ from b_1 and b_2. We estimate that M_T/M_b is ~10, which gives $\langle d_1 \rangle \approx 0.9$ and $\langle \square_2 \rangle \approx 0.2$. The CSRM results of Kuang (2008a) can also be viewed in this framework following the procedure described in the appendix of K08b. Regression of the column MSE tendencies against vertical velocities of the two vertical modes give a value for $1 - \langle a_1 \rangle$ that is

effectively zero and a value of $\langle a_2 \rangle \sim 0.4$. This indicates, allowing for uncertainties of the estimates, a close to neutral gross moist stability to the first baroclinic mode vertical motion, and the column MSE variations are almost entirely associated with second baroclinic mode vertical motion. When $\langle q \rangle$ is used, we have also estimated that $L_0 \times r_q$ is about 0.55. The resulting instabilities (not shown) are very similar to those resulting from the instability analysis of model using mid-troposphere moisture.

2.5 The role of energy flow efficiency

This model has previously been analyzed for Kelvin-like waves on the equator (K08b), revealing some of the mechanisms determining the instability spectrum. Specifically, the MCD effect (e.g., Emanuel 1993; Neelin and Yu 1994) damps high-frequency waves, and the tendency of the second baroclinic mode convective heating to reduce existing mid-tropospheric moisture perturbations tends to reduce the instability at low wavenumbers. Expansion of the model to the beta plane in this paper has revealed the existence of at least one more mechanism within the model, responsible for the differences in growth rates for waves with similar frequencies. We have already shown that the ITCZ configuration and projection of the mean state heating on to the modes' temperature anomaly profiles exert some control on the shape of the growth rate curves. However, this control does not seem to explain all the aspects. We hypothesize that the growth rate curves for the various wave types are further shaped by the relative efficiency with which the various waves convert input energy into the divergent winds, which in turn generate more energy input. In

this section, we will show that the growth rates can be directly linked to the generation of divergent winds in the modes. To explore the mechanisms that control the shape of the instability spectrum, in this section of the paper we consider a simplified system that has been modified to remove the mechanisms already identified in K08b and any ITCZ convective projection amplitude effects (discussed in section 2.3, above) through the choice of specific parameters. Some more detailed exploration of limiting cases within the model (in 1D) is conducted in K08b.

2.5.A Physical description of the simplified system

Our simplified system is based on the second limiting case of K08b, in which the convective mass flux is dominated by entraining parcels and the boundary layer is in quasi-equilibrium with the second mode temperature ($\gamma = 0$). The first temperature mode is essentially uncoupled from our system and can be ignored. The system is further simplified by setting $b_2 = 0$ to remove the influence of the second mode heating on the boundary layer moist static energy and $\epsilon = 0$ to remove the radiative damping; d_2 is also set to zero to remove the effect of second mode heating upon the midtropospheric moisture q. These changes remove the scale selection of the moisture–stratiform instability.

Let us further tighten quasi-equilibrium to "strict quasi-equilibrium" by enforcing instantaneous relaxation to the equilibrium values of L (by setting $\tau_L = 0$). This change removes the MCD effect.

A uniform L_0 profile is used, removing the ITCZ projection effects.

Importantly, the parameter r_q, which controls the coupling between moisture and heating, is set to a very small value so that the heating can be approximated as an infinitesimal perturbation on the dry system.

This modified case is evaluated numerically (figure 2-15) in the same manner as the control case. The simplified system shows many unstable modes, but for this section we will concentrate on the Kelvin, MRG, $n = 1$ ER, and $n = 1$ IG modes, so the modes with $n > 1$ are deliberately omitted in Fig. 2.13. The Kelvin wave has a constant growth rate for all wavenumbers greater than zero. The MRG wave growth rate increases monotonically from the very small for large negative wavenumbers to relatively large at high positive wavenumbers, with rapid increase in the region between $k = -5$ and $k = +5$. In the domain evaluated, the MRG growth rate approaches, but never reaches that of the Kelvin wave. The system also shows unstable ER and IG waves, with ER growth rates increasing from a low value for large (negative) wave-numbers to close to the Kelvin value for wavenumber zero, and $n = 1$ IG waves have a large growth rate for all wavenumbers, with growth increasing as |k| increases.

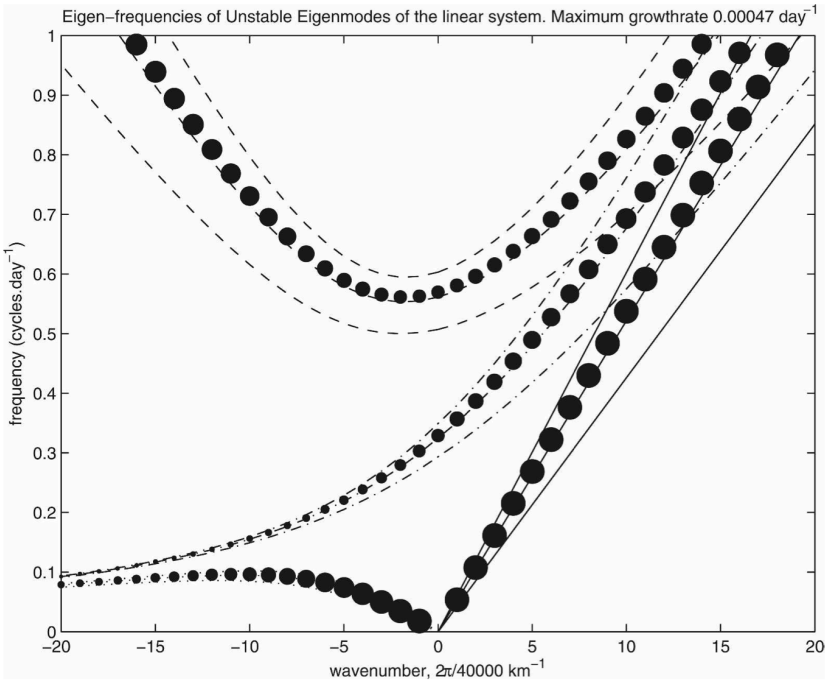

Figure 2-15. As in figure 2-3, but for the simplified system described in section 2.4 and with the dispersion curves for $\boldsymbol{h_{eq} = 80\ m}$ also plotted. All modes with meridional index n > 1 are deliberately not plotted, despite being unstable within this system.

Within the spectrum of unstable modes are several modes located at $k = 0, \omega = 0$. These modes indicate instability in our mean state that would lead to a mean-state drift away from the values we use here on a time scale comparable to the growth of the waves we are interested in. Here, this is not considered a serious shortcoming because we are looking at a very specific limiting case. In our more realistic cases treated earlier, such "climate drift" modes are not observed—all unstable $k = 0$ modes posses non-zero frequency and thus constitute oscillations about the mean state that, within the linear wave regime, do not affect other waves.

2.5.B Energy flow from heating into divergent winds and heating feedback

To demonstrate our hypothesis, let us consider how the energy that flows into the wave due to our convective heating goes into increasing the divergence of the flow. As we will show, the amplitude of the convective heating is proportional to the amplitude of the divergence, so this component of the energy drives the positive feedback, whereas energy that flows into the rotational component or the potential energy of the wave is essentially trapped there and cannot contribute to the further growth of the wave.

For this section, let us consider a wave that is essentially dry in character and that is forced by a diagnostic heating that approximates the simplified case discussed above. We will further consider how this wave changes with time over a short interval while the heating acts.

The heating can be approximately written as a diagnostic function of the dynamical variables as follows:

In our limiting case, equations (2.16) and (2.20) become

$$\partial_t q = (a_1 - d_1)J_1, \tag{2.29}$$

and

$$-b_1 J_1 = F\partial_t T_2, \tag{2.30}$$

where we have further assumed that the vertical velocity field is well approximated by the heating field (a good assumption for the first mode heating, as confirmed by the modal eigenstructures for the control model discussed above). Equation (2.29) states the combined effect of deep convection and the associated vertical moisture advection is to moisten the mid-troposphere. Equation (2.30) is a statement of deep convection maintaining strict quasi-equilibrium between the boundary layer and the lower troposphere.

Furthermore, we can also write [from equations (2.13), (2.14), and (2.15)]

$$J_2 = -r_q L_0 q \tag{2.31}$$

(letting $r_0 = 1$).

Combining the above equations, we have:

$$\partial_t J_2 = -r_q L_0 \partial_t q = -r_q L_0 (a_1 - d_1) J_1 = \frac{r_q L_0 (a_1 - d_1) F}{b_1} \partial_t T_2, \tag{2.32}$$

We can see that J_2 keeps the same phase as T_2. Further, because J_2 is a very small perturbation on the dry wave, we can also write

$$\partial_t T_2 \approx c_2^2 \delta_2, \tag{2.33}$$

where the divergence δ_2 is defined by

$$\delta_2 = \boldsymbol{\nabla_H} \cdot \boldsymbol{u_2}; \tag{2.34}$$

thus,

$$\partial_t J_2 = \frac{r_q(a_1-d_1)Fc_2^2}{b_1}\delta_2. \quad (2.35)$$

So, we now have

$$|J_2| \propto \frac{|\delta_2|}{\omega}. \quad (2.36)$$

Combining our above relations for the heating field, we define

$$J_2 = -\frac{B|\delta_2|T_2}{\omega|T_2|}, \quad (2.37)$$

where B is a constant of proportionality, considered to be very small, such that the heating is only a small perturbation to the waves:

$$B = -\frac{r_q(a_1-d_1)F\,c_2^2}{b_1}. \quad (2.38)$$

In this limiting case, out equation set reduces to:

$$\partial_t u_2 = \beta y\, v_2 + \partial_x T_2, \quad (2.39)$$

$$\partial_t v_2 = -\beta y v_2 + \partial_y T_2, \text{ and} \quad (2.40)$$

$$\partial_t T_2 = c_2^2\delta_2 + J_2. \quad (2.41)$$

2.5.C Energy feedback results

As shown in Appendix D, the amplitude of the Kelvin wave divergence grows exponentially with time at a rate that is independent of wavenumber, as observed in the numerical analysis above.

$$\frac{\Delta|\delta_{kw}|}{\Delta t} = \frac{Bc}{2H}|\delta_{kw}|, \quad (D.10)$$

Figure 2-16 shows the growth rate of the MRG, $n = 1$ ER, and $n = 1$ IG waves in this construction, normalized by the constant growth rate of the Kelvin waves, as calculated in the appendix.

$$\frac{\Delta|\delta_{MRG}|}{\Delta t} = \frac{Bc}{2H}|\delta_{MRG}|\left[\frac{c\beta}{c(ck^2+\beta)-2ck\omega+\omega^2}\right] = \frac{Bc}{2H}|\delta_{MRG}|\frac{\beta}{2\beta\mp\frac{k^2c}{2}\left(\mp1+\sqrt{1+\frac{4\beta}{k^2c}}\right)}, \quad \text{(D.20)}$$

where the upper sign applies for positive wavenumber and the lower sign applies for negative wavenumbers; and

$$\frac{\Delta|\delta|}{\Delta t} = \frac{Bc}{2H}|\delta|\frac{c\left(3c^2k^2+2ck\omega_{n=1}+3\omega_{n=1}^2\right)}{c^4k^4+3c^3k^2\beta+3c\beta\omega_{n=1}^2+\omega_{n=1}^4+2c^2k\omega_{n=1}(\beta-k\omega)}, \quad \text{(D.21)}$$

where

$$\omega_n \approx \left(-\frac{\beta k}{k^2+3\frac{\beta}{c}}, \sqrt{k^2c^2+3\beta c}\right) \quad \text{(D.22)}$$

for the Rossby and IG waves respectively (see, e.g., Gill 1982).

The growth rate of the MRG increases as the divergent component of the wave increases from a small value at negative wavenumbers (where the wave is very much like the low-divergence ER waves) to a large value at positive wavenumbers, where the wave most resembles the high-divergence Kelvin wave. Just as observed in the numerical study (figure 2-15), the growth rate increases rapidly between $k = -5$ and $k = +5$.

The growth rate of the $n = 1$ ER wave increases as k increases from $-\infty$ to zero, as observed in the numerical results. The growth rate of the $n = 1$ IG wave increases as $|k|$ increases from a small non-zero value at $k = 0$, as observed.

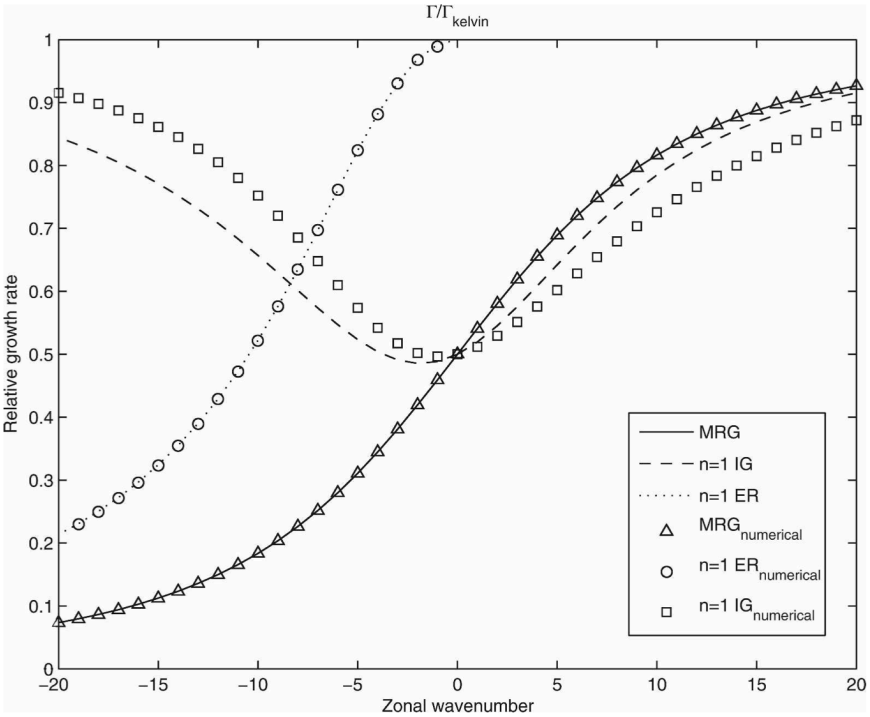

Figure 2-16. Analytic growth rate for the waves in the simplified limiting case, relative to the Kelvin wave growth rate (lines) and numerical growth rates (points), as described in the legend.

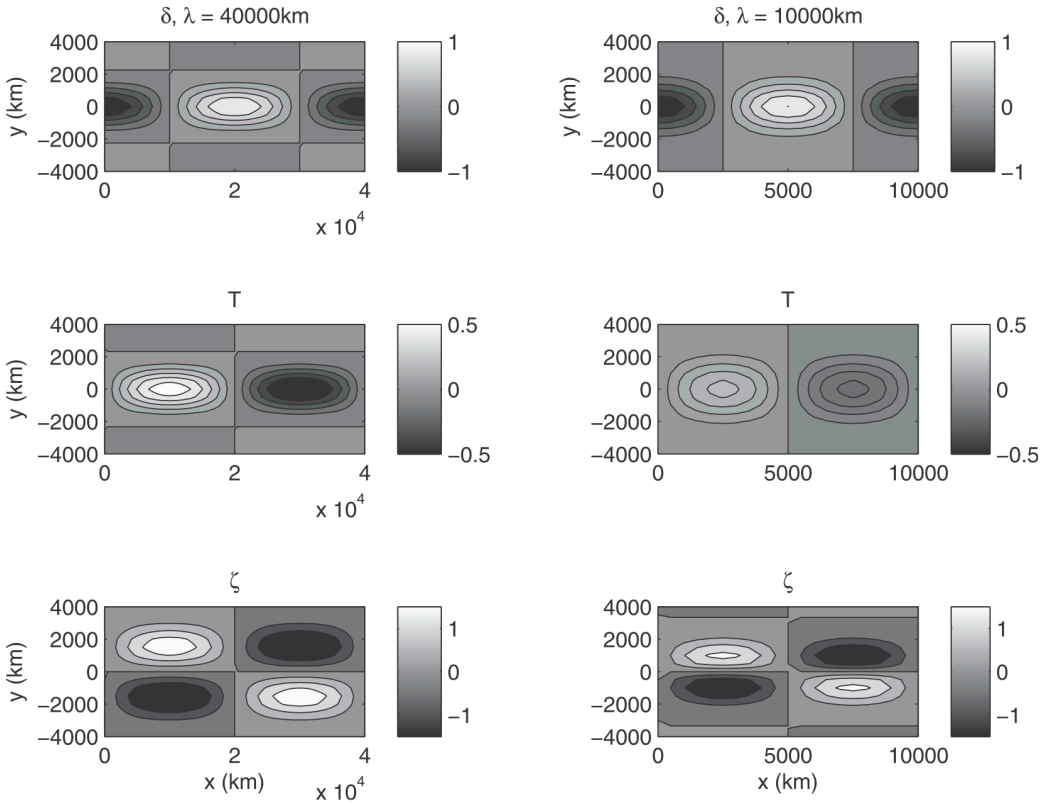

Figure 2-17. (top) Analytic divergence, (middle) temperature, and (bottom) vorticity fields for dry equatorial Rossby waves with (left) $\boldsymbol{\lambda = 4\times10^4}$ km and (right) $\boldsymbol{\lambda = 5\times10^4}$ km. It is important to note that the horizontal axis of the two columns have different scales, as demanded by the very different wavelengths depicted. Scale is in arbitrary units, normalized by the maximum divergence of the $\boldsymbol{\lambda = 4\times10^4}$ km wave.

It is interesting to note that the growth rates of the Rossby waves are greater at longer wavelengths. This can be explained by considering how the wave energy generated per unit divergence and the divergence increase per unit energy increase varies with wavenumber. For Kelvin waves, the wave energy generated per unit divergence is proportional to $1/k$, while the divergence increase per unit energy increase is proportional to k, leading to constant growth rates. Although for very long wavelength Rossby waves the divergence per unit wave energy is small relative to the Kelvin waves, the growth rate is still high because the wave energy generated per unit divergence is higher relative to the Kelvin waves (figure 2-18). The wave energy generation per unit divergence decreases very rapidly with wavelength (relative to the Kelvin waves) because of the rapid decrease with wavelength in temperature anomaly per unit divergence (see figure 2-17; in this simplified case, temperature and heating are collocated). However, the fraction of energy that is sent to the divergent flow (again normalized by that of the Kelvin waves) actually increases with wavenumber until intermediate wavelengths (around $k = 7$), slowing the decrease in growth rate. At large wavenumbers, both these terms are small, leading to small growth rates.

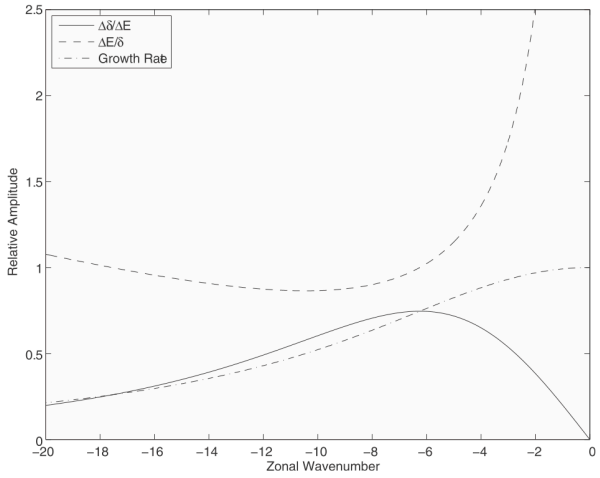

Figure 2-18. Relative amplitudes of the generation of wave energy per unit perturbation divergence ($\boldsymbol{\Delta}$E/d; dashed); the flow of energy into the divergent part of the wave per unit energy generation ($\boldsymbol{\Delta\delta/\Delta E}$; solid); and the product of these two quantities (dashed– dotted), which is equal to the divergence growth rate, as shown in figure. 2.15, for the n = 1 Rossby waves, normalized by the same values for the Kelvin wave (at the corresponding absolute wavenumbers).

The inertio-gravity wave spectrum is explained by similar logic, although the details are different because of the different structures of the waves, particularly the non-zero vorticity at zero wavelength and the increasing divergence with wavelength.

The numerical values of the corresponding growth rates (also normalized to the numerical Kelvin wave growth rate) are also plotted on this figure for comparison. The MRG and ER growth rates are essentially indistinguishable from the analytic solutions. The discrepancy for the inertio-gravity waves stems from the approximation used for the wave frequency in Eq. (D.23), which is only accurate to within 13% in this case (see, e.g., Gill 1982), whereas the error in the ER frequency is less than 2%.

The physical content of this argument is contained more in the method than the final expressions. The construction of instability mechanism here emphasizes the differing efficiencies with which the modes can convert input energy into divergent flow, driving more energy input. As the growth rates derived from this construction of the model resemble the numerical results closely, we feel that this vindicates our hypothesis, illuminating a further mechanism that influences the linear instability spectrum of the equatorial convectively coupled waves.

The specifics of our derivation assume the basic form of the moisture–stratiform instability where low-level divergence leads to second baroclinic convective heating a quarter-cycle later as discussed in the introduction. The detailed result is thus dependent on the existence of the moisture–stratiform (or similar) instability

mechanism.

2.6 Summary and Discussion

In this paper, we have demonstrated that our extension of the model of K08b to the equatorial beta plane allows us to produce a linear system with a spectrum of unstable modes that bear a good resemblance to the modes visible in the global OLR data, both in terms of excited wavenumber range and also in terms of the wave types present. The unstable Kelvin, MRG, and IG waves visible in the results of WK99 are reproduced well using this model.

Our model is closely related to that of Khouider and Majda (see, e.g., Khouider and Majda 2006a,b, 2008), especially in the inclusion of mid-tropospheric moisture as a control of convection depth. However, by making our model conceptually simpler than their model, the various instability and spectrum-shaping mechanisms are made clearer. The further extension of our model to the beta plane also allows the investigation of instability shaping due to the mean-state profile and the meridional winds of the various waves observed on the equatorial beta plane.

The model does fail to produce any significantly unstable ER or any MJO waves. As stated above, this may be due to our model possessing too great a low-frequency damping or lacking an effect that serves to destabilize the low-frequency waves. However, the observations of Yang et al. (2007) indicate that the Rossby wave signals detected in the OLR spectrum might have a different instability character. For example, they may be unstable only to finite disturbances, requiring a large extratropical Rossby or near-resonant MRG wave to excite them. Or possibly the

waves are simply stable, with their decay in balance to near-constant stochastic forcing from the extratropics and the MRG activity. The reason for the lack of MJO activity is at present unknown.

Previous interpretations of the spectrum, like those of Takayabu (1994) and WK99, use the differing projections of the mean-state heating onto the wave structure to explain the east–west asymmetry. In the context of our model, it was also observed that the position and size of the ITCZ affects the growth rates of the different waves: modes that possess a large spatial overlap with the ITCZ profile are enhanced, while those with a small overlap are weaker. However, even when the ITCZ configuration provides large overlap for the MRG or IG waves and small overlaps for the Kelvin waves, the Kelvin wave growth rates remain large compared to those of the MRG and IG waves, indicating that additional factors affect the growth rates of different wave types. We suggest that the efficiency with which waves convert input energy into divergent winds is an important factor. We note that Lindzen (1974) also argued that the east–west asymmetry in the n = 1, 2 IG waves may be related to the differing amounts of convergence in the different propagation directions. Our mechanism shares some characteristics with his argument in that the growth of modes is related to the strength of the divergent winds of that mode, except that our mechanism is based on the moisture–stratiform instability instead of the classical wave–conditional instability of the second kind (CISK) as in Lindzen (1974). We return with more discussions of wave-CISK at the end of the chapter.

With the addition of our energy flow divergence feedback mechanism, the basic shape of the wave spectrum is starting to become clearer. The linear part of the

spectrum is shaped by the combined actions of moist convective damping, which damps high-frequency waves; the damping effect of the second-mode convective heating on the mid-tropospheric moisture anomalies, which damps more strongly the lowest-frequency waves; the intertropical convergence zone (ITCZ) projection effect; and the energy flow feedback effect, which selects the wave types with larger divergent and/or geopotential components. In more realistic cases, the heating is not in general co- incident with the temperature (or geopotential) field, so it will also be necessary to consider the spatial correlation between the two.

Analytical extension of the energy flow feedback to our full set of equations is expected to be nontrivial; furthermore, our discussion is based on a simple linear model of convectively coupled waves. However, it seems likely that the principle of "wasted energy" in the rotational component of the velocity fields of the equatorial waves will also apply in the real atmosphere, helping to shape the observed spectrum of convectively coupled equatorial waves.

The present model does not make use of the column MSE budget so that it does not make a statement of the gross moist stability. It is, however, possible to use the vertically averaged free tropospheric moisture in place of the mid-tropospheric moisture and take advantage of column MSE conservation, as done in Khouider and Majda (2006a) and discussed in section 2.4. The gross moist stability to first baroclinic motions in the CSRM simulations of Kuang (2008a) is found to be close to neutral. Because we also neglect radiative and surface flux feedbacks, the moisture mode found in, for example, Fuchs and Raymond (2002), Raymond and Fuchs

(2007), and Sugiyama (2009a,b) is absent here. We plan to include the radiative and surface feedbacks to examine the moisture modes in the future.

Last, given the long history of wave-CISK (Yamasaki 1969; Hayashi 1970; Lindzen 1974), we would like to briefly discuss the relation between wave-CISK, the direct stratiform instability in Mapes (2000), and the moisture–stratiform instability in K08b and the present study. The direct stratiform instability may be viewed as a two-mode discretization of the classical wave-CISK envisioned in Lindzen (1974), in which waves modulate convection, which then further generates waves, and for waves of certain structures and phase speeds, the two can reinforce each other. Indeed, as shown in K08b, when the lag time between stratiform heating and deep convective heating is neglected, the growth rate of the direct stratiform instability increases linearly with wavenumber, similar to that observed in classical wave-CISK.

Our moisture–stratiform instability mechanism relies on the effect of midtropospheric moisture anomalies on convection, and hence differs from the classical wave-CISK (unlike the classical wave-CISK, it has bounded growth rates at short wave-lengths even without the MCD effect). The moisture–stratiform instability could be also viewed as wave-CISK in a very broad sense, if one defines wave-CISK as a self-exciting cooperative instability between wave and convection that does not require surface flux or radiative feedbacks (Bretherton 2003). However, it is unclear that this association is particularly meaningful because the definition of wave-CISK in this case would be so broad that it would not contain the actual physical processes that are at work.

Chapter 3 - Moist Static Energy Budget of the MJO-like Disturbances on an Aquaplanet in SP-CAM

In this chapter we describe the observation of a Madden-Julian Oscillation (MJO)-like spectral feature in the time-space spectra of precipitation and column-integrated Moist Static Energy (MSE) for a zonally symmetric aquaplanet simulated with Super-Parameterized Community Atmospheric Model (SP-CAM). This disturbance possesses the basic structural and propagation features of the observed MJO.

To explore the processes involved in propagation and maintenance of this disturbance, we analyze the MSE budget of the disturbance. We observe that the disturbances propagate both eastwards and polewards. The column-integrated longwave heating is the only significant source of column-integrated MSE acting to maintain the MJO-like anomaly balanced against the combination of column-integrated horizontal and vertical advection of MSE and Latent Heat Flux (LHF). Eastward propagation of the MJO-like disturbance is associated with MSE generated by both column-integrated horizontal and vertical advection of MSE, with the column long-wave heating generating MSE that retards the propagation.

The contribution to the eastward propagation by the column-integrated horizontal advection of MSE is dominated by synoptic eddies. Further decomposition indicates that the advection contribution to the eastward propagation is dominated by meridional advection of MSE by anomalous synoptic eddies caused by the suppression of eddy activity ahead of the MJO convection. This suppression is linked to the barotropic conversion mechanism; with the gradients of the low frequency

wind experienced by the synoptic eddies within the MJO envelope acting to modulate the Eddy Kinetic Energy (EKE). The meridional eddy advection's contribution to poleward propagation is dominated by the mean state's (meridionally varying) eddy activity acting on the anomalous MSE gradients associated with the MJO.

This is based upon Andersen and Kuang (2012).

3.1 Introduction

It is in the Recharge-Discharge paradigm (see section 1.4.D) that we will be interpreting our observations of the MJO, so it bears further exposition. The Recharge-Discharge mechanism, an extension of the thermodynamic feedback idea, is based upon the build up of MSE in the columns over the tropical ocean that occurs before the MJO deep convection. This convection and the succeeding processes discharge the column MSE anomaly, which is then recharged by the large-scale processes (e.g. Hendon and Liebmann 1990, Blade and Hartmann 1993, Hu and Randall 1994, Maloney and Hartmann 1998, Kemball-Cook and Weare 2001, Myers and Waliser 2003, Sobel and Gildor 2003, Kiladis et al. 2005, Agudelo et al. 2006, Tian et al. 2006, Benedict and Randall 2007, Maloney 2009). In order for Recharge-Discharge to constitute an instability mechanism, there must be sources of column MSE collocated in space and time with positive column MSE anomalies (similarly for sinks and negative MSE anomalies).

Recent studies appear to indicate that the moistening of the free troposphere (leading to a build up of MSE) is needed before the onset of strong deep convection (e.g. Brown and Zhang 1997, Sherwood 1999, Raymond 2000, Redelsperger et al. 2002, Ridout 2002, Bretherton et al. 2004, Derbyshire et al. 2004, Sobel et al. 2004, Takemi et al. 2004, Roca et al. 2005, Kuang and Bretherton 2006, Peters and Neelin 2006). Similarly, parameterizations that demonstrate a strong sensitivity to free-troposphere humidity have been shown to increase intraseasonal variability in GCMs (e.g. Wang and Schlesinger 1999, Woolnough et al. 2001). Ocean heat content may also be built up before the onset of convection, with the surplus heat flowing

into the atmosphere during the convective phase (e.g. Sobel and Gildor 2003, Stephens et al. 2004, Agudelo et al. 2006). In general, the MSE budget during MJO events is not well understood, although there have been recent numerical studies of this question (Maloney 2009, Maloney et al. 2010).

In another recent study of the MSE budget of large-scale tropical flows (Kuang 2011), it has been shown that the large-scale flow induced by MSE anomalies in a column, while acting to dissipate the column MSE anomaly, will become less efficient at doing so with longer wavelengths. This is because the temperature anomalies required for the generation of large-scale flow increases with wavelength, affecting the vertical distribution of convection. This is suggested as a possible scale selection mechanism explaining the limitation of the MSE driven waves to long wavelengths.

In analogy to the buoyancy driven KW theories, we will interpret the MJO growth and propagation as the overlap between "moist" air and "moistening". In this context and throughout this paper, "moist" is synonymous with a positive MSE anomaly and "moistening" with an MSE source.

The basic picture of the MSE budget in the MJO established to date is as follows: The shallow convection and circulations ahead of the convective anomaly have a moistening tendency, contributing to the MSE build up before the deep convection (e.g. Johnson et al. 1999, Kikuchi and Takayabu 2004, Kiladis et al. 2005, Benedict and Randall 2007). Column-integrated MSE may then be discharged during strong convective and stratiform heating. The large-scale circulations in the Western Pacific and Indian Ocean are strongly determined by the deep convection and have

been observed to export MSE for the convecting columns on average (e.g. Neelin and Held 1987, Back and Bretherton 2006). In this region the MJO amplitude is strongest and the MSE discharge appears to be enhanced by the MJO deep convective and stratiform stages (e.g. Johnson et al. 1999, Kiladis et al 2005).

MSE discharge during MJO convection may be modified by cloud-radiation and wind-evaporation feedbacks, which could reduce or change the sign of the MSE tendency (e.g. Raymond 2001, Lin and Mapes 2004, Peters and Bretherton 2006, Sugiyama 2009a, 2009b). Intraseasonal wind speed and latent heat flux anomalies are observed to have a positive covariance with the intraseasonal precipitation (e.g. Zhang 1996, Raymond et al. 2003, Masunaga et al. 2006, Maloney and Esbensen 2007, Araligidad and Maloney 2008) and wind-evaporation feedbacks have been found to be important for supporting the intraseasonal convection in modeling studies (e.g. Raymond 2001, Maloney and Sobel 2004, Fuchs and Raymond 2005, Sugiyama 2009a, 2009b). However, the WISHE feedbacks are not generally in the original sense of WISHE, where easterly anomalies interact with mean state easterlies to create enhanced flux under the warm anomaly region in KW-type circulation, pulling convection forwards in space (e.g. Emanuel 1987, Neelin et al 1987, Emanuel et al. 1994) to create overlap between the convective heating and the warm anomaly. The intraseasonal latent heat flux-precipitation relationships are consistent with the more general role of enhanced wind speed in supporting tropical precipitation – particularly in regions of high column relative humidity (e.g. Back and Bretherton 2005). Observations also suggest that horizontal advection of temperature and moisture from the cooler, drier subtropics is an important

regulatory mechanism for the atmospheric MSE budget and MJO deep convection (e.g. Mapes and Zuidema 1996, Myers and Waliser 2003, Back and Bretherton 2006).

Model analysis of the MSE budget in CAM3 with a realistic base state shows that horizontal advection plays an important role in regulating the recharge-discharge cycle. The advection effect is dominated by the tropical synoptic scale eddies (Maloney 2009). Maloney (2009) observed a buildup of column MSE in advance of intraseasonal precipitation within low-level easterly anomalies and a discharge of MSE during and after the precipitation, within low-level westerlies. The recharge-discharge budget of the MSE is driven by horizontal advection (somewhat opposed by a mostly out of phase latent heat flux), which is itself dominated by the meridional advection of dry subtropical air into the MJO region by atmospheric eddies, which are suppressed by the anomalous large-scale winds ahead of the convection and enhanced behind.

Budget calculations performed upon reanalysis data also show similar results (Kiranmayi and Maloney 2011), with horizontal advection acting as a significant source of MSE ahead of the MJO convection and as a sink behind, although some terms appear to more important in the reanalysis budget than previous model analyses have indicated. For example, the horizontal and vertical advection terms are of comparable amplitude in the reanalysis budget. However, there is a large residual in the calculated budget, indicating that the results may not be complete. The residual is largest ahead of the MJO, perhaps indicating the absence/misrepresentation of an MSE source (the authors suggest shallow

convection as a possibility) from the reanalyses.

In this chapter, we describe the observation and MSE budget analysis of an MJO-like disturbance in the Super-Parameterized CAM (SP-CAM) on a zonally symmetric aquaplanet. This work differs from similar, previous analyses in several ways. Firstly, our analysis is of a model using a more explicit representation of convection- the super-parameterization (described below). This improves aspects of the realism of the simulation. Secondly, we use a zonally symmetric basic state, which simplifies the analysis and diagnosis of the energy budget. Thirdly, the MJO observed in our model shows both eastwards and polewards propagation - a phenomenon not reported in earlier works - which allows us to investigate another aspect of the intraseasonal dynamics (albeit in simplified form).

In Section 2, the model and the experimental setup is described. Also, basics of the model output are analyzed: Time-space spectra are used to identify the MJO-like signals in the model, which are also visualized in Hovmöller diagrams of the tropics. Towards an understanding of the processes involved in this signal, we present a composite evaluation of the leading terms of the MSE budget of MJO-like signals in Section 3 and their impacts on the MJO-like disturbance's growth and/or propagation are discussed. Further discussion follows in Section 4, with conclusions in Section 5.

3.2 Model Description

3.2.A SP-CAM, forcing and Boundary Conditions

In this paper, we analyze output from SP-CAM version 3.5. SP-CAM is a modified version of the Community Atmosphere Model (CAM) where a small domain two-dimensional Cloud System Resolving Model (CSRM) is embedded within each grid point of CAM (Khairoutdinov and Randall, 2001; Khairoutdinov et al., 2005).

The embedded 2D CRSM are used to calculate the moist physics, convection, turbulence, and boundary layer processes as they respond to the large-scale forcing, which is evaluated by the GCM. The explicit calculation of convection in the CSRM avoids the simplifications associated with the parameterizations of these processes used in other models, at the cost of increased computation time.

Grabowski (2001, 2003) observed MJO-like disturbances in a super-parameterized model. Key to these disturbances was the buildup of humidity in the convecting region. Comparison of SP-CAM with standard CAM shows a much stronger MJO signal (Zhu *et al.* 2009), associated with an improved sensitivity of precipitation rate to column-integrated moisture.

Kim *et al.* (2009) also examined the MJO in a number of climate models using a large suite of diagnostics. They found that based upon the realism of the MJO structures (evaluated using multivariate empirical orthogonal functions), power spectra, the eastward propagating equatorial anomalies in OLR, latent heat flux and a number of other fields, SP-CAM (run with realistic boundary conditions) demonstrated the best skill at representing the MJO (along with the ECHAM4/OPYC model).

Benedict and Randall (2009) investigated the detailed dynamic and thermodynamic structures of the MJO they observed in SP-CAM using a realistic boundary condition.

We use the version of SP-CAM with semi-Lagrangian advection at T42 resolution for the CAM component. The model outputs have horizontal resolution of ~2.8 degrees. The embedded 2D CSRM is oriented in the north-south direction and has 32 grid points in the horizontal with a 4km resolution. There are 28 vertical levels in the CSRM aligned with the lower 28 vertical levels (out of 30) in the CAM model. The CAM time step is 15 minutes and the CSRM time step is 20 seconds.

The model is forced with a temporally and zonally constant Sea Surface Temperature (SST) given as a function of latitude ϕ, in degrees, by:

$$SST(\phi) = 2 + \frac{27}{2}(2 - \zeta - \zeta^2),$$

where the SST is in Celsius and

$$\zeta = \begin{cases} \sin^2\left(\pi \dfrac{\phi - 5}{110}\right) & 5 < \phi \leq 60 \\ \sin^2\left(\pi \dfrac{\phi - 5}{130}\right) & -60 \leq \phi < 5 \\ 1 & |\phi| < 60 \end{cases}$$

(plotted in figure 3-1a), and seasonally varying insolation for sixteen years, with output every three hours.

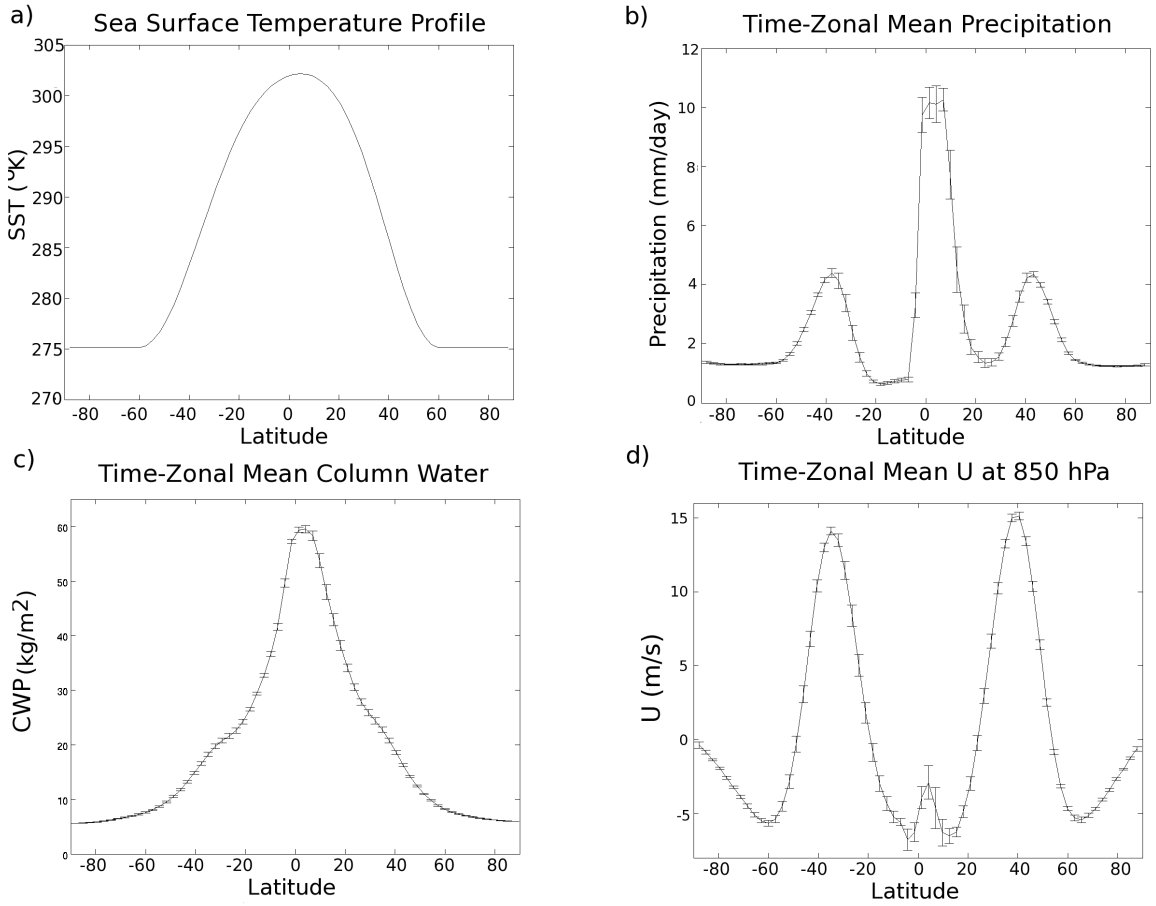

Figure 3-1. Time and zonal mean climate: a) Sea Surface Temperature, b) Precipitation, c) Column Moisture, and d) 850hPa Zonal Wind. Error bars indicate the standard deviation of the zonal mean of the time mean values.

3.2.B Simulated Climate

The model described produces a climate that is qualitatively similar to the central and east Pacific. Some interesting climate quantities are plotted in figure 3-1. The SST distribution used, which peaks at 5^oN, produces a single Inter-Tropical Convergence Zone (ITCZ) in the time mean, with strong precipitation peaked at around 5^oNorth (figure 3-1b), and secondary peaks in the storm tracks at around 40^o North and South.

The ITCZ is also the region of greatest column-integrated water (figure 3-1c) and low-level zonal winds (U850; figure 3-1d) within the tropics. The U850 field shows easterlies throughout the tropics, with strongest winds on the edges of the ITCZ. The time/zonal mean low-level meridional wind is weak, but it shows convergence into the ITCZ and the tropics (not shown). The presence of the zonal easterlies in the tropics is a significant deviation from the climate in the region around the warm pool on Earth, where mean westerlies are observed. It is expected that, all else being equal, this will lead to surface flux anomalies significantly different to those on the Earth, as the sign of the WISHE effect is dependent upon the signs of both the mean state and anomalous winds. While the presence of a warm pool in the imposed SST can generate a more realistic wind distribution with zonal westerlies, we have chosen to use a simpler setup for this initial investigation.

While the low-level extratropical winds are stronger in the Northern Hemisphere, the Southern Hadley Circulation is stronger (not shown). The associated Southern jet is also stronger and more equatorial than the Northern one. This is consistent with the SST boundary condition and explains the strong Southern Hemisphere

extra-tropical anomalies. It is only at very low levels that the Northern Hemisphere winds are slightly stronger.

3.2.C Spectral Analysis of Model Fields

The model equatorial precipitation shows a number of statistically significant peaks representing propagating disturbances (figure 3-2), when analyzed in zonal wavenumber-frequency space, just as observed in OLR from the satellite record (WK99). These waves represent a large part of the tropical synoptic-scale convective variability, organizing individual convective elements (typically 100 km across, persisting for a few hours) into wavepackets with large spatial (thousands of kilometers) and temporal (days) scales (e.g., Chang 1970; Nakazawa 1988). The wave activity peaks have been identified with the equatorially trapped waves of rotating shallow water wave theories (e.g., Matsuno 1966; WK99; Yang et al. 2007, Andersen and Kuang 2008). Not present in the classical shallow water wave system, and missing from most simple models is the large signal at intraseasonal (30-90 days) timescales and zonal wavenumbers 1-3 that is the spectral signal of the MJO.

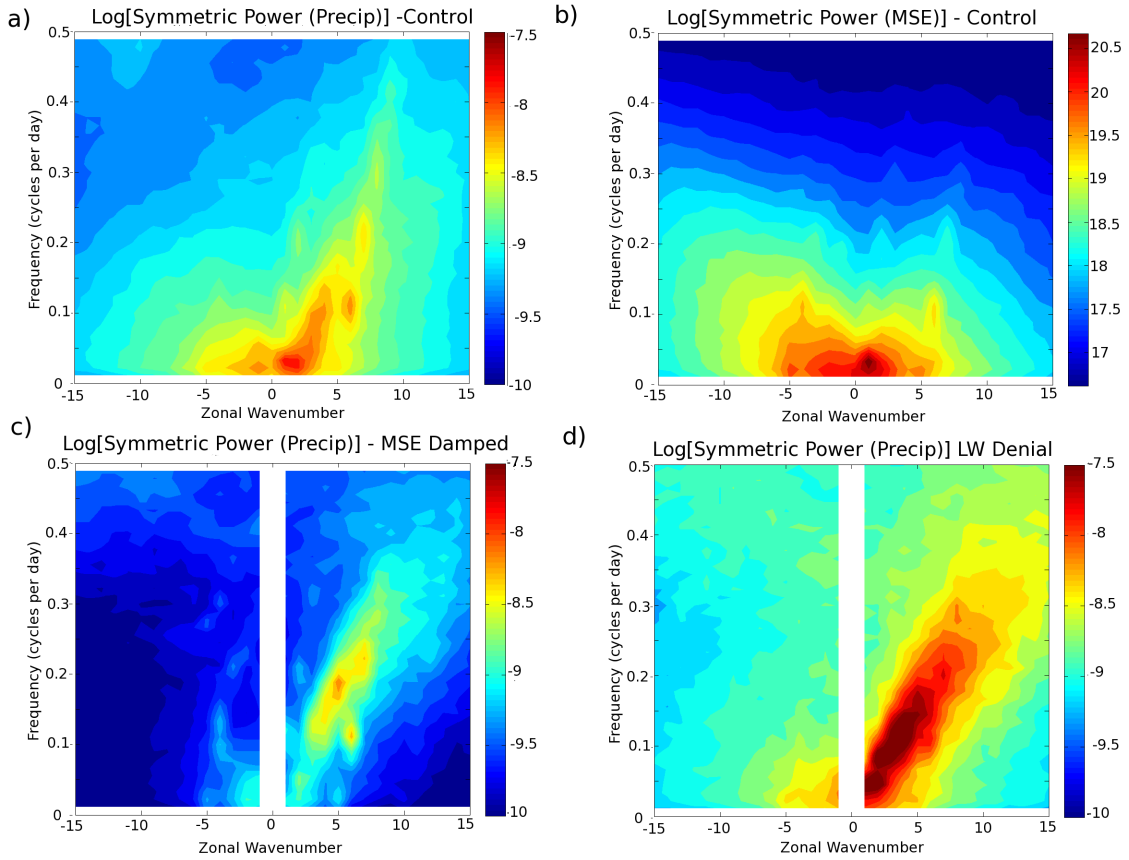

Figure 3-2. Logarithm (base 10) of the spectral power for signals symmetric about the equator in a) precipitation, and b) MSE for the control case and precipitation for the c) MSE Damped and d) LW Denial cases. The power spectrum is averaged over the region 15°S to 15°N and is constructed from model output (after WK99). The wavenumber zero data for panels c) and d) is deleted as it is rendered meaningless by the experimental procedure.

Figure 3-2a shows the precipitation power spectrum for disturbances symmetric about the equator. This is constructed following the procedure of WK99. These spectra are broadly similar to observations, with strong MJO, KW, and Rossby wave signals. The equivalent depth (a measure of the vertical scale of the wave structure, inferred from the phase speed) is approximately 25m, similar to that observed. SP-CAM, with a generally similar SST distribution, has previously been shown to possess MJO-like spectral features (Marat Khairoutdinov, 2009, personal communication).

The antisymmetric part of the SP-CAM spectrum (not shown) is not as realistic. For example, the Mixed Rossby-Gravity (MRG) waves are not well represented. However, we have observed that this feature is stronger in double ITCZ mean states. The mean state dependence of the features of the spectrum is an interesting and open question that we do not address here.

The spectrum of OLR (not shown) is generally similar. The spectra of MSE disturbances (figure 3-2b) are different to the precipitation and OLR spectra – the Kelvin and Rossby waves are weaker, while the MJO signal remains strong relative to the background (this is also seen in the observed spectra of precipitable water, e.g. Roundy and Frank 2004, Yasunaga and Mapes 2011). This is another indication that the MJO is a fundamentally different type of wave to the KW – one that is dominated by MSE fluctuations, rather than the buoyancy fluctuations that drive the shallow water wave type behavior of the other waves. The MSE spectrum also includes a number of peaks around wavenumber 6. These are the signatures of the strong extratropical waves present in our model entering the equatorial region. Care

must be taken to exclude these waves from our MJO signatures used for the regression study below.

In order to demonstrate that the column MSE anomalies are a fundamental part of the MJO-like disturbance (rather than simply being generated by it), we have conducted an experiment where the column MSE in the model (between 20^oN-20^oS) is damped towards its time- and zonal-mean values with a 12-hour timescale. To maintain the climatology, the zonally averaging prognostic variables (excluding temperature) are nudged to the climatological values of the control runs over a timescale of 30 minutes. Temperature is nudged weakly with a timescale of 10 days. We have verified that nudging alone, without adding the column MSE damping, produced a spectrum similar to that of the control experiment. In this case, while the Kelvin waves are still present in the simulated precipitation, the MJO-like signal is greatly reduced (figure 3-2c). Figure 3-2d shows an experiment where radiative heating is homogenized in the zonal direction. The results of this experiment are discussed below.

Figure 3-3a and figure 3-3b shows equatorial (0^o-6^oN) Hovmöller plots of precipitation for a short period of our model run. Even in the unfiltered field (figure 3-3a), a strong MJO event can be seen propagating eastwards, beginning at $\sim 300^o E$ and Day 5600, continuing around the globe coherently for at least two full circumferences over a period of approximately 120 days. The multi-scale nature of the MJO in the model can be seen in this field - the MJO envelope contains and modulates many faster moving, short-lived waves traveling in both easterly and westerly directions.

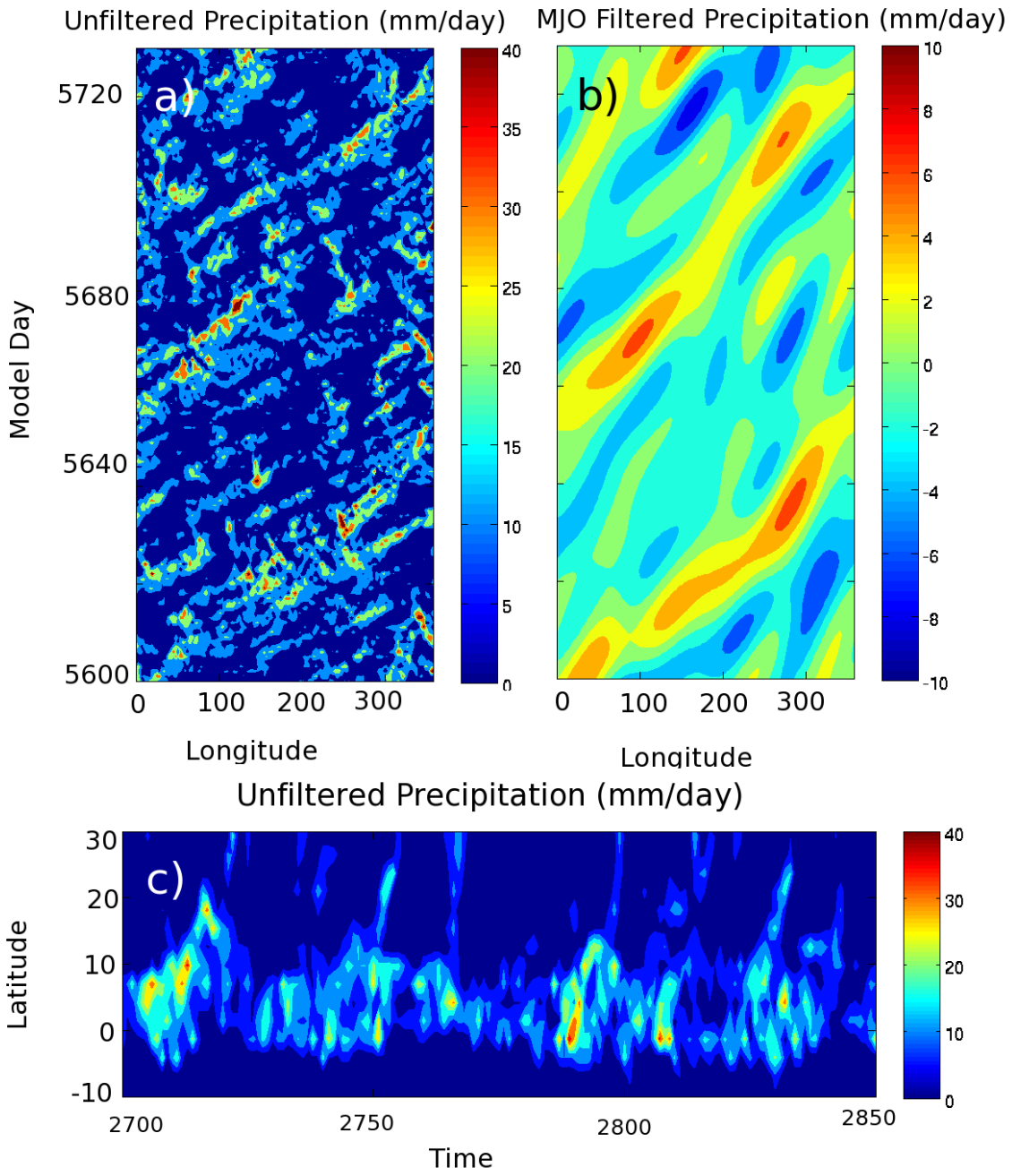

Figure 3-3. Hovmöller diagrams a) Unfiltered precipitation signal (averaged over **0^o**N-**6^o**N); b) MJO frequency-wavenumber filtered precipitation signal (averaged over **0^o**N-**6^o**N); c) Unfiltered precipitation signal (averaged over **160^o**E-**160^o**W);

Once the precipitation is filtered into the MJO frequency and wavenumber region of spectral space (wavenumbers 1—3, periods 20—100 days), the MJO signal is easily seen (figure 3-3b). MJO events tend to arise randomly, propagate for 1-2 circumnavigations and then die off, while another event arises elsewhere on the globe. The mechanisms involved in the events' beginnings and ends are beyond the scope of the current work and will not be investigated in this paper.

Poleward propagation can also be observed in the precipitation field. Figure 3-3c shows the time-latitude evolution of precipitation, averaged over 160^oE to 160^oW. Poleward propagating signals can be seen to move from near the equator to up to 25^oN.

3.3 Results

3.3.A Regressed dynamic fields

The model fields are regressed against the MJO-filtered OLR on the latitude of greatest mean variance as described in Appendix E to show the structure of the MJO-like disturbance in the model. Several model fields are shown in figure 3-4. The regression basis point at (180^oE, 4.2^oN) is indicated on the figures and the coastlines are included in the map to give a sense of the scale of the disturbances.

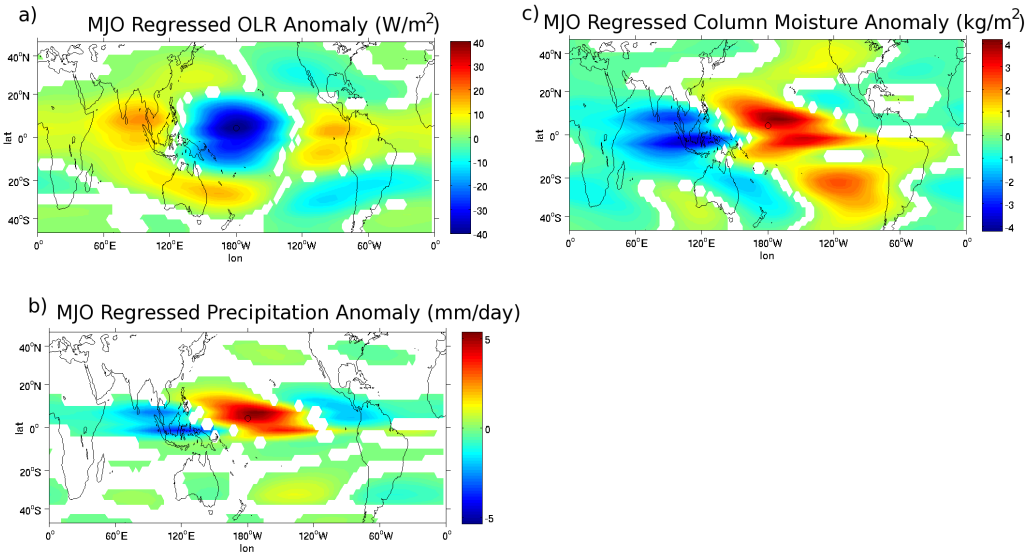

Figure 3-4. Composite anomalies for the MJO like disturbances produced by regression, scaled to a -40W/m² OLR anomaly. a) Outgoing Long-wave Radiation; b) Precipitation; c) column-integrated moisture.

The composite MJO's convective signal can be seen in the OLR field (figure 3-4a) – which is essentially a measure of the average temperature of the highest opaque surface visible to the satellite. There is a large region of reduced OLR around the regression point, caused by colder emissions from the larger number of higher cloud tops in the active phase. The suppressed convection is visible as the warm anomalies, which are caused by the warmer temperatures of the low cloud tops and the greater lower-troposphere and sea surface area visible from space in this region.

Precipitation (figure 3-4b) is likewise enhanced near the regression point and suppressed to the east and west of the convective signal, although the enhancement is much stronger in the region of the ITCZ where the mean conditions are much more conducive to precipitation (and the mean precipitation is larger). The enhanced precipitation also possesses a noticeable tilt, with the eastern edge closer to the equator and the western edge closer to the pole. The convective region also contains a positive moisture anomaly, seen as an increase in the integrated column moisture (figure 3-4c), that has a tilt similar to the precipitation. The large moist anomalies in at around 120^{o}W, 40^{o}N and 40^{o}S are due to the advection of moist tropical air by the MJO large-scale low-level winds. Similarly, the smaller dry anomaly at $\sim(160^{o}\text{E}, 30^{o}\text{S})$ is due to the advection of dry extratropical air into the tropics by the MJO large-scale flow.

The OLR signal has a greater spatial extent than the precipitation. This is not considered surprising, as we expect that the OLR anomalies can be generated by modification in the amount or depth of convection throughout the tropics, while the

precipitation anomalies are expected to be larger where the mean state conditions are more favorable for precipitation i.e. within the ITCZ.

The wind fields (850 hPa – figure 3-5a - and 200hPa – figure 3-5b) show circulation similar to that typical of the MJO, with low-level convergence near the convective center and divergence centered approximately halfway around the planet. The upper-level winds show a reversed pattern, with divergence above the reference point. The peak low-level winds are located near the ITCZ. While the westerlies peak to the west of the convective center, there is a small westerly signal under the convection. Also visible at low levels are the Rossby gyres associated with the MJO (e.g. Weickmann 1983, Hendon and Salby 1994, and Kiladis et al. 2005). However, the upper level gyre visible in the southern hemisphere is not the tropical response to the MJO heating. This gyre is located significantly closer to the equator, and the gyre is seen to tilt toward the pole with height, as seen in observations. In figure 3-5c, we can see the zonal wind structure at the reference longitude. The poleward tilt and the baroclinic nature of the gyre are visible near the equator. The gyre visible in the vector fields is due to the interaction with the extratropical response in the Southern jet, in the form of an equivalent barotropic gyre, which adds to the baroclinic tropical gyre to create the observed wind field.

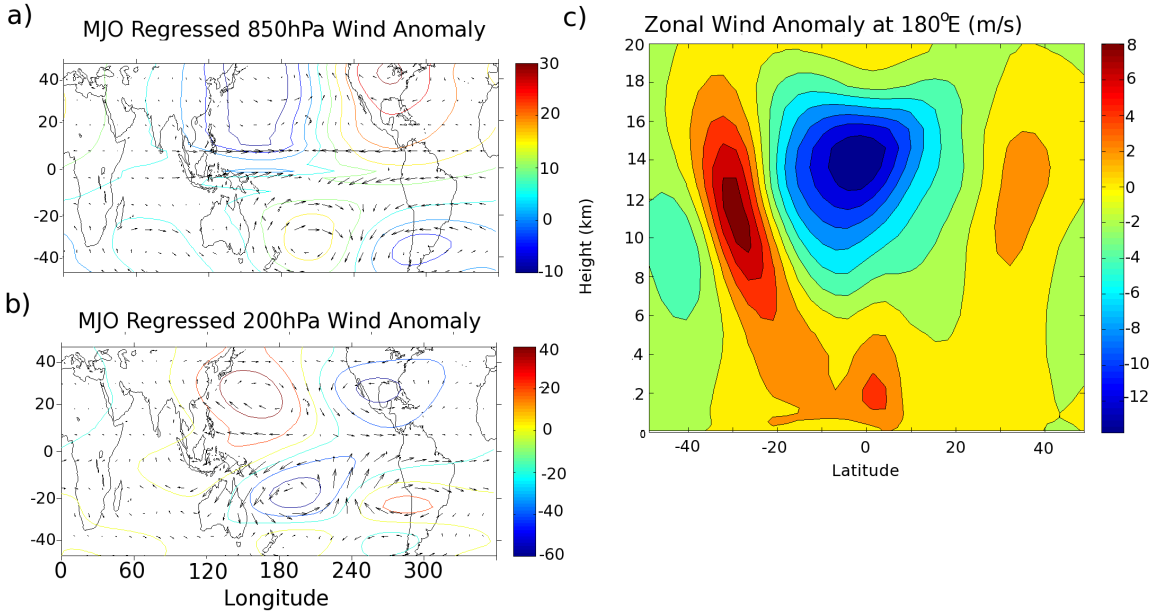

Figure 3-5. Composite winds anomalies (vectors) for the MJO like disturbances produced by regression and stream function (contours), scaled to a -40W/m^2 OLR anomaly. a) 850hPa (maximum wind speed 5.1 m/s); b) 200hPa (maximum wind speed 11.2 m/s); c) Vertical-meridional cross section of MJO regressed zonal wind at the reference longitude.

The regressed fields also show strong signals of extra-tropical waves, present in the strong jets within the model. To the south of the equator, these signals can be quite prominent and quite equatorial due to the stronger southern Hadley Cell.

Figure 3-6 shows the MJO regressed Long- and Short-Wave heating anomalies averaged over the ITCZ region. These are qualitatively similar (although generally of larger amplitude) to the radiative heating structures calculated by Ma and Kuang (2011) from Cloudsat observational data. Figure 3-7 shows the MJO regressed horizontal moisture transport, again averaged over the ITCZ region. This is comparable to the observations of Benedict and Randall (2009).

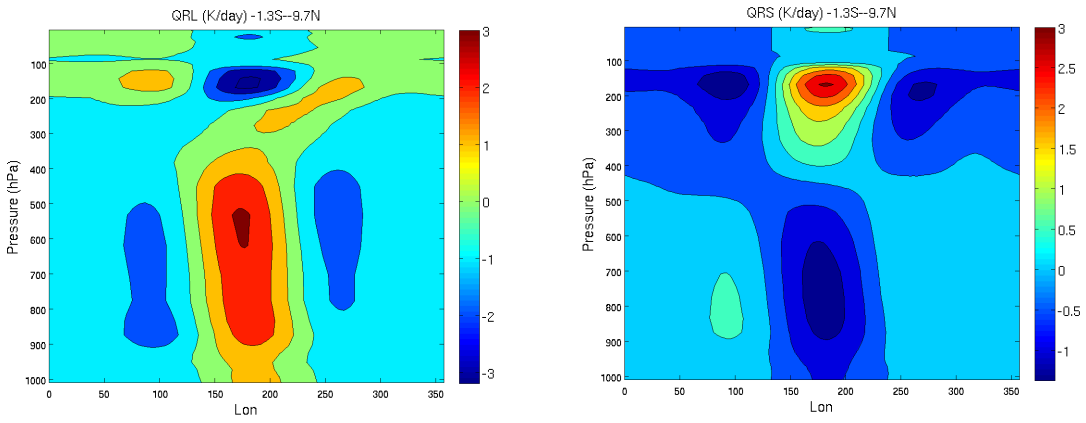

Figure 3-6. The MJO regressed a) Long- and b) Short-Wave heating anomalies, averaged across the ITCZ region ($\mathbf{1.3^o}$S – $\mathbf{9.7^o}$N).

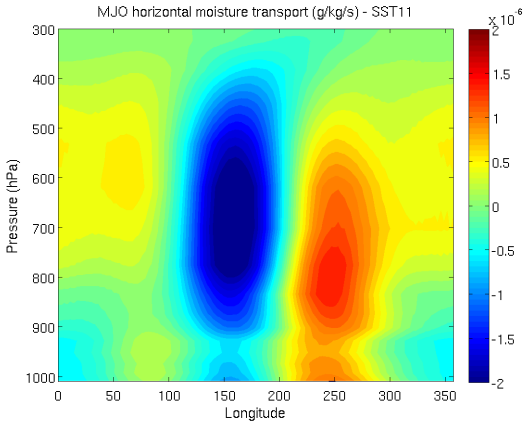

Figure 3-7. The MJO regressed horizontal moisture transport, averaged across the ITCZ region ($\mathbf{1.3^oS}$ – $\mathbf{9.7^oN}$).

3.3.B MSE budget and residual calculation

The MSE is calculated every three hours from the model instantaneous fields. The 3D MSE field and the column-integrated MSE are regressed against the MJO index to give a composite structure of the MSE anomalies associated with the MJO. Much like observations of the Earth's MJO, the observed anomalies have a tilted vertical structure (a), with preconditioning of the lower and middle troposphere ahead (east) of the convective signal (Kiladis et al. 2005). This MSE anomaly is dominated in the low and middle troposphere by the moisture anomaly (not shown) associated with the signal. The peak MSE anomaly in the model is approximately 2 kJ/kg, in approximate agreement with observed values (e.g., Kemball-Cook and Weare 2001; Kiladis et al. 2005).

The column-integrated MSE (figure 3-8b) closely follows the shape of the column-integrated moisture field (figure 3-4c) – as moisture anomalies dominate the column MSE anomalies at the MJO timescale – with a positive MSE anomaly running approximately along the ITCZ region, with the western end tilted polewards.

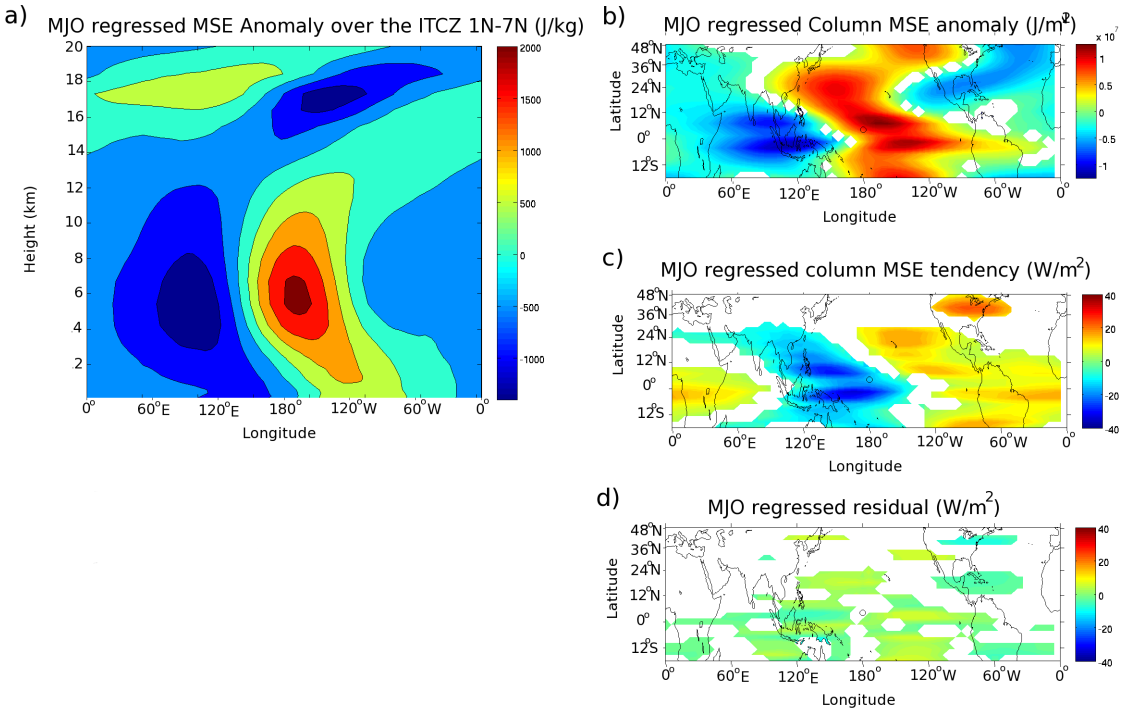

Figure 3-8. MJO regressed MSE and column MSE budget terms. a) Zonal-Vertical cross-section along the ITCZ peak; b) Column-integrated MSE anomaly; c) Column-integrated MSE time tendency; d) MJO regressed residual.

The column-integrated MSE tendency is calculated in two ways. We can calculate it indirectly from the column-integrated budget terms from the time mean fields over that three-hour interval:

$$\langle \partial_t h \rangle_{budget} = -\langle \omega \partial_p h \rangle - \langle v \cdot \nabla h \rangle + LH + SH + \langle LW \rangle + \langle SW \rangle, \quad (3.3)$$

where p is the pressure, v is the pressure-surface wind vector, ω is the pressure velocity, LH and SH represent the latent and sensible heat fluxes into the atmospheric column from the surface, and LW and SW are the long- and short-wave radiative heating rates. The left-hand side is the local tendency of $\langle h \rangle$, the first and second terms on the right represent advection of h by the winds, and the final four terms represent the external sources.

The MSE tendency can also be calculated directly by subtracting the MSE at the last time step from the current value before vertically integrating:

$$\langle \partial_t h \rangle_{explicit} = \langle \frac{h(t) - h(t - \Delta t)}{\Delta t} \rangle \quad (3.4)$$

Both these tendency terms are calculated explicitly from the eight times daily output of SP-CAM and then regressed against the MJO OLR as described above, allowing us to determine their contributions to the MJO-like signal's MSE tendency.

The calculated budget for the MJO-like anomalies shows positive MSE tendencies to the east and to the north of the convective center with negative anomalies to the west and equatorwards. This distribution indicates that the MSE anomaly is propagating to the east and towards the pole (figure 3-8c).

The difference between the two $\langle \partial_t h \rangle$ values is the residual, and is a combination of numerical effects, processes that slightly violate conservation of MSE, and errors

due to phenomena happening at time- and space-scales smaller than the scales in the output data. The residual is also regressed against the MJO OLR to determine its contribution to the MSE budget for the MJO (figure 3-8d). For the small number of points where it is statistically significant, the regressed residual is generally small compared to the leading h tendency terms, allowing us to have some confidence in our diagnosis of these terms' contribution to the MSE budget for the MJO.

3.3.C Budget decomposition and projections

By projecting anomalies in the budget quantities onto the MSE anomaly and its time derivative, we can determine which terms contribute most to the maintenance/dissipation of the anomaly and which contribute to or retard the propagation. In figure 3-9a, the fractional energy source for the MSE anomaly due to each term is displayed (sensible heat flux is negligible and not plotted). The contribution due to source x, S_x, is calculated as

$$S_x = \frac{\|x \cdot \langle h \rangle\|}{\|\langle h \rangle^2\|} \qquad (3.5)$$

where $\|y\| = \iint_{ITCZ} y dA$ is the integral of quantity y over the ITCZ (6^oS to 12^oN here, along all longitudes; The qualitative results are not particularly sensitive to the precise boundaries chosen, as shown in Appendix G). In this case, the "ITCZ" is defined as the region where precipitation is both strong and varies approximately linearly with column MSE.

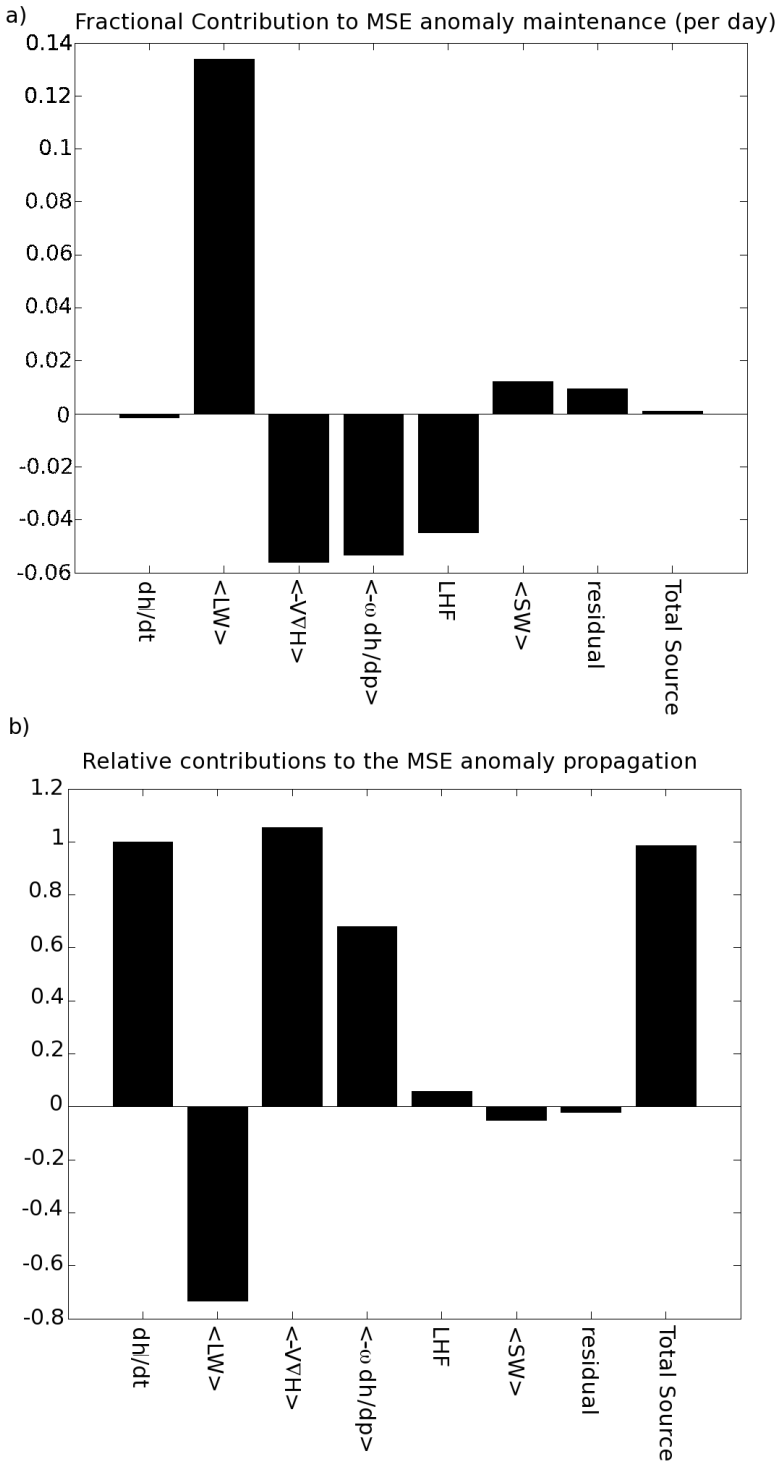

Figure 3-9. a) Fractional contributions of the MSE budget terms to the maintenance/dissipation of the MJO MSE anomaly. b) Fractional contributions of the MSE budget terms to the propagation of the MJO MSE anomaly.

From this we can see, firstly, that the MSE tendency is almost exactly in quadrature with the MSE anomaly, which is to be expected from the fashion in which we constructed the composites. We can also see that the long-wave heating, $\langle LW \rangle$, is the dominant source of column MSE for the MJO, with a small contribution from the short-wave heating, $\langle SW \rangle$, and the residual processes. The other terms shown - horizontal advection, $\langle \vec{V} \nabla h \rangle$, vertical advection, $\langle \omega \partial_p h \rangle$, and the latent heat flux (LHF)-- are all net sinks of column MSE. The sum of the sources is shown, for comparison with the projection of $\frac{dh}{dt}$. The difference is negligible compared to the sources shown.

The contribution each term x makes to the propagation, s_x, is shown in figure 3-9b. This is calculated in a similar way to the contribution to the anomaly:

$$s_x = \frac{\|x \cdot \langle dh/dt \rangle\|}{\|\langle dh/dt \rangle^2\|} \tag{3.6}$$

As can be seen, the long-wave is the only significant retarding quantity, while both advection terms are significant sources of MSE associated with the propagation of the anomaly.

Comparison of the amplitude of the regression coefficients in the MSE budget (equation 3.3) allows us to identify the leading terms in the MJO MSE budget for this experiment. These are:

1) Longwave heating (figure 3-10a) – The longwave heating anomaly, caused primarily by the anomalously low OLR from the enhanced anvil clouds, acts as a source of column-integrated MSE variability, balanced against the sinks due to the vertical and horizontal advection and latent heat flux anomalies in

the region around the convective center. The long-wave heating anomaly is approximately 26% of the precipitation anomaly (in power units) at the regression point, larger than that observed by Lin and Mapes (2004). To demonstrate the importance of the long-wave heating to our observed anomaly, we have conducted a mechanism denial experiment, wherein the radiative heating is homogenized zonally, while the climatology is maintained through the same methods as the MSE damping experiment described above. In this case (figure 3-2d), we observe that the Kelvin waves are still active, while the MJO-like disturbance is absent from the precipitation spectrum.

2) Horizontal advection (figure 3-10b) – Horizontal advection acts as a source of column MSE to the east and especially polewards of the convective center. The horizontal advection term is discussed in more detail below.
3) Vertical advection (figure 3-10c) – Vertical advection of MSE appears to be a source of column-integrated MSE to the east of the convective center, in the suppressed region, and a sink of column MSE in the convective region. This causes it to act as a damping on the anomaly. There is also a significant overlap between the vertical advection and the column MSE tendency, contributing to the eastward propagation. Vertical advection also appears to act against the polewards propagation, by counteracting some of the energy import by horizontal advection in the region polewards of the convective center. The Normalized Gross Moist Stability (NGMS) is defined as

$$NGMS = \frac{\langle \omega \partial_p h \rangle}{P}, \tag{3.7}$$

where P is the precipitation anomaly in power units.

Gross Moist Stability (GMS; Neelin and Held 1987) is a useful concept when considering the dynamics of convectively coupled systems. GMS is essentially the net export by horizontal flow through the boundary of the convective system of a quantity that is (at least approximately) conserved by moist processes, such as MSE or moist entropy. The GMS is typically normalized by a quantity that measures the amount of convection occurring in the system, such as precipitation rate or total mass flux.

A negative GMS indicates that the outflow of MSE (typically in the upper troposphere) is less than the inflow (typically at low levels). This can happen for a variety of reasons and indicates that convection is moistening its own environment – creating conditions favorable for further convections – an unstable situation.

For the composite disturbance in SP-CAM, the NGMS at the regression point is approximately 0.21. NGMS is a measure of the efficiency with which the divergent flow exports MSE. A positive value represents stability, although a small value is more easily overcome by other mechanisms, such as the long-wave heating discussed previously. The NGMS could decrease with horizontal wavelength (e.g. Kuang 2011), contributing to the scale selection of the MJO-like distrubances. Whether this wavelength dependence is the case in our present experiments is not clear.

The column-integrated MSE variability source represented by the advection at around 30^o to 40^oN is substantially polewards of the MSE tendency – this

appears to be a signal of the extratropical waves that are strong in this model, rather than the MJO. The extratropical waves appear at the northern edge of the analysis domain as large signals in horizontal and vertical advection. These sources mostly cancel together as shown by the total advection, in figure 3-10d.

Surface latent heat flux (figure 3-11a) has a small contribution to the MSE anomaly propagation. However, as latent heat flux anomaly is a significant sink of column-integrated MSE variability from the anomaly, this term deserves some investigation. The LHF anomaly is mostly negative under the positive column MSE anomaly, leading to damping of the MJO by LHF. This is not totally consistent with the simple WISHE picture and the mean state easterlies that exist near the equator.

The latent heating distribution observed can be explained in terms of a bulk surface flux formulation, which is a reasonable approximation for the surface scheme used in SP-CAM,

$$LHF = C\,\overrightarrow{|u|}\,(q^* - q_{sfc}), \tag{3.8}$$

where C is a constant; $\overrightarrow{|u|}$ is the windspeed near the surface; q^* is the saturation humidity at the surface temperature and pressure; and q_{sfc} is the actual humidity near the surface.

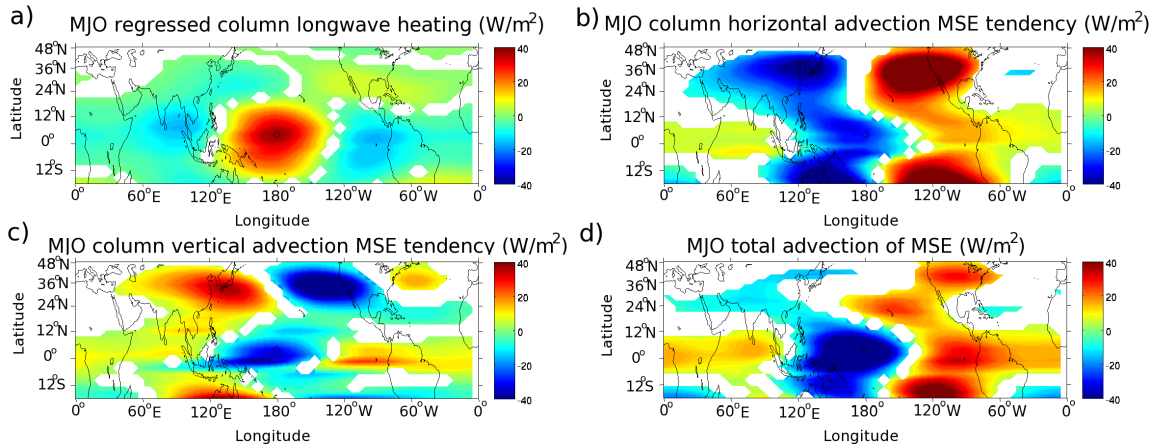

Figure 3-10. Leading terms in the MJO regressed column MSE budget. a) Column-integrated long wave radiation forcing; b) Column-integrated horizontal advection of MSE; c) Column-integrated vertical advection of MSE (equivalent to column-integrated MSE convergence); d) Total column-integrated advection of MSE.

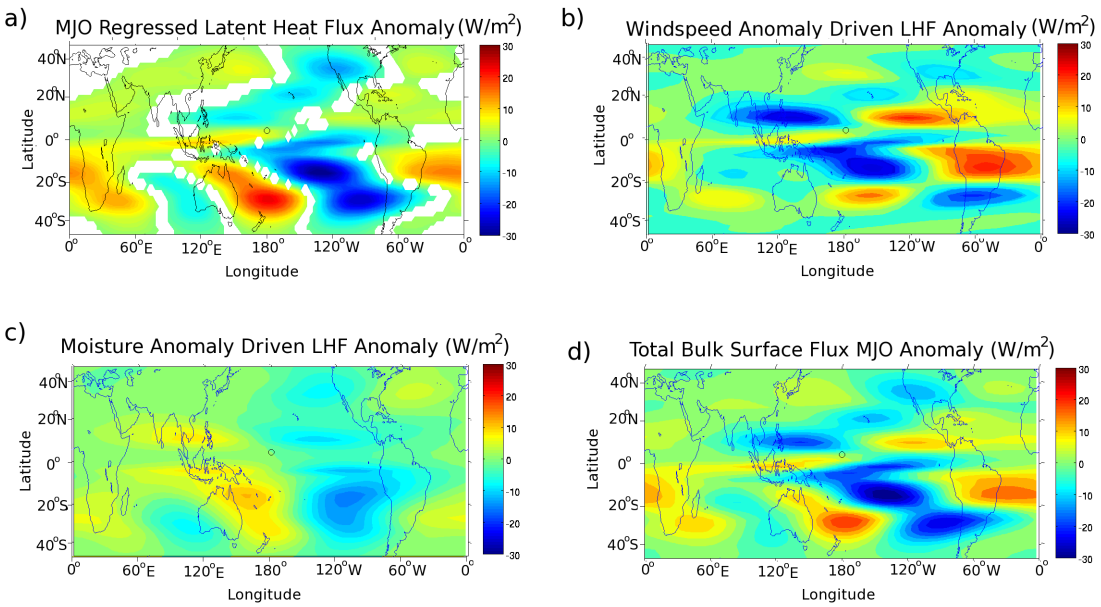

Figure 3-11. Latent Heating Terms. a) MJO regressed Latent Heat Flux Anomaly; b) MJO Latent Heating anomaly attributable to changes in surface level wind-speed in a bulk surface flux calculation; c) MJO Latent Heating anomaly attributable to changes in surface level moisture content in a bulk surface flux calculation; d) Total bulk surface scheme latent heat flux anomaly.

In the WISHE argument, the changes in $\overrightarrow{|u|}$ across a disturbance are assumed to dominate changes in LHF. The climate-zonal mean latent heat flux calculated with equation 5 is qualitatively the same as that calculated by the model surface scheme (not shown). In this calculation, C is estimated by finding the multiplier that minimizes the difference between the two time-zonal mean LHF curves.

In the bulk surface flux calculation, the flux anomalies can be linearly approximated by a sum of flux anomalies due to the various anomalies in the dynamic fields associated with the MJO:

$$LHF \approx C\,\overrightarrow{|u|}\,(q^* - q_{sfc}) + C\Delta\,\overrightarrow{|u|}\,(q^* - q_{sfc}) - C\,\overrightarrow{|u|}\,(\Delta q_{sfc}) + C\,\overrightarrow{|u|}\,(\Delta q^*), \quad (3.9)$$

The first term on the right is the mean LHF, the second is the anomaly due to the changed wind speed as the MJO passes (figure 3-11b); the third term is the flux anomaly due to the change in moisture as the MJO passes (figure 3-11c) and the last term is the anomaly due to the change in surface saturation humidity due to the surface pressure anomalies of the MJO (not shown) which is negligible compared to the other terms.

As can be seen, the surface latent heat flux anomaly of the MJO is not purely determined by the wind speed anomaly. For example, the negative LHF anomaly to the northeast and southeast of the convection is dominated by the moisture anomaly due to the MJO scale circulation carrying moist equatorial air into the dryer regions outside the ITCZ. In these regions the wind speed anomalies are relatively small. On the other hand, the heating along the equator, west of the center, is largely

due to the increased wind speed there, as the moisture anomaly near the surface is small in that region. As a third example, the weak negative anomaly to the west-northwest is due to the competition between a substantial slowing of the winds and a dry anomaly due to moisture advection. The reverse is also true to the east-northeast.

It is important to note that this decomposition should only be considered as a qualitative explanation of the flux anomalies, as the sum of the bulk flux derived anomalies does not match the actual flux anomaly quantitatively (compare figure 3-11a and figure 3-11d).

Due to the relative phases of the various terms, it appears that the propagation, especially the polewards part, is significantly driven by the horizontal advection of MSE, so we will now focus our attention on that term to gain further insight into the MJO propagation mechanisms.

Zonal and Meridional Advection

While the advection in the model is Semi-Lagrangian, it can be approximately decomposed into zonal ($hadv_Z$) and meridional ($hadv_M$) contributions:

$$\begin{aligned} hadv_Z &= -\langle u\partial_x h\rangle \\ hadv_M &= -\langle v\partial_y h\rangle \end{aligned} \qquad (3.10)$$

As can be seen in figure 3-12a, the zonal advection acts as a source of MSE to the northeast of the convective center. However, as discussed above, much of this MSE tendency is due to extratropical wave activity and is largely balanced by the vertical advection associated with the waves in the same area. The meridional MSE advection anomaly (figure 3-12b) also acts as a source of column-integrated MSE to

the east and to the northeast of the convective center and as a sink under the convective center and to equatorwards. This acts to propagate the MSE anomaly both eastwards and polewards.

Timescales of Meridional Advection

The meridional advection can be further divided into the contributions from various timescales:

$$-\langle v\partial_y h\rangle = -\langle v_{hf}\partial_y h_{hf}\rangle - \langle v_{lf}\partial_y h_{lf}\rangle - \langle v_{hf}\partial_y h_{lf}\rangle - \langle v_{lf}\partial_y h_{hf}\rangle \quad (3.11)$$

where the subscripts 'hf' indicates time filtered to periods T < 30 days; and 'lf' indicates T>30 days.

Each of the four product terms is regressed against the MJO OLR signal. The dominant term, -$\langle v_{hf}\partial_y h_{hf}\rangle$, is shown in figure 3-12c. The remaining terms (not shown) are much less significant for the MJO-like signal. This figure shows a source of MSE to the northeast of the convective center, and a sink at the center, to the west, and to the northwest. This term dominates the total meridional advection to the energy source in the northeast, and so seems to dominate the polewards part of the propagation of the MJO-like signal and is a significant part of the eastward propagation.

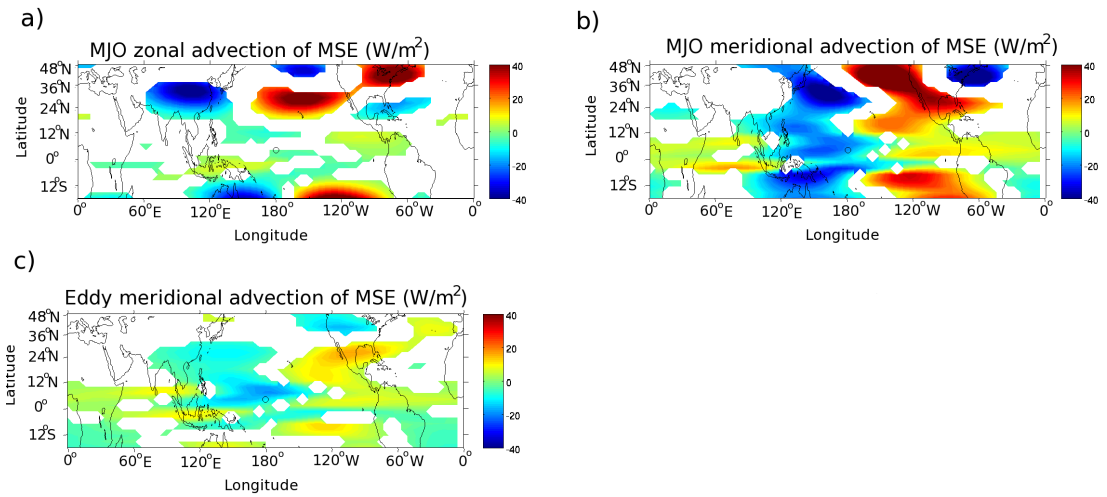

Figure 3-12. a) Column-integrated zonal advection of MSE; b) Column-integrated meridional advection of MSE; c) column-integrated, MJO regressed, high frequency $\boldsymbol{v}$-high frequency $\boldsymbol{h}$ advection.

The eddies in the model appear to act as a diffusion of MSE as we shall now show,

$$D \approx \kappa \nabla^2 \langle h \rangle, \tag{3.12}$$

where D is the diffusive source and κ is the eddy diffusion. To linear order, the eddy diffusion can be broken into the diffusion of the mean MSE profile by the MJO-associated eddy anomalies and the diffusion of the MJO MSE anomalies by the mean eddy activity. As a simple, dimensionally consistent, approximation, κ can be considered to be proportional to the square root of the Eddy Kinetic Energy (EKE):

$$\kappa = \bar{\kappa} + \kappa' \propto (\overline{EKE} + EKE')^{0.5}. \tag{3.13}$$

Expanding this to first order yields:

$$\kappa' \propto \frac{1}{2} \frac{EKE'}{\overline{EKE}^{0.5}}. \tag{3.14}$$

The diffusion can then be written as:

$$D \propto \frac{1}{2} \frac{EKE'}{\overline{EKE}^{0.5}} \nabla^2 \overline{\langle h \rangle} + \overline{EKE}^{0.5} \nabla^2 \langle h \rangle', \tag{3.15}$$

where the primed quantities are associated with the MJO and the overbar indicates the climate mean quantities. These two quantities are shown as figure 3-13a and figure 3-13b. The first term is the diffusion of the mean MSE by the eddies associated with the MJO. The second term is the diffusion of the MJO MSE anomalies by the mean eddy activity.

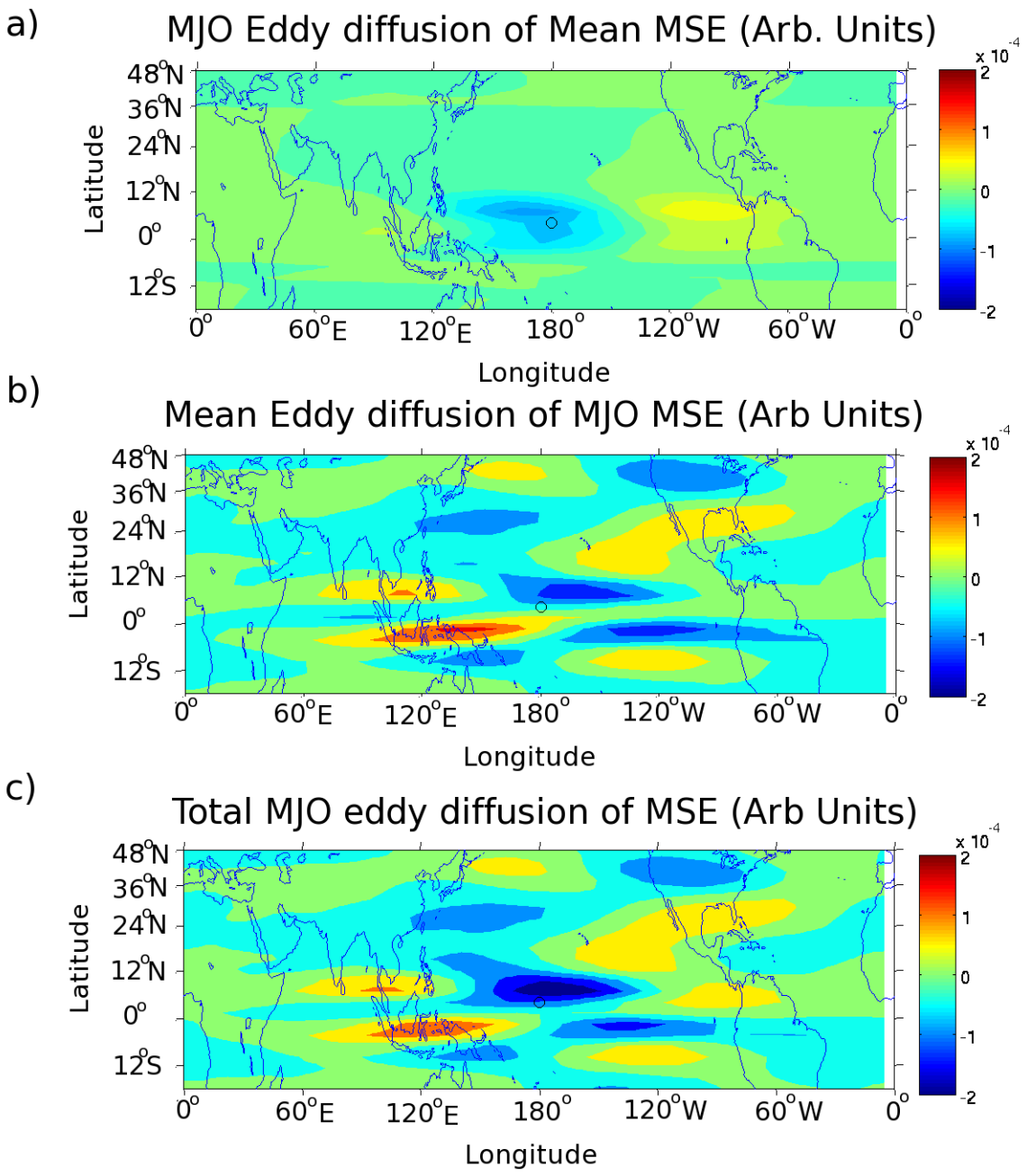

Figure 3-13. Eddy Diffusion of MSE anomalies. a) Diffusion of mean MSE by MJO eddy anomalies; b) Diffusion of eddy MSE anomalies by mean eddy activity; c) Total eddy diffusion of MSE. All figures are in arbitrary but consistent units.

As can be seen over the ITCZ latitudes, the MJO eddy term matches the meridional eddy MSE advection term to the east of the convection indicating that the MJO associated eddies are responsible for the meridional eddy advection in that region and thus provides the meridional advection's contribution to the eastward propagation. The mean eddy diffusion of the MSE anomaly, on the other hand, seems to be responsible for the advection to the north-east of the convection. Thus the gradients in the MJO MSE anomaly drive the poleward propagation of the MJO. The sum of the two diffusion terms is shown in figure 3-13c. The close correspondence between this and the eddy meridional advection (figure 3-12c) demonstrates the validity of representing the eddy advection terms as eddy diffusion, also shown to be the case in reanalysis data (Peters et al. 2008).

On the whole, what we seem to be seeing is a suppression of high-frequency eddy drying in the lower troposphere to the east of the convective center, and enhancement of the eddy drying to the west (figure 3-14a), in combination with MSE anomalies interacting with the mean eddy activity to create moistening to the northeast of the convection and drying near the convection. The vertical structure of the EKE anomaly (figure 3-14b) at 15^{o}N shows the suppression of eddy advection in the lower troposphere ahead of the convection, collocated with the anomalous moistening. Likewise, a positive EKE anomaly is collocated with anomalous drying. A similar picture emerges at 5^{o}N, where the anomalous moistening is closely tied to the suppressed EKE (figure 3-14c & figure 3-14d).

Figure 3-15a shows the 850hPa EKE anomaly, which can be seen to have a strong negative relationship to the column eddy meridional moisture advection anomaly

(Figure 3-14b). This relationship generally holds for the lower troposphere. The upper-level EKE anomalies generally have the opposite sign to the lower troposphere, but as the moisture gradient in the upper atmosphere is very small, the advection anomalies from the upper troposphere have a negligible influence upon the column-integrated MSE. This is in agreement with observations of the eddy activity in the tropics, where the eddy kinetic energy is reduced in the MJO easterlies and enhanced in the MJO westerlies, dominated by barotropic conversion terms (e.g. Maloney and Hartmann 2001, Maloney and Dickinson 2003). Barotropic conversion moves mean flow energy into eddy energy, caused by eddy advection of gradients in the large-scale winds. The tendency of EKE due to barotropic conversion is given by

$$\partial_t EKE_{barotropic} = -u_{hf}v_{hf}\left(\partial_y u_{lf} + \partial_x v_{lf}\right) - u_{hf}^2 \partial_x u_{lf} - v_{hf}^2 \partial_y v_{lf}, \qquad (3.16)$$

where $\left(u_{hf}, v_{hf}\right)$ is the high frequency wind and $\left(u_{lf}, v_{lf}\right)$ are the low frequency winds. Figure 3-15b shows the MJO regressed generation of EKE by barotropic conversion (the right-hand side of the above equation), also at 850 hPa. As can be seen, extra EKE is generated by barotropic conversion in region around the convective center and to the west and northwest. EKE is reduced by the negative barotropic conversion anomaly in the region to the east of the convective center, consistent with the observations (e.g. Maloney and Hartmann 2001, Maloney and Dickinson 2003).

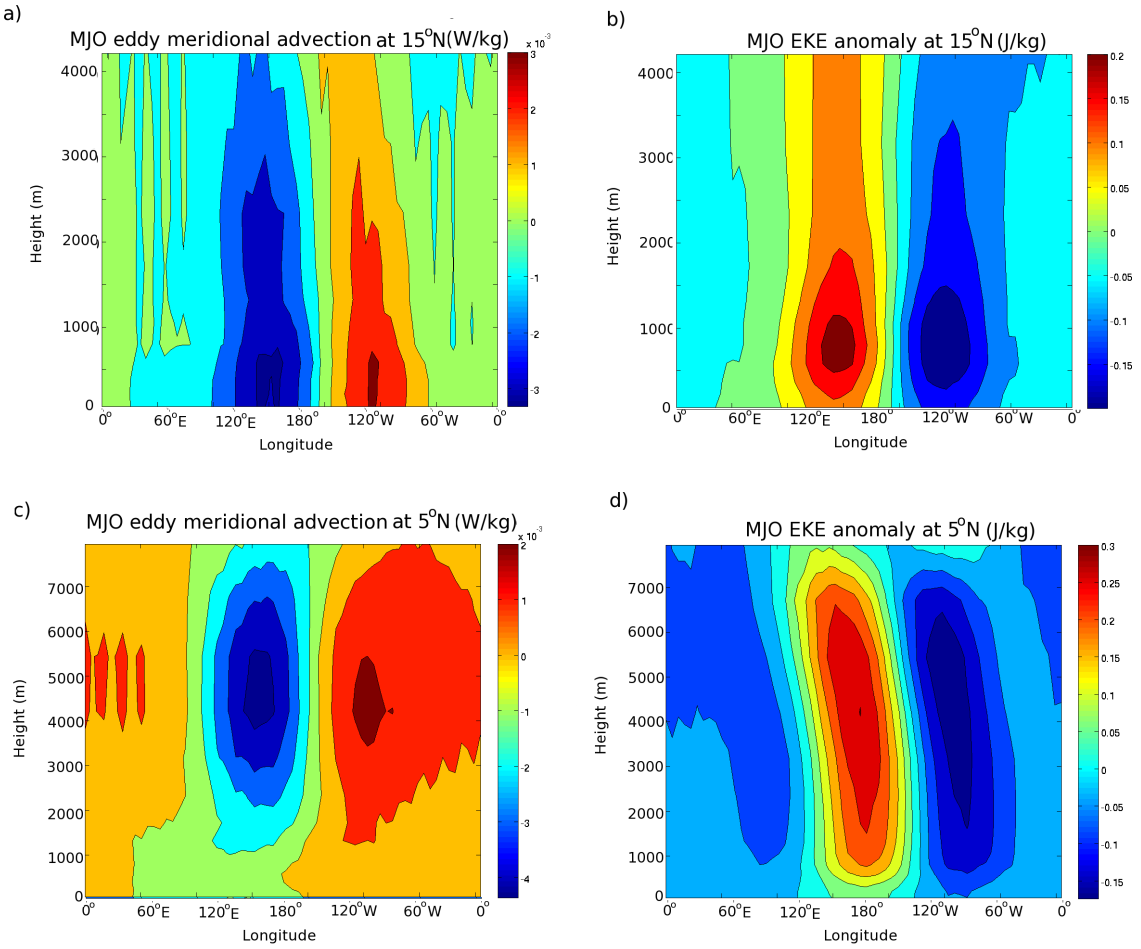

Figure 3-14. a) Anomalous eddy meridional advection of MSE at $\mathbf{15^o N}$; b) Eddy Kinetic Energy (EKE) anomaly at $\mathbf{15^o N}$; c) Anomalous eddy meridional advection of MSE at $\mathbf{5^o N}$; and d) Eddy Kinetic Energy (EKE) anomaly at $\mathbf{5^o N}$. MJO regression point is located at $\mathbf{180^o}$. Note the differences in vertical scale between the first and second pair of figures.

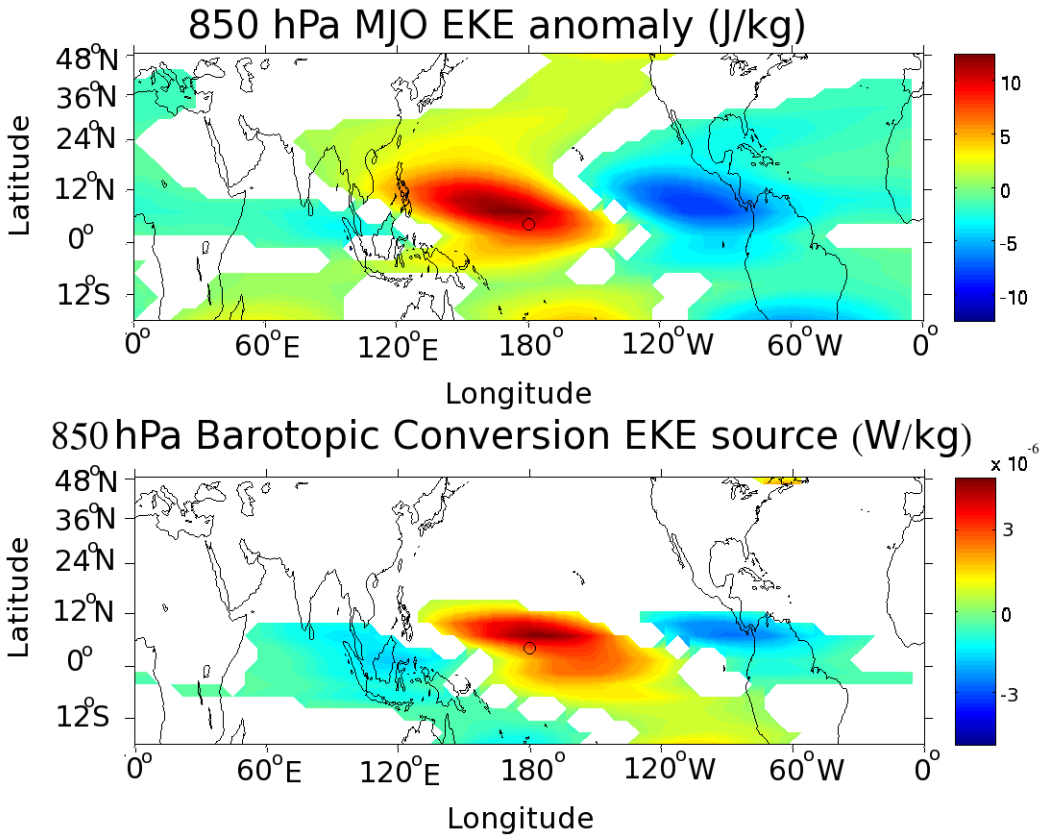

Figure 3-15. a) The MJO regressed EKE anomaly at 850 hPa; b) EKE source due to barotropic conversion of energy from the large-scale winds at 850 hPa.

3.4 Discussion

Many attempts have been made to explain the tropical OLR spectrum as coming from a system of convectively coupled shallow water waves. However, the current results take the view that the MJO disturbance is of a fundamentally different nature, stemming from anomalies in column MSE, rather than from anomalies in Convective Available Potential Energy (CAPE) and/or other similar quantities caused by the temperature anomalies of the waves, as seems to be the case for the convectively-coupled equatorial shallow water waves observed.

To correctly model the MJO, it appears that a simple model must account for these effects. More specifically, because the horizontal advection of MSE due to meridional winds – and anomalies in this caused by variations in barotropic conversion – appears to have such a significant effect on the MJO mode, both the influence of these anomalies on the convection and the feedback on these effects by the large-scale flow induced by the MJO convection ought to be included.

We have also observed that surface thermodynamic disequilibrium caused by moisture anomalies can be as important as windspeed anomalies in determining the LHF anomalies, at least in the situation modeled in this study.

It is worthwhile discussing the ways our results compare to some other investigations of the MJO energy sources.

- In a modeling study, Raymond (2001) investigated the importance of cloud-radiation feedback and surface energy fluxes in the genesis and propagation

of the MJO. Raymond observed that Cloud-Radiation feedback was crucial for MJO genesis, while surface heat fluxes were important for propagation. In the present analysis we do not investigate the genesis of the MJO events, but we do observe that cloud-radiation interactions (in the form of long-wave heating anomalies) are a major part of the MSE budget for the maintenance of the disturbance. Surface heat fluxes do not play a significant role in the propagation of the MJO-like anomaly we observe. Raymond also observed that a mean state similar to that above the warm pool is critical to the existence of the MJO. However, we have observed the MJO in our zonally symmetric SP-CAM experiment. It is not clear whether this observation is a strength or a weakness of SP-CAM.

- Lin and Mapes (2004) investigated the radiation budget of the MJO based upon observations from the Atmospheric Radiation Measurement (ARM) program and the Tropical Ocean Global Atmosphere Coupled Ocean Atmosphere Response Experiment (TOGA COARE) campaign. They observed that the net column radiative heating is almost in phase with the precipitation. We observe a similar phase relationship in SP-CAM, where the radiative heating is approximately in phase with the MSE anomaly, with a slight lag indicated by the retarding effect of the long wave term. In both Lin and Mapes and the present work, the radiative heating anomaly is dominated by the long wave anomaly that results from changes in the high clouds by the MJO modulation of convection. The ratio of radiative heating to latent heat

release we determine (26%) is significantly larger than the 15% estimated by Lin and Mapes.

- Our results are generally consistent with those of Maloney (2009). We see a buildup of column MSE in advance of the precipitation anomaly and a decay of column MSE during and after the precipitation. We also observe that the horizontal advection of MSE is among the leading terms in the column MSE budget. However, in contrast to Maloney (2009), we observe that latent heat flux has only a small budget contribution. The long-wave heating anomaly is observed to be more important in the present work than it appears to be in Maloney 2009.

Our investigation of the mechanisms by which the horizontal advection terms operate is largely in agreement with that of Maloney 2009. The horizontal advection is dominated by the meridional transport of moisture by synoptic scale eddies. The modulation of the eddy activity by the MJO large-scale state leads to modulation of the moisture transport, leading to anomalous moistening and drying effects.

However, in a follow up paper, Maloney *et al*. (2010) made a number of observations that are inconsistent with the results we report. Specifically Maloney *et al*. reported that, in the presence of reduced humidity gradients (i.e. reduced eddy meridional advection effects) and a warm pool SST, the MJO observed is stronger. They further observed, in this configuration, that the propagation of the MSE anomaly was primarily due to zonal advection of moisture by the mean low-level wind. It is important to note, however, that the mean surface westerlies in Maloney et al. (2010) are considerably stronger than those observed over the Indian Ocean

and the Western Pacific. We have not addressed the question of whether the mechanisms observed in SP-CAM would change in a similar way in the present study, but this is a planned avenue of further research.

The Hovmöller diagram in figure 3.3c demonstrates poleward propagation of the MJO-like disturbance. This is not surprising, given the tilted nature of the MSE and precipitation anomalies. The MSE budgets indicate that meridional advection of MSE is important in the poleward propagation of the disturbance, and is likely important in the poleward propagation of similar phenomena on the Earth, such as the Asian Monsoon. In a study by Boos and Kuang (2010), similar poleward propagating intraseasonal anomalies are observed in a nonhydrostatic model with zonally symmetric boundary conditions. These anomalies are seen to propagate through a similar mechanism, through the actions of small scale eddies upon the column MSE.

3.5 Conclusions

By analyzing the column integral, we have glossed over the specifics of how moist convection in the model redistributes MSE. However, the budget analysis provides a useful framework to assess the importance of various processes. Our arguments, based upon budget analysis, are not intended to show causality. We can, however, see terms that are "important" in various parts of the wave, in the sense that, an important part of the budget is one that would necessitate large changes in the other terms to maintain balance were that term removed. It is also possible to infer from the signs of the important terms some information about how the MSE anomaly

would react if a term were removed (e.g., moving faster or slower, growing or decaying), at least in a transient sense, before the other terms responded.

Our conclusions are:

a) The SP-CAM run in a zonally symmetric aquaplanet configuration shows an MJO-like feature in both the OLR and MSE spectra. This feature is similar to the Earth's MJO in structure and propagation.

b) The composite structure of the MJO-like signal shows enhanced moisture and precipitation in the convectively active region, coupled with a planetary scale circulation. The convective anomaly is preceded by low-level moistening, preconditioning the atmosphere for the convective activity. The anomalies propagate both eastwards at a realistic zonal speed and also polewards, similar to observations.

c) There are, however, some aspects of the disturbance that are less like the real-world MJO. Such differences are not surprising in an experiment conducted on an idealized zonally asymmetric aquaplanet set up, but we consider the system worth analyzing. The observation of realistic MJO events observed in experiments conducted in the same model with realistic boundary conditions, lends some confidence that our anomaly is related to the MJO, despite the differences. We believe that the analysis of this idealized experiment can be informative as to the mechanisms that are involved in the MJO maintenance and propagation.

d) The composite MJO-like feature appears as a large positive MSE anomaly located over and around the ITCZ and the center of MJO filtered OLR

variability. The composite MSE tendency has MSE increasing to the east and polewards of the convective center, and decreasing to the west and equatorwards.

e) The primary source of MSE in phase with the observed anomaly is the anomalous long-wave heating, caused by the enhanced deep convection (and reduced mean cloud top/emission temperature) in the convective region of the MJO. This source of energy is balanced by sinks, which are dominated by the advection of MSE. The importance of long wave heating appears to be consistent with other investigations of MJO like oscillations, such as Hu and Randall (1994) and Raymond 2001. The importance of <LW> is confirmed by a mechanism denial experiment. When the radiative heating is homogenized zonally, the MJO-like disturbances disappear.

f) The latent heat flux anomalies associated with the MJO in our model are driven by both surface moisture anomalies and wind speed anomalies, contrary to the typical understanding of WISHE. Latent heat flux is also shown to be relatively unimportant to both the maintenance and the propagation of the MJO-like disturbance, in the sense of having only a small contribution to the MSE energy budgets either in phase or in quadrature with the MSE anomaly. The relative unimportance of LHF in our energy budget is in direct contradiction to many studies that have observed LHF playing an important role in the MJO, such as Maloney (2009) and Maloney *et al.* (2010).

g) The MSE sources associated with Eastward propagation of the anomaly are dominated by to the combined actions of the horizontal and vertical

advection of MSE, which together create a positive MSE tendency ahead of the convective center and a negative one over and behind it, retarded by the long-wave heating.

h) The MSE sources associated with poleward propagation are dominated by the effect of horizontal advection of MSE, creating a positive tendency to polewards and to the east of the convective center and a negative tendency to the west and towards the equator. This advection is dominated by the meridional advection by high frequency eddies – anomalous moistening ahead of the convection due to suppression of eddy activity in this region – as observed by Maloney 2009. The robustness of this result across several different modeling studies speaks of its possible importance to the MJO on the Earth. Further, the good fit between our parameterized eddy diffusion and the eddy meridional advection indicates the validity of such a treatment.

i) The eddy advection, parameterized as diffusion, can be linearly approximated as the sum of diffusion of the mean MSE by eddy anomalies and the diffusion of the anomalous MSE by the mean eddies. The first quantity is seen to act as a source of MSE associated with the eastward propagation, while the second dominates the MSE sources associated with polewards propagation.

j) The eddy modulation is consistent with the modulation of barotropic conversion in the lower troposphere, due to the combined large-scale flow of the MJO and the mean state – suppressing conversion to the northeast and enhancing it to the northwest.

k) The absence of an interactive ocean or an ENSO cycle in our model does not preclude these mechanisms having an important role in the Earth's MJO. However, the observation of the MJO in our fixed SST experiment does imply that SST anomalies are not critical to the existence and propagation of MJO-like disturbances.

Such is the nature of the current understanding of the MJO that the observations reported here are consistent with (parts of) some studies and at odds with others. For example, our results generally contradict those of Raymond (2001) regarding the importance of latent heat flux while confirming the importance of cloud-radiation feedback. Our results are also in agreement with Lin and Mapes (2004) regarding the role of cloud-radiation feedback for the maintenance and propagation of the disturbance; and Maloney (2009) on the importance of the meridional eddy advection of MSE for the propagation of the anomaly. Investigation of the dependence of the budget upon the mean state in the style of Maloney *et al.* (2010) is beyond the scope of the current study, as we have limited our discussion to a single mean state. However, the response of the observed mechanisms in SP-CAM to variations in the mean state is an avenue of research that we intend to pursue. Specifically, we will be analyzing how the balance between the budget terms varies with ITCZ width in the following chapter.

Chapter 4 - Sensitivity of MSE Budget Terms to variations in boundary conditions.

The arguments of the previous chapter are mostly based upon budget analyses; as such, it is difficult to ascertain actual causality in the various processes involved with the MJO. In further support of these arguments, in this chapter, we investigate the response of the MJO MSE budget to variations in the climate, by modifying the width of the SST distribution used to force the model. The different boundary conditions show differences in the strength and propagation speeds of the MJO-like disturbances observed. It is observed that the variations in speed are due to changes in the advection of the mean state MSE profile by the MJO winds, which are in turn due to the changes in the gradients of the mean state MSE profiles that stem from changes in the width of the imposed SST.

4.1 Introduction

As discussed in the introductory chapter the Madden-Julian Oscillation is a phenomenon with important consequences for the global climate. However, the MJO is poorly represented in most global climate models and poorly understood from a theoretical perspective. MJO-related variations are among the dominant intraseasonal variabilities of the tropical ocean-atmosphere system, spanning the timescales between climate and weather.

In the previous chapter, we examined in detail the MSE budget for an MJO-like anomaly observed in a zonally symmetric integration of SP-CAM. It was observed that:

a) The column-integrated longwave heating is the only significant source of column-integrated MSE acting to maintain the MJO-like anomaly balanced against the combination of column-integrated horizontal and vertical advection of MSE and Latent Heat Flux (LHF).
b) Eastward propagation of the MJO-like disturbance is associated with MSE generated by both column-integrated horizontal and vertical advection of MSE, with the column longwave heating generating MSE that retards the propagation.
c) The contribution to the eastward propagation by the column-integrated horizontal advection of MSE is dominated by synoptic eddies.
d) Further decomposition indicates that the advection contribution to the eastward propagation is dominated by meridional advection of MSE by anomalous synoptic eddies caused by the suppression of eddy activity

ahead of the MJO convection. This suppression is linked to the barotropic conversion mechanism; with the gradients of the low frequency wind experienced by the synoptic eddies within the MJO envelope acting to modulate the Eddy Kinetic Energy (EKE).

One inherent weakness of budget analyses is the difficulty in differentiating causation and correlation between the various fields. In order to better illuminate the causality in this system, we will discuss an initial investigation of possible variations of the MJO under changes in the model mean state—the variations of the propagation speed of the MJO-like anomalies with variations in imposed Sea Surface Temperature (SST)—from the perspective of the MSE budget.

This is done as an initial exploration of ways the MJO may change under climate change. By studying the response of the modeled MJO to various warming scenarios, it may be possible to better understand the potential risk changes associated with the many processes the MJO influences.

Recent work in a conventional version of the NCAR CAM with a realistic MJO shows that the change in overall intraseasonal variance and the MJO strength is acutely sensitive to the pattern of SST warming (Eric Maloney and Shang-Ping Xie 2011 – private communication). A globally uniform warming strengthens the MJO, whereas a more realistic warming pattern such that warming is enhanced locally near the equator (esp. east Pacific) appears to weaken the MJO.

Another recent study (Posselt *et al.* 2012) investigated the variations in convection observed in a CSRM under increases in the SST. Using a narrow equatorial-channel type domain, they were able to simulate convectively coupled KW, which do not

appear to have been particularly sensitive to the SST used. However, since their model configuration did not allow the existence of an MJO, no direct conclusions can be drawn. They do report a number of ways that convection and its coupling to the large-scale flow may vary under increases in SST, such as a slowing of large-scale overturning and an increase in convective intensity as SST increases.

In section two we discuss the experimental setup used and the resulting climatologies. Section three discusses the spectral identification of the MJO-like anomalies and demonstrates the variations in propagation speed observed. In section four, the MSE budget terms for the various cases are compared. The interesting terms (meridional advection of the mean MSE profile by the MJO-related wind anomalies and the meridional eddy advection term) are investigated in more detail in section five, followed by further discussion and conclusions in sections six and seven respectively.

4.2 Experimental Setup

4.2.A Boundary Conditions

The MJO-like anomalies we analyze occur within integrations of the same version of SP-CAM as that analyzed in the previous chapter (see section 3.2.A). The model runs are forced with a temporally and zonally constant SST given by

$$SST(\phi) = 2 + \frac{27}{2}(2 + a\zeta + b\zeta^2), \tag{4.1}$$

where the SST is in Celsius, ϕ is the latitude, and

$$\zeta = \begin{cases} \sin^2\left(\pi \frac{\phi - 5}{110}\right) & 5 < \phi \leq 60 \\ \sin^2\left(\pi \frac{\phi - 5}{130}\right) & -60 \leq \phi < 5, \\ 1 & |\phi| < 60 \end{cases} \tag{4.2}$$

(plotted in figure 4-1a; These are variations on the Control_5N case from the APE study e.g. Williamson *et al.* 2012), and seasonally varying insolation for sixteen years, with output every six hours (three in the control case). The different cases vary through choices of (a,b). The five experiments discussed in this chapter are described in Table 4.1. The (-1,-1) case is the same case as analyzed in the previous chapter, and is referred to as the control case. The (-3,+1) experiment has the narrowest SST profile and (-0.5,-1.5) has the broadest. The (-1.5,-0.5) case is intermediate between the control and (-3,+1) - narrowest - cases. The (-0.75,-1.25) case lies between the control and the (-0.5,-1.5) – broadest – cases.

4.2.B Climatologies

The climate of the control case is discussed in more detail in Section 3.2.B. For comparison we show how the time-zonal mean precipitation and 850 hPa zonal winds vary between the various cases in figure 4-1b and figure 4-1c. As the SST distribution is made wider, the precipitation and MSE profiles become wider with lower peak amplitude and the jets move away from the equator. The reverse is true for the narrower SST cases. The climates are generally similar to those produced with the same SST profiles in other models (e.g. Williamson *et al.* 2012).

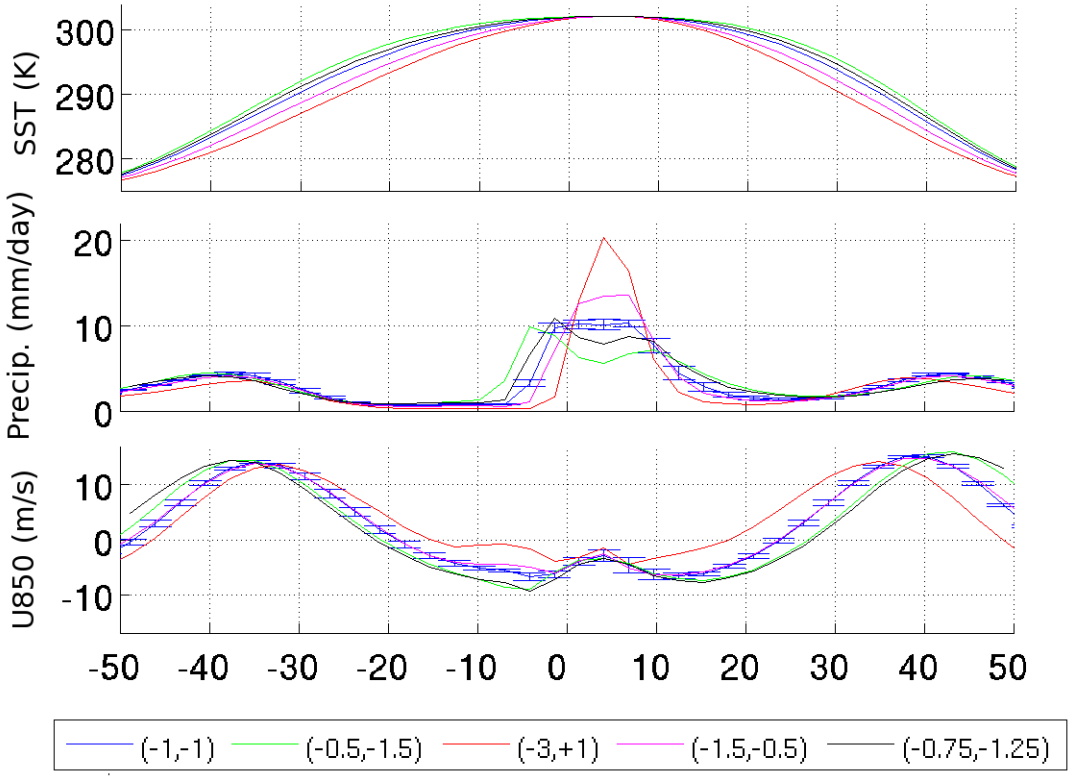

Figure 4-1. Time- and zonal-mean climate for the experiments analyzed in this chapter: a) Sea Surface Temperature; b) Precipitation; and c) 850 hPa zonal wind. Error bars indicate the standard deviation of the time mean values from their zonal mean at each latitude, and are only shown for the Control experiment, which is representative of the other cases.

TABLE 4.1. SST profile parameters

SST Distribution	*a*	b
Control	-1	-1
Narrowest	-3	+1
Broadest	-0.5	-1.5
Narrow	-1.5	-0.5
Broad	-0.75	-1.25

It is interesting to note the slight southern bias of the two precipitation peaks observed in the two "broad" SST cases. In these cases, it appears that the SST imposed is sufficiently flat that a double ITCZ arises. However, while the time-zonal mean precipitation is slightly stronger in the southern hemisphere (as is the MJO filtered precipitation variance), the time-zonal mean OLR is lowest (indicating stronger convection) in the northern hemisphere. The MJO filtered OLR variance is also higher in the north. It appears that in this experiment, there are MJO events in both hemispheres – we have chosen to analyze the northern hemisphere events for two reasons: 1) the stronger OLR signal, as OLR is the variable we use as our indicator of MJO activity in most cases; and 2) for ease of comparison with the other cases, where the primacy of the northern hemisphere is more clear-cut.

4.3 Identification of the MJO

4.3.A Spectral Analysis

The equatorial precipitation for each experiment shows a number of statistically significant peaks representing propagating disturbances (figure 4-2), just as observed in the control case (see Section 3.2.C). The spectrum for the four experiments are broadly similar – each experiment shows activity in the Kelvin, Equatorial Rossby and MJO spectral regions, although the spectral power in each mode varies from experiment to experiment. For example, the Kelvin waves are strongest in the narrow case and weakest in the broad case.

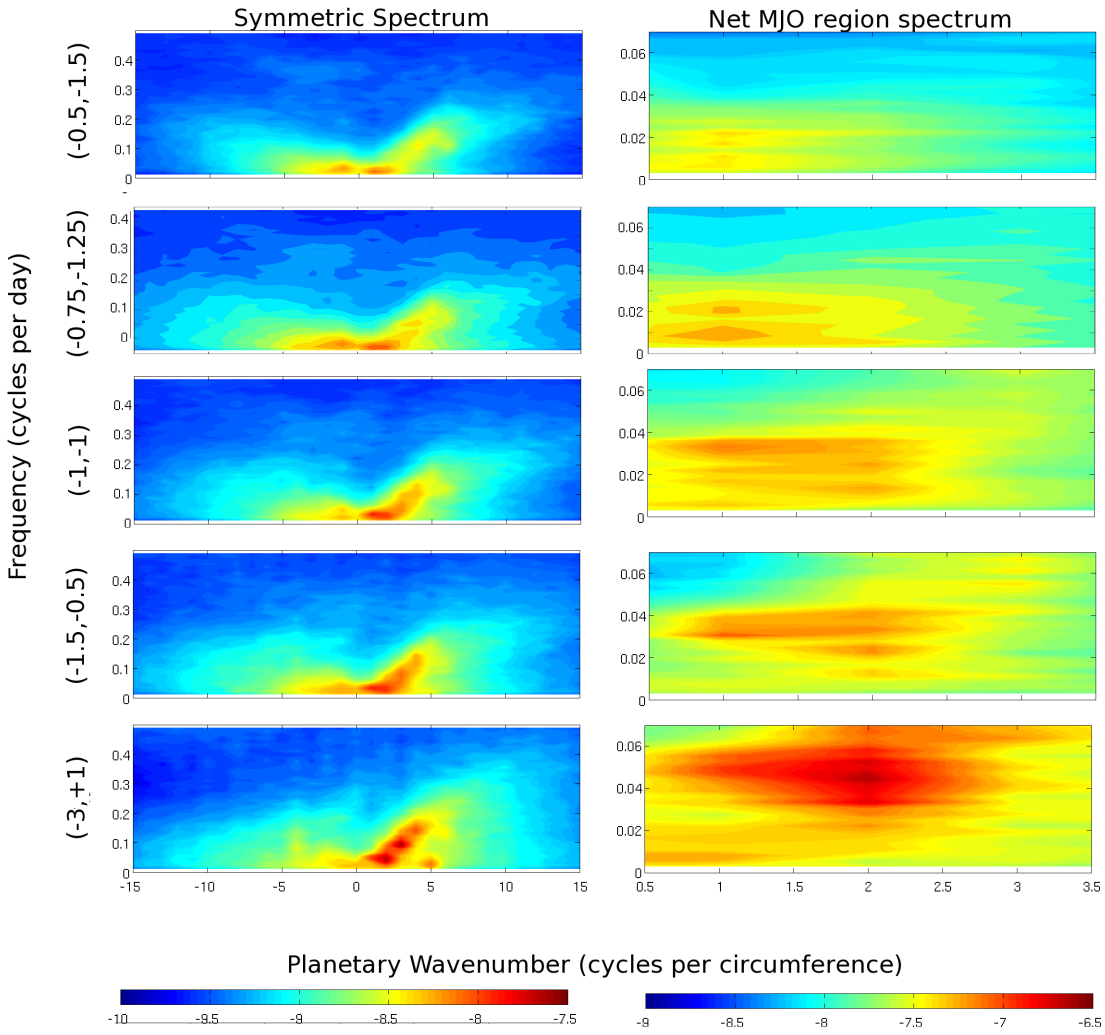

Figure 4-2. Logarithm (base 10) of the spectral power for signal symmetric about the equator in precipitation narrowest (top) to broadest (bottom; left column). These experiments are ordered from broadest to narrowest SST profiles. The right column shows the MJO region of the spectrum in more detail, calculated using longer time windows to achieve greater resolution in frequency. These figures are also calculated for the total spectrum in the region from the equator to $\mathbf{10^o N}$.

The narrower cases - (-3,+1) and (-1.5,-0.5) - also show some additional power at low frequencies around wavenumber 5 (this is most obvious in the narrowest case). This signal is due to the edges of the subtropical jet impinging upon the "tropical" region chosen for the spectral calculation. The jet tends to shift towards the equator as the SST distribution becomes narrower (not shown).

If we zoom in to the MJO region (right hand column), we can see that the location of peak MJO activity varies between the experiments. The "zoomed in" spectra are calculated for the region stretching from the equator to $10^o N$ and without any sort of separation into symmetric and anti-symmetric parts. This is done to capture the peak of the MJO signal. The zonal mean of the temporal variance of the MJO filtered OLR is plotted for each experiment in figure 4-3, which shows that the MJO variance peaks in the northern hemisphere (at $5^o N$, above the SST peak) for all cases and a large part of the total variance is contained in the region bounded by the equator and $10^o N$. The lack of symmetry (or anti-symmetry) in the variance field also demonstrates that it is better to keep the entire field, rather than trying to split it into symmetric and anti-symmetric parts.

While it is difficult to quantify by eye, there is the general impression that the phase speed of the MJO increases as the SST width decreases. This is made more precise in the next section; however, we can also see that the MJO appears to be stronger in the narrow cases and weaker in the broad cases.

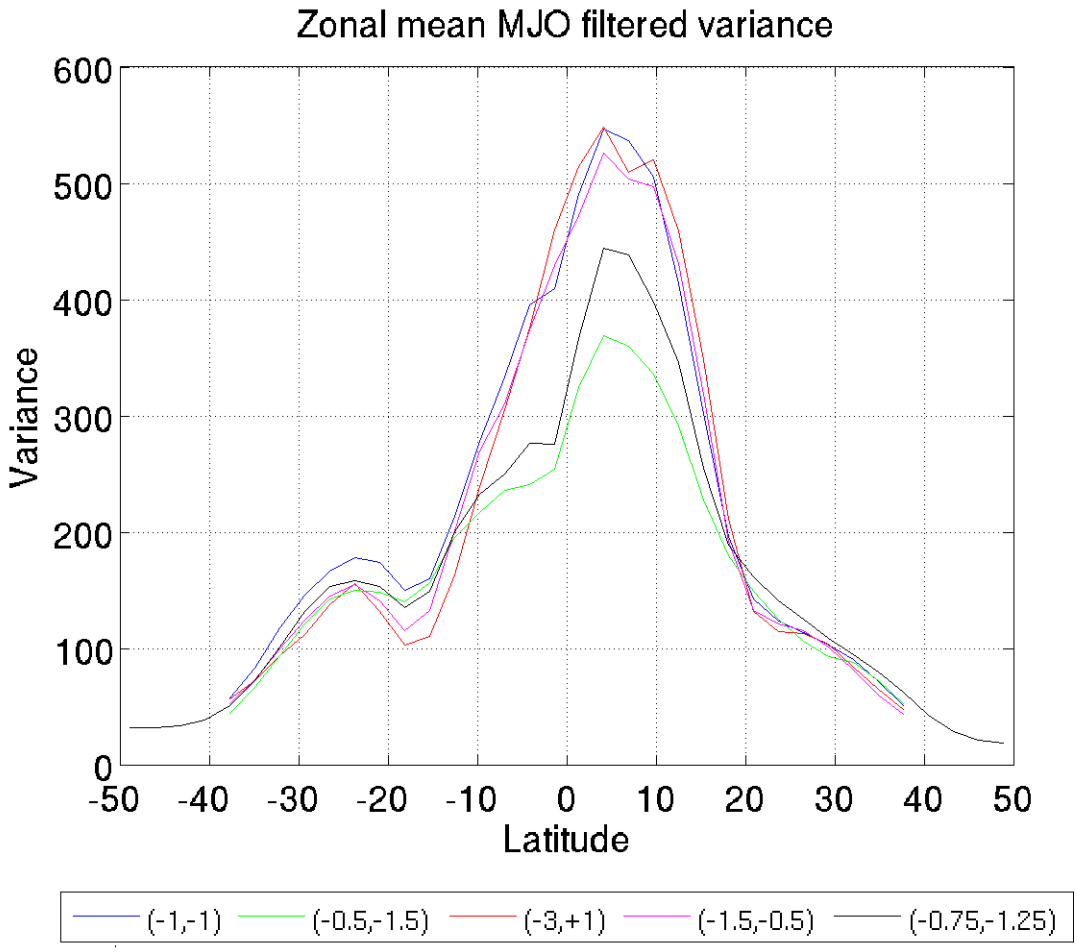

Figure 4-3. Zonal mean of the temporal variance in the MJO filtered OLR field for the experimental cases.

4.3.B Phase Speed Differences

Hovmöller

Shown in figure 4-4 are Hovmöller diagrams for unfiltered precipitation (averaged 0^oN—6^oN) for a representative sample of the model run (left); and MJO-filtered precipitation for the same period (colors) with the control case MJO-filtered precipitation (contours; lines at 0 and 3 mm/day; right), for both the narrowest (top) and broadest (bottom) cases. It is hard to quantify the phase speeds from this diagram, but the general impression of faster propagation in the narrow case can be drawn from the comparison. Similarly, the MJO in the broadest is quite clearly slower than that of the control case.

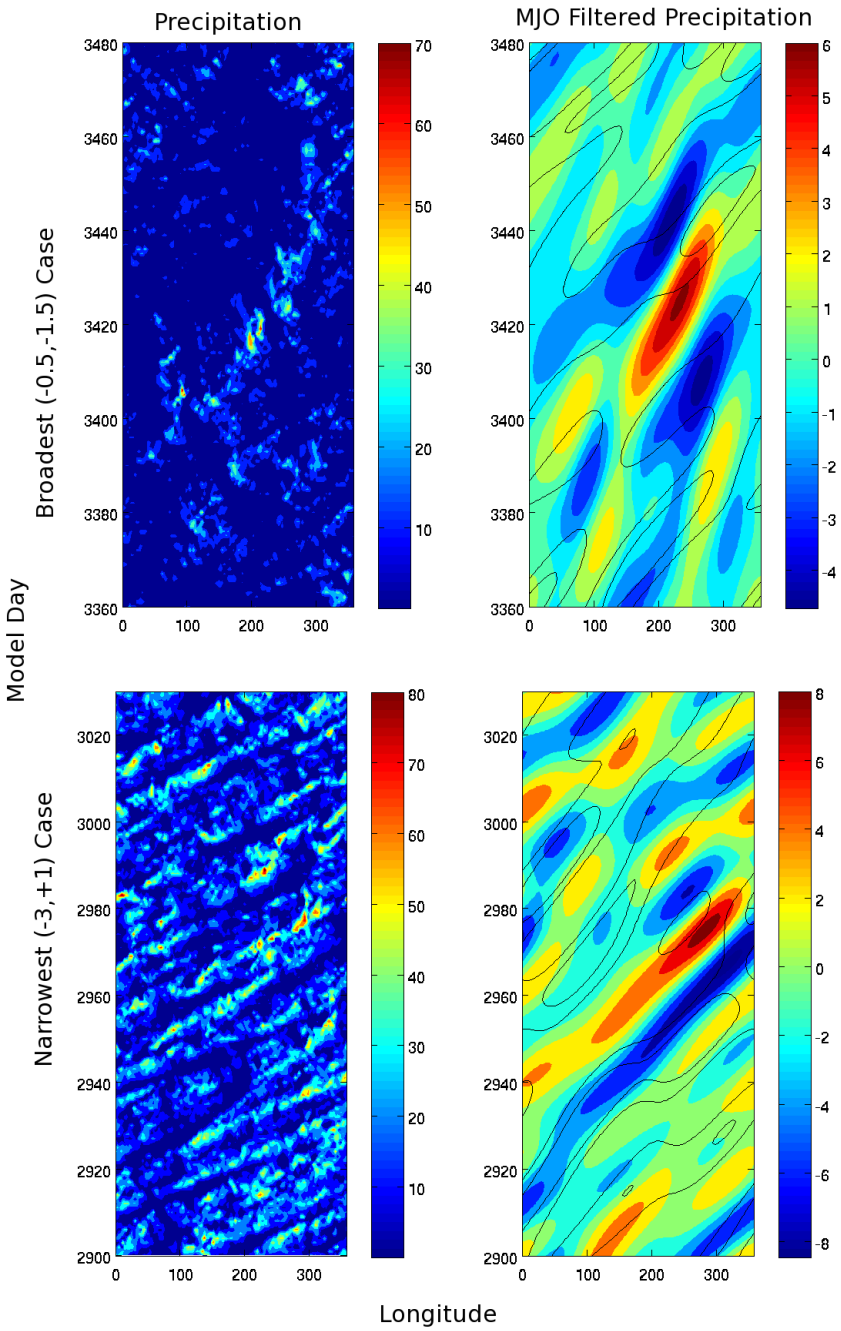

Figure 4-4. Hovmöller diagrams for the broadest (top) and narrowest (bottom) cases. Left column: Unfiltered precipitation (averaged $\mathbf{0^oN}$— $\mathbf{6^oN}$) for a representative sample of the model run. Right Column: MJO filtered precipitation for the same period (colors) with the control-filtered precipitation (contours; lines at 0 and 3 mm/day).

MJO Speed Estimation

In order to estimate the phase speed of the MJO signals observed, we attempt to follow the convective center of the MJO anomaly and record its velocity. This is done by identifying, for each model day, the longitude of the peak MJO convection (which corresponds to the minima in MJO filtered OLR). The path of this point with time is tracked and its velocity is found through linear regression of location against time. We do this for each MJO event separately, defining an MJO event as beginning when the filtered OLR anomaly dips below a threshold value of $-10\mathrm{W/m}^2$ and ending when the anomaly finally rises above the threshold. We also declare a new event to have started if the position of the OLR anomaly minima jumps discontinuously to a distant point, as happens when one MJO event is growing while another decays. The technique is demonstrated in figure 4-5 for a segment of the control case. The algorithm identifies the locations of the MJO when a sufficiently active anomaly exists, and it also chooses the most active anomaly when two MJO coexist.

The paths of the MJO anomalies allow us to calculate each MJO event's group velocity. Figure 4-6 shows the histograms of the velocities (with each MJO event weighted by the length of the event). The results are also summarized in Table 4.2. Using the Wilcoxon-Rank-Sum test, we have compared the weighed anomaly velocities for the experiments, using the null hypothesis that the experimental velocity distributions are drawn from the same population as the control case. In all cases, the probability of the null hypothesis being true is essentially zero.

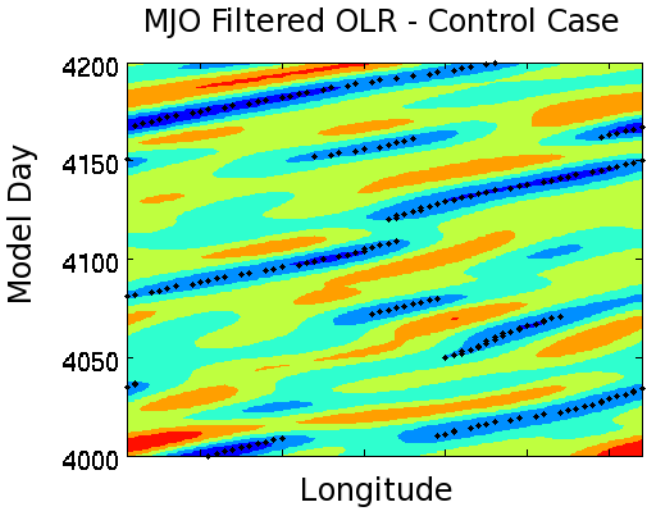

Figure 4-5. Demonstration of convective center following technique. The colored contours show the meridionally averaged (from $\mathbf{15^oS}$ to $\mathbf{15^oN}$) MJO-filtered OLR field for a segment of the control experiment. The black dots show the locations of the identified MJO convective centers. As can be seen, there are periods with no active MJO, and periods with several – when the technique chooses the strongest.

TABLE 4.2. Propagation speed variations of the MJO-like disturbance, as measured by the convective-center tracking method.

SST Distribution	c_p *(m/s)*
Narrowest (-3,1)	8.35
Narrow (-1.5,-0.5)	6.64
Control (-1,-1)	7.07
Broad (-0.75,-1.25)	5.62
Broadest (-0.5,-1.5)	5.60

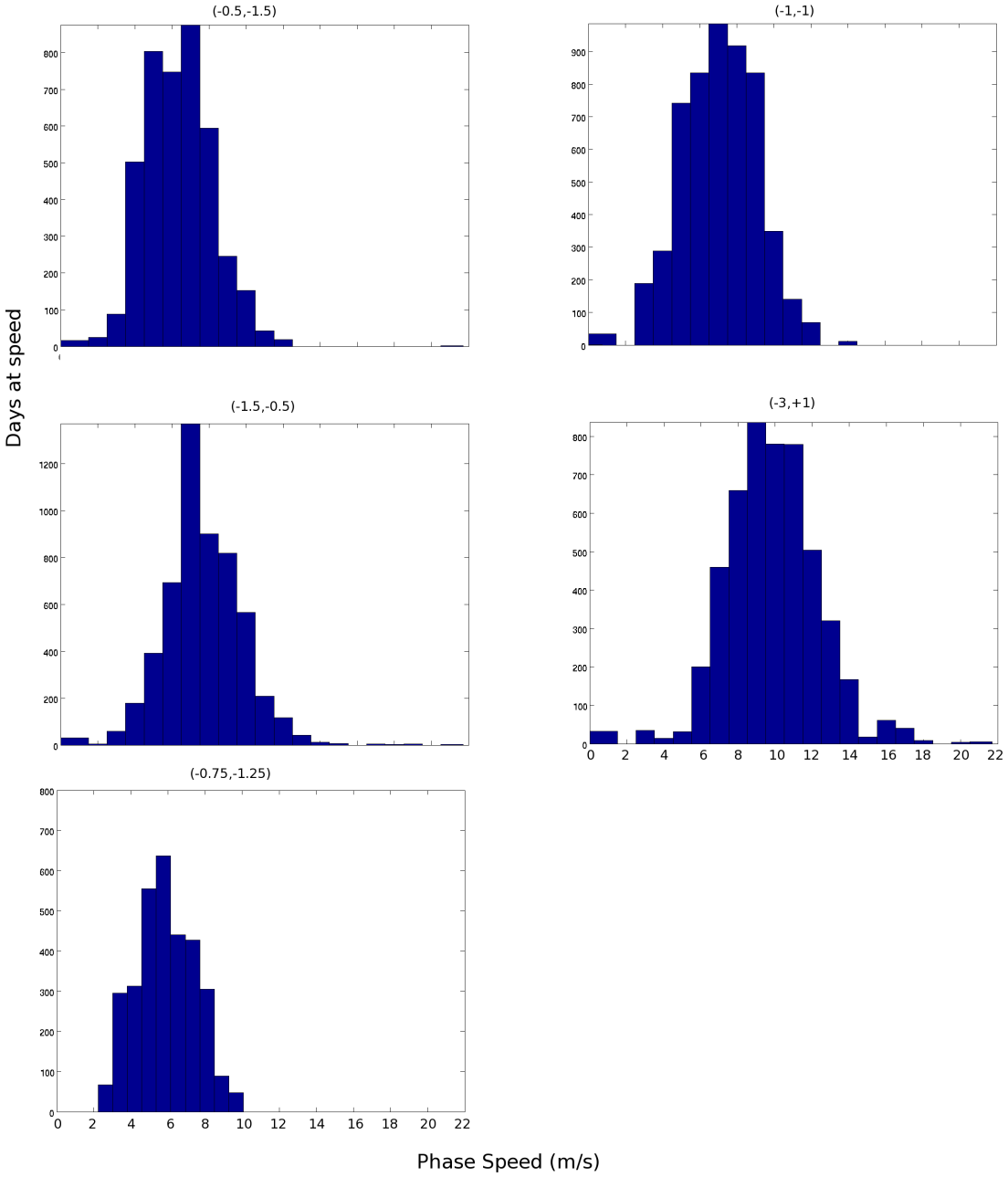

Figure 4-6. Histograms of "Convective Center" following estimated MJO phase speed. The horizontal axis is the propagation speed in m/s and the vertical axis shows the accumulated duration (in days) of all the MJO events that fall within each velocity bin. Each bin is 1 m/s wide, centered upon the integer values for the a) Broadest, b) Control, c) Narrow, d) Narrowest, e) and Broad cases.

4.4 Budget Analysis

4.4.A Definition of MSE, Budget

As discussed in Section 1.5, the Moist Static Energy (denoted as h) is given by

$$h = c_p T + gZ + L_v q - L_f q_i \quad (1.1)$$

where T is temperature, c_p is the specific heat at constant pressure, Z is the height, g is the gravitational acceleration, L_v and L_f are the latent heats of vaporization and sublimation (at 0°C), and q and q_i are the specific quantities of water vapor and ice respectively. The column-integral of this quantity is approximately conserved, so we can write the budget thus (as discussed in Chapter 3):

$$\langle \partial_t h \rangle_{budget} = -\langle \omega \partial_p h \rangle - \langle v \cdot \nabla h \rangle + LH + SH + \langle LW \rangle + \langle SW \rangle, \quad (3.3)$$

where p is the pressure, v is the pressure-surface wind vector, ω is the pressure velocity, LH and SH represent the latent and sensible heat fluxes into the atmospheric column from the surface, and LW and SW are the long- and short-wave radiative heating rates. The left-hand side is the local tendency of $\langle h \rangle$, the first and second terms on the right represent advection of h by the winds, and the final four terms represent the external sources.

4.4.B Projection of Budget terms onto the MSE anomaly and Tendency

In the style of Chapter 3, we calculate the MSE budget for the three new cases and regress them against their respective MJO-filtered OLR time series, although in this case we perform the vertical integral to 1 hPa, rather that 100 hPa as before; the contribution of changes in the surface pressure to the residual is taken into account. Advection is also calculated through a full 3D semi-Lagrangian calculation, rather

than the approximate form used in Chapter 3. The regressed budget structures for the new cases are generally similar to the control case. Although differences can be seen, it is difficult to understand the differences between various terms by eye.

It is for this reason that we again project the various terms onto the MSE budget and the MSE tendency, in order to see how these terms contribute to the maintenance and propagation of the MJO disturbances. This is done essentially in essentially the same manner as in Section 3.3.C. For each projection, any pixel where either of the terms involved are not statistically significant is discarded. This requirement has only a small impact on the resulting values (not shown) but is done to make the results more rigorous.

The earlier technique is further refined by applying a threshold to the MJO filtered OLR – only times where the amplitude of the OLR anomaly exceeds the threshold are considered for the regressions. This is intended to reduce the effect of those anomalies that appear within the MJO filter window but are not really "the MJO" – such as the fast-moving signals that arise as MJO one MJO event replaces another which are visible in the filtered fields shown in figure 4-4.

The interesting budget projections are presented in figure 4-7. The confidence interval of the budget projections are calculated through a jackknife where the statistical spread of the result is evaluated by calculating the projection many times for restructures calculated from regressions of randomly selected subsets of the data. In each of the cases shown here, an ensemble of 60 projections, each calculated from 70% of the total data set, is generated. The values presented are the means of

these ensembles and the intervals shown are the standard deviations of the ensembles.

Details

The meridional advection is generally a stronger sink of MSE, dominating the horizontal advection term. This term decreases slightly from the broadest to the second narrowest cases, but is stronger in the narrowest case**.** The significant sink of MSE comes from the relatively large negative overlap between the advection term and the MSE anomaly – even though the tendency is almost in quadrature with the anomaly, the amplitude of the meridional advection tendency is large. We show the column-integrated MSE tendencies due to meridional advection for the broadest, control and narrowest cases in figure 4-8. While there is little difference between the projections of the meridional advection of MSE upon the MSE anomaly for the broad and control cases, as the meridional SST (and thus MSE) gradients increase, the advection becomes stronger. The increase in the advection amplitude is somewhat compensated by the shift in the phasing. The peak advective sink is slightly to the west of the regression point for all cases – but the MSE anomaly peak also is slightly to west in the broad case (relative to the control). This lessens the phase difference between these terms, over-compensating for the changes in amplitude.

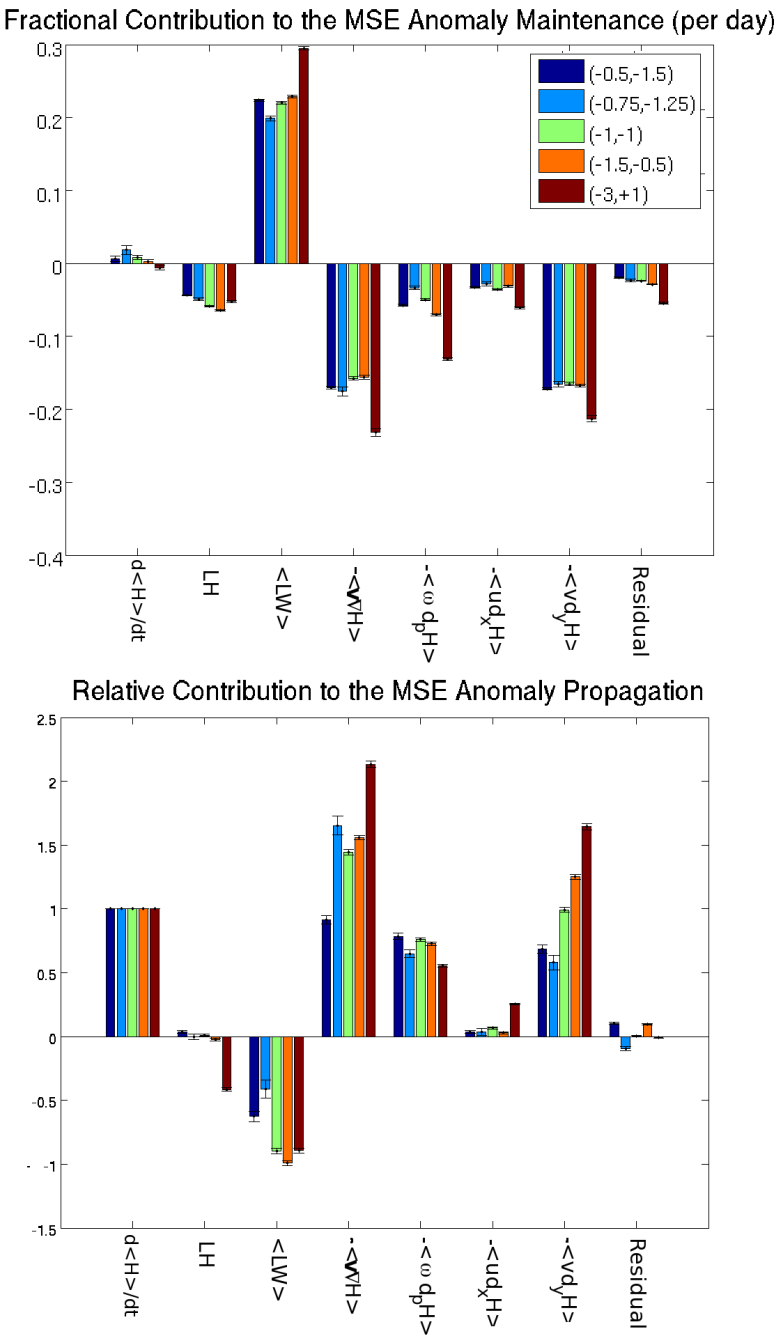

Figure 4-7. a) Fractional contributions of the MSE budget terms to the maintenance/dissipation of the MJO MSE anomaly. b) Fractional contributions of the MSE budget terms to the propagation of the MJO MSE anomaly. The five experiments are ordered (left to right) from broadest to narrowest SST.

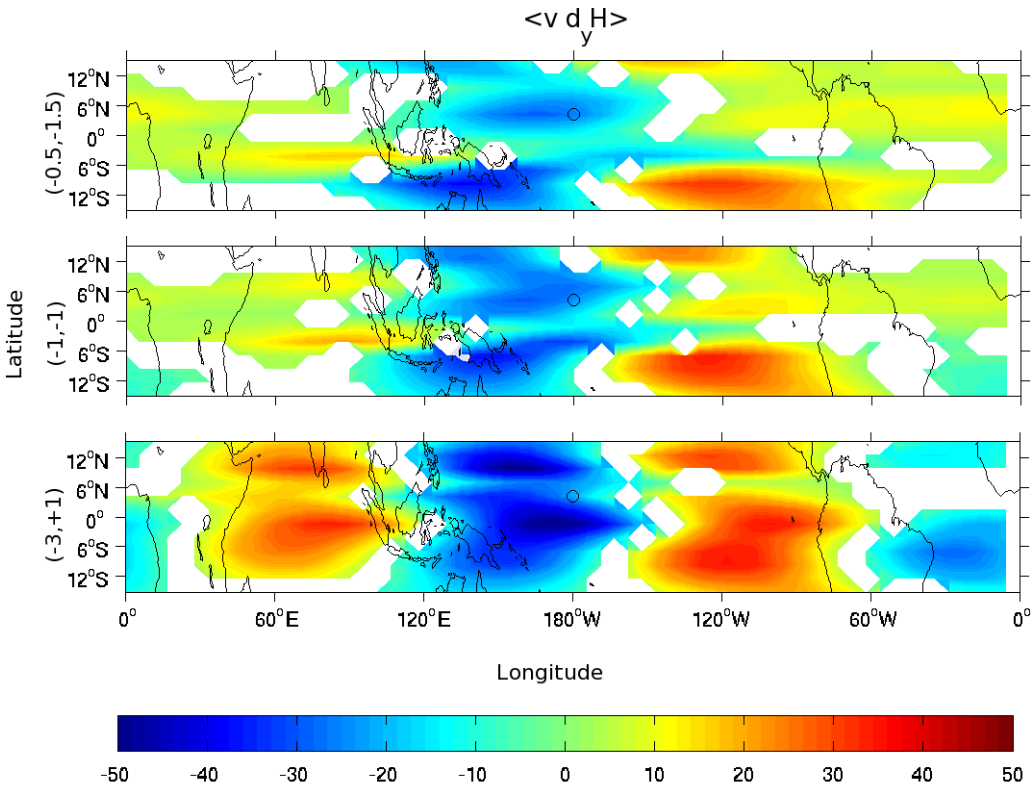

Figure 4-8. Column-integrated MSE tendencies due to meridional advection for the broadest (-0.5,-1.5; top), Control (-1,-1; middle), and narrowest (-3,+1; bottom) cases.

However, the meridional advection in the narrowest case is a significantly stronger sink of MSE. Despite the increased phase difference between the advection tendency and the MSE anomaly, the advection term is significantly stronger, leading to the increased MSE sink observed.

4.4.C Time-scale of Meridional Advection

We see that the variation is mostly due to changes in the meridional advection term, which we then decompose into the effects of various time-scale processes.

In this case, we do not use the same decomposition as in section 3.3.C. Because the faster MJO has significant amplitude in the 20-30 day bands, the eddy terms (referred to as '*hf*') are better defined as T<20 days. Also, it is illuminating (as will be shown) to separate the MJO time-scale (20-100 days, denoted 'mjo') from the longer timescales (100+ days, denoted 'mean'). The period cut-off chosen to separate MJO and eddy time-scales places some of the activity for the narrowest case that would be better described as MJO into the eddy category (see figure 4-2). Moving the cut-off to even higher frequencies to accommodate this would move more eddy activity into the MJO regions for the other cases, so we have chosen 20 days as a compromise between the time scales of the other experiments. The effect of this choice of cut-off is discussed in Appendix I.

$$v = v_{hf} + v_{mjo} + v_{mean} \tag{4.1}$$

$$\partial_y \langle h \rangle = \partial_y \langle h \rangle_{hf} + \partial_y \langle h \rangle_{mjo} + \partial_y \langle h \rangle_{mean} \tag{4.2}$$

The total meridional advection is then the sum of the nine terms that result from the

product of $v \times \partial_y \langle h \rangle$.

The parts of the meridional advection are projected upon the MSE anomaly and the MSE tendency, as shown in figure 4-9. Only terms that are interesting/significant are shown, along with the residual – which is shown for ease of comparison.

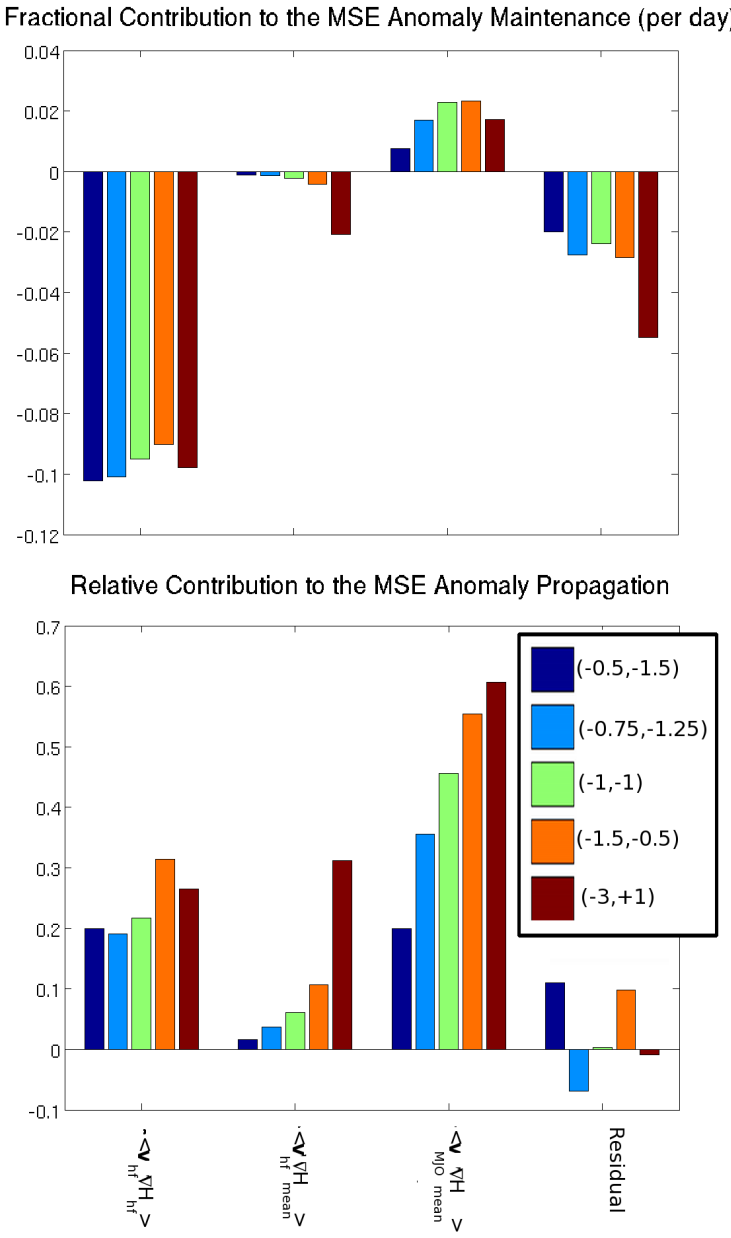

Figure 4-9. a) Fractional contributions of the meridional advection terms to the maintenance/dissipation of the MJO MSE anomaly. b) Fractional contributions of the meridional advection terms to the propagation of the MJO MSE anomaly. The five experiments are ordered from broadest to narrowest SST.

4.5 Discussion

4.5.A Interpretation of the MJO-mean advection term

Looking at the propagation contributions, we see that the major difference between the cases is in the advection term – specifically the meridional advection, which is increased significantly in the narrow ITCZ cases. The decomposed advection terms show that the advection of mean moist static energy by the MJO scale winds is the primary driver of the budget change, while the eddy term, which we had previously suspected to be most important remains roughly constant between the cases.

The *hf-mean* term, describing advection of long time-scale MSE anomalies by high-frequency winds is generally small, apart from the narrowest case. This term is significant in this case because, as mentioned above, the period cut-off chosen to separate MJO and eddy time-scales (20 days) places some of the activity that would be better described as MJO into the eddy category. Thus a definition of MJO time-scales tuned for that particular experiment would yield an even stronger MJO-mean term (not shown) and a less significant *hf-mean* term, as discussed in Appendix I.

Diagnosis of the causes of the differences

To diagnose how the changes to the mean state and the MJO between the different cases contribute to the changes in the budget, we have calculated the MSE tendency due to the product of the MJO regressed winds and the long time-scale MSE gradient for different combinations of experiments. We can then, for example, calculate the advection that would occur if the winds associated with the narrow case MJO were to act upon the gradient of the control case's mean MSE profile. That is, we take the

100+ day filtered MSE gradient from the narrowest (-3+1) case and combine it with the 20-100 day meridional winds for the control case and regress the result against the control MJO filtered OLR. We perform a similar operation with the control "mean" and the (-3,+1) winds. The regressed fields are shown in figure 4-10, along with the "unswapped" MJO-mean advection fields for comparison. As can be seen, despite some quantitative differences, the advection fields are qualitatively determined by the mean MSE profile they are calculated from – especially in the regions near the MJO anomalies. This supports our hypothesis that the changes in this term between the various cases are primarily due to the changes in the mean MSE gradients caused by the differences in the SST.

In figure 4-11 we have the vertical-meridional cross-sections of time-mean MSE (colors) and meridional wind (negative values dashed, zero contour dotted) at $160^o E$ and $260^o E$ – approximately the locations of the maximum $\langle v_{mjo} \partial_y h_{mean} \rangle$ – for the control and the narrowest cases. It can be seen from these figures that the advection terms for most of the lower- and mid-troposphere are in the sense of the vertically integrated value. There are strong meridional winds above this level, but the MSE gradient is small, so these levels do not contribute substantially to the column-integrated budget. There is also, in the area to the east of the MJO (the $260^o E$ figures), a low level wind near the equator that is in the opposite direction – probably a signal of frictional convergence – but this wind occurs where the MSE gradient is weak, so it does not have a substantial effect upon the budget. While the winds are slightly stronger in the narrowest case, it is apparent that the major

difference between the advection terms for the two experiments is due to the differences in the time-mean MSE profiles.

As a further test, we present in figure 4-12 vertical cross-sections of the MJO-regressed products of MJO filtered meridional wind and the meridional gradient of the long time-scale filtered MSE for the control and (-3,+1) cases, as well as the control winds and the (-3,+1) MSE (regressed against the control MJO OLR). The advection for the control and (-3,+1) cases are as expected from the previous figure, while the $v_{mjo(control)}\partial_y h_{mean(-3,+1)}$ figures are qualitatively the same as in the (-3,+1) case.

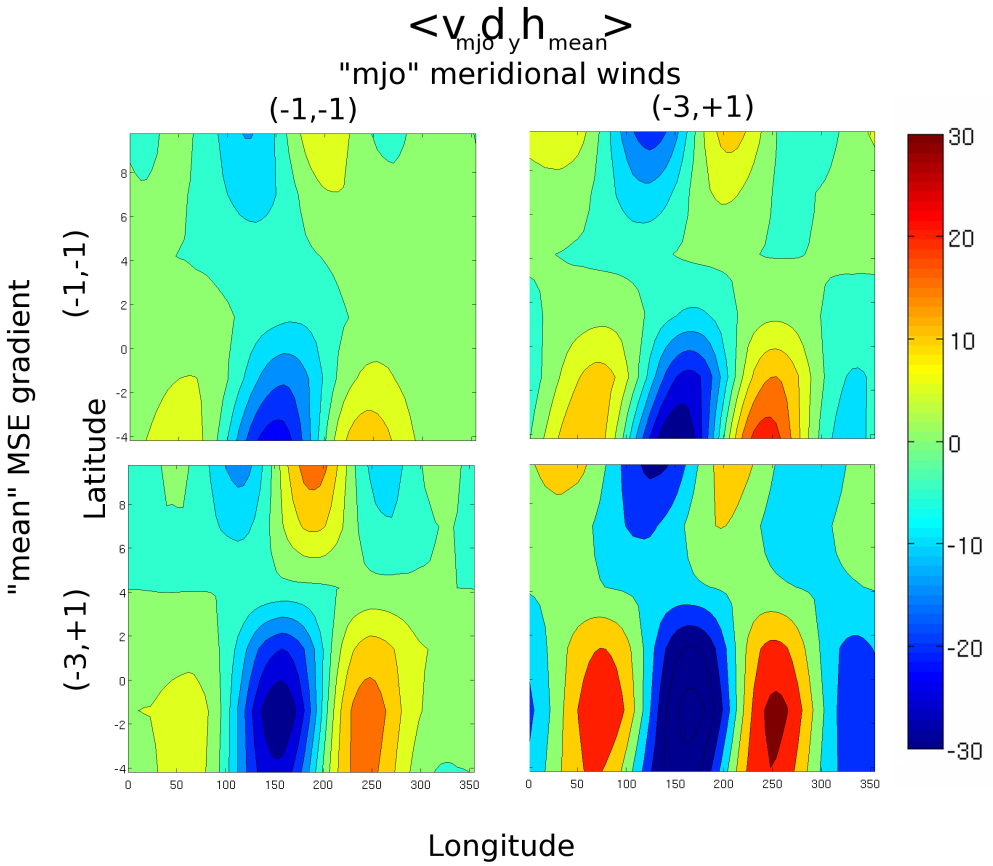

Figure 4-10. MJO regressed advection fields for the MJO-scale meridional wind acting on the long time-scale MSE gradients. The advection terms are calculated using the control (left column) and the narrowest (right column) meridional wind fields acting on the MSE gradients for the control case (top row) and the narrowest case (bottom row). Each case is regressed against the MJO-filtered OLR associated with the wind field used, to maintain the relationship between the MJO winds and the MJO convection.

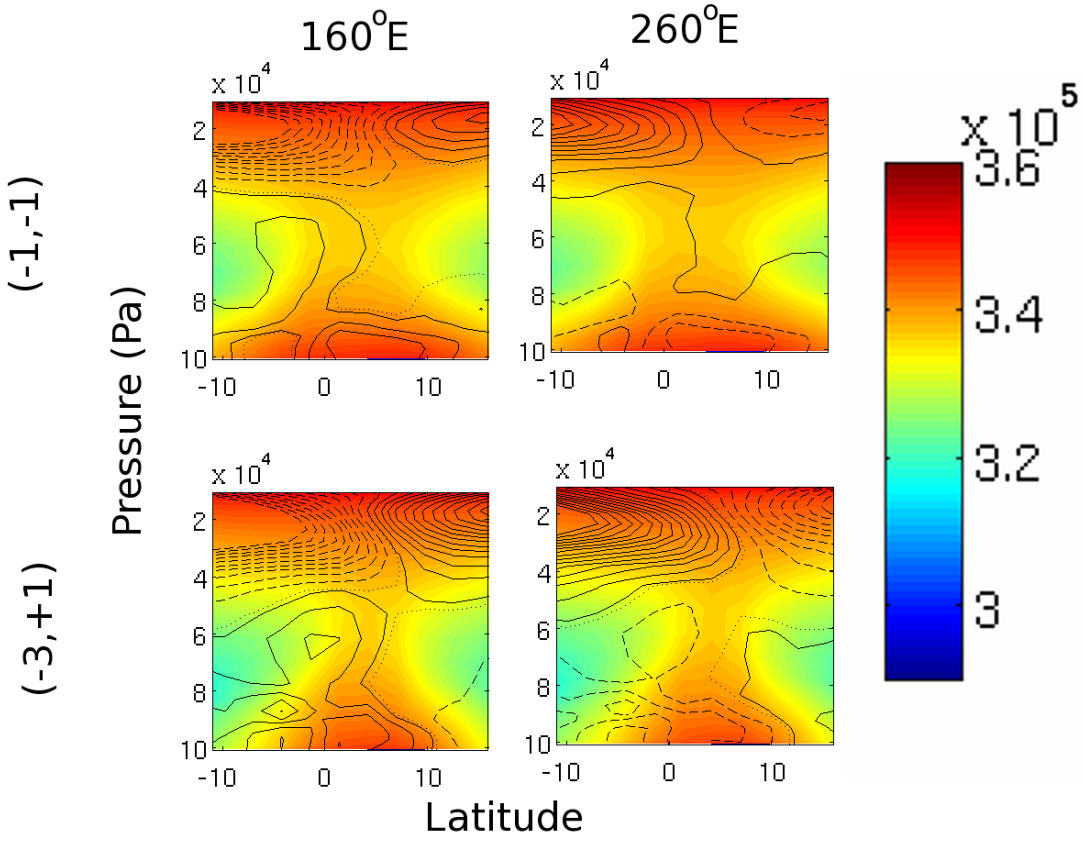

Figure 4-11. Vertical-Meridional cross-sections of the time-mean MSE (colors) and MJO-regressed meridional wind (contours – negative values dashed, zero contour dotted) at **160°**E (left) and **260°**E (right), for the control (-1,-1; top) and narrowest (-3,+1; bottom) cases.

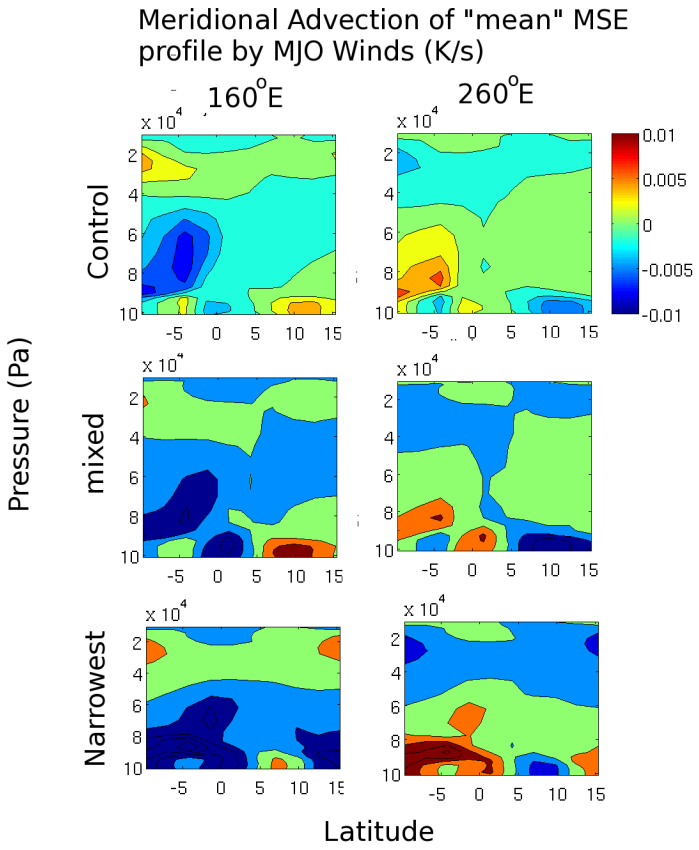

Figure 4-12. Vertical-Meridional cross-sections of the MJO-regressed products of the MJO time-scale meridional winds and the long time-scale meridional MSE gradient at **160°**E (left) and **260°**E (right) for control (-1,-1; top), narrowest (-3,+1; bottom), and the control winds combined with the (-3,+1) MSE gradient, regressed against the control MJO OLR signal (middle).

4.5.B Constancy of the Eddy Advection Term

As discussed in Chapter 3, advection by eddies is often described as a diffusion effect. In the control case analyzed in that chapter, the diffusion by the eddy field associated with the MJO diffuses the mean state MSE, leading to the moistening ahead of the MJO (where the eddies are suppressed) and drying behind (where the eddies are enhanced). All other things being equal, such diffusion effects ought to be stronger in situations where the mean state MSE profile is narrower (i.e. has a larger second derivative e.g. figure 4-13a). This is not what is observed in these experiments – there is no systematic change in the eddy term between the various experiments.

The obvious explanation of this observation is that the eddy activity changes in the opposite sense to the mean state MSE profile, so that the diffusivity decreases as the profile gets narrower. This can be seen to be the case in the EKE fields (figure 4-13b) – the narrower cases have weaker MJO EKE anomalies – and in the anomalous diffusivity fields (calculated as in Section 3.3.C, figure 4-13b) - showing that the diffusivity varies in the opposite sense to the MSE profile – leading to a relatively constant eddy advection term. The variation in EKE can be associated with variations in the barotropic conversion rate (section 3.3.C). For example figure 4-14 shows the barotropic conversion rates for the narrowest and broadest cases.

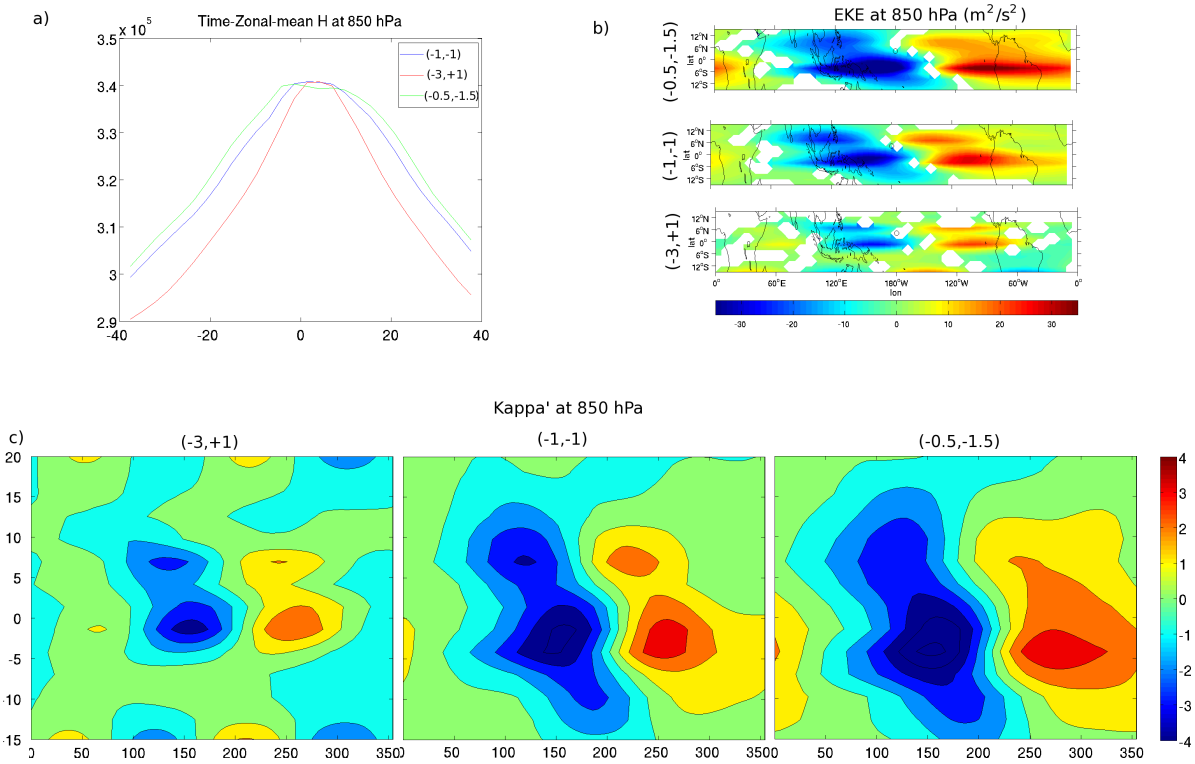

Figure 4-13. a) Time-zonal mean MSE at 850 hPa; b) 850 hPa EKE anomalies for the broadest, control and narrowest cases; c) Anomalous eddy diffusivity for the, narrowest, control, and broad case.

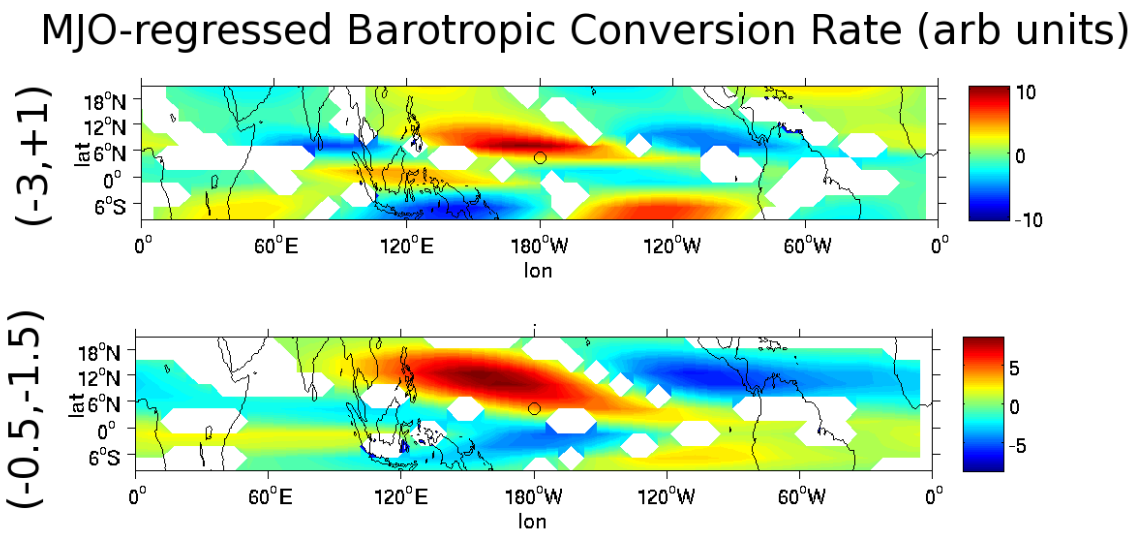

Figure 4-14. Barotropic conversion rates at 850hPa for the narrowest (top) and broadest (bottom) SST profiles.

Although the peak barotropic conversion is slightly higher in the narrowest case, the total anomalies in the rate of generation of EKE in the tropics is significantly higher in the broader case. The barotropic conversion rate is dominated by the zonal wind term:

$$\partial_t EKE_{barotropic} \approx -u_{hf}^2 \partial_x u_{lf}$$

In a zonally symmetric experiment, the zonal gradient of the low frequency winds will consist entirely of the MJO winds, as the mean state zonal winds are zonally symmetric.

We might hypothesize an eddy advection feedback acting to control the MJO amplitude – if the MJO became stronger, this would increase the amplitude of the MJO winds and also increase their gradients. This increase in wind gradient should increase the barotropic conversion rate, increasing the amplitude of the EKE anomalies, which would serve to reduce the MJO amplitude (as the eddy advection term is seen to be a strong sink upon the MJO MSE anomaly).

Similarly, this sort of feedback may be in play keeping the MJO eddy advection terms roughly constant – for example, if the MSE profile of a given experiment became suddenly narrower, the eddy advection would become stronger (assuming no change in the EKE profile). This would cause the MJO to weaken, which would reduce the amplitude of the zonal wind gradients and thus decrease the barotropic conversion rate. This, in turn, would decrease the eddy activity and reduce the eddy advection.

Arnold *et al.* (in preparation) performed a similar analysis on the changes in the MJO signal observed in SP-CAM when the SST is increased. When the SST is increased

uniformly the MJO activity appeared to strengthen. Their results suggest that the increase in variability with SST is related to the vertical advection term, which has an increasingly positive projection on the MSE anomaly with SST. Decomposition of the vertical advection by time scale indicated that the trend was associated with the MJO-vertical velocity acting on the mean MSE. At least part of this change appears to be related to a steepening of the mean vertical MSE gradient in the lower troposphere, which occurs throughout the tropics.

4.6 Conclusions

In this chapter, we have extended the MSE analysis of the MJO observed in SP-CAM to several sets of boundary conditions – zonally symmetric imposed SST profiles with differing widths. We see the MJO propagation speed decreasing as the SST profile becomes wider. MSE analysis indicates that the variation in speed is due to the variations in the advection of mean state MSE by the MJO-timescale meridional winds. The MJO time scale winds advect moist air from the ITCZ into the tropical region, allowing more convection to occur ahead of the MJO convective anomaly and carry dry sub-tropical air into the tropics, suppressing convection behind the MJO convective anomaly.

This variation is dominated by the changes in the mean MSE profile, as demonstrated by calculations of the advection terms when the MSE profiles are swapped between different experiments.

The eddy term, which was seen to dominate the propagation in the control case, is still strong, but it is not observed to vary systematically between the cases. This is shown to be due to the competing effects of the changes in the mean MSE profile

curvature (which is stronger in narrower cases) and the eddy anomalies responsible for the eddy advection terms (which are of lower amplitude in the narrower cases). These variations can be related to variations in the barotropic conversion of mean state energy into EKE, which is reduced in amplitude for the narrower case.

It is suggested that this may be related to a feedback effect – in which the net sink of MSE by the eddy advection causes the MJO winds to respond to the width of the MSE profile in order to keep the eddy drying relatively constant.

Other observations about changes in the equatorial spectrum, such as variations in the KW intensity and speed, or the MJO intensity are not dealt with in this work, although these questions are of great theoretical interest and will be investigated in the future.

Chapter 5 - The Moist Static Energy Budget in a realistic SP-CAM integration

A brief investigation of the MSE budget for a more realistic case shows an increase in the MSE sink due to meridional advection as the MJO progresses from genesis over the Indian Ocean to decay in the central Pacific. The increase in this sink appears to be the cause of MJO's demise.

5.1 Introduction

The work described in the previous chapters has analyzed the MSE budget for the MJO-like phenomenon observed in SPCAM in a zonally symmetric aquaplanet configuration. In such experiments, the MJO tends to spend most of its time in the mature phase, where its amplitude is approximately constant. The aquaplanet MJO tends to survive for several trips around the planet. This greatly simplifies the analysis but constitutes a weakness in the results, as the modeled MJO occurs in a climate that differs from that experienced in reality.

SPCAM MJO MSE Budgets in more realistic settings

In reality, the MJO tends to grow over the Indian Ocean, remaining mature for a relatively short period of time over the vicinity of Indonesia and the Western Pacific, before decaying near the date line. In order to compare our idealized aquaplanet results with reality, in this chapter we examine the MSE budget for MJO events occurring in an integration of SP-CAM in a realistic configuration, similar to those used in Maloney (2009) and Maloney *et al.* (2010) which contain both a realistic SST distribution with continents, and also a more idealized aquaplanet configuration with a warm pool.

MJO Initiation

The topic of MJO initiation has received much attention recently given the DYNAMO field program, which was partially motivated by the need to improve the representation of MJO initiation in climate models. Models typically have difficulty forecasting MJO initiation, which limits their ability to predict downstream effects of the MJO such as cyclogenesis in the Atlantic. In fact, most numerical weather

prediction models had difficulty predicting the onset of the first MJO initiation event during the DYNAMO[1] project that occurred in late 2011. In a recent calculation of the MSE budget for the MJO in reanalysis data, (Kiranmayi and Maloney, 2011) it was observed that the equatorial Indian Ocean moistens in anomalous low level easterly flow during the initiation of an MJO event. This is also consistent with initiation events observed during DYNAMO (Adam Sobel and Eric Maloney, private communication, 2011). A leading hypothesis is that this is due to advection by the anomalous low-level easterly flow acting on the mean moisture gradient. However, in some aquaplanet GCM simulations, the moistening process for MJO genesis appears to be quite different and dominated by off-equatorial processes. For example, in a version of the NCAR CAM3 with modified convection, the moistening process appears to be dominated by the Rossby gyres associated with the preceding suppressed convection phase, although Kelvin wave circumnavigation also seems to contribute in a more indirect way (Eric Maloney, private communication, 2011).

5.2 Experimental Description

SP-CAM is run is a realistic configuration, forced with observed SSTs (Hadley Center Optimally Interpolated SST, running from September 1905 to February 2002; e.g. Rayner *et al.* 2006) and with seasonally varying insolation and realistic topography. In the same manner of the experiments described in Chapters 3 and 4, the thermodynamic fields required to calculate the MSE are output every 6 hours as

[1] See http://www.eol.ucar.edu/projects/dynamo/ for description of the DYNAMO project.

accumulated averages and instantaneous fields. The other fields needed for the budget are also saved as averages every 6 hours.

The climate resulting from this sort of experiment has previously been shown to be quite realistic (e.g. Khairoutdinov *et al.* 2008). For example, figure 5-1 shows the time-mean precipitation for the model run. The figure shows the ITCZ, South Pacific Convergence Zone (SPCZ), and Western Pacific warm pool that compare qualitatively with observations of the Earth.

As discussed in Khairoutdinov *et al.* (2008), this sort of integration of SP-CAM does have some definite biases relative to observations. For example, precipitation is weaker than expected over the eastern part of the Indian Ocean; in the Western Pacific ITCZ, and over the Amazon. Conversely, modeled precipitation is stronger North-West Pacific and near the equator over South America. This has been attributed to an overly strong monsoon circulation in the SP-CAM model (Khairoutdinov *et al.,* 2008; Khairoutdinov *et al.,* 2005).

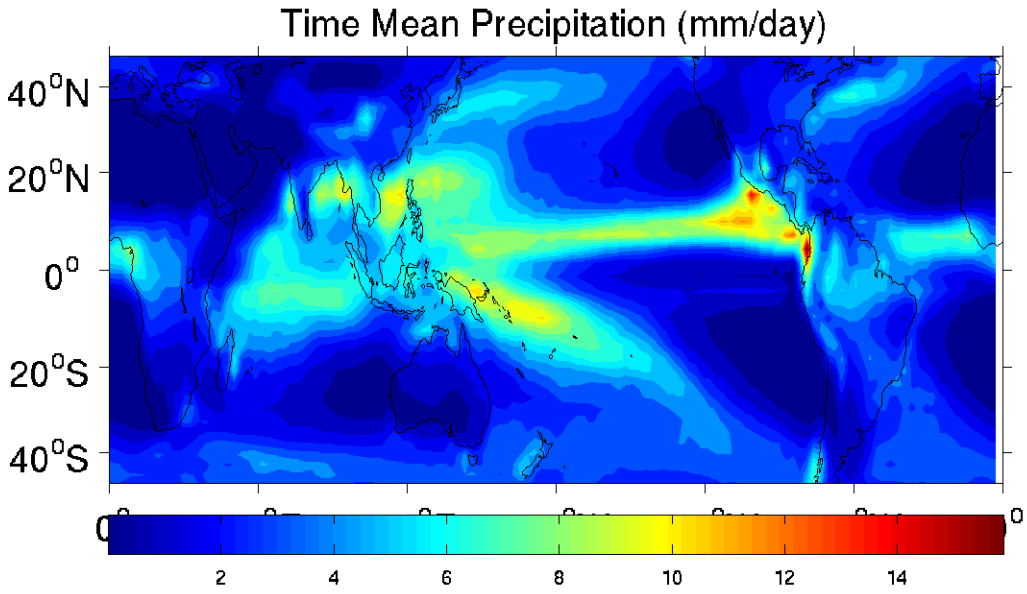

Figure 5-1. Time mean precipitation for SP-CAM is a realistic configuration.

5.3 Spectral analysis

In the same manner as discussed above, we calculate the time-space spectra of the OLR anomalies in the model. The spectrum for the symmetric part of the OLR field is shown in figure 5-2 (normalized against an estimated red background) and in figure 5-3 (as the logarithm of the spectral power, unnormalized). In either presentation, the spectrum contains signals of the MJO, KW and the ER, just as seen in the observed spectrum (see figure 1-2). Again, this has been discussed in previous work (e.g. Khairoutdinov *et at.,* 2008), where they noted that the simulated MJO is active in the region $1 \leq k \leq 4$ and $50 \leq T \leq 100$ days. The simulated KW and ER signals lie on the shallow water wave curves for equivalent depth 25m. These results are very close to the observed results – the most striking difference between the simulations and the observations is a weakness of the KW in the simulated spectrum.

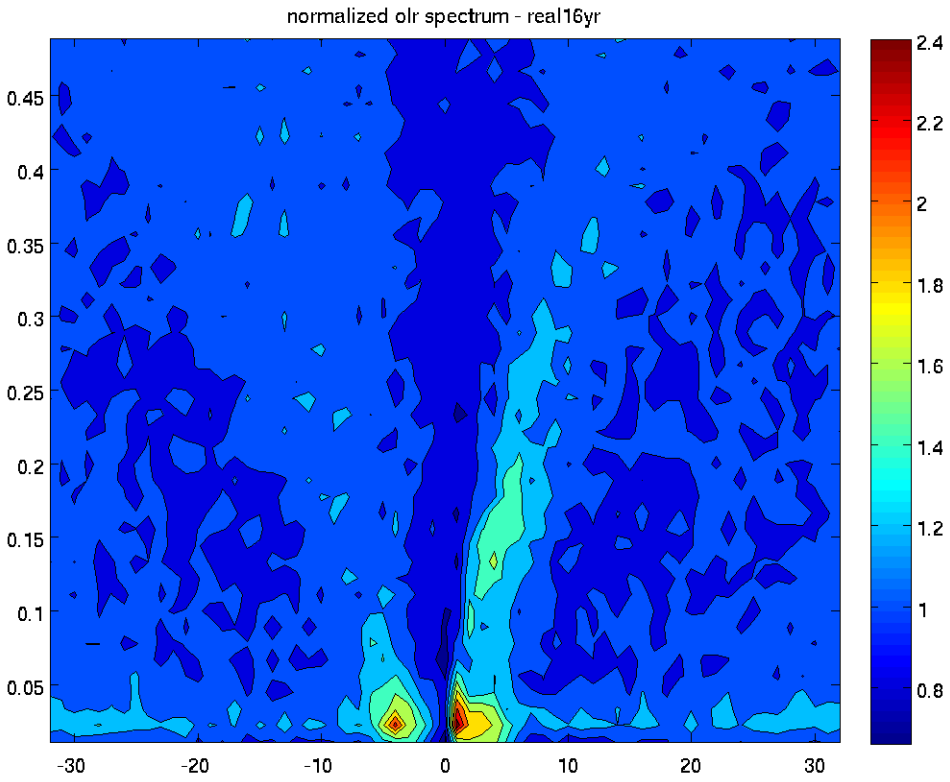

Figure 5-2. Spectral power of the OLR anomalies (symmetric about the equator) in SP-CAM under the realistic configuration, divided by an estimated red background, as described in the text.

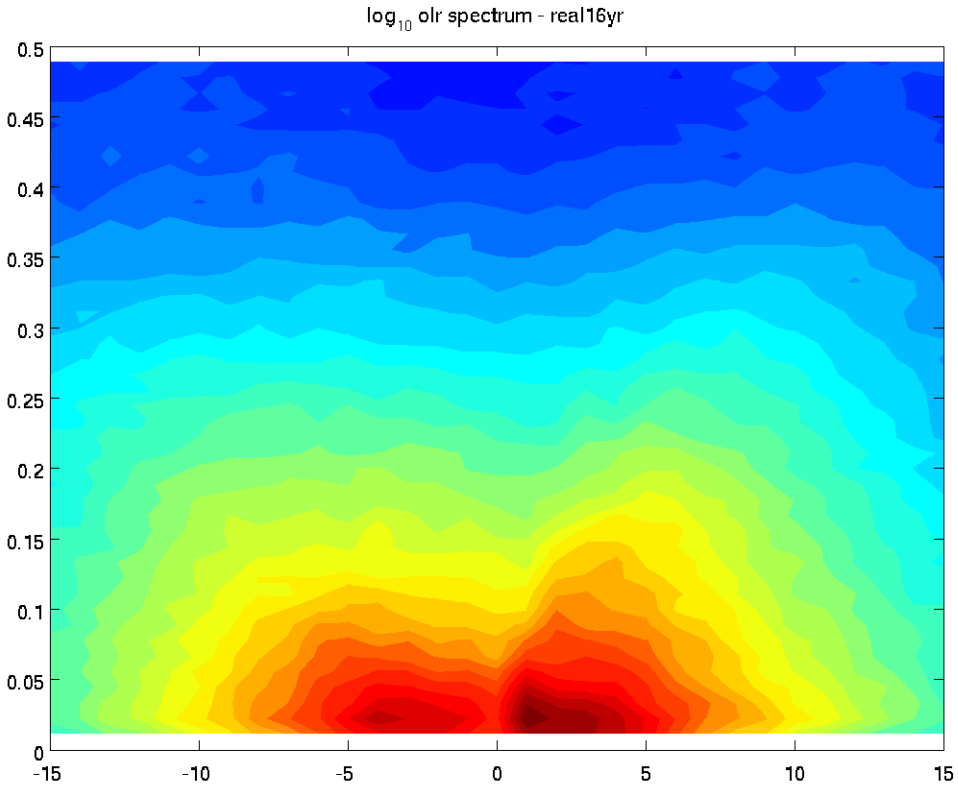

Figure 5-3. Logarithm (base 10) of the symmetric part of the OLR spectrum for SP-CAM in the realistic configuration, as described in the text.

5.4 MJO in the Model

The MJO-like anomaly in this configuration of the model has been previously studied (e.g. Khairoutdinov *et at.,* 2008; Benedict and Randall, 2009) and has been seen to be a reasonable approximation to the observed MJO.

Our calculations of the spectra and the spatial distribution of MJO band variance agree with the results of these papers.

5.4.A MJO Growth and Decay and Spatial Localization

The variance of the MJO-filtered precipitation and OLR fields as functions of space are shown in figure 5-4 and figure 5-5. There are several qualitative differences between the precipitation and OLR variances, which deserve mention: The precipitation variance maximum in the North-West pacific is expected to be due to the over-estimate of the monsoon activity in the model (mentioned above) which projects onto the MJO band; the weaker OLR variance in the eastern end of the Pacific ITCZ stems from the climatological convection in this area being shallower than in the central and western Pacific while the mean precipitation there is still quite strong; and the Eastward shift of the filtered precipitation variance relative to the filtered OLR variance in the region near the northern edge of Australia is due to the MJO precipitation having a stronger signal in the SPCZ region where the mean precipitation is stronger.

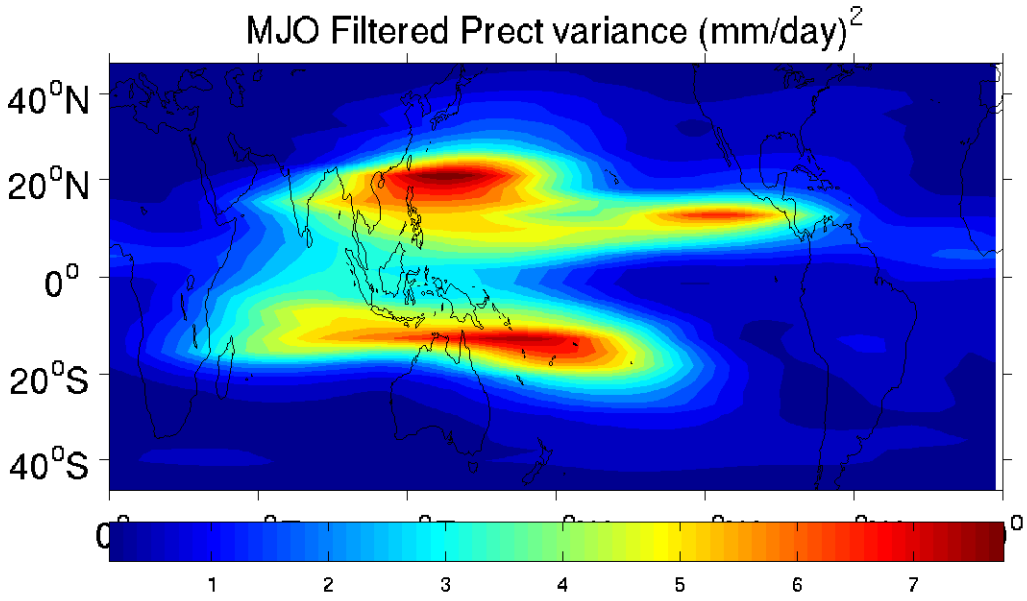

Figure 5-4. Spatial distribution of MJO-filtered precipitation variance.

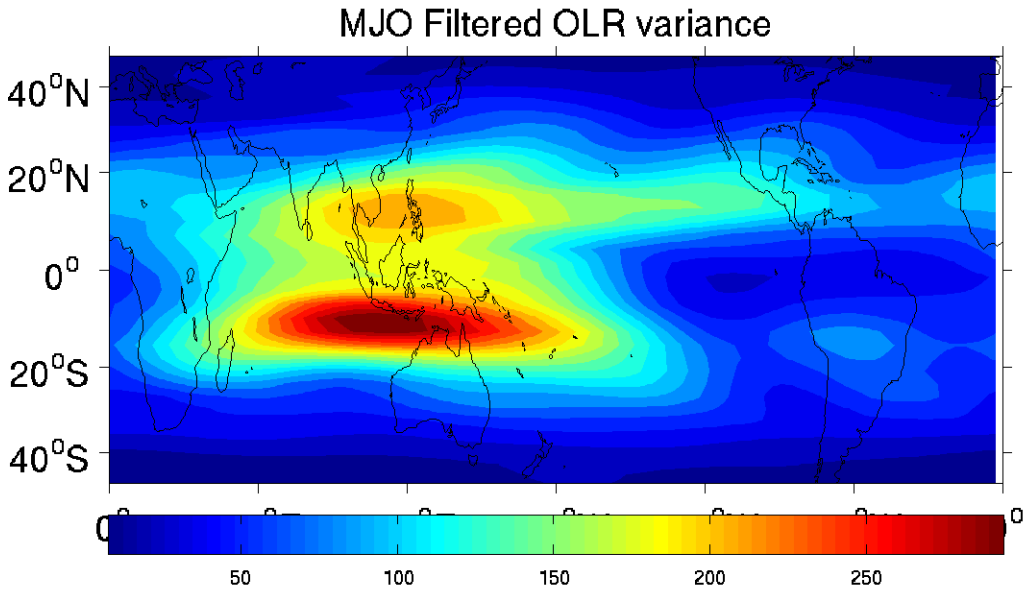

Figure 5-5 as figure 5-4, except for Outgoing Longwave Radiation.

The peak variance lies along the line of latitude at $12.5^{o}S$ (e.g. figure 5-6). The MJO-filtered precipitation along this latitude is shown in figure 5-7, demonstrating how the MJO grows and decays in space. The spatial distribution of the MJO genesis and decay events is also demonstrated in figure 5-8, which shows a Hovmöller diagram of OLR at $12.5^{o}S$. This figure shows the vast majority of MJO events arising around $90^{o}E$ and decaying around $180^{o}E$.

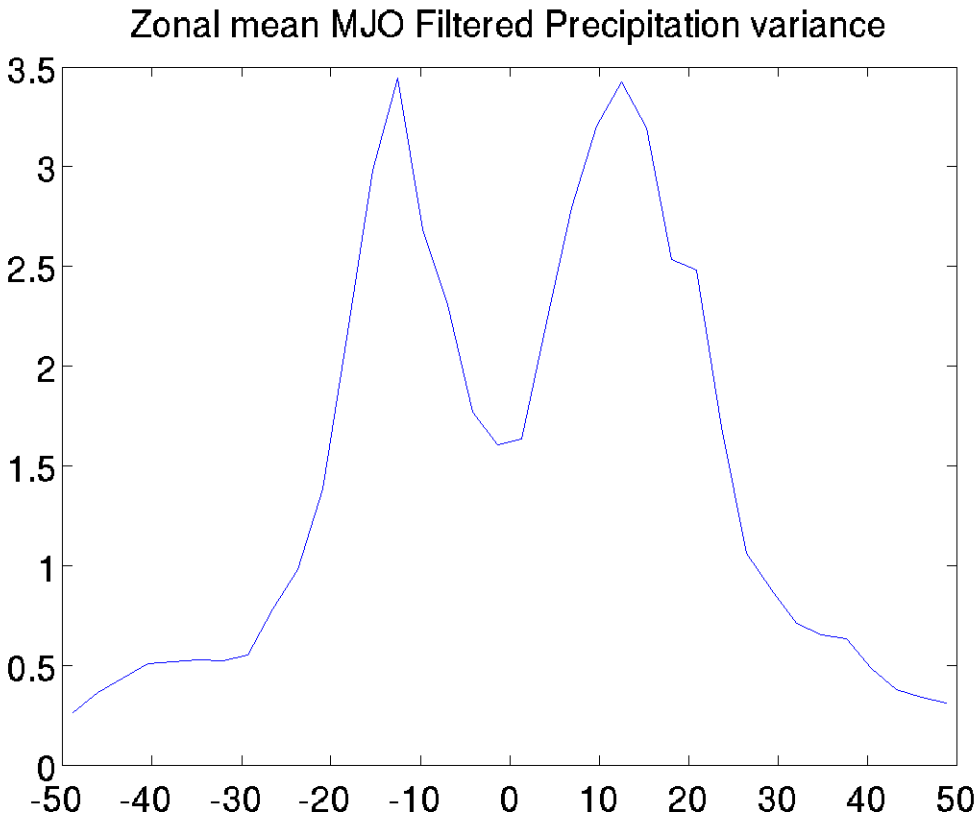

Figure 5-6. The zonal mean of MJO-filtered precipitation variance as a function of latitude.

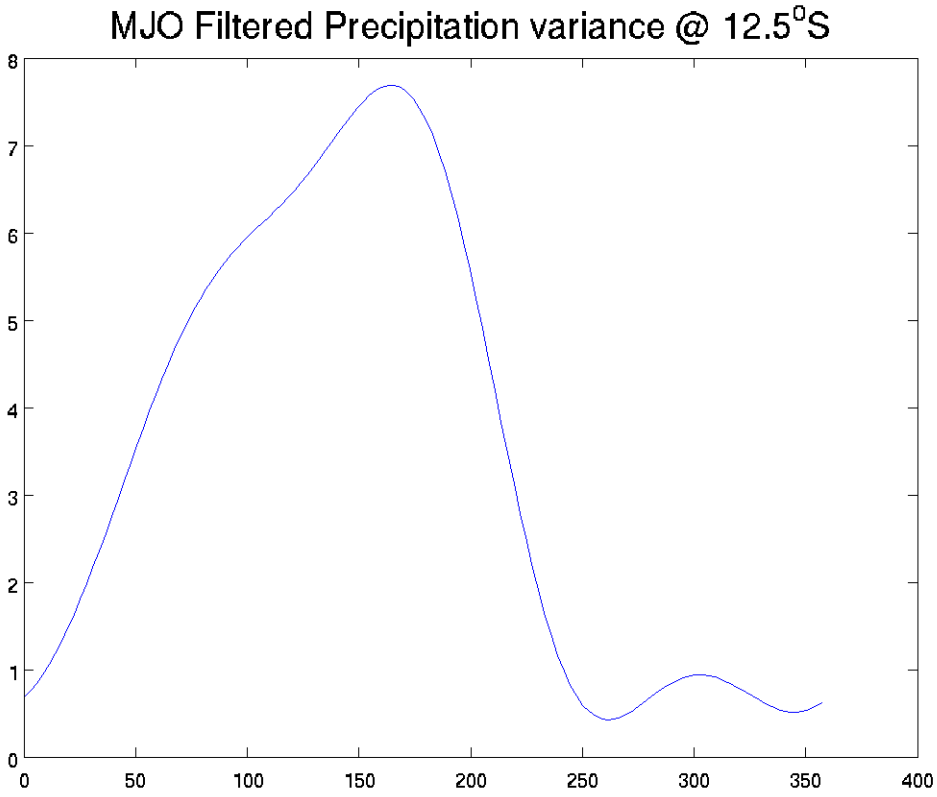

Figure 5-7. The MJO-filtered precipitation variance at **12. 5°**S, as a function of longitude, showing the MJO signal growing and then decaying in space.

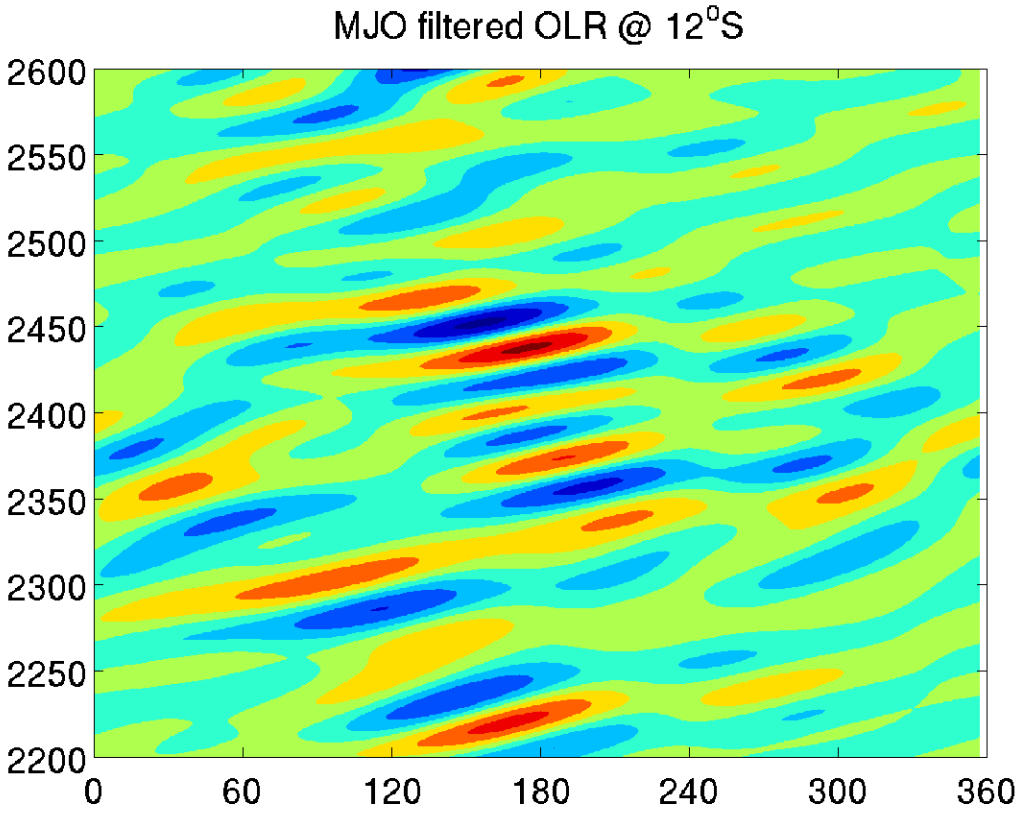

Figure 5-8. Hovmöller digram of the MJO-filtered OLR at **12**. **5***o*S for a representative period of the model run, showing the spatial distribution of the MJO activity.

5.5 MSE budget

5.5.A MJO budget projections

The projection of the composite budget terms onto the composite MSE anomaly and tendency are calculated in the same way as the previous chapters. In order to follow the life cycle of the MSE budget, we calculate these projections for the composite anomalies that arise from choosing a number of different longitudes for our reference point.

Figure 5-9a shows how the various terms in the MSE budget contribute to the growth/decay of the MSE anomaly. The balance between the terms changes as the MJO moves from initial growth (cool colors) through its mature phase (peak amplitude occurs near $135^{o}E$) and into the decay phase (warm colors). The largest variation with longitude is in the meridional advection term, which acts as a sink of MSE, and generally increases in strength as the MJO progresses to the East. The MSE source due to the longwave forcing does increase slightly at the same time, but too slowly to balance the strong changes in meridional advection.

Figure 5-9b shows the projections of the MSE budget terms on to the MSE tendency composite. This is not strictly the propagation term, as the tendency is further from quadrature with the anomaly than in the previous zonally-symmetric experiments, but it is still possible to draw some conclusions about MJO propagation from this figure. The dominant term is the meridional advection of MSE, which reinforces eastward propagation, as observed in the previous experiments.

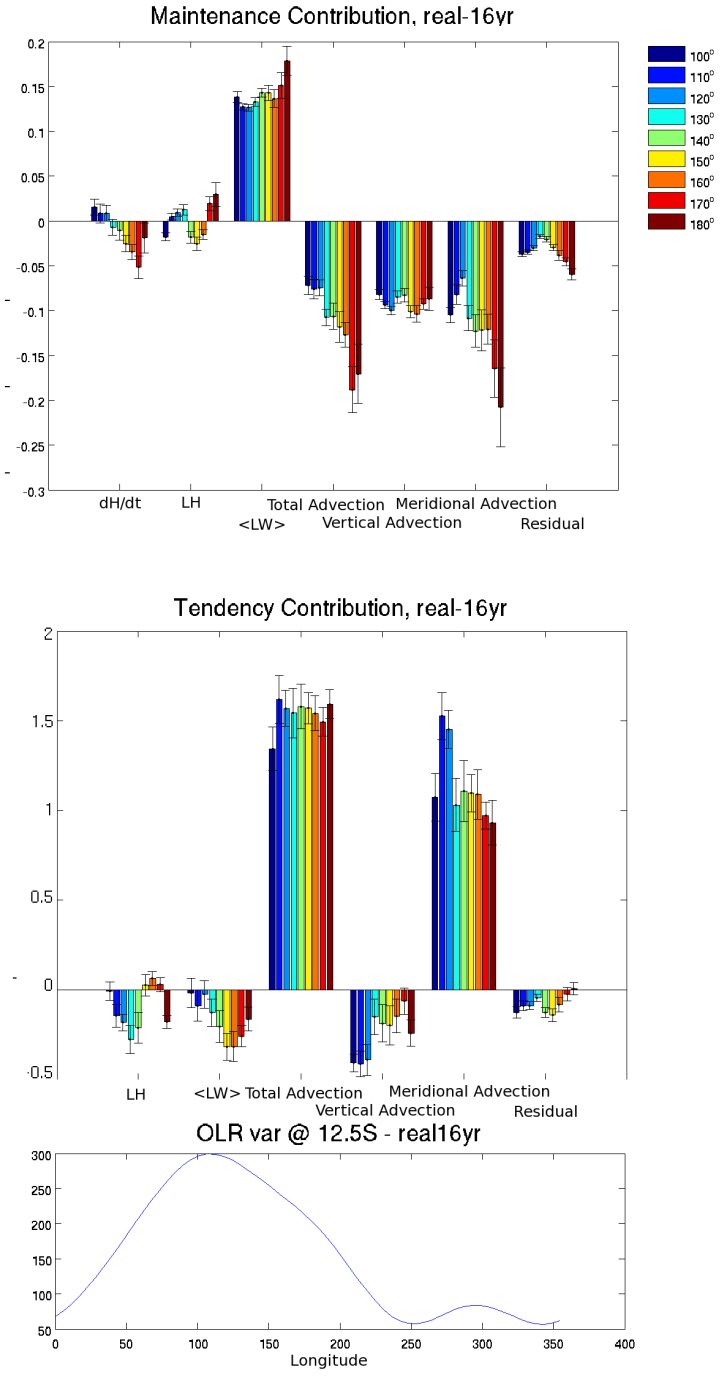

Figure 5-9. a) Projection of the MSE budget terms upon the MSE anomaly, for MJO composites regressed against the OLR at **12**. **5**^{o}S at the indicated longitudes; b) Projection of the same terms upon the MSE tendency for the same experiments; c) the Variance of the MJO filtered OLR at **12**. **5**^{o}S as a function of longitude, showing how the MJO grows and then decays in space.

5.5.C Time-filtered meridional advection

In the spirit of the previous experiments, we have decomposed the meridional advection terms by time-scale in order to investigate which processes are responsible for the observed increase in the sink of MSE as the MJO propagates to the east. As in chapter 4, we have used a cut-off of 20 days to separate the high frequency ("*hf*") terms from the "*mjo*"-scale terms. The interesting terms are shown in figure 5-10. We can see that the sink of MSE is dominated by the eddy (or "*hfhf*") term, although a number of terms are observed to become stronger sinks of MSE as the MJO moves towards its eventual demise.

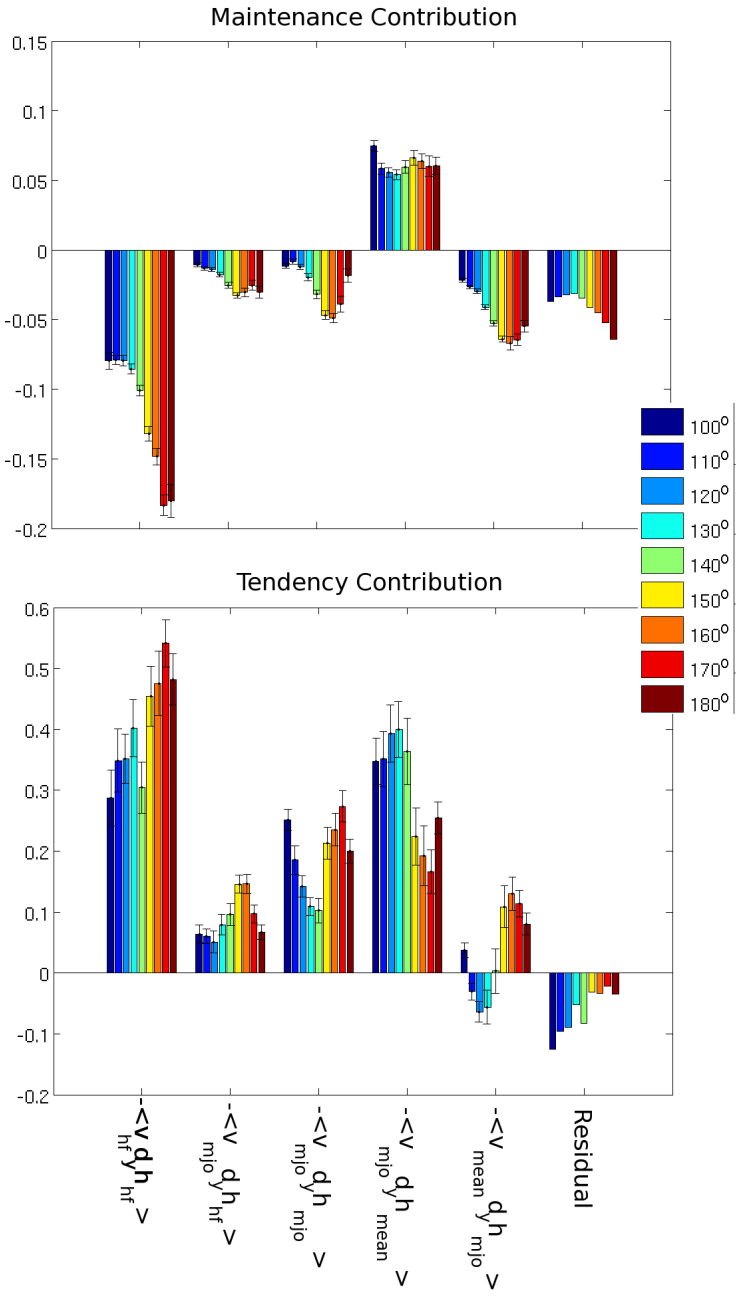

Figure 5-10 a) Projection of the time-filtered MSE meridional advection terms upon the MSE anomaly, for MJO composites regressed against the OLR at $\mathbf{12.5}^{o}$S at the indicated longitudes; b) Projection of the same terms upon the MSE tendency for the same experiments;

5.6 Discussion

5.6.A Lack of balance in the advection decomposition

One puzzling issue with the current analysis is the large residual in the decomposition of the advection terms. Specifically, this refers to the fact that the sum of the three upwind advection terms is quite different from the total advection calculated through the semi-lagrangian method. This error is most obvious in the MSE anomaly projection of the advection terms, where the total upwind advection is roughly twice that of the semi-lagrangian calculation. The discrepancy is smaller in the MSE tendency projection – this is due to the localization of the advection "error" to the vicinity of the convective region, as shown in figure 5-9. This appears to indicate that some aspect of the convective motion (or perhaps the stronger large-scale winds associated with convection in this experiment) is responsible for the error. However, at the preliminary stage of this investigation, the cause of the error has not been definitively determined.

5.6.B MSE budget variations between the realistic and idealized experiments

In the realistic experiment, the MJO demise appears to be mostly due to an increase in the MSE sink represented by the high-frequency eddies term, which advect dry sub-tropical air into the MJO convective region, damping the MSE anomaly. The eddy term increases in amplitude as the MJO moves from the Indian Ocean to the West Pacific and the date line.

The SST profile in this situation moves from the broad, warm, profile of the Warm Pool to the narrower peaked profile in the Central Pacific. Despite the qualitative

similarity of these SST profiles and those used in the aquaplanet experiments, the realistic case shows a significantly different variation of the projections of the meridional advection terms. The realistic case shows no systematic variation in the net tendency projection of meridional advection, and the variation of the projection of the "*mjo-mean*" advection on the MSE tendency is (to the extent that it can be said to exist at all) in the opposite sense as the MJO moves from a wide SST to a narrow SST as might be expected from the idealized experiments.

Also in contrast to the idealized experiments, the MSE sink due to the eddy advection term is not constant – it rather increases as the MJO moves to narrower SST profiles.

5.7 Conclusions

The MJO in the realistic integration of SP-CAM shows a life-cycle from genesis over the Indian Ocean to decay towards the date-line that is qualitatively similar to that observed in reality. The MSE budget regressed onto the MJO events that pass through the Australian monsoon region is analyzed. The projection of the budget terms onto the MSE tendency shows no systematic changes in the way the terms contribute to propagation of the MJO as the anomaly passes through its life-cycle. The projection of the budget terms onto the MSE anomaly shows that the sink of MSE due to meridional advection increases as the MJO propagates from the Indian Ocean to the date-line. This increasing sink appears to dominate the changing amplitude of the MJO as it progresses from genesis, through a mature phase, to demise.

In apparent conflict with the earlier aqua-planet analysis, the tendency projection of the advection of the long time-scale MSE gradient by the MJO time-scale winds does not appear to increase simply as the MJO moves from the broad SST profiles in the west to the narrower profile in the east. Also in contrast to the observations on the aqua-planets, the eddy advection term does increase as the MJO moves, indicating that the eddy activity in the MJO envelope does not decrease to compensate for the changes in MSE gradient.

It must be acknowledged that the MJO events analyzed in this chapter are centered significantly further from the equator than those in the aqua-planet experiments. This change in location may have a large influence upon how the advection terms vary with SST profile.

Chapter 6 - Conclusions, Future Directions

In this chapter, I summarize the results of the work described in this document, and describe several possible avenues of further research that may prove fruitful.

6.1 Summary

This work has covered an extended exploration of the fundamental mechanisms related to the existence of Convectively Coupled Equatorial Waves (CCEW) in the tropical atmosphere, especially the Madden-Julian Oscillation (MJO). In particular, the interactions between cumulus convection and the larger-scale atmospheric flows in the tropics are investigated in both a simplified wave model and numerical simulations of the atmosphere.

The work consisted of four major parts:

Chapter 2 - Shallow Water Convectively Coupled Wave Model – Linear Analysis of a toy model

The equatorial atmospheric variability shows a spectrum of significant peaks in the wavenumber–frequency domain. These peaks have been identified with the equatorially trapped wave modes of rotating shallow water wave theory. Chapter 2 addressed the observation that the various wave types (e.g., Kelvin, Rossby, etc.) and wavenumbers show differing signal strength relative to a red background. It is hypothesized this may be due to variations in the linear stability of the atmosphere in response to the various wave-types depending on both the specific wave-type and the wavenumber. A simple model of the convectively coupled waves on the equatorial beta plane has been constructed to identify processes that contribute to this dependence. The linear instability spectrum of the resulting coupled system, evaluated by eigenvalue analysis, shows unstable waves with phase speeds, growth rates, and structures (vertical and horizontal) that are broadly consistent with the results from observations. The linear system, with an idealized single intertropical

convergence zone (ITCZ) as a mean state, shows peak unstable Kelvin waves around zonal wavenumber 7 with peak growth rates of ~0.08 day^{-1} (e-folding time of ~13 days). The system also shows unstable Mixed Rossby–Gravity (MRG) and inertio-gravity waves with significant growth in the zonal wavenumber range from -15 (negative indicates westward phase speed) to $+10$ (positive indicates eastward phase speed). The peak MRG ($n = 0$) eastward inertio-gravity wave (EIG) growth rate is around one-third that of the Kelvin wave and occurs at zonal wavenumber 3. The Rossby waves in this system are almost stable, with very small growth-rates, and the Madden–Julian Oscillation is not observed. Within this model, it is shown that in addition to the effect of the ITCZ configuration, the differing instabilities of the different wave modes are also related to their different efficiency in converting input energy into divergent flow and also the efficiency with which the resulting convection couples to the temperature anomalies, generating more energy for the wave. This energy conversion efficiency difference is suggested as an additional factor that helps to shape the observed wave spectrum. In this chapter we investigated the linear regime of infinitesimal waves with a zonally and temporally fixed background state. We see this as a first step toward an understanding of the spectrum. Further investigation of the non-linear effects is planned. Also planned is an investigation of other interpretations of the observations, such as stable waves continually excited by stochastic or extratropical forcing (e.g., Zhang and Webster 1992; Hoskins and Yang 2000) in the context of this model.

Chapter 3 – Moist Static Energy Budget of the MJO-Like Disturbance on an Aquaplanet in SP-CAM

A Madden-Julian Oscillation (MJO)-like spectral feature has been observed in the time-space spectra of precipitation and column-integrated Moist Static Energy (MSE) for a zonally symmetric aquaplanet simulated with Super-Parameterized Community Atmospheric Model (SP-CAM). This disturbance possesses the basic structural and propagation features of the observed MJO.

To explore the processes involved in propagation and maintenance of this disturbance, we have analyzed the MSE budget of the disturbance. It is observed that the disturbances propagate both eastwards and polewards. The column-integrated longwave heating is the only significant source of column-integrated MSE acting to maintain the MJO-like anomaly balanced against the combination of column-integrated horizontal and vertical advection of MSE and Latent Heat Flux (LHF). Eastward propagation of the MJO-like disturbance is associated with MSE generated by both column-integrated horizontal and vertical advection of MSE, with the column long-wave heating generating MSE that retards the propagation.

The contribution to the eastward propagation by the column-integrated horizontal advection of MSE is dominated by synoptic eddies. Time-scale decomposition of the meridional advection indicated that the advection contribution to the eastward propagation is dominated by meridional advection of MSE by anomalous synoptic eddies caused by the suppression of eddy activity ahead of the MJO convection. This suppression is linked to the barotropic conversion mechanism; with the gradients of the low frequency wind experienced by the synoptic eddies within the MJO envelope

acting to modulate the Eddy Kinetic Energy (EKE). The meridional eddy advection's contribution to poleward propagation is dominated by the mean state's (meridionally varying) eddy activity acting on the anomalous MSE gradients associated with the MJO.

Chapter 4 – Sensitivity of MSE Budget Terms to Variations in Boundary conditions

The MSE budget for the MJO-like spectral feature observed in SP-CAM running on a zonally symmetric aquaplanet is examined for several different Sea Surface Temperature (SST) configurations. The propagation speed of this feature has been shown to increase as the width of the SST decreases. The budget analysis allowed diagnosis of the contributions of the various MSE sinks to the changes in propagation speed. It was determined that the variation in propagation speed is primarily due to the differences in meridional advection of the mean MSE profile by the MJO winds. The narrower SST cases, having stronger MSE gradients, experience a greater MSE source due to this term, which is phased relative to the convection to increase the propagation speed. The meridional eddy advection, previously shown to be a dominant contribution to the MSE budget for propagation, is seen to be quite constant between the various cases.

Chapter 5 – The Moist Static Energy Budget in a Realistic SP-CAM Integration

A brief investigation of the MSE budget for a more realistic case shows an increase in the MSE sink due to meridional advection as the MJO progresses from genesis over the Indian Ocean to decay in the central Pacific. The increase in this sink appears to be the cause of MJO's demise.

6.2 Proposed future projects

This MJO work described in the previous chapters has so far focused upon the MSE budget during the mature phase of the MJO, in a relatively simplified setting. As extensions of this work, we are interested in looking at the MJO using more realistic SST basic states; during the MJO initiation phase; and under the effects of global climate change. These new experiments are discussed below.

SPCAM MJO MSE Budgets in more realistic settings

The majority of the work described in this document has analyzed the MSE budget for the MJO-like phenomenon observed in SPCAM in a zonally symmetric configuration. This greatly simplifies the analysis but constitutes a weakness in the results, as the modeled MJO occurs in a climate that differs from that experienced in reality. In order to improve our understanding of the MJO, we propose to extend the analysis of the more realistic configuration, which contains both a realistic SST distribution with continents and topography.

The existing analysis of the realistic case has shown some interesting hints of the MSE processes involved in the MJO life-cycle.

MJO Initiation

The topic of MJO initiation has received much attention recently given the DYNAMO field program, which was partially motivated by the need to improve the representation of MJO initiation in climate models. Models typically have difficulty forecasting MJO initiation, which limits their ability to predict downstream effects of the MJO such as cyclogenesis in the Atlantic. In fact, most numerical weather prediction models had difficulty predicting the onset of the first MJO initiation event

during DYNAMO that occurred in October 2011. In a recent calculation of the MSE budget for the MJO in reanalysis data, (Kiranmayi and Maloney, 2011) it was observed that the equatorial Indian Ocean moistens in anomalous low level easterly flow during the initiation of an MJO event. This is also consistent with initiation events observed during DYNAMO (Adam Sobel and Eric Maloney, private communication, 2011). A leading hypothesis is that this is due to advection by the anomalous low-level easterly flow acting on the mean moisture gradient. However, in some aquaplanet GCM simulations, the moistening process for MJO genesis appears to be quite different and dominated by off-equatorial processes. For example, in a version of the NCAR CAM3 with modified convection, the moistening process appears to be dominated by the Rossby gyres associated with the preceding suppressed convection phase, although Kelvin wave circumnavigation also seems to contribute in a more indirect way (Eric Maloney, private communication, 2011). The hypothesized mechanism requires zonal asymmetry for the east-west moisture gradient to exist.

We plan to investigate the initiation mechanism for the MJO in SP-CAM, in both simplified aquaplanet and realistic model configurations. We plan to assess the initiation process in this model, which has been documented to produce an outstanding MJO (e.g. Kim et al. 2009), and hence may provide insights on MJO initiation more realistic and very different than those derived from other models. These experiments will test the importance of different terms in the MSE budget for column MSE growth which will be compared to observations from the DYNAMO field experiment. If properly validated against DYNAMO observations, the SP-CAM

fields will be able to provide insight on the MSE budget during MJO initiation that is not possible from limited observations alone.

MJO Demise

The MJO convective anomaly does not generally propagate eastwards beyond the dateline and the eastern edge of the Warm Pool. In our initial investigation, we have observed hints that the demise of the MJO is driven by the increased advection of dry air from outside the ITCZ region once the MJO begins to emerge from the warm, moist air above the Western Pacific. However, this analysis has been limited to the MJO events that occur in the Australian Monsoon region and has not allowed a detailed examination of the sensitivity of the MJO's life-cycle to the various factors that appear to be important.

The realistic case analysis would extend the initial investigations begun in Chapter 5.

MJO Variations under climate change

We are also interested in how the MJO will change as the climate changes. Recent work in a conventional version of the NCAR CAM with realistic MJO shows that the change in overall intraseasonal variance and the MJO strength is acutely sensitive to the pattern of SST warming (Eric Maloney and Shang-Ping Xie 2011 – private communication). A globally uniform warming strengthens the MJO, whereas a more realistic warming pattern such that warming is enhanced locally near the equator (esp. east Pacific) seems to weaken the MJO.

In Chapter 4, we observed that, in SP-CAM, as the ITCZ width changes (through changes in the width of the SST peak), the MJO intensity and phase speed varies. The

phase speed variation is driven by the advection of MSE down the mean state gradient by the low-level MJO scale winds. The MJO winds in front of the convective center blow from the equator into the tropics, carrying moisture into the drier air, which allows the convection to propagate. When the ITCZ is narrower, the MSE gradient is greater and the advection is stronger, leading to an increased phase speed. The reverse is also true when the ITCZ is made wider.

We propose to extend this investigation by testing the sensitivity of the SP-CAM MJO to different patterns of warming perturbations. Some recent studies have tried to assess how the MJO might change to climate warming by imposing a globally homogenous warming signal, which differs from that predicted by climate models in which warming is expected to be enhanced in the central and east Pacific equatorial cold tongue region (e.g. Johnson and Xie 2010). Rather, based upon the principle of Gross Moist Stability (GMS), we might expect that the intraseasonal variability at each location will increase or decrease in the same sense as the local changes in SST move relative to the tropical mean SST. The conventional CAM3 results mentioned above provide some support for this view. However, the SP-CAM provides a uniquely useful tool to conduct such investigations since it produces one of the most realistic simulations of intraseasonal variability among models, notably better than the MJO simulations in the conventional version of CAM3 mentioned above (Kim et al. 2009).

We are also interested in following up other aspects of this work in future projects:

a) Further investigation of the non-linear effects with in the simple model of convectively coupled waves is planned. Also planned is an investigation of

other interpretations of the observations, such as stable waves continually excited by stochastic or extratropical forcing (e.g., Zhang and Webster 1992; Hoskins and Yang 2000) in the context of this model.

b) Combine MSE mechanisms seen here with existing simple model to see if simple model can support an MJO. Currently the understanding of the MJO as a MSE anomaly is still in its formative stages, but it is possible that a combination of horizontal moisture advection and a parameterization of eddy diffusion may allow the existence of an MJO-like anomaly in a simplified wave system.

Appendices

Within the appendices, we show various detailed derivations and tangential discussions that, while important, would detract from the flow of the body of the document.

Appendix A. Calculation of the spectrum

The space-time spectra shown in this work are calculated using the methods published in Wheeler and Kiladis (1999), which is briefly detailed here for completeness.

A.1 Spectrum

i. Chunk data into 90 day long segments, overlapping at each end by 30 days. This is done so that a) statistics can be calculated and b) when windowing is applied to each segment, there is less loss of data.

ii. Remove time mean and any linear time trend at each point in each segment.

iii. Apply a Tukey window to each time series to prevent spectral ringing from the ends.

iv. Take the Fourier transform in time and the zonal direction of each segment, at each latitude.

v. The symmetric component is calculated:

$$S_{sym} = \sum_{j=1}^{\frac{N_y}{2}} \frac{F(j)+F(N_y-j)}{2} \quad \text{(A1.1)}$$

vi. Similarly the anti-symmetric spectrum can be calculated:

$$S_{antisym} = \sum_{j=1}^{\frac{N_y}{2}} \frac{F(j)-F(N_y-j)}{2} \quad \text{(A1.2)}$$

vii. Then, the raw spectra are found by taking the mean over the set of segments of the symmetric and antisymmetric spectra.

A.2 Red Noise Background (options)

i. The raw spectra generally contain a significant amount of power in a red noise spectrum, upon which is superposed the interesting wave spectra (eg figure 1-1a and b). In some cases, it is useful to estimate the red noise spectrum and remove it, to show the waves more clearly.

ii. A simple method of estimating the red noise spectrum is to take the average of the symmetric and antisymmetric spectra and then apply a 1-2-1 smoothing to the resulting spectrum many times in both wave number and frequency. This is a somewhat subjective process. In the background spectrum of Figure A-1, the 1-2-1 smoothing is applied 10 times in both directions and then an additional 10 times for frequencies higher than 0.5/4, 20 times for f>0.5/2 and 30 times for f> 0.5*3/4.

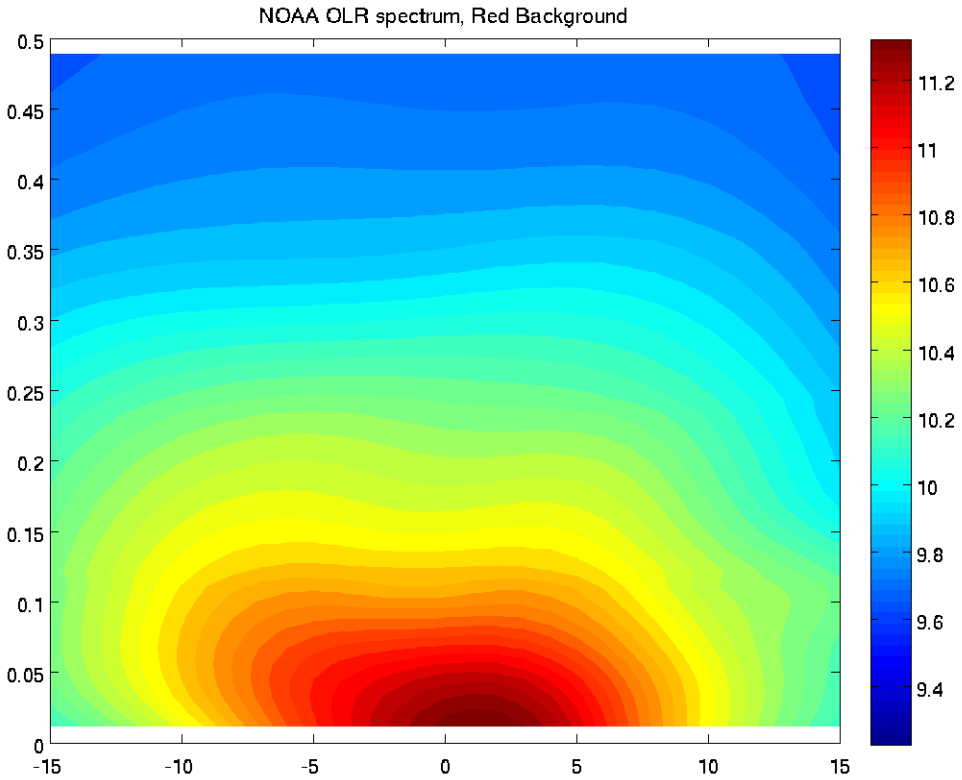

Figure A-1. The logarithm (base 10) of the red noise background in the observed OLR calculated by smoothing of the observed spectrum.

Appendix B Matsuno Mode Calculations

A simple way to derive an equatorial wave spectrum is from a shallow water wave system (after Matsuno 1966 and Holton 2004). We begin with the linearized momentum and continuity equations for a fluid system of mean depth h_e in a motionless basic state, on an equatorial β plane where the Coriolis parameter is approximated by

$$f(y) \approx \beta y, \tag{B.1}$$

where y is the meridional distance from the equator and $\beta = \frac{2\Omega}{a}$ (if Ω is the Earth's rotational velocity and a is its radius).

The shallow water equations for small perturbations about the resting mean state are given by:

$$\partial_t u - \beta y\, v = -\partial_x \phi, \tag{B.2}$$

$$\partial_t v + \beta y\, u = -\partial_{xy} \phi, \text{ and} \tag{B.3}$$

$$\partial_t \phi + g\, h_e (\partial_x u + \partial_y v) = 0. \tag{B.4}$$

In the above, $\phi = g\, h$ is the geopotential disturbance and u and v are the zonal and meridional perturbation velocities respectively. The x and t dependence is seperated by assuming zonally propagating plane wave solutions:

$$\begin{pmatrix} u \\ v \\ \phi \end{pmatrix} = \begin{bmatrix} \hat{u} \\ \hat{v} \\ \hat{\phi} \end{bmatrix} \exp[i(kx - \nu t)]. \tag{B.5}$$

Substituting (B.5) into (B.2)—(B.4) yields:

$$-i\nu\, \hat{u} - \beta y\, \hat{v} = -i\, k\, \hat{\phi}, \tag{B.6}$$

$$-i\nu \hat{v} + \beta y\, \hat{u} = -\partial_y \hat{\phi}, \text{ and} \tag{B.7}$$

$$-i\,\nu\hat{\phi} + g\,h_e\left(i\,k\,\hat{u} + \partial_y\hat{v}\right) = 0. \tag{B.8}$$

(B.6) can be solved for $\hat{u}$:

$$\hat{u} = \frac{\beta y\,\hat{v} - i\,k\,\hat{\phi}}{-i\nu}, \tag{B.9}$$

which can be substituted into (B.7) and (B.8):

$$(\beta^2 y^2 - \nu^2)\hat{v} = i\,k\,\beta y\,\hat{\phi} + i\,\nu\partial_y\hat{\phi}\,, \tag{B.10}$$

$$(\nu^2 - gh_e k^2)\hat{\phi} + i\nu g\,h_e\left(\partial_y - \frac{k}{\nu}\beta y\right)\hat{v} = 0\,, \tag{B.11}$$

Rearranging (B.11) to isolate $\hat{\phi}$

$$\hat{\phi} = -i\nu g\,h_e\frac{\left(\partial_y - \frac{k}{\nu}\beta y\right)}{(\nu^2 - gh_e k^2)}\,\hat{v}\,,$$

and using this to remove it from (B.10) yields:

$$\partial_y^2\hat{v} + \left[\left(\frac{\nu^2}{gh_e} - k^2 - \frac{k}{\nu}\right) - \frac{\beta^2 y^2}{gh_e}\right]\hat{v} = 0\,, \tag{B.12}$$

In order for (B.12) to have solutions that are finite, it must be the case that:

$$\frac{\sqrt{gh_e}}{\beta}\left(-\frac{k}{\nu}\beta - k^2 + \frac{\nu^2}{gh_e}\right) = 2n + 1; n = 0,1,2,\ldots \tag{B.13}$$

(See, for example, Byron and Fuller 1969, section 5.10).

This gives us a dispersion equation, relating the frequency and wavenumber of the solutions. This determines the frequencies of the permitted modes as functions of zonal and meridional wavenumber (*k* and *n*, respectively).

Then, the solution for v will be:

$$v(\xi) = v_0 H_n(\xi)\exp\left(-\frac{\xi^2}{2}\right), \tag{B.14}$$

where

$$\xi = \left(\frac{\beta}{\sqrt{gh_e}}\right)^{\frac{1}{2}} y \tag{B.15}$$

and $H_n(\xi)$ is the nth Hermite polynomial.

For $n \geq 1$ the dispersion relationship (B.13) has three solutions for each n, which correspond to the Eastward and Westward propagating Inertia-gravity waves and the westward moving Equatorial Rossby waves.

For $n = 0$, there is only a single solutions. Consider, in this case, the dispersion relationship becomes

$$\frac{\sqrt{gh_e}}{\beta}\left(-\frac{k}{\nu}\beta - k^2 + \frac{\nu^2}{gh_e}\right) = 1,$$

$$\frac{\sqrt{gh_e}}{\beta}\left(-\frac{k}{\nu}\beta - k^2 + \frac{\nu^2}{gh_e}\right) - 1 = 0\,,$$

$$\left(-\frac{k}{\nu}\beta - k^2 + \frac{\nu^2}{gh_e} - \frac{\beta}{\sqrt{gh_e}}\right) = 0\,,$$

$$\left(\frac{\nu}{\sqrt{gh_e}} - \frac{\beta}{\nu} - k\right)\left(\frac{\nu}{\sqrt{gh_e}} + k\right) = 0\,. \tag{B.16}$$

The root corresponding to the right parentheses cannot exist, as $\left(\frac{\nu}{\sqrt{gh_e}} + k\right)$ is assumed to be non-zero in the derivation of (B.12).

Then, the allowed roots are given by:

$$\nu = k\sqrt{gh_e}\left[\frac{1}{2} \pm \frac{1}{2}\left(1 + \frac{4\beta}{k^2\sqrt{gh_e}}\right)^{\frac{1}{2}}\right]. \tag{B.17}$$

The positive root of this equation corresponds to an Eastward propagating inertia-gravity wave. The negative root represents a westward propagating wave; This is

similar to an inertia-gravity wave for long wavelengths and an Equatorial Rossby wave for short wavelengths; called the Mixed Rossby Gravity wave.

While, in our derivation, we have made the assumption that v was not everywhere zero. However, it is possible to derive a further mode with the assumption of zero meridional velocity, in which case the shallow water system (B.6-B.8) reduces to a simpler set of equations:

$$-iv\hat{u} = -ik\hat{\phi}, \tag{B.18}$$

$$\beta y\,\hat{u} = -\partial_y\hat{\phi}, \text{ and} \tag{B.19}$$

$$-iv\hat{\phi} + gh_e(ik\hat{u}) = 0. \tag{B.20}$$

We can rearrange (B.18):

$$\hat{\phi} = \frac{v}{k}\hat{u}, \tag{B.21}$$

and remove $\hat{\phi}$ from (B.20):

$$\left(-\frac{iv^2}{k} + \text{?}kgh_e\right)\hat{u} = 0, \tag{B.22}$$

which requires, if u is non-zero somewhere,

$$\left(-\frac{iv^2}{k} + ikgh_e\right) = 0,$$

$k^2gh_e = v^2$, or

$$c^2 = \left(\frac{v}{k}\right)^2 = gh_e, \tag{B.23}$$

the dispersion relationship for ordinary shallow water waves.

Using (B.21) and (B.23) in (B.19), we can find a relationship for the meridional structure of this mode:

$$\beta y\hat{u} = -\partial_y(c\hat{u}), \tag{B.24}$$

which has the solution:

$$u = u_0 \exp\left(-\frac{\beta y^2}{2c}\right). \tag{B.25}$$

It can be seen that, for the solutions to be finite, the phase speed, *c*, must be positive – so these waves are required to be eastward propagating. These waves are referred to as the Kelvin waves, and are also sometimes referred to as the $n = -1$ mode, as their dispersion relationship satisfies (B.13) for $n = -1$.

The dispersion curves for the various modes (up to n=3) are plotted in figure B-1, showing frequency against zonal wavenumber. Positive wavenumbers indicate eastward propagation for the Kelvin, MRG and EIG waves. The negative wavenumbers indicate the westward propagating ER, MRG and WIG waves.

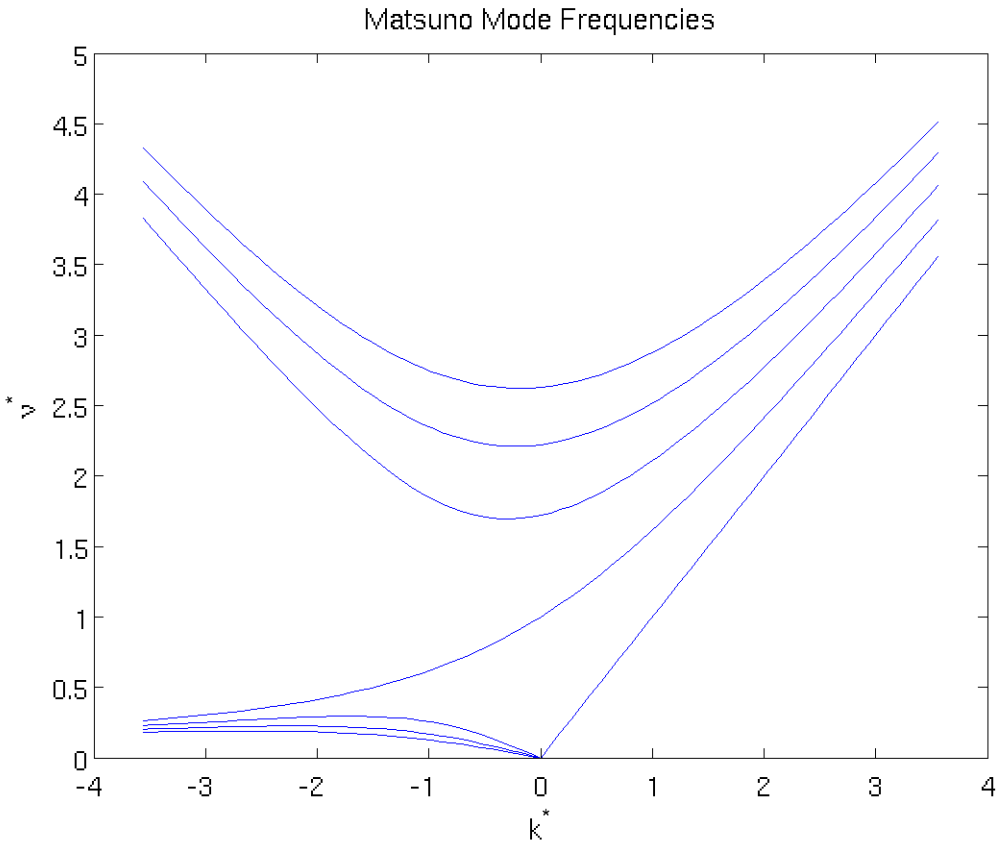

Figure B-1. Dispersion diagram for the equatorial rotating shallow water system. Frequency and zonal wavenumbers have been nondimensionalized with $\boldsymbol{\nu}^* = \frac{\boldsymbol{\nu}}{\boldsymbol{\beta}\sqrt{\boldsymbol{g}\boldsymbol{h}_e}}$, and $\boldsymbol{k}^* = \boldsymbol{k}\left(\frac{\sqrt{\boldsymbol{g}\boldsymbol{h}_e}}{\boldsymbol{\beta}}\right)$

Appendix C Detailed Derivation of Shallow Water wave equations

C.1 Derivation of the Dynamical Equations

Anelastic Equations

We start with the equations of motion for a shallow fluid with rigid lid and base, on a rotating sphere:

$$\partial_t u - fv + \boldsymbol{u} \cdot \nabla u = -\frac{1}{\rho}\partial_x p, \tag{C.1}$$

$$\partial_t v + fu + \boldsymbol{u} \cdot \nabla v = -\frac{1}{\rho}\partial_y p\,, \tag{C.2}$$

$$\partial_x(\rho u) + \partial_y(\rho v) + \partial_z(\rho w) = 0, \tag{C.3}$$

$$\partial_t \theta + w\partial_z \theta = \tilde{J} - \epsilon\theta, \text{ and} \tag{C.4}$$

$$\partial_z p = -g\rho. \tag{C.5}$$

Where ρ and θ represent the density and potential temperature[2]; u, v, and w represent the velocities in the zonal, meridional and vertical directions, respectively; and J represents the convective heating (in potential temperature). A linear damping on temperature, denoted by ϵ, represents radiative cooling/heating toward the mean temperature profile.

We expand these equations in terms of the (balanced, time invariant but potentially non-zero, non-symmetrical) mean and perturbation fields. Eg:

$$u = \bar{u} + u'. \tag{C.6}$$

[2] Potential Temperature is defined as $\theta = T\left(\frac{p_s}{p}\right)^{R/c_p}$ and describes the temperature a parcel of air would achieve if it were moved adiabatically from its origin level (at pressure p) to sea level pressure (p_s).

Overbars represent mean quantities and primes denote deviation from this mean state (assumed to be small). ρ' is assumed to be zero in all equations (except for its dependence upon T' in the hydrostatic balance).

$$\partial_t u' - f\bar{v} - fv' + (\overline{\boldsymbol{u}} + \boldsymbol{u}') \cdot \nabla(\bar{u} + u') = -\frac{1}{\bar{\rho}}\partial_x(\bar{p} + p'),$$

$$\partial_t u' - fv' + \overline{\boldsymbol{u}} \cdot \nabla u' + \boldsymbol{u}' \cdot \nabla \bar{u} = -\frac{1}{\bar{\rho}}\partial_x p' \quad \text{(C.7)}$$

similarly,

$$\partial_t v' + fu' + \overline{\boldsymbol{u}} \cdot \nabla v' + \boldsymbol{u}' \cdot \nabla \backslash \bar{v} = -\frac{1}{\bar{\rho}}\partial_y p', \quad \text{(C.8)}$$

and

$$\partial_x(\bar{\rho}u') + \partial_y(\bar{\rho}v') + \partial_z(\bar{\rho}w') = 0, \quad \text{(C.9)}$$

Regarding the thermodynamic equation, we have:

$$\partial_t\theta' + \overline{\boldsymbol{u}} \cdot \nabla\theta' + \boldsymbol{u}' \cdot \bar{\nabla}\theta = J' - \epsilon\theta', \quad \text{(C.10)}$$

then:

$$\partial_t T' + \bar{w}\left(\partial_z T' + \frac{g}{c_p}\right) + w'\left(\partial_z \bar{T} + \frac{g}{c_p}\right) + \bar{u} \cdot \nabla_H T' + \boldsymbol{u}' \cdot \nabla_H \bar{T} = J' - \epsilon T', \quad \text{(C.11)}$$

where J is the convective heating in temperature.

The Hydrostatic equation yields:

$$\partial_z p' = \frac{g\bar{\rho}}{\bar{T}} T', \quad \text{(C.12)}$$

Assuming the mean winds are zero yields

$$\partial_t u' - \beta y v' = -\frac{1}{\bar{\rho}}\partial_x p' \quad \text{(C.13)}$$

$$\partial_t v' + \beta y u' = -\frac{1}{\bar{\rho}}\partial_y p', \quad \text{(C.14)}$$

$$\partial_x(\bar{\rho}u') + \partial_y(\bar{\rho}v') + \partial_z(\bar{\rho}w') = 0, \quad \text{(C.15)}$$

$$\partial_t T' + w'\left(\partial_z \bar{T} + \frac{g}{c_p}\right) = J' - \epsilon T', \quad \text{(C.16)}$$

$$\partial_z p' = \frac{g\bar{\rho}}{\bar{T}} T', \quad \text{(C.17)}$$

βy is the linear expansion of the Coriolis parameter, *f*, for small displacements away from the equator

Vertical Structure Equations

Assuming a rigid lid on the atmosphere and a constant buoyancy frequency, we can now expand the perturbation fields in terms of the baroclinic modes:

$$\frac{g\bar{\rho}}{\bar{T}}\left[T', J, w'\left(\partial_z \bar{T} + \frac{g}{c_p}\right)\right] = \sum_j [T, J, w]_j (x, y, t) \frac{\pi}{2} sin\left(\frac{j\pi z}{H_T}\right), \quad \text{(C.18)}$$

$$[\bar{\rho}u', \bar{\rho}uv', p'] = \Sigma_j [u, v, p]_j (x, y, t) \frac{H_T}{2j} \cos j\pi \frac{z}{H_T}, \quad \text{(C.18)}$$

The buoyancy frequency, N, is given by

$$N^2 = \frac{g}{\bar{T}}\left(\partial_z \bar{T} + \frac{g}{c_p}\right), \quad \text{(C.19)}$$

Inserting the modal expansion into the first of the equations of motion, we have:

$$\partial_t \Sigma_j \frac{u_j(x,y,t)}{\bar{\rho}} \frac{H_T}{2j} \cos j\pi \frac{z}{H_T} - \beta y \Sigma_j \frac{v_j(x,y,t)}{\bar{\rho}} \frac{H_T}{2j} \cos j\pi \frac{z}{H_T} = -\frac{1}{\bar{\rho}} \partial_x \Sigma_j p_j(x, y, t) \frac{H_T}{2j} \cos j\pi \frac{z}{H_T}.$$

Collecting like terms yields:

$$\frac{1}{\bar{\rho}} \Sigma_j \left(u_j(x, y, t) - \beta y v_j(x, y, t) + \partial_x p_j(x, y, t)\right) \frac{H_T}{2j} \cos j\pi \frac{z}{H_T} = 0, \quad \text{(C.20)}$$

As the equality has to hold at all heights, it must be the case that:

$$\left(u_j(x, y, t) - \beta y v_j(x, y, t) + \partial_x p_j(x, y, t)\right) = 0. \quad \text{(C.21)}$$

Similarly,

$$\left(v_j(x,y,t) + \beta y u_j(x,y,t) + \partial_y\ p_j(x,y,t)\right) = 0. \tag{C.22}$$

Or

$$\partial_t \boldsymbol{u}_j = -\beta y\ \hat{k}\times\boldsymbol{u}_j - \nabla p_j, \tag{C.23}$$

The continuity equation yields

$$\partial_x \left(\Sigma_j\ u_j(x,y,t)\frac{H_T}{2j}\cos j\pi\frac{z}{H_T}\right)\ + \partial_y \left(\Sigma_j\ v_j(x,y,t)\frac{H_T}{2j}\cos j\pi\frac{z}{H_T}\right) +$$

$$\partial_z \left(\sum_j w_j\ (x,y,t)\frac{\pi}{2} sin\left(\frac{j\pi z}{H_T}\right)\right)\frac{\bar{T}}{g\left(\partial_z\bar{T} + \frac{g}{c_p}\right)}\ = 0,$$

$$\Sigma_j \left[\left(\partial_x u_j(x,y,t)\ + \partial_y\ v_j(x,y,t)\right)\frac{H_T}{2j}\cos j\pi\frac{z}{H_T} + w_j(x,y,t)\frac{\pi}{2}\partial_z sin\left(\frac{j\pi z}{H_T}\right)\frac{1}{N^2}\right]\ = 0,$$

$$\Sigma_j \left[\left(\partial_x u_j(x,y,t)\ + \partial_y\ v_j(x,y,t)\right)\frac{H_T}{2j} + w_j(x,y,t)\frac{\pi}{2}\frac{j\pi}{H_T}\frac{1}{N^2}\right]\ \cos j\pi\frac{z}{H_T} = 0,$$

$$\Sigma_j \left[\left(\partial_x u_j(x,y,t)\ + \partial_y\ v_j(x,y,t)\right) + w_j(x,y,t)\frac{j^2\pi^2}{N^2H_T^2}\right]\ \frac{H_T}{2j}\cos j\pi\frac{z}{H_T} = 0.$$

And then, using $c_j = \frac{NH_T}{j\pi}$,

$$c_j^2\left(\partial_x u_j(x,y,t)\ + \partial_y\ v_j(x,y,t)\right) + w_j(x,y,t) = 0, \tag{C.24}$$

or

$$w_j = -c_j^2\nabla_H\cdot\boldsymbol{u}_j, \tag{C.25}$$

The thermodynamic equation yields:

$$\partial_t \sum_j T_j\ (x,y,t)\frac{\pi}{2} sin\left(\frac{j\pi z}{H_T}\right) + \sum_j w_j\ (x,y,t)\frac{\pi}{2} sin\left(\frac{j\pi z}{H_T}\right) = \sum_j J_j\ (x,y,t)\frac{\pi}{2} sin\left(\frac{j\pi z}{H_T}\right) -$$

$$\epsilon\ \sum_j T_j\ (x,y,t)\frac{\pi}{2} sin\left(\frac{j\pi z}{H_T}\right),$$

$$\sum_j\left[\partial_t T_j(x,y,t) + \ w_j(x,y,t) - J_j(x,y,t)\ + \epsilon\ T_j(\text{?},y,t)\right]\frac{\pi}{2} sin\left(\frac{j\pi z}{H_T}\right) = 0,$$

$$\partial_t T_j(x,y,t) + w_j(x,y,t) - J_j(x,y,t) + \epsilon T_j(x,y,t) = 0. \quad \text{(C.26)}$$

Or

$$\partial_t T_j - c_{2j}\nabla_H \cdot \boldsymbol{u_j} = J_j - \epsilon T_j \quad \text{(C.27)}$$

Finally, the hydrostatic equation yields

$$\partial_z \Sigma_j \, p_j(x,y,t)\frac{H_T}{2j}\cos j\pi\frac{z}{H_T} = \sum_j T_j(x,y,t)\frac{\pi}{2}sin\left(\frac{j\pi z}{H_T}\right)$$

$$\Sigma_j \left[p_j(x,y,t)\frac{H_T}{2j}\partial_z \cos j\pi\frac{z}{H_T} - T_j(x,y,t)\frac{\pi}{2}sin\left(\frac{j\pi z}{H_T}\right)\right] = 0$$

$$\Sigma_j \left[-p_j(x,y,t)\frac{H_T}{2j}\frac{j\pi}{H_T}\sin j\pi\frac{z}{H_T} - T_j(x,y,t)\frac{\pi}{2}sin\left(\frac{j\pi z}{H_T}\right)\right] = 0$$

$$\Sigma_j \left[-p_j(x,y,t) - T_j(x,y,t)\right]\frac{\pi}{2}sin\left(\frac{j\pi z}{H_T}\right) = 0.$$

Again, as this must hold for all z, we have:

$$-p_j(x,y,t) - T_j(x,y,t) = 0, \text{ or} \quad \text{(C.28)}$$

$$p_j(x,y,t) = -T_j(x,y,t) \quad \text{(C.29)}$$

Using this to remove the pressure from the system, we are left with:

$$\partial_t \boldsymbol{u}_j = -\beta y\,\hat{k}\times\boldsymbol{u}_j + \nabla_H T_j,$$

$$\partial_t T_j - c_{2j}\nabla_H \cdot \boldsymbol{u_j} = J_j - \epsilon T_j$$

In practice, we will limit ourselves to the first two baroclinic modes.

C.2 Convective parameterization

For the purposes of the convective parameterization, the heating is rewritten in terms of lower- (L) and upper- (U) tropospheric heating anomalies:

$$L = \frac{1}{2}(J_1 + J_2) \quad \text{(C.30)}$$

and

$$U = \frac{1}{2}(J_1 - J_2) \quad \text{(C.31)}$$

Rearranging this gives us:

$$J_1 = L + U, \text{ and} \quad \text{(C.32)}$$

$$J_2 = L - U. \quad \text{(C.33)}$$

The total upper-tropospheric heating is considered to be a fraction of the lower-tropospheric heating:

$$\frac{U_0+U}{L_0+L} = r_0 + r_q q. \quad \text{(C.34)}$$

This can also be rearranged:

$$U_0 + U = \left(r_0 + r_q q\right) \times (L_0 + L)$$

$$U = r_0 L_0 + r_0 L + r_q q L_0 + r_q q L - U_0 .$$

Using the fact that U_0 and L_0 are the values for the upper and lower total heating when the moisture anomaly (q) is zero, we have:

$$U = r_0 L + r_q q L_0 + r_q \square L. \quad \text{(C.35)}$$

In order to enforce convective quasi-equilibrium, we require that the time derivatives of boundary layer MSE and lower-tropospheric saturation MSE are equal. That is,

$$\partial_t h_b = \langle \partial_t h^* \rangle_{LT}. \quad \text{(C.36)}$$

That is,

$$-b_1 J_1 - b_2 J_2 = F[\gamma \partial_t T_1 + (1-\gamma)\partial_t T_2], \quad \text{(C.37)}$$

where he term b_j describes the reduction of boundary layer moist static energy by the convection J_j; F is a proportionality constant relating the change in lower-

troposphere temperature to the change in moist static energy in the same region, and γ describes the relative influence of the two modes on the temperature of the lower troposphere.

We can expand (C.41) using the relationships derived above:

$$-b_1 J_1 - b_2 J_2 = F[\gamma \partial_t T_1 + (1-\gamma)\partial_t T_2]$$

$$-b_1(L+U) - b_2(L-U) = F[\gamma(c_1^2 \nabla_H \cdot \boldsymbol{u_1} + J_1 - \epsilon T_1) + (1-\gamma)(c_2^2 \nabla_H \cdot \boldsymbol{u_2} + J_2 - \epsilon T_2)]$$

$$-(b_1+b_2)L - (b_1-b_2)U = F[\gamma(c_1^2 \nabla_H \cdot \boldsymbol{u_1} + L + U - \epsilon T_1) + (1-\gamma)(c_2^2 \nabla_H \cdot \boldsymbol{u_2} + L - U - \epsilon T_2)]$$

$$-(b_1+b_2)L - (b_1-b_2)U - F[\gamma(L+U) + (1-\gamma)(L-U)] = F[\gamma(c_1^2 \nabla_H \cdot \boldsymbol{u_1} - \epsilon T_1) + (1-\gamma)(c_2^2 \nabla_H \cdot \boldsymbol{u_2} - \epsilon T_2)]$$

$$-[b_1+b_2+F(\gamma+1-\gamma)]L - [b_1-b_2+F(\gamma+\gamma-1)]U = F[\gamma(c_1^2 \nabla_H \cdot \boldsymbol{u_1} - \epsilon T_1) + (1-\gamma)(c_2^2 \nabla_H \cdot \boldsymbol{u_2} - \epsilon T_2)]$$

$$-[b_1+b_2+F]L - [b_1-b_2+F(2\gamma-1)](r_0 L + r_q q L_0 + r_q q L) = F[\gamma(c_1^2 \nabla_H \cdot \boldsymbol{u_1} - \epsilon T_1) + (1-\gamma)(c_2^2 \nabla_H \cdot \boldsymbol{u_2} - \epsilon T_2)]$$

Defining $A = (b_2 - b_1) + F(1-2\gamma)$, we have:

$$\left[-b_1 - b_2 - F + A\left(r_0 + r_q q\right)\right]L = -A r_q q L_0 + F[\gamma(c_1^2 \nabla_H \cdot \boldsymbol{u_1} - \epsilon T_1) + (1-\gamma)(c_2^2 \nabla_H \cdot \boldsymbol{u_2} - \epsilon T_2)]$$

$$-BL = -A r_q q L_0 + F[\gamma(c_1^2 \nabla_H \cdot \boldsymbol{u_1} - \epsilon T_1) + (1-\gamma)(c_2^2 \nabla_H \cdot \boldsymbol{u_2} - \epsilon T_2)],$$

where $B = F + (b_1 + b_2) - A\left(r_q q + r_0\right)$.

$$L = \frac{A r_q q L_0}{B} + \frac{F}{B}[\gamma(c_1^2 \nabla_H \cdot \boldsymbol{u_1} - \epsilon T_1) + (1-\gamma)(c_2^2 \nabla_H \cdot \boldsymbol{u_2} - \epsilon \square_2)], \qquad \text{(C.38)}$$

Appendix D Heating-Divergence Feedback Calculations

As described in Chapter 2, we investigate the role of wave structure upon the growth rates of the convectively coupled equatorial shallow water waves by considering a simplified convective parameterization that acts as a small perturbation on the dry waves.

For this section, the first mode is mathematically superfluous, so we can drop the subscripts without ambiguity.

D.1 Kelvin wave heating-divergence feedback

We start with a neutral Kelvin wave, with the standard form (assuming the dry dispersion relationship to be sufficiently accurate given the arbitrarily small heating) for the complex wave:

$$\tilde{u} = u_0 e^{-\left(\frac{\beta y^2}{2c}\right)} e^{i(kx-\omega t)}, \tag{D.1}$$

$$\tilde{v} = 0, \text{ and} \tag{D.2}$$

$$T = -\frac{c^2 k}{\omega} u_0 e^{-\left(\frac{\beta y^2}{2c}\right)} e^{i(kx-\omega t)} = c u_0 e^{-\left(\frac{\beta y^2}{2c}\right)} e^{i(kx-\omega t)}, \tag{D.3}$$

where the amplitude of $\tilde{T}$ is determined using the standard wave relations (in wavenumber–frequency space) and the dry dispersion equation (see, e.g., Gill 1982).

We can then calculate the total energy (per unit length in the x direction) stored in the wave (H is the equivalent depth of the second mode):

$$E = \frac{1}{2}\overline{u^2}H + \frac{1}{2}\frac{\overline{T^2}}{g} = \frac{H}{2}\left[u_0^2 + \frac{(cu_0)^2}{c^2}\right]\overline{\left[e^{-\left(\frac{\beta y^2}{c}\right)}\cos^2(kx-\omega t)\right]} =$$

$$\frac{Hu_0^2\omega}{2\pi}\frac{k}{2\pi}\int_0^{\frac{2\pi}{\omega}}\int_0^{\frac{2\pi}{k}}\cos^2(kx-\omega t)dxdt\int_{-\infty}^{\infty}e^{-\left(\frac{\beta y^2}{2c}\right)}dy = \frac{H}{2}\sqrt{\frac{c\pi}{\beta}}u_0^2. \tag{D.4}$$

The overbar denotes the time and zonal mean of a quantity, integrated over its meridional extent. The energy input in time Δt is given by

$$\Delta E = \overline{JT}\Delta t = -\frac{\overline{B|\delta|T^2}}{\omega|T|}\Delta t = \frac{B\delta c u_0}{\omega}\overline{e^{-\left(\frac{\beta y^2}{c}\right)}\cos^2(kx-\omega t)}\,\Delta t = \frac{B|\delta|u_0\Delta t}{2k}\sqrt{\frac{c\pi}{\beta}} \quad \text{(D.5)}$$

($|T| = -cu_0$, $|\delta|$ is defined similarly).

With the increased energy in the wave after this interval, the amplitude of the wave (given by u_0) will have increased:

$$\Delta u_0 = \left(\partial_{u_0} E\right)^{-1}\Delta E = \frac{B|\delta|\Delta t}{2Hk}. \quad \text{(D.6)}$$

Now, the divergence in the wave can also be determined:

$$\delta = \partial_x u = -k u_0 e^{-\left(\frac{\beta y^2}{2c}\right)}\sin(kx-\omega t). \quad \text{(D.7)}$$

We can calculate how the divergence increases in this time interval:

$$\Delta\delta = -k\Delta u_0 e^{-\left(\frac{\beta y^2}{2c}\right)}\sin(kx-\omega t). \quad \text{(D.8)}$$

Because $\Delta\delta$ is exactly in phase with δ, we can also say that

$$\Delta|\delta| = k\Delta u_0 = k\frac{B|\delta|\Delta t}{2Hk}, \quad \text{(D.9)}$$

And so,

$$\frac{\Delta|\delta|}{\Delta t} = \frac{Bc}{2H}|\delta|, \quad \text{(D.10)}$$

D.2 Mixed Rossby-gravity wave heating divergence feedback

The basic dry MRG wave is well described by its y-velocity field

$$\tilde{v} = v_0 e^{-\left(\frac{\beta y^2}{2c}\right)}e^{i(kx-\omega t)} \quad \text{(D.10)}$$

and a dispersion relationship

$$\omega = \pm\frac{kc}{2}\left(1 \pm \sqrt{1+\frac{4\beta}{k^2 c}}\right). \tag{D.11}$$

Then, using the standard forms,

$$\tilde{T} = -\frac{i\omega c^2}{\omega^2 - c^2k^2}\left(-\partial_y + \frac{k}{\omega}\beta y\right)\tilde{v} = \frac{icv_0\beta y e^{-\left(\frac{\beta y^2}{2c}\right)}}{ck-\omega}e^{i(kw-\omega t)}, \text{ and} \tag{D.12}$$

$$u = \frac{\beta y\tilde{v} + ik\tilde{T}}{-i\omega} = -\frac{iv_0\beta y e^{-\left(\frac{\beta y^2}{2c}\right)}}{ck-\omega}e^{i(kx-\omega t)}. \tag{D.13}$$

Similarly to the Kelvin wave example, we can calculate the energy per unit length stored in the wave:

$$E = \frac{\frac{H}{4}v_0^2[c(ck^2+\beta)-2ck\omega+\omega^2]}{(\omega-ck)^2}\sqrt{\frac{\pi c}{\beta}}. \tag{D.14}$$

Then, the increase in the wave amplitude due to an increase in energy ΔE is given by:

$$\Delta v_0 = \frac{2\Delta E(\omega-ck)^2}{Hv_0[c(ck^2+\beta)-2ck\omega+\omega^2]}\sqrt{\frac{\beta}{\pi c}}, \tag{D.15}$$

And the increase in energy over Δt is

$$\Delta E = \overline{JT}\Delta t = \frac{Bc^4 v_0|\delta|\Delta t}{4\beta\omega(\omega-ck)} \tag{D.16}$$

Where $|\delta|$ is the amplitude of the divergence anomaly. This increase in energy leads to an increase in the wave amplitude:

$$\Delta v_0 = \frac{Bc^3|\delta|\Delta t(\omega-ck)}{2H\omega[c(ck^2+\beta)-2ck+\omega^2]}. \tag{D.17}$$

As the divergence of the MRG wave is:

$$\delta = \frac{v_0\omega\beta}{c^2k-c\omega}ye^{-\left(\frac{\beta y^2}{2c}\right)}\cos(kx-\omega t), \tag{D.18}$$

the magnitude of the divergence is:

$$|\delta| = \frac{v_0 \omega \beta}{\omega^2 - c^2 k} \tag{D.19}$$

(note the change of sign, so that the magnitude of the divergence is positive, simplifying the interpretation).

Thus,

$$\frac{\Delta|\delta|}{\Delta t} = \frac{Bc}{2H}|\delta|\left[\frac{c\beta}{c(ck^2+\beta)-2ck\omega+\omega^2}\right] = \frac{Bc}{2H}|\delta|\frac{\beta}{2\beta \mp \frac{k^2 c}{2}\left(\mp 1+\sqrt{1+\frac{4\beta}{k^2 c}}\right)}, \tag{D.20}$$

where the upper sign applies for positive wavenumber and the lower sign applies for negative wavenumbers.

D.3 Equatorial Rossby and inertia-gravity wave heating divergence feedback

A similar analysis for the $n = 1$ Equatorial Rossby and inertia-gravity waves yields:

$$\frac{\Delta|\delta|}{\Delta t} = \frac{Bc}{2H}|\delta|\frac{c\left(3c^2k^2+2ck\omega_{n=1}+3\omega_{n=1}^2\right)}{c^4k^4+3c^3k^2\beta+3c\beta\omega_{n=1}^2+\omega_{n=1}^4+2c^2k\omega_{n=1}(\beta-k\omega)}, \tag{D.21}$$

where

$$\omega_n \approx \left(-\frac{\beta k}{k^2+3\frac{\beta}{c}}, \sqrt{k^2c^2+3\beta c}\right) \tag{D.22}$$

for the Rossby and IG waves respectively (see, e.g., Gill 1982), obtained from the dispersion relationship

$$\left(\frac{\omega}{c}\right)^2 - k^2 - \frac{\beta k}{\omega} = \frac{3\beta}{c} \tag{D.23}$$

by ignoring the first and last terms on the left hand side, respectively.

Appendix E Regression technique

To look at the structure of the MJO disturbances, we regress unfiltered model fields against the MJO filtered OLR field, with the following procedure:

1) Model OLR is filtered to the MJO spectral region ($1 \leq k \leq 3, 0.01/day \leq f \leq 0.05/\text{day}$), in the fashion of WK99, using a time-space Fourier transform followed by masking to the MJO region and then an inverse Fourier transform. The spectral region chosen is narrower than that used in WK99 in order to reduce the contamination of the MJO signal by the very strong extra-tropical waves.
2) The time variance of the filtered OLR is calculated at each point and we identify the latitude that has the largest zonal mean variance – all of the reference points will come from this latitude. The reference latitude for the mean state considered is 4.2^oN, the location resolved with the model closest to the peak SST.
3) We concatenate the filtered OLR time series for every point on the latitude chosen as our reference. This allows us to use the MJO from all parts of the globe to construct our regression improving the signal-to-noise, although it also introduces complications due to the various correlations in the fields.
4) The model fields are similarly concatenated into one long time series at each model point, appropriately circle shifted so that the spatial relationship with the reference points is maintained.
5) For each field of interest, at each spatial point in the model we estimate a regression coefficient, b – the slope of the model fields at that point versus

the reference MJO OLR time series – using standard least-squares linear regression (e.g. Wilks 2006).

6) We consider the regression results statistically significant at each point if the null hypothesis ($b = 0$) can be rejected at the 95% confidence level for that point. For this purpose, we calculate confidence ranges for the slopes, by estimating the standard deviation, σ, of the population the slope is drawn from (again, through the standard techniques of least-squares linear regressions e.g. Wilks 2006). As there are time and space correlations in the various fields, we estimate the effective number of degrees of freedom (or independent MJO events) to be ~35000. This accounts for both the time correlations at each point and the spatial correlations between neighboring point's time series. We base this estimate upon observations of a correlation time of approximately 4 days and correlation length of approximately 8 degrees in the unfiltered fields such as zonal wind. We have also made estimates using the larger correlations in the filtered fields; this has little impact on the results that we present. We assume that the population of slopes has a Gaussian distribution, then the 95% confidence interval spans a region almost two standard deviations from the slope b:

$$b_{range} = b \pm 1.92 \times \sigma \qquad \text{(E.1)}$$

Points where the null hypothesis cannot be sufficiently rejected are discarded.

7) The regression coefficients that pass the significance test are multiplied by a typical OLR peak anomaly (-40W/m^2), to give the magnitudes of the field anomalies associated with an MJO event.

This regression technique focuses on the mature phase of the MJO-like disturbance, which is, due to the zonal symmetry, the dominant phase in our model. The relationships between the model fields and the disturbance could be quite different during the initiation and decay phases of the disturbance.

Appendix F Effect of surface pressure variations on the MSE budget

In chapter 3, we neglected variations in surface pressure upon the column MSE budget. In this section, we will discuss the influence of this term upon the budget. The surface pressure comes into the budget via a more accurate evaluation of the column integral of the MSE tendency:

$$\partial_t \int_{P_{top}}^{P_{surface}} h\, dp = \int_{P_{t\square p}}^{P_{surface}} \partial_t h\, dp + h_{surface}\partial_t P_{surface} - h_{top}\partial_t P_{top} \quad \text{(F.1)}$$

The top-level pressure is effectively constant, as the hybrid level scheme of the model used is almost exactly isobaric at the upper levels (Collins *et al.*, 2004), but the surface pressure varies quite considerably as an MJO anomaly passes above. This extra term can be considered a correction to the calculated residual (here referred to as Res_1, as shown:

$$\partial_t \int_{P_{top}}^{P_{\square urface}} h\, dp - \langle \text{budget} \rangle = Res_1 \quad \text{(F.2)}$$

Now, the budget term (the sum of the individual sources and sinks described above) is effectively the column integral of the MSE tendency:

$$\langle \text{budget} \rangle \approx \int_{P_{top}}^{P_{surface}} \partial_t h dp \quad \text{(F.3)}$$

Then, from (F.1), we have:

$$\partial_t \int_{P_{top}}^{P_{surface}} h\, dp - \langle budget \rangle - h_{surface}\partial_t P_{surface} = Res_2 \quad \text{(F.4)}$$

Thus,

$$Res_2 = Res_1 - h_{surface}\partial_t P_{surface} \quad \text{(F.5)}$$

This correction generally reduces the residual, as shown in figure F-1, where the change in residual for the narrowest case (from chapter 4) is evaluated with and

without the surface pressure correction. The difference between the residuals is small, especially in the tropics, but the residual is reduced in size in most of the tropics.

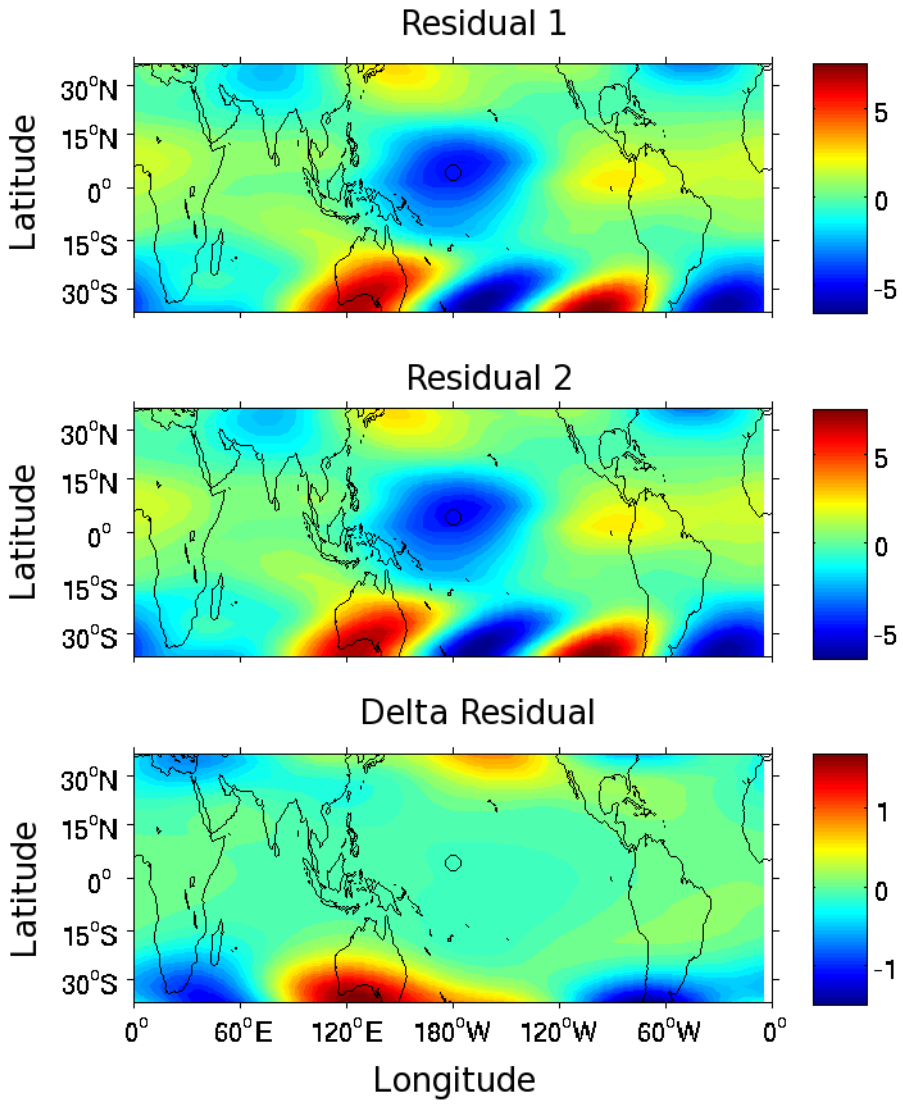

Figure F-1. MJO-regressed residual for the narrowest case (from Chapter 4). A) Residual ignoring variations in surface pressure; b) residual accounting for surface pressure variations; c) change in residual.

Appendix G Boundaries of integration for the budget bar-chart calculations.

The bar charts are calculated by taking integrals over a region of the tropics. We have chosen to define the tropics for this calculation as extending from 6.5^oS to 12.5^oN. This is a somewhat arbitrary choice, but we justify it based upon the following observation:

The barcharts have been calculated for the control and narrowest SST experiments used in chapter four, over a varying range of boundaries. In figure G-1, we show the accumulated results of a number of calculations. In this figure, the southern boundary is held at 12.5^oS, while the northern boundary is stepped from 17.5^oN to the equator with jumps of 2.5 degrees.

As can be seen, the budget bars are relatively insensitive to the precise northern boundary, until it is brought quite close to the equator – around 5^oN.

Figure G-2 is similar; although in this case the northern boundary is kept at 12.5^oN while the southern boundary is stepped form 12.5^oS to 5^oN, in 2.5 degree jumps. Again, the budget values are relatively insensitive to the motion of the boundary until the boundary approaches the equator.

Figures G-3 and G-4 repeat the above calculations upon the (-3,+1) experiment, with similar results.

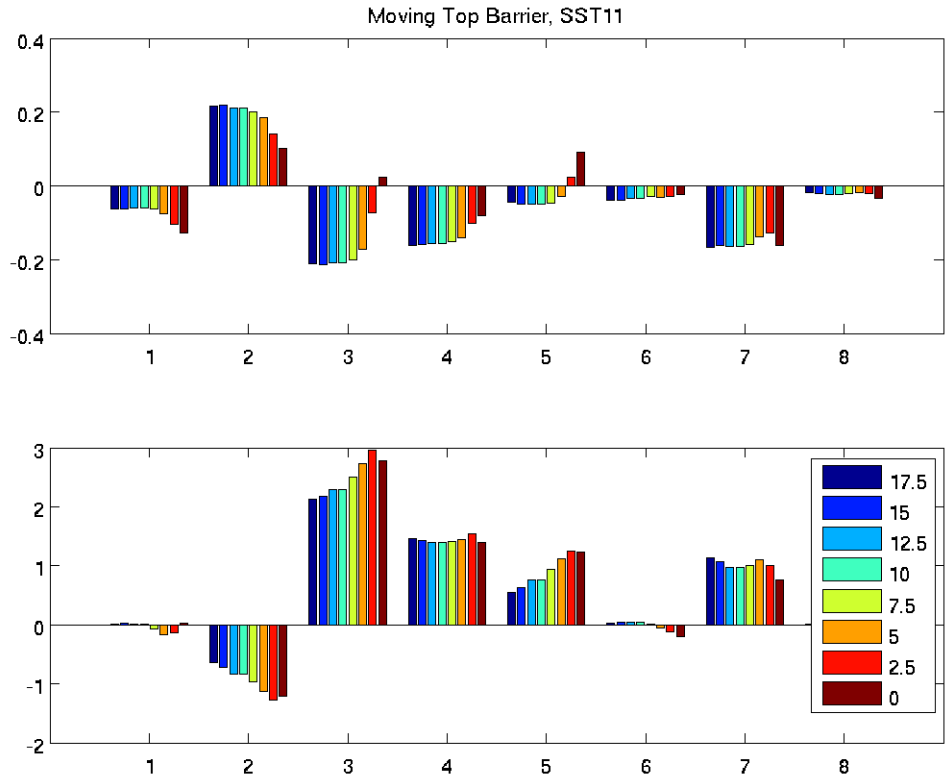

Figure G-1. Contributions due to various terms towards the (a) maintenance and (b) propagation of the MJO anomaly in the control experiment. The contributions are calculated for the region extending from $\mathbf{6.5^{o}S}$ to the northerly latitudes given in the legend. The budget terms shown correspond to: 1) $\boldsymbol{\partial_t \langle h \rangle}$; 2) $\boldsymbol{\langle LW \rangle}$; 3) $\boldsymbol{\langle v \cdot \nabla h \rangle}$; 4) $\boldsymbol{\langle v \cdot \nabla h \rangle_H}$; 5) $\boldsymbol{\langle \omega \partial_p h \rangle}$; 6) $\boldsymbol{\langle u \, \partial_x h \rangle}$; 7) $\boldsymbol{\langle v \partial_y h \rangle}$; 8) residual.

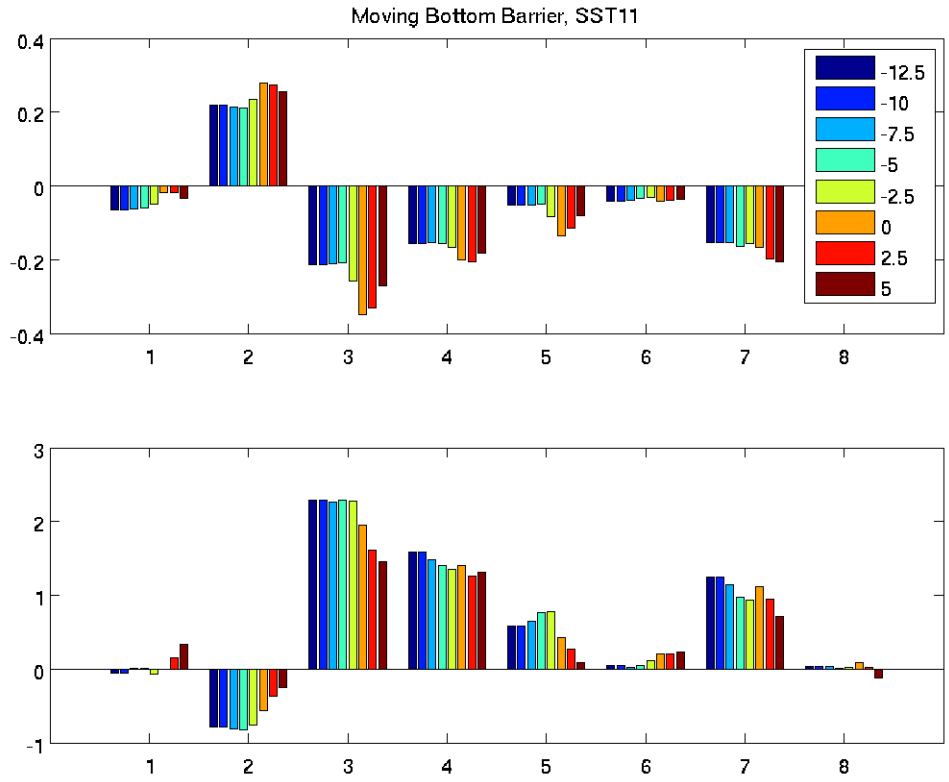

Figure G-2 Contributions due to various terms towards the (a) maintenance and (b) propagation of the MJO anomaly in the control experiment. The contributions are calculated for the region extending from $\mathbf{12.5}^{o}$N to the southerly latitudes given in the legend.

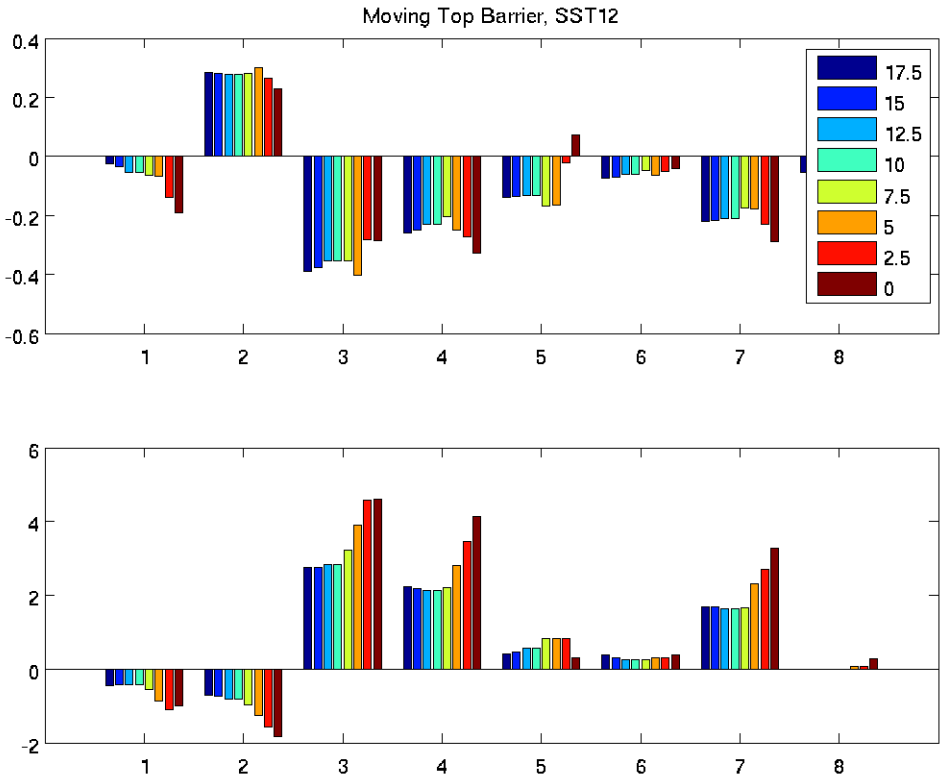

Figure G-3 As Figure G-2, but for the (-3,+1) case.

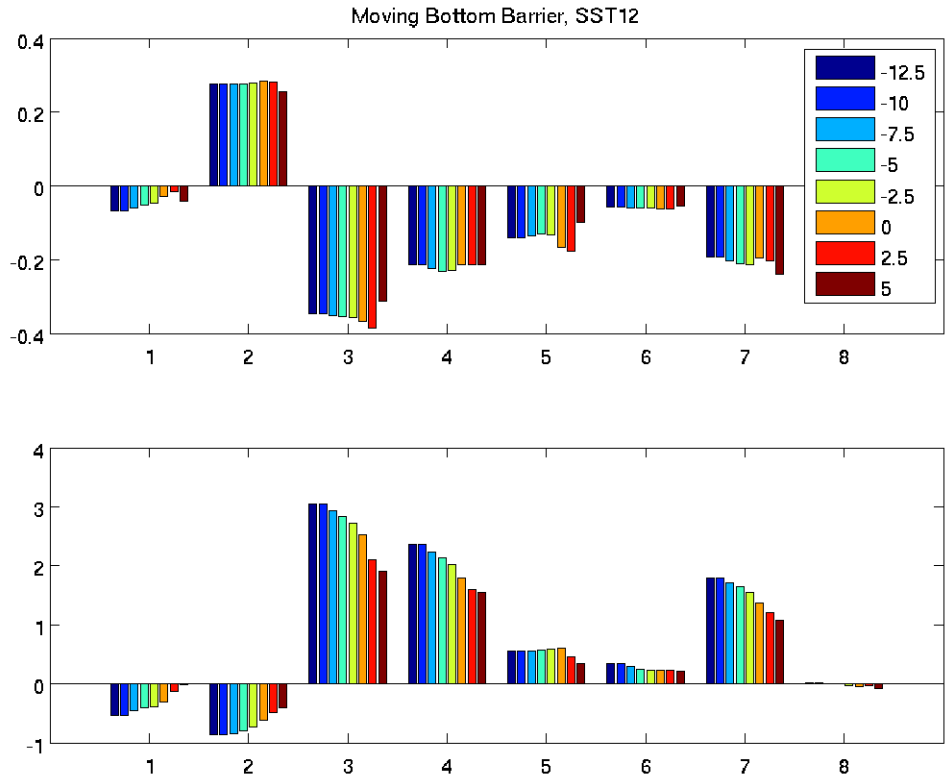

Figure G-4. As figure G-3, for the (-3,+1) case.

Appendix H – Brief Investigations of other terms within the MSE budget

There are many differences in the projected budget terms between the various cases investigated in Chapter 4. However, the details of these terms are generally beyond the scope of this project (other than the horizontal advection term, which dominates the results discussed in that chapter). In this appendix, we present a brief, initial, investigation of these terms.

H anomaly projection

The projection of latent heat onto the MSE anomaly increases slightly from the broadest case to the second narrowest. The latent heat for the narrowest (-3,+1) case acts as a significantly smaller sink.

Comparing the regressed LHF profile of this case to the control case (figure H-1) we can see that, one major difference between these two cases is the zonal phase of the LHF anomaly just to the south of the equator. For example, in the control case the negative anomaly extends as far west as about $130^{o}E$, while in the narrow SST case, the anomaly is located east of $180^{o}W$. These shifted anomalies dominate the difference between the two projections, even with the slight shifting of the MSE anomalies to the west in the same region. This can be seen by calculating the spatial overlap between (for example) the control MSE anomaly and the (-3,+1) LH anomaly; which is approximately equal to the overlap calculated when both anomalies are taken from the (-3,+1) case (not shown). The shift in the MSE does not significantly compensate for the change in LHF.

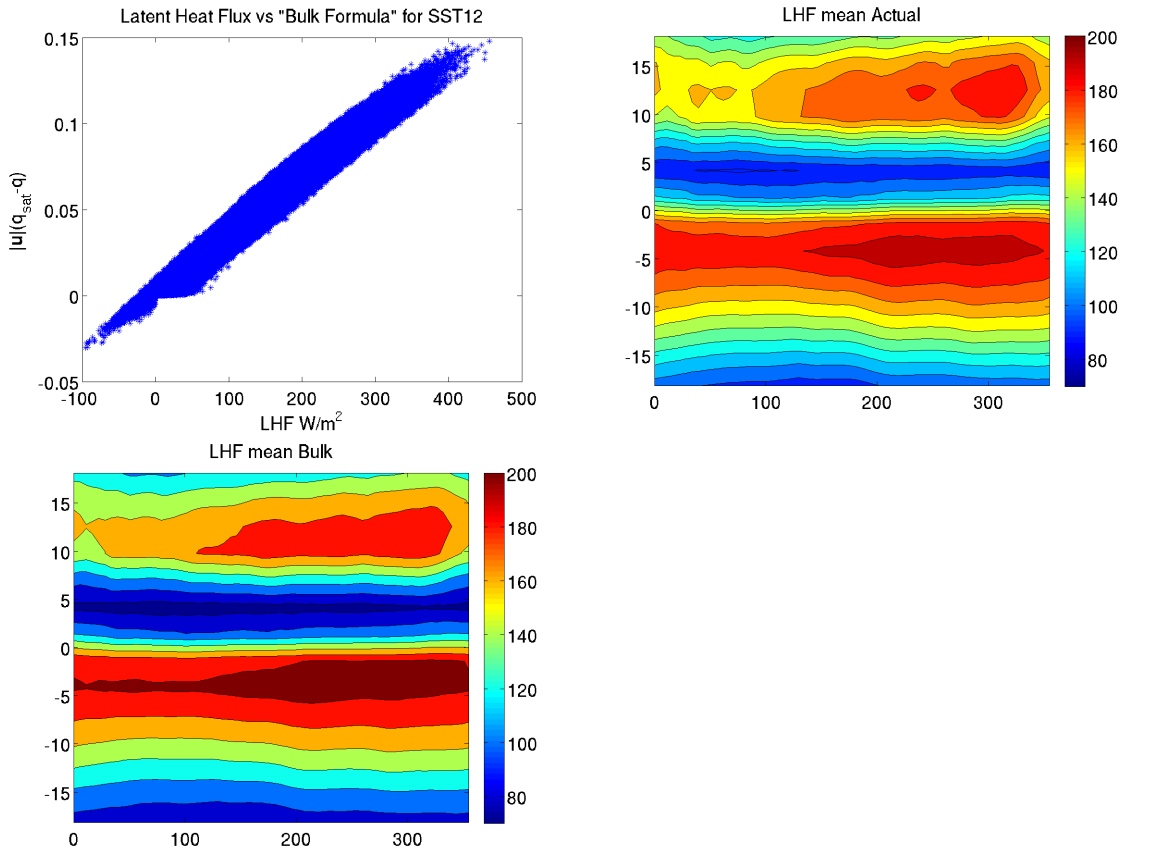

Figure H-1. Evaluation of the bulk surface flux approximation in the (-3,+1) case. a) the "bulk flux" evaluated from the model fields plotted against the model output latent heat flux; b) the time mean model latent heat flux ("actual"); c) the "bulk" approximation to the "actual" flux, using the numerical constant that minimizes the total difference between the "bulk" and "actual" values.

We can understand the very different LHF profiles in the narrowest case by examining the various terms that contribute to this flux. Beginning by making the bulk surface flux approximation, we have:

$$LHF_{bulk} = C|\boldsymbol{u}|(q_{sat} - q_{sfc}), \quad \text{(H.1)}$$

where $|\boldsymbol{u}|$ is the surface wind speed, q_{sat} is the saturation vapor mixing ratio corresponding to the surface pressure and the SST, and q_{sfc} is the actual vapor mixing ratio at the surface. C is a constant, which we can estimate by minimizing the difference between the modeled time-zonal mean LHF and LHF_{bulk}. In figure H-2a we plot the bulk LHF (with C set to unity) against the modeled LHF values for a representative month of the model. C is estimated to be 2844 $Wm^{-3}s\left(\frac{kg}{\text{kg}}\right)$. As can be seen, the bulk approximation is a reasonably good fit for the modeled flux. In figure H-2b and c, we show the time mean LHF for the bulk approximation and model, which are in reasonable agreement. As in section 3.3.C, the flux anomalies (figure H-3a) can be linearly approximated by a sum of flux anomalies due to the various anomalies in the dynamic fields associated with the MJO:

$$\Delta LHF \approx C\Delta\,\overrightarrow{|u|}\,(q_{sat} - q_{sfc}) - C\,\overrightarrow{|u|}\,(\Delta q_{sfc}) + C\,\overrightarrow{|u|}\,(\Delta q_{sat}), \quad \text{(H.2)}$$

The first term on the right is the anomaly due to the changed wind speed as the MJO passes (figure H-3b); the second term is the flux anomaly due to the change in moisture as the MJO passes (figure H-3c); and the last term is the anomaly due to the change in surface saturation humidity due to the surface pressure anomalies of the MJO which is negligible compared to the other terms (figure H-3d). In figure H-

3e, we show the sum of these three terms, which can be seen to be a good approximation to the actual LHF anomaly.

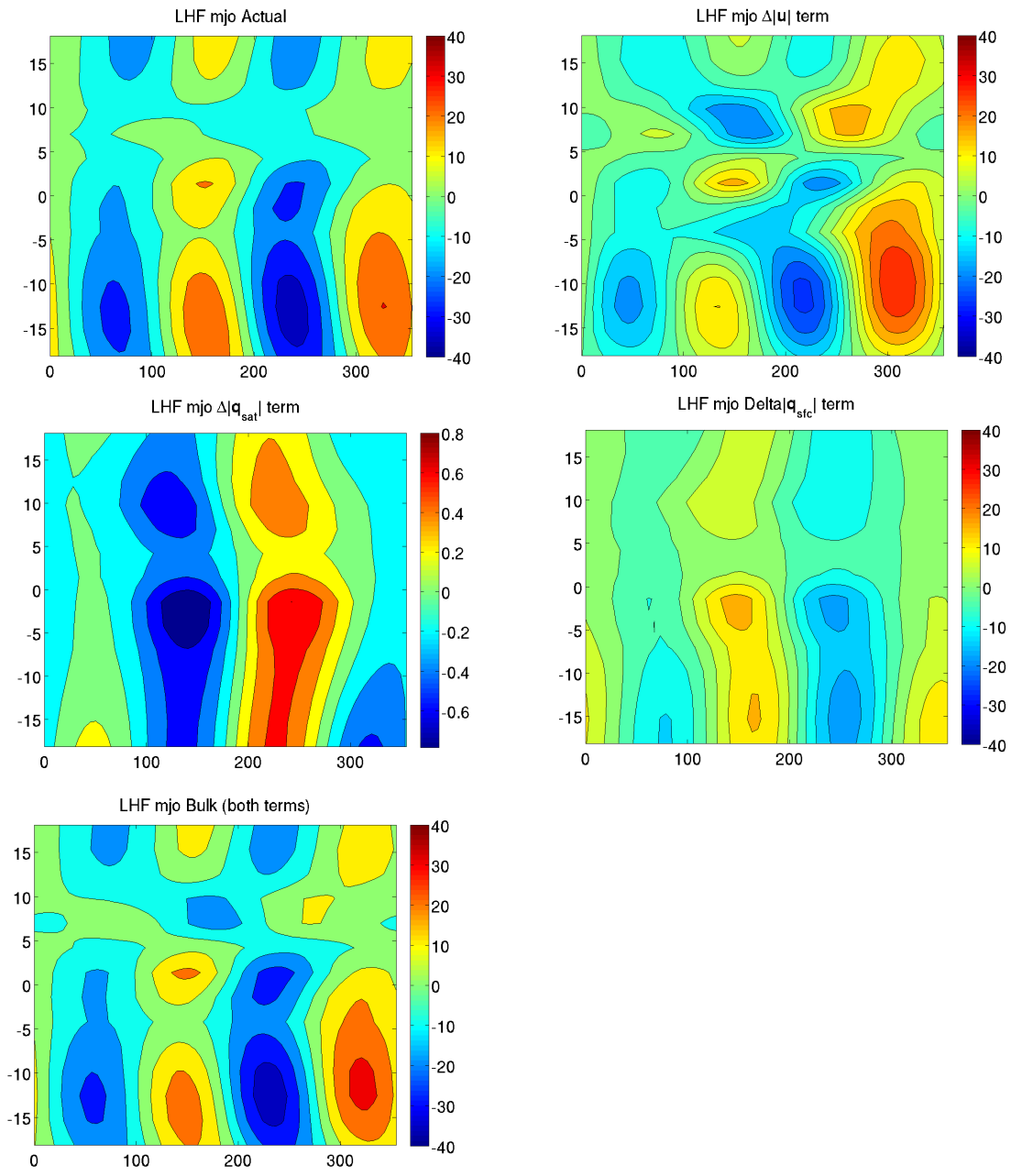

Figure H-2. MJO regressed surface flux for the (-3,+1) case: a) the "actual" flux anomaly; b) the flux anomaly in the bulk approximation due to MJO regressed changes in surface wind speed; c) flux anomalies due to MJO regressed surface saturation pressure anomalies; d) flux anomalies resulting from MJO moisture

anomalies near the surface; e) total MJO regressed “bulk” flux anomaly.

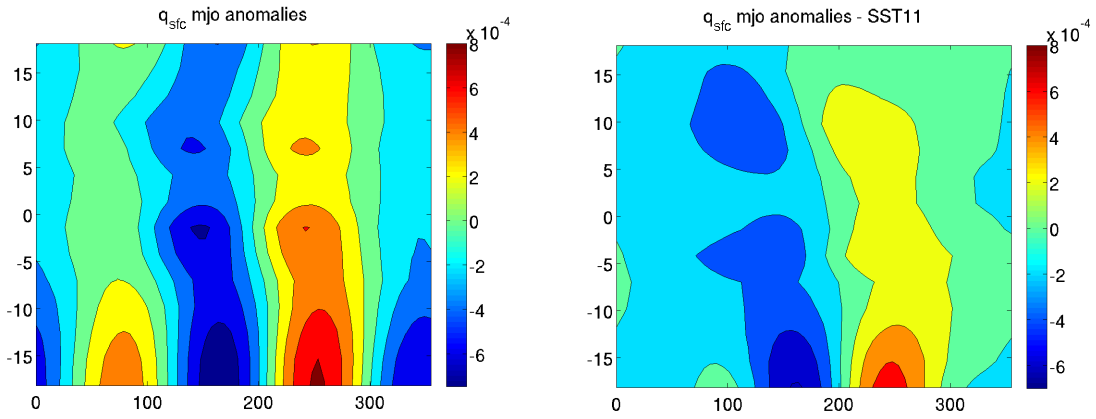

Figure H-3. MJO regressed surface moisture anomalies in the narrow (left) and control (right) experiments.

Just as was seen for the control case, the surface latent heat flux anomaly of the MJO is not purely determined by the wind speed anomaly. Instead, the moisture anomalies are seen to play an important role in setting the flux values as well. Comparing the various terms in the decomposition of the LHF between the narrow and control cases (figure 3.9), we can see that the wind speed driven anomalies are quite similar, while the moisture anomaly term is significantly stronger in the narrow case. We can further show that, despite the differences in the mean wind speeds between the two models (figure H-3c), the differences in the LHF flux is primarily due to differences in the low-level moisture anomalies between the two cases. This is demonstrated in figure H-4, comparing the MJO regressed near surface moisture anomalies in the narrow (figure H-4a) and the control (figure H-4b) cases. The moisture anomalies are significantly stronger in the Narrow case, due to the increased meridional MSE (and hence moisture) gradient in that case.

The other cases show a similar dependence of the moisture anomalies upon the meridional gradient although, like the control case, the broad and the second narrowest cases' LHF are more strongly determined by the wind speed anomalies and have thus a similar behavior to the control case. The small trend observed – an increase in the sink of MSE from broad to narrow is caused by a slight decrease of the amplitude of the moisture anomalies in these regions (not shown), reducing the amount the sink due to the wind-speed anomalies is offset.

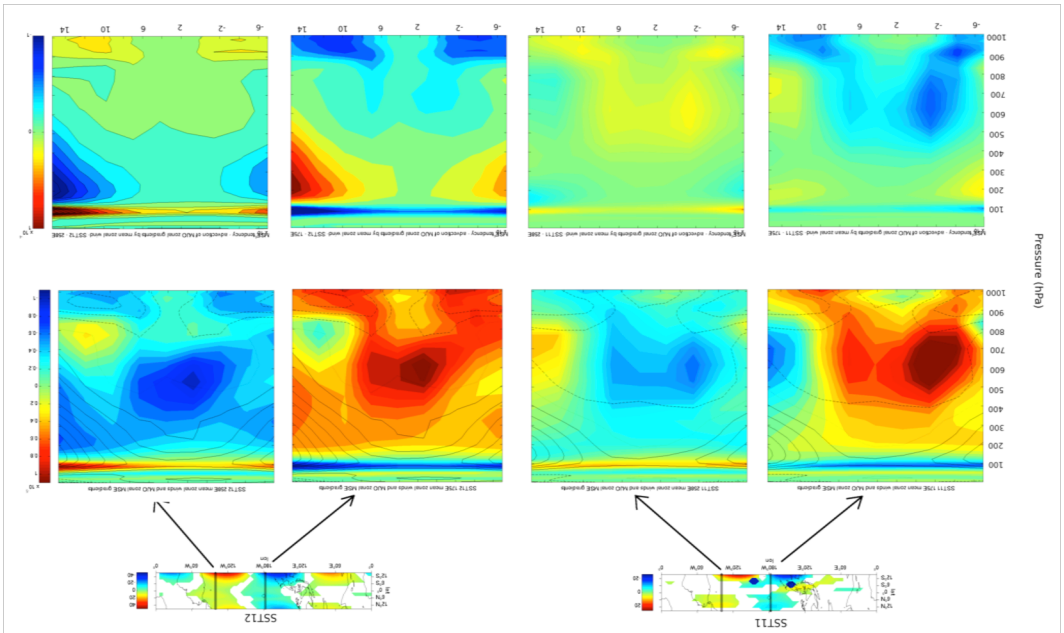

Figure H-4. Comparison of zonal advection terms for the control (control; left columns) and narrowest (-3,+1; right columns) cases. Column-integrated, MJO regressed zonal advection MSE tendencies (top row); Vertical-Meridional cross-sections of MJO regressed MSE anomalies (colors) and time-zonal-averaged zonal winds (contoured, negative dashed, zero contour dotted; middle row); and Vertical-Meridional cross-sections of the MSE tendencies resulting from advection of MJO MSE anomalies by the time-zonal mean wind. Cross-sections are shown at $\mathbf{175^{o}}$E (left sub-columns) and $\mathbf{258^{o}}$E (right sub-columns).

The longwave forcing acts as a source of MSE in all case. The size of the source is roughly constant for all but the narrowest case, for which the source is somewhat larger. As the longwave anomalies are similar for all the cases (e.g. figure H-5e and f), the difference between the LW projections must come mostly from the differences in the MSE profile. The most striking difference between control and (-3,+1) cases that is relevant to the LW term appears to be the Southern Hemisphere MSE signal in the control case, which extends a significant distance to the east, in to the region of suppressed convection. This acts as a sink of MSE, reducing the total source for the control case (and for the other cases). This southern hemisphere MSE anomaly is much smaller in the (-3,+1) case and it does not stretch into the region of suppressed convection. Thus, the (-3,+1) case is not subject to the sink of MSE in the region ahead of the main convection and so has a stronger overall LW source.

The total advection is a sink of energy that is roughly constant between the experiments, apart from the narrowest case, where the sink is significantly stronger. Again, the sink in the broader cases is reduced because of the extension of the MSE anomaly to the east, leading to a region of positive overlap between the MSE anomaly and the advection term, which somewhat reduces the net sink.

The horizontal advection term decreases in amplitude from the broad case to the second narrowest case, but the narrowest case shows the strongest sink. The strength of the narrowest case's sink is enhanced for the same reason as the total advection – The lack of strong eastward projection of the anomalies. The increased sink for the broad experiment relative to the control in this term appears to be due to an eastward phase shift of the broad case's horizontal advection term, leading to a

larger negative overlap with the MSE anomaly. Conversely, the (-1.5,-0.5) case has a westward phase shift to the advection term, leading to a smaller negative overlap. This shift is even larger in the (-3,+1) case, although the reduction in the sink in that case is vastly outweighed by the increase in the sink discussed above.

As can be seen, the sink due to vertical advection increases as the SST profile becomes narrower, apart from the broadest case, where the sink is stronger, lying between that of the control and the next narrowest cases. The regressed vertical advection profiles show the vertical advection anomaly moving from south to north as the MSE gradient shifts due to the narrowing of the MSE profile - as the SST gets narrower. This increases the negative overlap between the sink due to vertical advection and the MSE anomaly. In the broadest case, the overlap between the northern hemisphere MSE anomaly is less, but the vertical advection region is sufficiently far to the south that the overlap with the southern lobe of the MSE anomaly is increased, leading to the slight strengthening of the sink relative to the control that is observed.

The horizontal advection can be further broken into zonal and meridional components. The zonal parts are small and roughly equal, apart from the narrowest case. The smallness of this term is due to the zonal advection being generally small. In figure H-5, we compare the zonal advection terms for the control and narrowest cases. The column-integrated tendency is clearly stronger in the narrower case, which can be seen to be due to the increased MJO regressed MSE anomalies in the boundary layer on the edges of the ITCZ region (roughly 6^oS-2^oS and 6^oN-14^oN), which are the strongest zonal gradients that are co-located with strong time-zonal-

mean zonal winds. The advection tendency due to this combination of winds and gradients are also shown, demonstrating that these regions are the dominant terms. Advection by the sub-tropical jets also forms a large signal in the narrowest case; however this tendency is largely outside the region of interest for the budget projections.

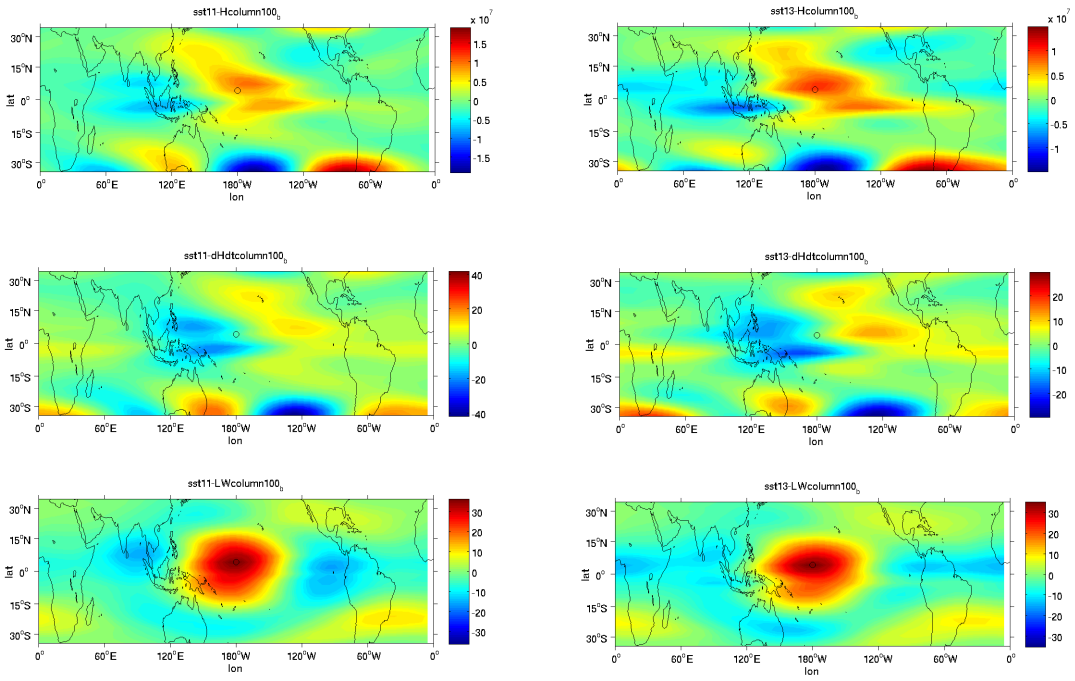

Figure H-5. Regressed budget terms for the MJO for the control (left) and the broad (right) cases. Shown are the column-integrated MSE anomaly ($\langle h \rangle$, top row); the MSE anomaly tendency (middle row); and the column-integrated Long-Wave heating anomaly ($\langle LW \rangle$, bottom row);

The larger MSE anomalies in the low levels of the narrowest case stem directly from the shape of the SST distribution (and the resulting low-level time-mean MSE distribution). The greater meridional gradient of MSE in this region in the narrower case leads to stronger meridional advection of MSE by the MJO meridional winds, which creates larger MSE anomalies near the edges of the ITCZ in this case.

The shortwave and sensible heat terms are trivial and not shown. The residual is also small, although it is shown for completeness.

The total advection term increases monotonically from broadest to narrowest, which can be seen to be dominated by the horizontal advection term, which increases strongly from the broad case to the narrowest case. Vertical advection is roughly constant, although the narrowest case is somewhat weaker than the others.

The zonal advection term is almost zero.

The horizontal advection term is almost entirely due to the meridional advection, which also increases monotonically from broadest to narrowest. This is largely caused by an increase in the magnitude of this term, which increases as the SST gets narrower, as the phase difference between the advection term and the MSE tendency anomaly is small and remains quite constant between the cases examined.

The shortwave and sensible heat terms are again trivial and not shown. The residual is also small, although it is shown for completeness.

H tendency projection

The latent heat projects weakly onto the MSE tendency. Apart from the narrowest

case, where it constitutes a strong retarding factor upon the anomaly's propagation. This is due to the same difference in shape of the LHF anomaly in the (-3,+1) case, as discussed above. In this case, the positive flux anomaly in the 6^oS, $120^oE - 180^oE$ region act against the MSE tendency in a way that is not observed in the other cases that all have negative anomalies in this region.

The long wave term is consistently a retarding factor, which increases in magnitude from the broadest to the second narrowest case. This is due to the phase shift of the LW anomaly relative to the convective center for these cases – in the broadest case, the tendency is shifted to the west, decreasing the negative overlap with the LW term. The reverse is true for the (-1.5,-0.5) case.

However, the narrowest case is a weaker retardation that the other cases (except the broadest) because, in much the same way as discussed above, the MSE anomaly (and its tendency) in the (-3,+1) case is primarily in the northern hemisphere, while the LW heating is much more symmetric abut the equator. The reduction in overlap between this term and the tendency, reducing the retarding effect in this case. The tendency is also phase shifted to the east in this case, however the increase in negative overlap due to this shift is outweighed by the general reduction in overlap.

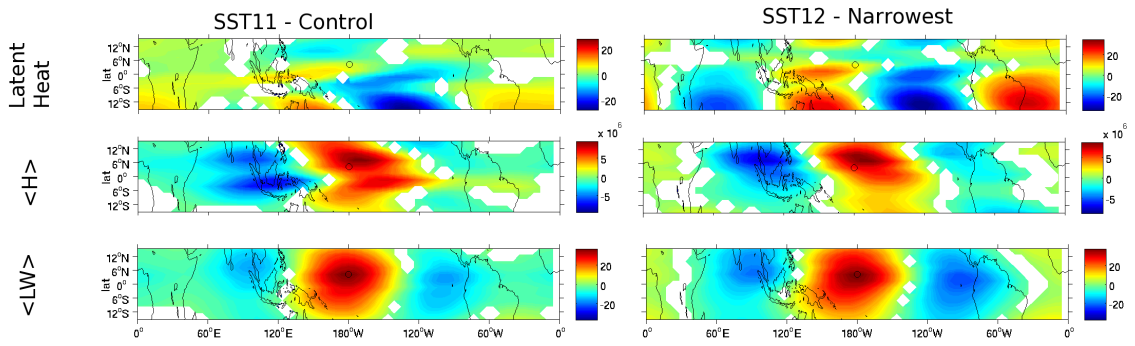

Figure H-6. Regressed budget terms for the MJO for the control (left) and the narrowest (right) cases. Shown are the Latent Heat Flux anomalies (LH, top row); column-integrated MSE anomaly ($\langle \boldsymbol{h} \rangle$, middle row); and the column-integrated Long-Wave heating anomaly ($\langle \boldsymbol{LW} \rangle$, bottom row);

Appendix I - Effect of the choice of 20 days as cutoff timescale

As pointed out in Chapter 4, we have made the arbitrary choice of 20 days as the cut-off between the "high frequency" and the "MJO" frequency bands. In order to investigate the effect of other possible choices, we have repeated the calculations with cut-offs of 14.2 and 30 day periods – corresponding to the MJO frequencies of the narrowest (-3,+1) case's MJO and the values used for the original analysis of the control case in chapter 3. The results are shown in figures I-1 and I-2 respectively. As the cut-off time scale is decreased to accommodate the higher MJO frequency in the narrowest case, the eddy-mean term in the propagation contribution for that case decreases in amplitude and the MJO-mean term increases. This indicates that the "eddy-mean" advection term for the narrowest experiment observed in Chapter 4 is primarily due to the higher frequency parts of the MJO in that experiment, which are projected into the eddy frequency regime by the choice of cut-off. Similarly, when we increase the cut-off time scale to 30 days to match the values used in Chapter 3, we see the tendency contribution for the narrowest experiment is now dominated by "eddy-mean" while the "eddy-eddy" term becomes more important for the control case, as observed in Chapter 3.

The choice of 20 days as the time-scale for the cutoff between MJO and eddy activity is arbitrary, and represents a compromise between the various MJO frequencies observed in the different experiments. An analysis with the cut-off tuned specifically for each experiment may be easier to interpret in some ways – however a fixed cut-off seems over-all a more defendable choice.

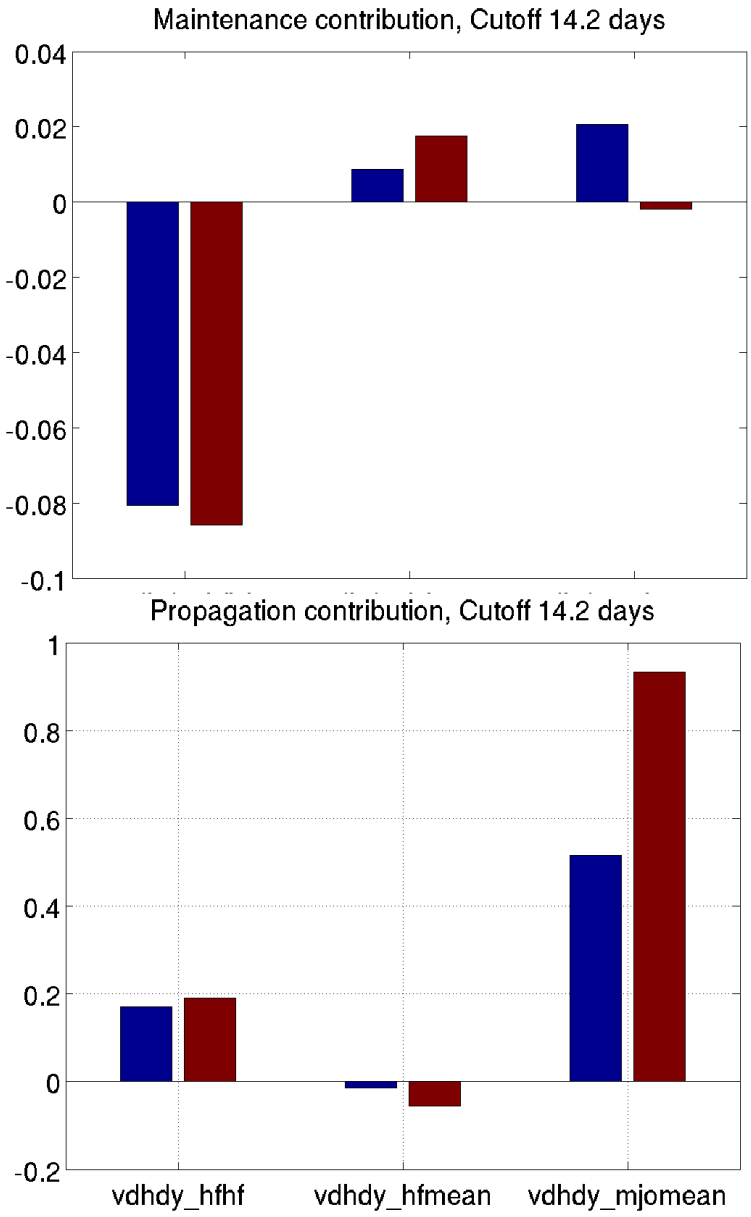

Figure I-1. As figure 4-9, except with "*hf*" defined as faster than 14.2 day period signals (and only for the control and narrowest experiments), to accommodate the higher frequency of the MJO in the narrowest case.

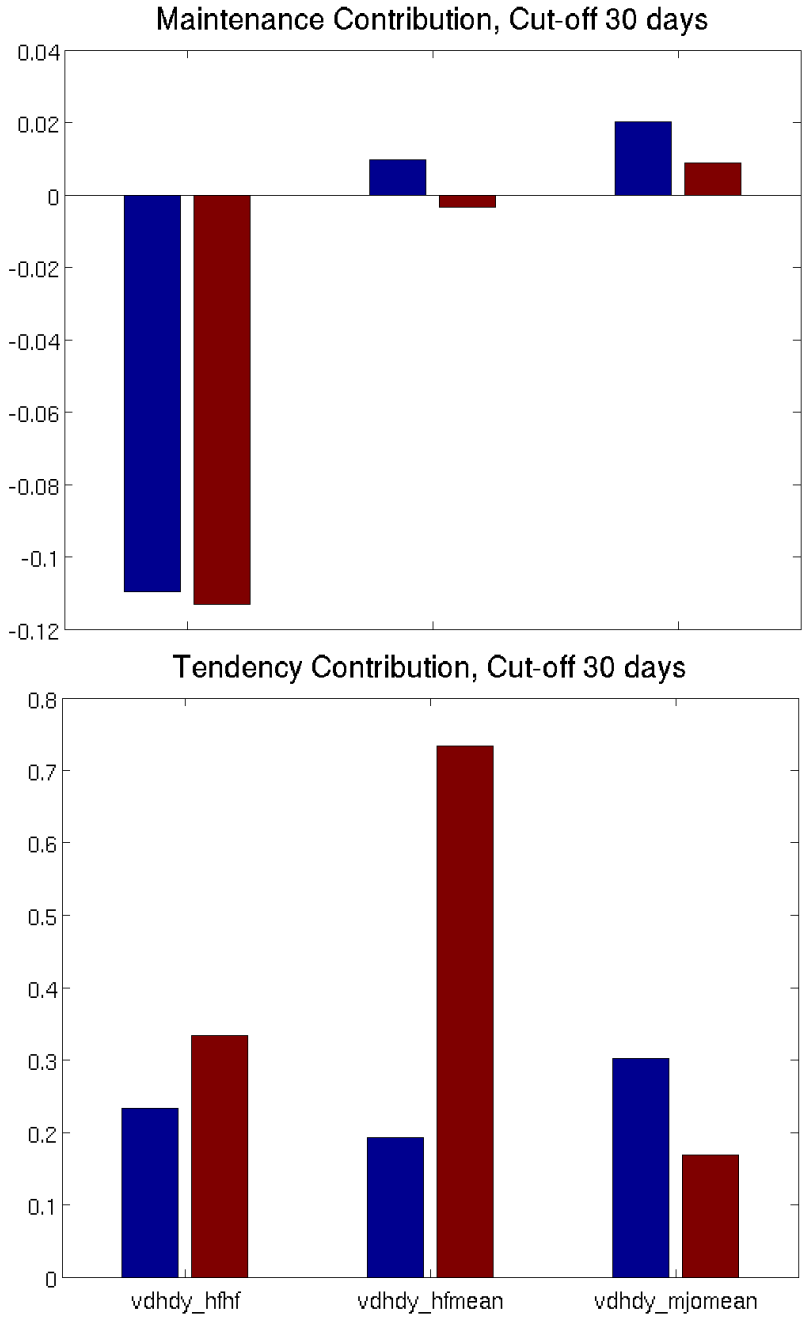

Figure I-2 As figure 4-9, except with "*hf*" defined as faster than 30 day period signals (and only for the control and narrowest experiments), to accommodate the lower frequency of the MJO in the control case.

Appendix J – A different estimate of the phase speeds.

Spectral Weighted Average

In order to quantify the phase speed changes observed in the above spectra, we calculate a power-weighted average phase speed of the MJO-like anomalies in the simulations. This is done by defining an MJO box in spectral space, such that

$$0 < k < 4 \;\&\; 0.01 < f < 0.05 \qquad \text{(J.1)}$$

The phase speed of an anomaly at each point is given by:

$$c_p = f\lambda = f/k \qquad \text{(J.2)}$$

In the units of the spectral figures, this gives a phase speed in circumferences per day, which is easily converted to meters per second.[3]

As an example, the average phase speed on the averaged raw spectrum of the control case (figure 3-2) is 8.6 m/s. However, the calculation is not linear, so it is not correct to take the phase speed of the average spectrum – instead we should take the average phase speed of the whole spectrum.

In the same manner as the initial calculation of the spectrum, we break the data into 90-day segments. To improve the identification of the MJO in all the experimental cases, rather than using the symmetric spectrum calculated over the tropics, we limit the spectrum to the Northern Hemisphere (where the ITCZ resides and the MJO variance is concentrated). This choice also renders the distinction between symmetric and anti-symmetric meaningless, so we use the whole precipitation field for the calculation.

[3] The choice of upper frequency limit somewhat underestimates the phase speed and amplitude of the faster MJO, as there is some power at frequencies above the cutoff for the narrow SST cases.

The phase speed is calculated on each segment's spectrum individually before being averaged across the set of segments. The average phase speed is seen to increase monotonically as the SST distribution becomes narrower. The differences in amplitude can also be quantified, by comparing the total power within the MJO box for the different cases. As can be seen, the narrower SST cases have a more active MJO than the control case, which in turn is more active than the broad case. The resulting phase speeds and amplitudes are given in Table J.1 (See also the histograms of phase speed and amplitude in figure J-1).

We also wish to quantify whether the differences are significant. However, as the distributions of phase speeds are not particularly Gaussian, we use the Wilcoxon-Mann-Whitney Rank Test to determine the probability, *p*, of any of the "experimental" distributions being samples of the same population as the control case. As also shown in Table J.1, the probabilities of each of the null hypotheses being true are very small[4]. This allows us to have confidence in our observation of the phase speed and amplitude trends.

[4] Apart from SST15's phase speed, which we can only say has a different median with about 90% confidence. However, a) the amplitudes are very significantly different; and b) the actual distributions of phase speeds are more different than the chosen test would imply.

TABLE J-1. Phase speed and amplitude variations of the MJO-like disturbance, as measured by the weighted average method.

SST Distribution	c_p *(m/s)*	p value (compared to control)	Mean Amplitude (Arb. Units)	p value (compared to control)
Narrowest (SST12)	9.21	3.7e-12	1.82	4.9e-47
Narrow (SST15)	8.57	0.096	1.38	2.8e-25
Control (SST11)	8.34	NA	1.00	NA
Broad (SST13)	7.91	9.8e-4	0.46	2.4e-58

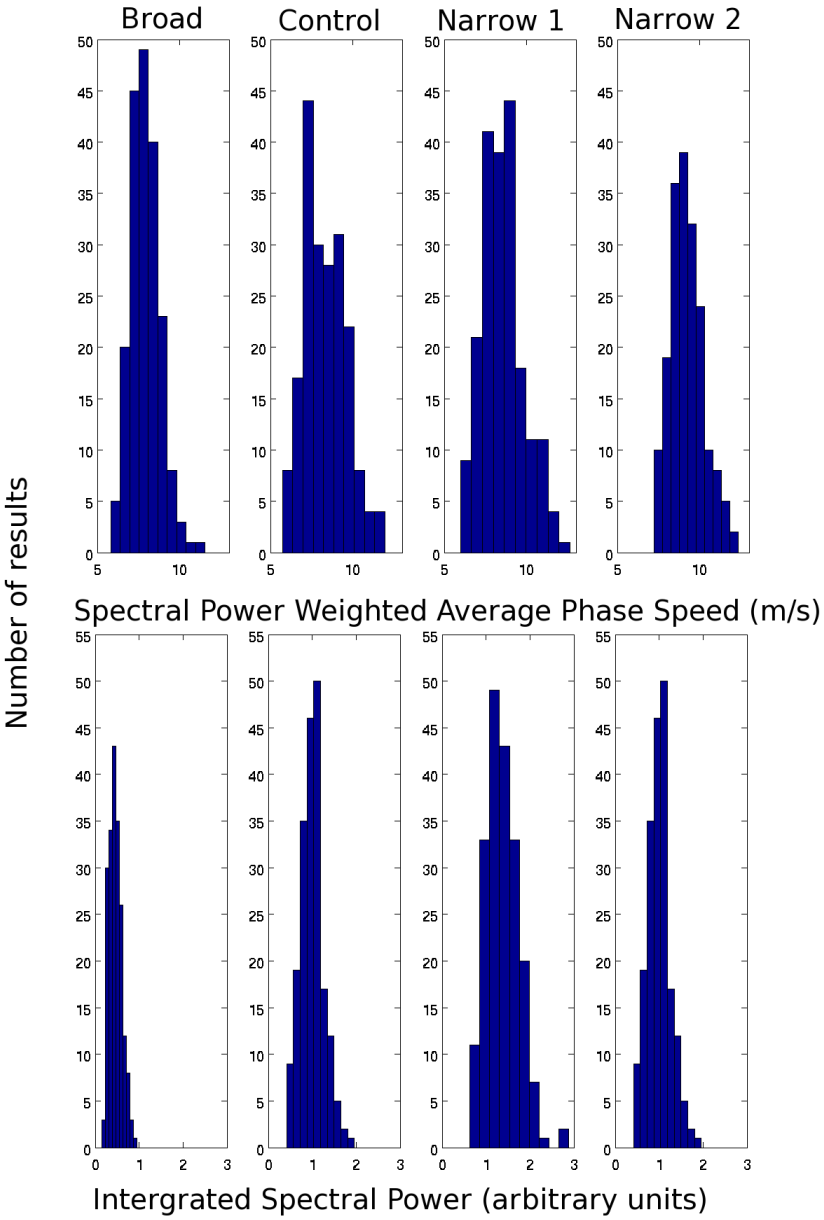

Figure J-1. The histograms of (top) spectral power weighted phase speeds and (bottom) integrated spectral power for the MJO-like anomaly in each experiment, calculated as a discussed in the text (see section 4.3.b) for 90 day windows.

Appendix K – Effect of the choice of Out Going Longwave Radiation as reference time series.

In this section, the choice of OLR as the reference time series for the linear regressions is investigated. The use of OLR may mean that the Longwave signal is particularly coherent, while other terms will be less coherent, which may artificially increase the contribution of the longwave heating relative to other terms. To test the influence of the selection of regression index, figure K-1 shows the budget projection for the control case when the MJO filtered precipitation as the regression index instead of OLR, as used in the other experiments within this document. Comparing figure K-1 to figure 4-7, we can see that the projections of the tendency terms onto the MSE anomaly and MSE tendency are essentially unchanged.

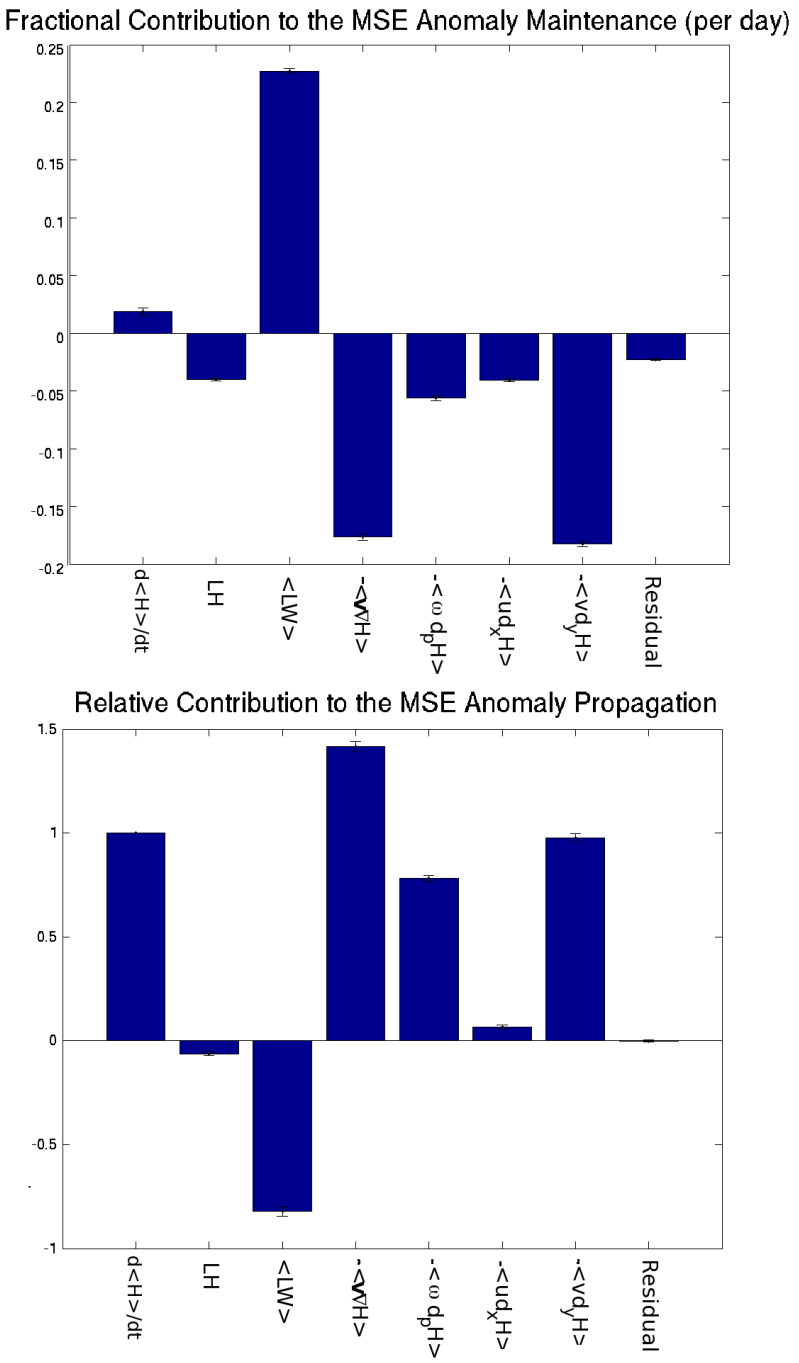

Figure K-1. As figure 4-7, for the control experiment only, using MJO filtered precipitation as the regression index.

References

Agudelo, P. A., J. A. Curry, C. D. Hoyos, and P. J. Webster, 2006: Transition between suppressed and active phases of intraseasonal oscillations in the Indo-Pacific warm pool. *J. Clima*te, **19**, 5519–5530.

Andersen, J. A. and Z. Kuang, 2008: A Toy Model of the Instability in the Equatorially Trapped Convectively Coupled Waves on the Equatorial Beta Plane, *J. Atmos. Sci*., **65**, 3736-3757.

Andersen, J. A. and Z. Kuang, 2012: Moist Static Energy Budget of MJO-like disturbances in the atmosphere of a zonally symmetric aquaplanet, *J. Climate*, **25**, 2782–2804, doi: 10.1175/JCLI-D-11-00168.1

Andersen, J. A. and Z. Kuang, 2012b: The sensitivity of propagation of the MJO-like anomaly observed in SPCAM to variations in the Aquaplanet Climate. In preparation.

Anyamba, E., E. Williams, J. Susskind, A. Fraser-Smith, and M. Fullekrug, 2000: The manifestation of the Madden-Julian Oscillation in global deep convection and in the Schumann resonance intensity, *J. Atmos. Sci*., **57**, 1029–1044.

Arakawa, A., and W. H. Schubert, 1974: Interaction of a cumulus cloud ensemble with the large-scale environment. Part I. *J. Atmos. Sci*., **31**, 674–701.

Araligidad, N. M., and E. D. Maloney, 2008: Wind-driven latent heat flux and the intraseasonal oscillation. *Geophys. Res. Lett.,* **35**, L04815.

Arkin, P. A., and P. E. Andanuy, 1989: Estimating climatic-scale precipitation from space: A review. *J. Climate*, **2**, 1229–1238.

Arnold, N. and E. Tziperman, 2012: Enhanced MJO-like Variability at High SST in Aquaplanet Simulations with a Super-Parameterized GCM. In preparation.

Back, L. E., and C. S. Bretherton, 2005: The relationship between wind speed and precipitation in the east Pacific ITCZ. *J. Climate*, **18**, 4317–4328.

Back, L. E., and C. S. Bretherton, 2006: Geographic variability in the export of moist static energy and vertical motion profiles in the tropical Pacific. *Geophys. Res. Lett.*, **33**, L17810.

Benedict, J., and D. A. Randall, 2007: Observed characteristics of the MJO relative to maximum rainfall. *J. Atmos. Sci*., **64**, 2332–2354.

Benedict, J., and D. A. Randall, 2009: Structure of the Madden-Julian Oscillation in the Superparameterized CAM. *J. Atmos. Sci.,* **66**, 3277—3296.

Blade, I., and D. L. Hartmann, 1993: Tropical intraseasonal oscillation in a simple nonlinear model, *J. Atmos. Sci.,* **50**, 2922– 2939.

Bond, N. A. and G. A. Vecchi, 2003: The Influence of the Madden–Julian Oscillation on Precipitation in Oregon and Washington. *Wea. Forecasting*, **18**, 600-613

Boos, W. R. and Z. Kuang, 2010: Mechanisms of poleward-propagating, intraseasonal convective anomalies in cloud-system resolving models. *J. Atmos. Sci*., **67**, 3673-3691.

Bretherton, C. S., 2003: Wave-CISK. Encyclopedia of Atmospheric Sciences, J. R. Holton, J. A. Pyle, and J. Curry, Eds., Elsevier, 1019–1021.

Bretherton, C. S., M. E. Peters, and L. E. Back, 2004: Relationships between water vapor path and precipitable water over the tropical oceans. *J. Climate*, **17**, 1517–1528.

Brown, R. G., and C. S. Bretherton, 1995: Tropical wave instabilities: Convective interaction with dynamics using the Emanuel cumulus parameterization. *J. Atmos. Sci.,* **52**, 67–82.

Brown, R. G., and C. Zhang, 1997: Variability of midtropospheric moisture and its effect on cloud-top height distribution during TOGA COARE. *J. Atmos. Sci*., **54**, 2760—2774

Byron, F. W., and R. W. Fuller, 1969: Mathematics of Classical and Quantum Physics. Dover, New York.

Chang, C. P., 1970: Westward-propagating cloud patterns in the tropical Pacific as seen from time-composite satellite photographs. *J. Atmos. Sci.*, **27**:133–138.

Collins, W. D., P. J. Rasch, and Others, Description of the NCAR Community Atmosphere Model (CAM 3.0), Technical Report NCAR/TN-464+STR, National Center for Atmospheric Research, Boulder, Colorado, **210** pp., 2004.

Derbyshire, S. H., I. Beau, P. Bechtold, J. -Y. Grandpeix, J. -M. Piriou, J. -L. Redelsperger, and P. M. M. Soares, 2004. Sensitivity of moist convection to environmental humidity. *Q. J. R. M. S.,* **130**, 3055--3079.

Emanuel, K. A., 1987: An air-sea interaction model of intraseasonal oscillations in the tropics, *J. Atmos. Sci*., **44**, 2324–2340.

Emanuel, K. A., 1993: The effect of convective response time on WISHE modes. *J. Atmos. Sci.,* **50**, 1763–1775.

Emanuel, K. A., J. D. Neelin, and C. S. Bretherton, 1994: On large-scale circulations in convecting atmospheres. *Q. J. R. M. S.*, **120**, 1111-1143

Ferranti, L., T. N. Palmer, F. Molteni, and E. Klinker 1990: Tropical-extratropical interaction associated with the 30 – 60 day oscillation and its impact on medium and extended range prediction, *J. Atmos. Sci.,* **47**, 2177–2199.

Frank, W. M., and P. E. Roundy, 2006: The relationship between tropical waves and tropical cyclogenesis. *Mon. Wea. Rev.*, **134**, 2397-2417.

Fuchs, Z., and D. J. Raymond, 2002: Large-scale modes of a non-rotating atmosphere with water vapor and cloud–radiation feedbacks. *J. Atmos. Sci.,* **59**, 1669–1679.

Fuchs, Z., and D. J. Raymond, 2005: Large-scale modes in a rotating atmosphere with radiative–convective instability and WISHE. *J. Atmos. Sci*., **62**, 4084–4094.

Gill, A. E., 1982: Atmosphere–Ocean Dynamics. Academic Press, 438–439.

Goswami, B. N., 2005: South Asian Summer Monsoon: An overview: in The Global Monsoon System: Research and Forecast Edited by C.-P. Chang, Bin Wang, Ngar-Cheung Gabriel Lau, Chapter 5, pp 47

Grabowski, W. W., 2001: Coupling cloud processes with the large-scale dynamics using the Cloud-Resolving Convection Parameterization (CRCP). *J. Atmos. Sci.*, **58**, 978-997.

Grabowski, W. W., 2003: MJO-like coherent structures: Sensitivity simulations using the Cloud-Resolving Convection Parameterization (CRCP). *J. Atmos. Sci.*, **60**, 847-864

Gruber, A. 1974: Wavenumber-frequency spectra of satellite measured brightness in tropics. *J. Atmos. Sci.,* **31**, 1675—1680

Gutzler, D. S., and R. M. Ponte 1990: Exchange of momentum among atmosphere, ocean, and solid earth associated with the Madden-Julian Oscillation, *J. Geophys. Res*., **95**, 18,679– 18,686.

Hall, J. D., A. J. Matthews, and D. J. Karoly 2001: The modulation of tropical cyclone activity in the Australian region by the Madden-Julian Oscillation, *Mon. Weather Rev.*, **129**, 2970– 2982.

Haertel, P. T., and G. N. Kiladis, 2004: Dynamics of 2-day equatorial waves. *J. Atmos. Sci.,* **61**, 2707–2721.

Haertel, P. T., G. N. Kiladis, A. Denno, and T. Rickenbach, 2008: Vertical mode decompositions of 2-Day waves and the Madden Julian Oscillation. *J. Atmos. Sci.,* **65**, 813-833.

Hayashi, Y. A., 1970: A theory of large-scale equatorial waves generated by condensation heat and accelerating the zonal wind. *J. Meteor. Soc. Japan*, **48**, 140–160.

Hayashi, Y.-Y., and A. Sumi, 1986: The 20–30-day oscillations simulated in an "aquaplanet" model. *J. Meteor. Soc. Japan,* **64**, 451–467.

Hendon, H. H. and B Liebmann, 1990: The Intraseasonal (30-50 day) Oscillation of the Australian Summer Monsoon. *J. Atmos. Sci.,* **47**, 2909-2923.

Hendon, H. H., B. Liebmann, M. E. Newman, J. D. Glick, and J. E. Schemm 2000: Medium-range forecast errors associated with active episodes of the Madden-Julian Oscillation, *Mon. Weather Rev.,* **128**, 69–86.

Hendon, H. H. and M. L. Salby, 1994. The Life Cycle of the Madden-Julian Oscillation, *J. Atmos. Sci.*, **51**, 2225-2237

Hendon, H.H., M. C. Wheeler, and C. Zhang 2007: Seasonal dependence of the MJO-ENSO relationship. *J. Climate,* **20**, 531-543.

Hidayat, R. and S. Kizu, 2010: Influence of the Madden–Julian Oscillation on Indonesian rainfall variability in austral summer, *Int. J. Clim*., **30**, 1816-1825.

Higgins, R. W., and W. Shi, 2001: Intercomparison of the principal modes of interannual and intraseasonal variability of the North American monsoon system, *J. Climate,* **14**, 403–417.

Holton, J. R. 2004: An Introduction to Dynamic Meteorology, (4th Ed.), Elsevier, pp 290-291

Hoskins, B. J., and G.-Y. Yang, 2000: The equatorial response to higher-latitude forcing. *J. Atmos. Sci.*, **57**, 1197–1213.

Hu, Q., and D. A. Randall, 1994: Low-frequency oscillations in radiative-convective systems, *J. Atmos. Sci*., **51**, 1089–1099.

Hu, Q., and D. A. Randall, 1995: Low-frequency oscillations in radiative-convective systems. Part II: An idealized model, *J. Atmos. Sci*., **52**, 478–490.

Jiang, X., T. Li, and B. Wang, 2004: Structures and Mechanisms of the Northward Propagating Boreal Summer Intraseasonal Oscillation. *J. Climate*, **17**, 1022–1039.

Johnson, R. H., T. M. Rickenbach, S. A. Rutledge, P. E. Ciesielski, and W. H. Schubert, 1999: Trimodal characteristics of tropical convection. *J. Climate*, **12**, 2397–2418.

Jones, C., 2000: Occurrence of Extreme Precipitation Events in California and Relationships with the Madden–Julian Oscillation. *J. Climate*, **13**, 3576–3587.

Jones, C., and J.-K. E. Schemm 2000: The influence of intraseasonal variations on medium-range weather forecast over South America, *Mon. Weather Rev.,* **128**, 486–494.

Kemball-Cook, S. R., and B. C. Weare, 2001: The onset of convection in the Madden Julian Oscillation, *J. Climate*, **14**, 780–793.

Kessler. W. S., M. J. McPhaden, and K. M. Weickmann, 1995: Forcing of intraseasonal Kelvin waves in the equatorial Pacific. *J. Geophys. Res.*, **100**, 613—631.

Khairoutdinov, M. F. and D. A. Randall, 2001: A cloud resolving model as a cloud parameterization in the NCAR Community Climate System Model: Preliminary results. *Geophys. Res. Let.*, **28**, 3617--3620.

Khairoutdinov, M. F., D. A. Randall, and C. DeMott, 2005: Simulations of the atmospheric general circulation using a cloud-resolving model as a superparameterization of physical processes. *J. Atmos. Sci.*, **62**, 2136--2154.

Khairoutdinov, M., C. A. DeMott, and D. A. Randall, 2008: Evaluation of the simulated interannual and subseasonal variability in an AMIP-style simulation using the CSU Multiscale Modeling Framework. *J. Climate*, **21**, 413-431.

Khouider, B., and A. J. Majda, 2006a: Multicloud convective parameterizations with crude vertical structure. *Theor. Comput. Fluid Dyn.*, **20**, 351–375.

Khouider, B., and A. J. Majda, 2006b: A simple multicloud parameterization for convectively coupled tropical waves. Part I: Linear analysis. *J. Atmos. Sci.*, **63**, 1308—1323

Khouider, B. and A. J. Majda, 2008: Multicloud models for organized tropical convection: Enhanced congestus heating. *J. Atmos. Sci.*, **65**, 895–914.

Kikuchi, K., and Y. N. Takayuba, 2004: The development of organized convection associated with the MJO during TOGACOARE IOP: Trimodal characteristics. *Geophys. Res. Lett.,* **31**, L10101.

Kiladis, G. N., K. H. Straub, and P. T. Haertel, 2005: Zonal and vertical structure of the Madden-Julian Oscillation. *J. Atmos. Sci.,* **62**, 2790-2809.

Kiladis, G. N., M. C. Wheeler, P. T. Haertel, K. H. Straub, and P. E. Roundy, 2009: Convectively coupled equatorial waves. *Rev. Geoph.*, **47**, 2008RG000266

Kim, D., K. Sperber, W. Stern, D. Waliser, I.-S. Kang, E. Maloney, W. Wang, K. Weickman, J. Benedict, M. Khairoutdinov, M.-I. Lee, R. Neale, M. Suarez, K. Thayer-Calder, and G. Zhang, 2009: Application of MJO Simulation Diagnostics to Climate Models. *J. Climate,* **22**, 6413—6436.

Kiranmayi, L., and E. D. Maloney, 2011: Intraseasonal moist static energy budget in reanalysis data. *J. Geophys. Res.*, **116**, D21117

Krishnamurti, T. N., D. Subrahmanyam, 1982: The 30–50 Day Mode at 850 mb During MONEX. *J. Atmos. Sci*., **39**, 2088–2095.

Kuang, Z., and C. S. Bretherton, 2006: A mass-flux scheme view of a high-resolution simulation of a transition from shallow to deep cumulus convection. *J. Atmos. Sci.*, **63**, 1895--1909.

Kuang, Z., 2008a: Modeling the interaction between cumulus convection and linear gravity waves using a limited-domain cloud system–resolving model. *J. Atmos. Sci.*, **65**, 576–591.

Kuang, Z., 2008b: A Moisture-Stratiform Instability for Convectively Coupled Waves. *J. Atmos. Sci.,* **65**, 834--834.

Kuang, Z. 2011: The wavelength dependence of the gross moist stability and the scale selection in the instability of column integrated moist static energy, *J. Atmos. Sci.,* **68**, 61-74.

Langley, R. B., R. W. King, I. I. Shapiro, R. D. Rosen, and D. A. Salstein, 1981: Atmospheric angular momentum and the length of the day: A common fluctuation with a period of 50 days, *Nature*, **294**, 730–732.

Lau, K.-M. and P. H. Chan, 1986: Aspects of the 40-50 day oscillation during the northern summer as inferred from outgoing longwave radiation. *Mon. Wea. Rev*., **114**, 1354-1367.

Lau, K.-M., and L. Peng, 1987: Origin of low-frequency (intraseasonal) oscillations in the tropical atmosphere. Part I: Basic theory, *J. Atmos. Sci*., **44**, 950–972.

Lau, K-M., L. Peng, 1990: Origin of Low Frequency (Intraseasonal) Oscillations in the Tropical Atmosphere. Part III: Monsoon Dynamics. *J. Atmos. Sci.*, **47**, 1443–1462.

Lau, K.-M. and H.-T. Wu, 2010: Characteristics of Precipitation, Cloud and Latent Heating Associated with the Madden-Julian Oscillation. *J. Climate*., **23**, 504-518

Lau, K-M., C-H. Sui, 1997: Mechanisms of Short-Term Sea Surface Temperature Regulation: Observations during TOGA COARE. *J. Climate*, **10**, 465–472.

Lau, N. C., and K. M. Lau, 1986: Structure and Propagation of Intraseasonal Oscillation Appearing in a GFDL GCM. *J. Atmos. Sci*., **43**, 2023-2047.

Lawrence, D. and P. J. Webster, 2002: The boreal summer intraseasonal oscillation and the South Asian monsoon. *J. Atmos. Sci*., **59**, 1593-1606.

Leroy, A. and M. C. Wheeler, 2008: Statistical Prediction of Weekly Tropical Cyclone Activity in the Southern Hemisphere, *Mon. Wea. Rev.*, **136**, 3637-3657.

Liebmann, B., H. Hendon, and J. Glick, 1994: The relationship between tropical cyclones of the western Pacific and Indian oceans and the Madden-Julian Oscillation*, J. Meteorol. Soc. Jpn*., **72**, 401–411.

Liebmann, B., and C. A. Smith, 1996: Description of a complete (Interpolated) outgoing longwave radiation dataset. *Bul. of the Amer. Meteorol. Soc.*, **77**, 1275-1277.

Liebmann, B, G. N. Kiladis, C. S. Vera, A. C. Saulo, and L. M.V. Carvalho, 2004: Subseasonal variations of Rainfall in South America in the Vicinity of the Low-Level Jet East of the Andes and Comparison to Those in the South Atlantic Convergence Zone. *J. Climate*, **17**, 3829-3842.

Lin, J.-L., and B. E. Mapes, 2004: Radiation budget of the tropical intraseasonal oscillation. *J. Atmos. Sci*., **61**, 2050–2062.

Lin, J.-L., G.N. Kiladis, B.E. Mapes, K.M. Weickmann, K.R. Sperber, W. Lin, M.C. Wheeler, S.D. Schubert, A. Del Genio, L.J. Donner, S. Emori, J.-F. Gueremy, F. Hourdin, P.J. Rasch, E. Roeckner, and J.F. Scinocca, 2006: Tropical intraseasonal variability in 14 IPCC AR4 climate models. Part I: Convective signals. *J. Climate*, **19**, 2665-2690, doi:10.1175/JCLI3735.1

Lindzen, R. S., 1974: Wave-CISK in the tropics. *J. Atmos. Sci.*, 31, 156–179.

Lindzen, R. S., 2003: The interaction of waves and convection in the tropics. *J. Atmos. Sci.,* **60**, 3009–3020.

Liu, F., G. Huang, and L. Feng, 2011: Why do 2-day waves propagate westward? *Theor. Appl. Climatol.*, **106**, 443—448.

McPhaden, M. J. 2008: Evolution of the 2006-2007 El Nino: The role of intraseasonal to interannual time scale dynamics. *Adv. Geosci.*, **14**, 219—230.

Ma, D., Z. Kuang, 2011: Modulation of radiative heating by the Madden-Julian Oscillation and convectively coupled Kelvin waves as observed by CloudSat. *Geophys. Res. Lett.,* **38**, L21813.

Madden, R. A., and P. R. Julian 1971: Detection of a 40–50 day oscillation in the zonal wind in the tropical Pacific, *J. Atmos. Sci*., **28**, 702–708.

Madden, R. A., and P. R. Julian 1972: Description of global-scale circulation cells in the tropics with a 40 – 50 day period, *J. Atmos. Sci*., **29**, 1109–1123.

Madden, R. A., 1986: Seasonal variations of the 40 – 50 day oscillation in the tropics, *J. Atmos. Sci.,* **43**, 3138–3158.

Majda, A. and M. Schefter, 2001: Waves and instabilities for model tropical convective parameterizations, *J. Atmos. Sci.*, **8**, 896-941.

Maloney, E. D., and D. L. Hartmann, 1998: Frictional moisture convergence in a composite life cycle of the Madden-Julian Oscillation, *J. Climate*, **11**, 2387–2403.

Maloney, E. D., and D. L. Hartmann 2000: Modulation of eastern North Pacific hurricanes by the Madden-Julian Oscillation, *J. Climate*, **13**, 1451–1460.

Maloney, E. D., and D. L. Hartmann 2001: The Madden-Julian oscillation, barotropic dynamics, and North Pacific tropical cyclone formation. Part I: Observations, *J. Atmos. Sci.,* **58**, 2545–2558.

Maloney, E. D., and M. J. Dickinson, 2003: The intraseasonal oscillation and the energetics of summertime tropical western North Pacific synoptic-scale disturbances. *J. Atmos. Sci.,* **60**, 2153–2168.

Maloney, E. D., and A. H. Sobel, 2004: Surface fluxes and ocean coupling in the tropical intraseasonal oscillation. *J. Climate*, **17**, 4368–4386.

Maloney, E. D., and S. K. Esbensen, 2007: Satellite and buoy observations of boreal summer intraseasonal variability in the tropical northeast Pacific. *Mon. Wea. Rev.,* **135**, 3–19.

Maloney, E. D., 2009: The Moist Static Energy Budget of a Composite Tropical Intraseasonal Oscillation in a Climate Model. *J. Climate*., **22**, 711–729.

Maloney, E. D., A. H. Sobel, and W. M. Hannah, 2010: Intraseasonal Variability in an Aquaplanet General Circulation Model. *J.A.M.E.S*., **2**, 5.

Mapes, B. E., and P. Zuidema, 1996: Radiative-dynamical consequences of dry tongues in the tropical troposphere. *J. Atmos. Sci.,* **53**, 620–638.

Mapes, B. E., 2000: Convective inhibition, subgrid-scale triggering energy, and stratiform instability in a toy tropical wave model. *J. Atmos. Sci*., **57**, 1515--1535.

Mapes, B. E., and R. A. Houze Jr., 1995: Diabatic divergence profiles in western Pacific mesoscale convective systems. *J. Atmos. Sci.*, **52**, 1807–1828.

Masunaga, H., T. S. L'Ecuyer, and C. D. Kummerow, 2006: The Madden–Julian oscillation recorded in early observations from the Tropical Rainfall Measuring Mission (TRMM). *J. Atmos. Sci.,* **63**, 2777–2794.

Matsuno, T., 1966: Quasi-geostrophic motions in the equatorial area. *J. Meteor. Soc. Japan,* **44**, 25–43.

Matthews, A. J., 2000: Propagation mechanisms for the Madden- Julian Oscillation, *Q. J. R. M. S.*, **126**, 2637–2651.

Matthews AJ, 2004: Intraseasonal variability over tropical Africa during northern summer. *J. Climate*, **17**, 2427-2440.

Mo, K. C. and R. W. Higgins, 1998: Tropical influences on California precipitation. *J. Climate,* **11**, 412-430.

Myers, D. S., & Waliser, D. E., 2003: Three-Dimensional Water Vapor and Cloud Variations Associated with the Madden-Julian Oscillation during Northern Hemisphere Winter. *J. Climate*, **16**, 929-950.

Nakazawa, T., 1988: Tropical super clusters within intraseasonal variations over the western Pacific, *J. Meteorol. Soc. Jpn*., **66**, 823 – 836.

Neelin, J. D., and I. M. Held, 1987: Modeling tropical convergence based on the moist static energy budget. *Mon. Wea. Rev.,* **115**, 3–12.

Neelin, J. D., I. M. Held, and K. H. Cook, 1987: Evaporation- wind feedback and low-frequency variability in the tropical atmosphere, *J. Atmos. Sci*., **44**, 2341–2348.

Neelin, J. D., and J. Y. Yu, 1994: Modes of tropical variability under convective adjustment and the Madden–Julian oscillation. Part I: Analytical theory. *J. Atmos. Sci.*, **51**, 1876–1894.

Nieto Ferreira, R., W. H. Schubert, and J. J. Hack, 1996: Dynamical aspects of twin tropical cyclones associated with the Madden-Julian Oscillation, J. Atmos. Sci., 53, 929–945.

Paegle, J. N., L. A. Byerle, and K. C. Mo, 2000: Intraseasonal modulation of South American summer precipitation. *Mon. Wea. Rev*., **128**, 837-850.

Peters, M. E., and C. S. Bretherton, 2006: Structure of tropical variability from a vertical mode perspective. *Theor. Comput. Fluid. Dyn.*, **20**, 501–524, doi:10.1007/s00162-006-0034-x.

Peters, M. E., Z. Kuang, and C. Walker, 2008: Analysis of atmospheric energy transport in ERA40 and implications for simple models of the mean tropical circulation, *J. Climate*, **21**, 5229-5241

Peters, O., and J. D. Neelin, 2006: Critical phenomena in atmospheric precipitation. *Nature Phys.,* **2**, 393–396.

Posselt, D. J., S van den Heever, G. Stephens, and M. R. Igel, 2012: Changes in the Interaction between Tropical Convection, Radiation, and the Large-Scale Circulation in a Warming Environment. *J. Climate*, **25**, 557—571.

Raymond, D. J., 2000: Thermodynamic control of tropical rainfall. *Q. J. R. M. S.,* **126**, 889–898.

Raymond, D. J., 2001: A new model of the Madden–Julian oscillation. *J. Atmos. Sci*., **58**, 2807–2819.

Raymond, D. J., G. B. Raga, C. S. Bretherton, J. Molinari, C. Lopez-Carrillo, and Z. Fuchs, 2003: Convective forcing in the intertropical convergence zone of the eastern Pacific. *J. Atmos. Sci.*, **60**, 2064–2082.

Raymond, D. J., and Z. Fuchs, 2007: Convectively coupled gravity and moisture modes in a simple atmospheric model. *Tellus*, **59A**, 627–640.

Raymond, D.J., and Z. Fuchs, 2009: Moisture Modes and the Madden-Julian Oscillation. *J. Climate*, **22**, 3031—3046.

Rayner, N.A., P. Brohan, D. E. Parker, C. K. Folland, J. J. Kennedy, M. Vanicek, T. Ansell and S. F. B. Tett, 2006: Improved analyses of changes and uncertainties in sea surface temperature measured *in situ* since the mid-nineteenth century: the HadSST2 data set. *J. Climate,* **19**, 446-469

Redelsperger, J,-L., D. B. Parsons, and F. Guichard, 2002: Recovery processes and factors limiting cloud-top height following the arrival of a dry intrusion observed during TOGA COARE. *J. Atmos. Sci*., **59**, 2438--2457.

Ridout, J. A., 2002: Sensitivity of tropical Pacific convection to dry layers at mid- to upper levels: Simulation and parameterization tests. *J. Atmos. Sci*., **59**, 3362--3381.

Roca, R., S. Louvet, L. Picon, and M. Desbois, 2005: A study of convective systems, water vapor and top of the atmosphere cloud radiative forcing over the Indian Ocean using INSAT-1B and ERBE data. *Meteorol. Atmos. Phys.,* **90**, 49--65.

Roundy, P. E., and W. M. Frank, 2004: Climatology of Waves in the Equatorial Region. *J. Atmos. Sci*., **61**, 2105--2132

Rui, H., and B. Wang, 1990, Development characteristics and dynamic structure of tropical intraseasonal convection anomalies, *J. Atmos. Sci*., **47**, 357–379.

Salby, M. L., and H. H. Hendon 1994: Intraseasonal behavior of clouds, temperature, and winds in the tropics, *J. Atmos. Sci.,* **51**, 2207 – 2224.

Sherwood, S. C., 1999: Convective precursors and predictability in the tropical western Pacific. *Mon. Wea. Rev*., **127**, 2977--2991.

Sikka, D. R. and S. Gadgil, 1980: On the maximum cloud zone and ITCZ over the Indian longitudes during the southwest monsoon. *Mon. Wea. Rev*., **108**, 1122-1135.

Slingo, J. M., Boyle, J. S., Ceron, J.-P., Dix, M., Dugas, B., Ebisuzaki, W., Fyfe, J., Gregory, D., Gueremy, J.-F., Hack, J., Harzallah, A., Inness, P., Kitoh, A., Lau, W. K.-M., McAvaney, B., Madden, R., Matthews, A., Palmer, T. N., Park, C.-K., Randall, D., and Renno, N. (1996). Intraseasonal oscillations in 15 atmospheric general circulation models: Results from an AMIP diagnostic subproject. *Climate Dynamics*, **12**, 325-357.

Sobel, A. H. and H. Gildor 2003: A Simple Time-Dependent Model of SST Hot Spots. *J Climate,* **16**, 3978-3992.

Sobel, A. H., S. E. Yuter, C. S. Bretherton, and G. N. Kiladis, 2004: Large-scale meteorology and deep convection during TRMM KWAJEX. *Mon. Wea. Rev*., **132**, 422–444.

Sobel, A. H., E. D. Maloney, G. Bellon, and D. M. Frierson, 2010: Surface Fluxes and Tropical Intraseasonal Variability: a Reassessment. *J.A.M.E.S.*, **2**, 2, doi:10.3894/JAMES.2010.2.2

Stephens, G. L., P. J. Webster, R. H. Johnson, R. Engelen, and T. L'Ecuyer, 2004: Observational evidence for the mutual regulation of the tropical hydrological cycle and tropical sea surface temperatures. *J. Climate*, **17**, 2213–2224.

Straub, K. H., and G. N. Kiladis, 2002: Observations of a convectively coupled Kelvin wave in the eastern pacific ITCZ. *J. Atmos. Sci*., **59**, 30–53.

Sugiyama, M., 2009a: The Moisture Mode in the Quasi-Equilibrium Tropical Circulation Model. Part I: Analysis Based on the Weak Temperature Gradient Approximation. *J. Atmos. Sci*., **66**, 1507–1523.

Sugiyama, M., 2009b: The Moisture Mode in the Quasi-Equilibrium Tropical Circulation Model. Part II: Nonlinear Behavior on an Equatorial β Plane. *J. Atmos. Sci.*, **66**, 1525–1542.

Sui, K. -H. and K. -M. Lau, 1992: Multiscale Phenomenon in the Tropical Atmosphere over the Western Pacific. *Mon. Wea. Rev*., **120**, 407-430.

Takayabu, Y. N., 1994: Large-scale cloud disturbances associated with equatorial waves. Part II: Westward-propagating inertio-gravity waves. *J. Meteor. Soc. Japan*, **72**, 451–465.

Takemi, T., O. Hirayama, and C. Liu, 2004: Factors responsible for the vertical development of tropical oceanic cumulus convection. *Geophys. Res. Lett*., **31**, L11109.

Tian, B., D. E. Waliser, E. J. Fetzer, B. H. Lambrigtsen, Y. Yung, and B. Wang, 2006: Vertical moist thermodynamic structure and spatial–temporal evolution of the MJO in AIRS observations. *J. Atmos. Sci.,* **63**, 2462–2485.

Vitart, F. (2009):Impact of the Madden Julian Oscillation on tropical storms and risk of landfall in the ECMWF forecast system, *Geophys. Res. Lett.*, **36**, L15802, doi:10.1029/2009GL039089.

Waliser, D. E., K. Jin, I.-S. Kang, W. F. Stern, S. D. Schubert, M.L.C. Wu, K.-M. Lau, M.-I. Lee, V. Krishnamurthy, A. Kitoh, G. A. Meehl, V. Y. Galin, V. Satyan, S. K. Mandke, G. Wu, Y. Liu, and C.-K. Park, 2003: AGCM Simulations of Intraseasonal Variability Associated with the Asian Summer Monsoon, *Clim. Dyn*., **21**, 423-446

Waliser, D. E., K. Weickmann, R. Dole, S. Schubert, O. Alves, C. Jones, M. Newman, H.-L. Pan, A. Roubicek, C. Smith, H. van den Dool, F. Vitart, M. Wheeler, J. Whitaker, 2006: The Experimental MJO Prediction Project. Bull. American Meteo. Soc., 87, 425-431

Wang, B., 1988: Dynamics of tropical low-frequency waves: An analysis of the moist Kelvin wave, *J. Atmos. Sci*., **45**, 2051 – 2065.

Wang, B., and H. Rui, 1990a: Synoptic climatology of transient tropical intraseasonal convective anomalies: 1975 – 1985, *Meteorol. Atmos. Phys*., **44**, 43–61.

Wang B., and H. Rui, 1990b: Dynamics of the Coupled Moist Kelvin-Rossby Wave on an Equatorial B-Plane. *J. Atmos. Sci,* **47**, 397-413

Wang, B. and X. Xie, 1997: A model for the boreal summer Intraseasonal Oscillation. *J. Atmos. Sci*., **54**, 72-86.

Wang, W., and M. E. Schlesinger, 1999: The dependence on convection parameterization of the tropical intraseasonal oscillation simulated by the UIUC 11-layer atmospheric GCM. *J. Climate*, **12**, 1423–1457.

Webster, P. J., 1983: Mechanisms of Monsoon Transition: Surface Hydrology Effects. *J. Atmos. Sci*., **40**, 2110-2124.

Weickmann, K. M., 1983: Intraseasonal Circulation and Outgoing Longwave Radiation Modes During Northern Hemisphere Winter. *Mon. Wea. Rev*., **111**, 1838--1858.

Weickmann, K. M., G. N. Kiladis, and P. D. Sardeshmukh, 1997: The dynamics of intraseasonal atmospheric angular momentum oscillations, *J. Atmos. Sci*., **54**, 1445–1461.

Wheeler, M. and G. N. Kiladis, 1999: Convectively Coupled Equatorial Waves: Analysis of Clouds and Temperature in the Wavenumber-Frequency Domain. J. *Atmos. Sci.*, **56**, 374–399.

Wilks D. S., 2006: Statistical Methods in the Atmospheric Sciences (2nd Ed.), Elsevier, pp 180-196

Williamson D. L., M. Blackburn, B. J. Hoskins, K. Nakajima, W. Ohfuchi, Y. O. Takahashi, Y.-Y. Hayashi, H. Nakamura, M. Ishiwatari, J. L. McGregor, H. Borth, V. Wirth, H. Zhao, P. Bechtold, N. P. Wedi, H. Tomita, M. Satoh, M. Zhao, I. M. Held, M. J. Suarez, M.-I. Lee, M Watanabe, M. Kimoto, Y. Liu, Z. Wang, A. Molod, K. Rajendran, A. Kitoh, and R. Stratton, 2012: The APE Atlas. *NCAR Technical Note*, NCAR/TV-484+STR

Woolnough, S. J., J. M. Slingo, and B. J. Hoskins, 2001: The organization of tropical convection by intraseasonal sea surface temperature anomalies. *Q. J. R. M. S.,***127**, 887– 907.

Xie, P., and P. A. Arkin, 1997: Global precipitation: A 17-year monthly analysis based on gauge observations, satellite estimates, and numerical model outputs. *Bull. Am. Meteorol. Soc.*, **78**, 2539–2558.

Yamasaki, M., 1969: Large-scale disturbances in a conditionally unstable atmosphere in low latitudes. *Pap. Meteor. Geophys.* **20**, 289—336.

Yanai, M, B Chen, W.-W Tung, 2000: The Madden–Julian Oscillation Observed during the TOGA COARE IOP: Global View. *J. Atmos. Sci*., **57**, 2374–2396.

Yang, G-Y., B. Hoskins, and J. Slingo, 2007: Convectively coupled equatorial waves. Part I: Horizontal and vertical structures. *J. Atmos. Sci*., **64**, 3406–3423.

Yasunaga, K., and B. E. Mapes, 2011: Differences between more-divergent vs. more-rotational types of Convectively Coupled Equatorial Waves. Part I: Space-Time Spectral Analyses. *J. Atmos. Sci.,* **69**, 3—16, doi: 10.1175/JAS-D-11-033.1

Yasunari, T., 1979: Cloudiness fluctuations associated with the Northern Hemisphere summer monsoon, *J. Meteorol. Soc. Jap*., **57**, 227–242.

Zangvil, A. 1975: Temporal and spatial behavior of large-scale disturbances in tropical cloudiness deduced from satellite brightness data. *Mon. Wea. Rev.*, **103**, 904—920.

Zhang, C., and P. J. Webster, 1992: Laterally forced equatorial perturbations in a linear model. Part I: Stationary transient forcing. *J. Atmos. Sci*., **49**, 585–607.

Zhang, C., and H. H. Hendon, 1997: On propagating and stationary components of the intraseasonal oscillation in tropical convection, *J. Atmos. Sci*., **54**, 741–752.

Zhang, C., 1996: Atmospheric intraseasonal variability at the surface in the western Pacific Ocean. *J. Atmos. Sci.,* **53**, 739–758.

Zhang, C., 2005: Madden-Julian Oscillation. *Rev. Geophys.,* **43**, RG2003.

Zhang, C, M. Dong, S. Gualdi, H. H. Hendon, E. D. Maloney, A. Marshall, K. R. Sperber, and W. Wang, 2006: Simulations of the Madden-Julian Oscillation by Four Pairs of Coupled and Uncoupled Global Models. *Climate Dynamics*, **27**, 573-592. doi: 10.1007/s00382-006-0148-2.

Zhang, C. and J. Ling, 2012: Potential Vorticity of the Madden-Julian Oscillation. *J. Atmos. Sci.*, **69**, 65—78.

Zhu, H., H. Hendon, and C. Jakob, 2009: Convection in a Parameterized and Superparameterized Model and Its Role in the Representation of the MJO. *J. Atmos. Sci.*, **66**, 2796–2811.